Particle Acceleration in Dynamical Collisionless Reconnection

by

Panagiota Petkaki Ptychion

Thesis
submitted to the
University of Glasgow
for the degree of
Ph.D.

Astronomy and Astrophysics Group
Department of Physics and Astronomy,
University of Glasgow,
Glasgow G12 8QQ

December 1995

ProQuest LLC.
789 East Eisenhower Parkway
P.O. Box 1346
Ann Arbor, MI 48106 – 1346

To my parents

Στη Μαριανθη και στο Γιωργο

Acknowledgements

I want to the thank all the people in the Astronomy and Astrophysics group for their help and friendship during my PhD in Glasgow.

I would especially like to thank both my supervisors, Dr Alec L. MacKinnon and Prof. John C. Brown for their help and guidence during my study at Glasgow. With out them this work would not have been possible. Specially Alec for finding time to discuss with me when a thousand other things were going on at the same time and for always being enthousiastic about solar physics. John, thank you for providing the opportunities for international travelling and for having a critical eye for research.

Dr Keith Macpherson and Dr Andy Newsam have provided me with invaluable help with computers. Thanks, Andy, especially for all the guidance in British and international theatre and Keith for your general introduction to malt whisky and Scottish country dancing. Dr Lyndsay Fletcher, thank you for being a lovely friend and landlady, Dr Kenny Wood for being always a cheerful person, Dr David Alexander for all those jokes and cracks, Dr Richard Barrett, Ute Barrett and Dr Lorna Richardson for numerous pub-goings.

Dr Shashi Kanbur thank you for dancing with me in Club Cubana, Dr Norman Gray for lots of (not entirely sober) philosophical discussions. Dr Valentina Zarkova, Sarah Matthews, Dr Andrew Conway for useful "discussions", Aidan Keane and Iain Coleman for being a cheerful duo of officemates. Dr Kostas Papadakis for his friendly Greek presence in the department. Thanks Dr John F.L. Simmons for being a good friend and for asking lots of difficult questions. A special thank you also to Daphne Davidson for her friendly presence and valuable help with British bureaucracy. Also thanks to Dr David Clarke and Dr Robin Green.

Luke Taylor, Dr Rebecca Crawford and Dr Baz Ewins thank you for having cold bottles

of Budvar on the roof with me. Aggeliki Malliri, thank you for your friendship and your hospitality and Natalie Menager for being a wonderful flatmate.
Most of all I want to thank my parents, Georgo and Marianthi Petkaki for their emotional support. My sister Fotini Petkaki, I want to thank for always being there to listen to my problems and complaints and to share my joys. Without the continuous presence (even remotely) of my family I couldn't have completed this work.

Summary

The work presented in this thesis is concerned with how particle acceleration can take place in the context of dynamical magnetic reconnection in collisionless coronal plasmas. The energy production mechanism in solar flares has been a long standing problem of solar physics. The mechanism that provides the energy during solar flares is thought to be magnetic reconnection. However, timescales from different models disagree. Most magnetohydrodynamic models do not explain the high energy particles observed during solar flares and most collisionless models fail in that they do not account for the dynamic evolution of the solar flare environment.

This thesis is divided in seven chapters. I will summarise each chapter individually. Chapter 1 contains a brief overview of the properties of the Sun and the structure of its atmosphere. Then follows a much more detailed discussion of energetic phenomena in the Sun concentrating primarily on solar flares and solar noise storms, and their manifestations in the electromagnetic spectrum and production of high energy particles.

An introduction to magnetic reconnection is given in Chapter 2. Magnetic reconnection is defined as the process whereby plasma flows across a surface that separates regions containing topologically different magnetic field lines. We briefly discuss some of the most important models for magnetic reconnection. The models are divided in hydromagnetic and collisionless models. We also discuss mechanism for particle acceleration in cosmic plasmas. The mechanisms of particle acceleration are: diffusive shock acceleration, stochastic acceleration and electric field acceleration. I review some mechanism of particle accelaration in X-type neutral points and their implications for energy distributions produced.

In Chapter 3 we present the results of a non self-consistent calculation for collisionless magnetic reconnection. First we assume the form of the electric and magnetic fields, a

procedure which is not necessarily self-consistent. The magnetic field is taken to have an X-type neutral point. Two cases for the imposed electric fields are considered, one constant and the other time-varying. The amplitude of the electric field is treated as a parameter. We calculate the particle orbits in these fields and the resulting energy distributions and show that protons and electrons may gain relativistic energies in times $< 1s$ for plausible (small) electric field amplitudes and active region magnetic fields. We note the effectiveness of acceleration of protons and electrons varies according to the frequency of oscillation invoked. It seems that electrons, when they are accelerated, are accelerated more rapidly than protons, although numerical limitations prevented us from investigating this possibility in full. Protons are accelerated to γ ray producing energies.

In Chapter 4 we formally derive an analytical description for the time and space dependence of a linear incompressible, azimuthally symmetric disturbance propagating in a medium with a neutral point. In deriving the expression for the magnetic disturbance we follow Craig and McClymont (1991) fairly closely. There are however the important differences between our treatment and theirs: we recast the problem in dimensionless variables for consistency with the integration of the particle orbits, and introduce a slight restriction on the possible modes of interest. The latter has the consequence that the final, hypergeometric function form of the solution is always exact (cf. Craig, 1994). Also we give heavier emphasis than other work to the numerical evaluation of the eigenfunctions. We use this description to study the detailed form and behaviour of reconnective eigenvalues, as a preliminary step in addressing the problem of the particle orbits.

In the Chapter 5 we study particle orbits in the presence of such a disturbance. A general feature of the orbits is that particles remain relatively close to the neutral point during the integration time of 1 second. The particles that are accelerated to high energies are those that are trapped close to neutral point area. This happens for specific values of the 'resistivity' owing to the spatial form of the electric and magnetic field perturbation. Particle orbits are calculated for the fundamental and higher eigenmodes.

In Chapter 6 we attempt to match the MHD and test particle calculations. To do this we compare the energy loss of the wave during 1 second and the energy gained by the particles during the same time. For all the vaues of the resistivity investigated, the wave loses energy much faster than the particles gain energy. The calculations presented in this Chapter force us to re-examine the nature of 'resistivity'. Particles trapped for long

periods near the neutral point are freely accelerated and clearly extract energy from the wave. However, they do not contribute to the resistivity. Despite the difficulties in defining the 'correct' value of the 'resistivity', we have demonstrated that the passage of such a reconnective disturbance may accelerate protons to γ ray producing energies, and certainly to energies where they could play a role in energy transport.

Contents

List of Tables

List of Figures

Chapter 1

Solar Magnetic Activity and Flares

In this first chapter I give a brief description of solar phenomena that are related to my research. I start by describing the place where these phenomena take place, the solar corona and the chromosphere. Then I talk about the phenomenon itself, the solar flare. I am trying to give an idea of the complexity of the phenomenon by describing briefly its manifestations in different parts of the electromagnetic spectrum. Then I concentrate more on discussing the most energetic of its manifestations, in hard X-rays, γ-rays and energetic particles.

1.1 The Solar Chromosphere

The chromosphere is that part of the solar atmosphere lying between the temperature minimum and T=25000 K, in which the temperature increases outwards. It is split into two, the lower and the upper chromosphere (Athay, 1986). The lower chromosphere lies between the temperature minimum and the first plateau in the temperature at about 6000 K (after the standard semi-empirical quiet Sun model of the chromosphere by Vernazza, Avrett and Loeser, 1981). In this region the magnetic flux tubes that are anchored in the photosphere are well confined by the gas pressure, so the larger part of the plasma is free from magnetic fields. As one moves upwards, and the temperature rises, the density and pressure drop and so the magnetic flux tubes expand. This magnetically dominated part is called upper chromosphere.

Radiation from the chromosphere is dominated by emission and absorption lines. There is strong emission in the Hα line, which gives the eclipsing chromosphere a beautiful red color. The calcium K line at 3933 Åis also strong and it indicates a temperature of 6000 K. Other lines come from the highly ionised states of magnesium, carbon and potassium and they indicate regions with a temperature of $\sim$ 10000 K. The chromosphere is optically thin and all the photons generated in this region escape (except the Lyman series).

1.2 The Solar Corona

The corona is that part of the solar atmosphere above the visible photospheric layer and the chromosphere. It reaches temperatures of the order of a million degrees or more. It can be divided into two components: the quiet corona, which is present throughout the solar cycle, and the 'active' corona which is the sum of the different active regions present in the corona at any time. A very puzzling question not yet answered is what is heating the corona. Since the corona is so much hotter than the underlying photosphere (temperature of the photosphere is 5800 K), the mechanisms that heat the corona must be non-thermal. Several mechanisms have been proposed to heat the corona, and the subject is very controversial (see Zirker 1993). These mechanisms include wave (usually Alfven) heating, electric currents, with or without magnetic reconnection (to be discussed later), and MHD turbulence.

The 'active' corona was not always known. When studies of the corona advanced in the sense that the Sun was observed outside eclipses from space borne experiments, one could see that there is always a lot of structure in the corona. Observations showed that there exist very detailed structures which have large local variations in intensity. (see figure (1.1)) One of the most important sources of nonuniformities in the solar corona are the so called active regions. Active regions are observed to be sites of several dynamical phenomena on the Sun, where large amounts of energy are released (see later in this chapter). Solar flares are one class of these phenomena. Others are: coronal mass ejections (which have been thought to cause flares in some cases), prominence eruptions, radio noise storms, etc. Stars that have similar atmospheric layers to our Sun (in particular outer convective envelopes) exhibit very energetic phenomena like solar flares (Pallavicini, 1993). In soft X-rays the corona emits thermally and can be viewed directly, since the contribution

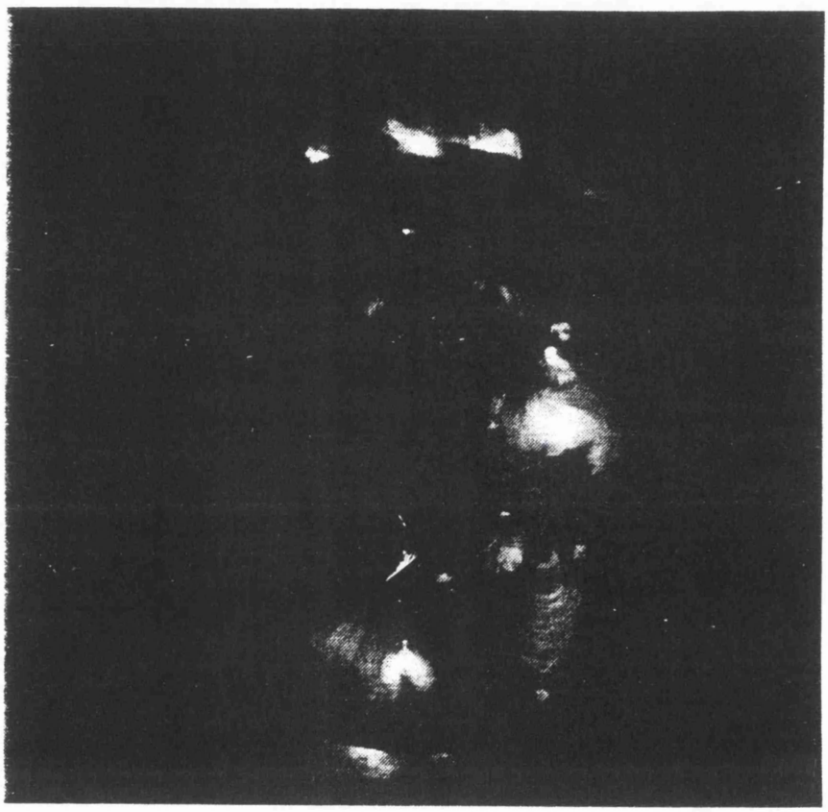

Figure 1.1: X-ray image of the Solar Corona, showing active regions, the quiet corona and coronal holes. This image was acquired by the Soft X-ray Telescope on the Yohkoh solar research spacecraft. (Gabriel 1992)

from the lower atmosphere is negligible. When the corona is observed in soft X-rays two distinct regions appear. Those in which the magnetic field is predominately open appear relatively dark and are known as coronal holes. Here the plasma is outflowing and gives the solar wind. Those in which the magnetic field is closed consist of myriads of coronal loops. Small intense features called X-ray bright points are scattered over the whole disk.

1.2.1 Prominences

Prominences are really chromospheric phenomena, although they extend to the corona and are sometimes the site of very energetic events. A traditional way of looking at the chromosphere of the Sun is by a Lyot filter with bandpass of 1/4 of an Ångstrom usually. At the center of the line, the Sun appears totally without features during minimum and with a lot of plages and filaments when at maximum. Prominences extend 50000 km or more above the photosphere when observed in $H\alpha$ and Ca K lines at the limb of the Sun. When observed on the disk they are in absorption, are called filaments and appear dark. Away from active regions we find the most common prominences. They are high, bladelike quiescent prominences and can last for months. They begin their lives as small active region filaments which are located either along the magnetic inversion line between the two main polarity regions or at the edge of an active region where it meets a surrounding area of opposite polarity. As the active region declines, the prominence grows in size and moves towards the nearest pole. Direct measurements of the prominence magnetic field (using Zeeman and Hanle effects) give values of 5-10 G in quiescent prominences.

The plasma confined in the prominence magnetic field is at t $\sim$ 7000 K, which is cooler than the surrounding plasma at the same height but its density is higher ($10^{10} - 10^{11} cm^3$). Typical prominence dimensions are 200000 km length, 50000 km height and 6000 km width. Studies of line widths in quiescent prominences indicate substantial turbulence near their tops, whereas motions near the prominence bottom are smaller and the structure is also more sharply defined (Priest 1982).

Filaments can be observed to fade away. They are formed within extended volumes of low coronal emission called filament cavities. They are situated along neutral lines of the longitudinal magnetic field (i.e. in regions of horizontal field).

Close to active regions, one often observes matter condensing and falling, particularly into sunspots. Even quiescent filaments and prominences contain plasma moving at high speed

(downflowing motion ~ 5 km sec^{-1}).

Active prominences are usually located in active regions and are usually associated with flares. They are dynamic, violent motions and have lifetimes of only minutes to hours. Both their magnetic field and their density are much higher than those of quiescent prominences. In active region filaments material is seen flowing along the filament axis, and generally into a sunspot located at one end of the structure (Priest 1982).

1.2.2 Active regions

When new emerging flux starts to emerge from below the photosphere of the Sun (emerging flux region), the atmosphere is heated and produces an X-ray bright point. Most of this flux fades away in less than a day. In some though (especially those close to the equatorial plane) magnetic flux keeps emerging and an active region is formed. Active regions are bipolar and at first give rise to a small Hα plage connected by a few small filaments. After a couple of days, the bipolar region typically consists of a pair of sunspots joined by a system of dark loops. The sunspots have opposite polarity. This region evolves more and in a fully developed active region there can be a complex group of sunspots in the photosphere.

The size of a fully developed region can be 200000 km across and it extends up to the corona. It is surrounded by photospheric faculae (brightenings) while its upper part appears as an X-ray enhancement. During all this time material falls down near both ends of the loops at 50 km s^{-1}. The active region decays slower than it emerges. Typically after four solar rotations it has disappeared leaving behind a dark quiescent filament that sometimes can erupt and cause a two-ribbon flare.

In the photosphere the most intense concentrations of magnetic flux show up as sunspots. Even after the disappearance of a sunspot an active region can remain active. The enhanced magnetic field can persist for weeks or months. Active region filaments, which may have formed when the active region was quite young, become more prominent and increase in size as the region develops. Such filaments always lie along a magnetic inversion line. Major solar flares usually occur near the peak of an active region's development, when sunspots are present and when the magnetic structure is more complex (Priest 1982).

The corona above active regions possesses a density and temperature that are typically enhanced by factors of 10 and 2 respectively, actual values being 10^{10} cm^{-3} and in excess

of 3×10^6 K respectively. This makes the active corona visible in white light at the limb during eclipses and also in EUV, X-ray and radio wavelengths against the disk.

1.3 Introduction to Solar Flares

In the present chapter I will discuss the very interesting phenomenon of solar flares and processes associated with them, from an observational viewpoint.

A flare is a phenomenon of the solar atmosphere that produces rapid increases in the electromagnetic radiation from gamma rays to radio wavelengths and high energy particles up to GeV. Its spatial extent is usually 10^4 to 10^5 Km. The total energy released during a flare varies from 10^{28} to 10^{32} ergs. Complex energy release and transport processes are involved. The stored energy of the coronal magnetic field is thought to be responsible for solar flares. In figure (1.2) we can see the basic time behaviour of flare emission in a wide range of frequencies (Zirin 1988).

An initial "preflare" brightening lasting generally a few minutes (but up to tens of hours in some cases) can usually be detected in EUV and soft X-ray radiations. The peak intensity is reached, in most cases, during the flash phase. Impulsive spikes of emission are often seen in metric and microwaves, EUV and hard X-rays during the flash phase. These spikes have time scales of seconds or less and the impulsive phase generally lasts for a few minutes. Hα and soft X-ray emission may continue to increase for 10-20 minutes after the flash phase. The gradual decrease of the flare may last up to several hours.

In the visible part of the spectrum the Hα is strongly affected by a flare. The characteristic feature of a flare is a very fast increase in brightness followed by a much slower decay. We observe the most intense and optically thick portion of a flare in the center of an Hα line. The net Hα emission in the maximum phase of a large flare is of the order 10^{26} erg/sec. In the white light the flare emission does not exceed the emission of the solar disk. This is not the case however for the EUV, X-ray and radio emission. In these wavelengths the flare emission exceeds that emitted by the whole solar disk integrated.

An important type of flare is the so called two-ribbon flare. In such an event, changes in the large-scale arrangement of the active region can typically be observed well before the flash phase. The active region filament that often marks a magnetic neutral line of the active region, begins to move about noticeably. The flash phase of such an event in Hα

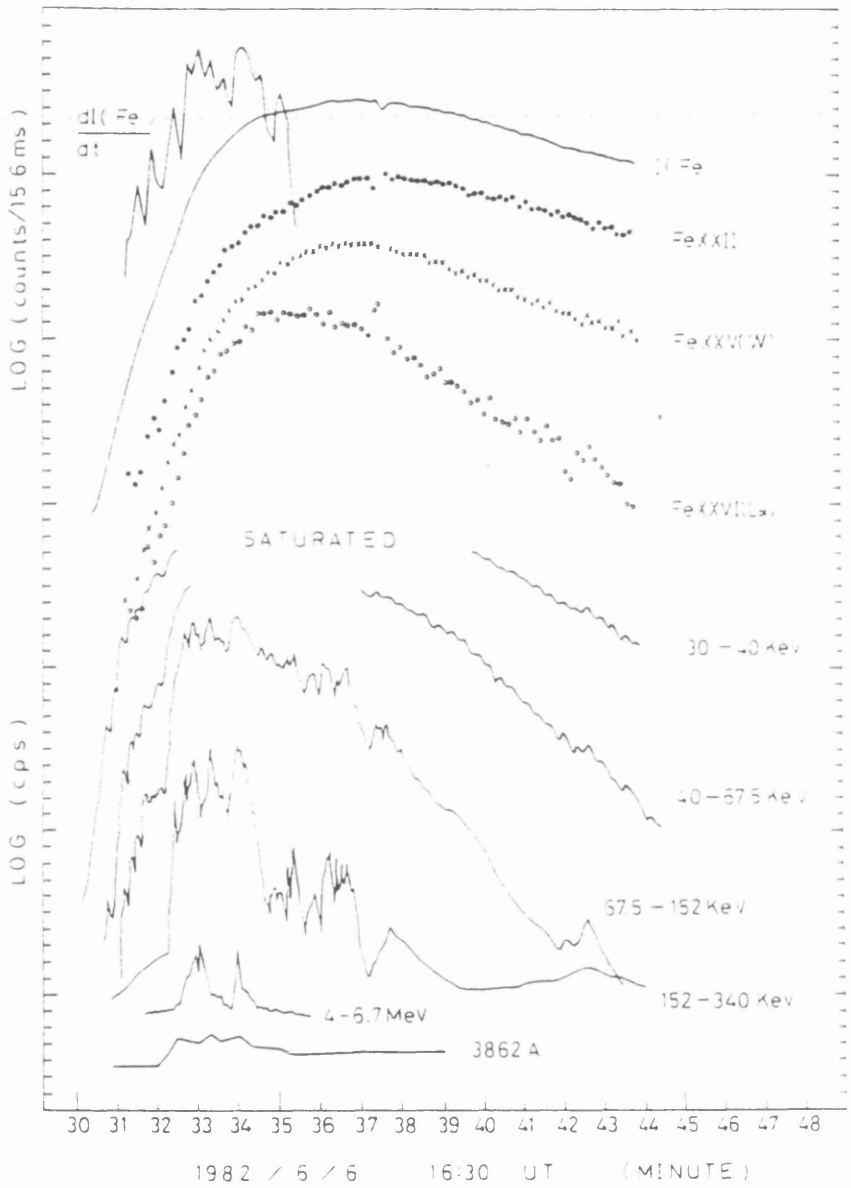

Figure 1.2: The appearance of a flare in different wavelengths as it develops with time. There is great variation in the duration and complexity of various phases. In a large event the preflare phase lasts, typically 10 minutes, the impulsive phase a minute, the flash phase 5 minutes, and the main phase an hour (Zirin 1988).

is marked by the brightening of two narrow ribbons. When the event is also imaged in EUV or soft X-rays we see that the Hα brightenings are happening at the footpoints of an arcade of bright coronal loops that go over the neutral line (Foukal (1990)).

The largest two-ribbon flares can involve energies of 10^{32} ergs or more. These energies are partitioned between thermal energy of plasma observed in soft X-rays, EUV and strong visible lines, nonthermal energy of charged particles accelerated to the GeV range and kinetic energy of plasma and associated shock waves propagating out from the sun. Now 10^{32} ergs of energy in a few minutes is a very impressive rate of energy release but is still insignificant in comparison with the Sun's bolometric luminosity. So, solar flares are not as significant as some stellar flares, where we can see the consequences on the light curve of the star (Pallavicini 1986).

From soft X-ray images of the solar corona it was realized that the structure of the corona is dominated by magnetic fields. Using vector magnetographs we can reconstruct the geometry of these fields in the photosphere and then, assuming a potential field, extrapolate into the chromosphere and the corona. Little convincing evidence exists of substantial change in the observed fields even after major flares (see later in this chapter); moreover only a small fraction of the magnetic energy stored in the observed fields has to be released to account for a flare.

Despite the difficulties in proving it, there seems to be a relation between flares and magnetic fields. For example, large flare occur more often in active regions whose magnetic fields are relatively complex. Sunspots of type δ (umbrae of opposite polarity in single penumbra) are those that show the most frequent activity (flaring). Also, there is no other form of energy stored in the corona that is adequate to produce solar flares (see e.g. Brown and Smith 1980).

In soft X-rays the flaring plasma occupies a closed loop, or system of parallel closed loops called an arcade. Loops seem to be aligned or they consist of magnetic flux tubes, full of plasma, that is trapped by the presence of the magnetic field. These flux tubes cross over the active region neutral line and connect to photospheric footpoints with opposite polarity, on either side of the neutral line. From the flash phase images it is indicated that very hot plasma exists in these loops with temperatures as high as $10 - 20 \times 10^6$ K and densities, found from emission measure and from EUV line intensity ratios, can be as high as 10^{13} cm^{-3}.

Many flares produce microwave bursts whose time behaviour is generally very similar to the impulsive hard X-rays bursts (for a comprehensive review see MacKinnon 1983) Microwaves are most intensely emitted in those loop footpoints and condensations which are also brightest in H_α and soft X-rays. The emission must be gyrosynchrotron radiation by relativistic particles, possibly the same ones that produce the hard X-rays also (see eg Klein, Trottet and Magun 1986).

1.3.1 Magnetic field Changes during flares

The most common flare producing field configuration is characterised by strong shear across the polarity inversion line. An inversion, or 'neutral' line is a locus across which the line of sight field component changes sign. The field near such an inversion line is far from potential and holds an ample amount of energy for flares. A magnetic field is potential if the current density vanishes everywhere and contains the minimum energy within a closed volume, if the perpendicular component on the surface is prescribed (minimum energy theorem). Thus a magnetic field with non zero currents but the same perpendicular component on the boundary should contain more energy than the potential field.

The formation of sheared configurations leading to flares often involves relative motion, and even collisions, of sunspots of opposite polarity (Moore and Rabin 1985). In a detailed study of the magnetic shear and flares along the inversion line, Hagyard et al. (1984) found that the points of flare onset were where both the magnetic shear and the field strength were greatest. This suggests that a flare is triggered when the magnetic shear stress exceeds some critical amount. This can be achieved either by the overall development of the sheared configuration or by local interaction of a small dipole emerging into a larger sheared field. A flare in the larger extent configuration is triggered at the site of the intruding dipole (Moore et al. 1984). If the flare energy comes from the sheared magnetic field then some long lasting magnetic change in the field should result as well. Lasting magnetic changes have proven to be slight and difficult to detect in most flares. In a few cases, lasting changes have been observed in a sequence of photospheric magnetograms (Paterson and Zirin (1981), Tanaka (1978)) not always in the best interest of contemporary solar flare theories (Paterson and Zirin (1981).

It is often observed that a flare brightens, within observational limitations, in the same position and exhibiting the same geometrical outline as a previous flare in that region.

Such flares have been studied extensively, based on the point of view that the form of the magnetic field configuration is a determining factor in the process that lead to a flare and that there is a rebuilding of the stressed magnetic filed after such successive flares (Moore and Rabin 1985).

As I mentioned before magnetic fields on the Sun and stars are measured by the Zeeman and Hanle effects. The Zeeman effect is produced when a magnetic field removes the degeneracy of an atomic level, and instead of a single emission or absorption line, we observe more. These are located symmetrically about the position of the undisturbed line.

Resonance polarization is affected by the presence of a magnetic field in a radiating plasma. This is called the Hanle effect. The resulting polarization depends on the direction of the polarization of the exciting radiation as well as on both the direction and strength of the magnetic field (see discussion in Stenflo 1994).

1.3.2 Radio Observations

Radio observations in meter wavelengths provide direct information on radiation from beams, plasma and shock waves starting from the flare region. During flares radiation in the radio band is observed usually in the form of bursts. In (1.3) we see a description of the radio spectrum of a flare. For a full discussion of the radio emission of the quiet and active Sun see Dulk (1985), and McLean and Labrum (1985).

There are,

- Type I bursts, which are long lasting (hours to days) noise storms that happen above active regions and are not generally connected with flares. Their emission is continuum and their frequencies in the range 50-400 MHz. Their production is a bit of a mystery, but their high brightness temperature and close to 100 % polarization are best understood in terms of plasma oscillations excited by energetic electrons. I will discuss noise storms later.

- Type II bursts which are connected with large flares and are not very frequent. Their usual interpretation is that they are plasma emission excited from MHD shock wave that propagates outward from the flare. They are connected with Type IV bursts, which radiate due to gyrosynchrotron. Type IV bursts have frequencies from

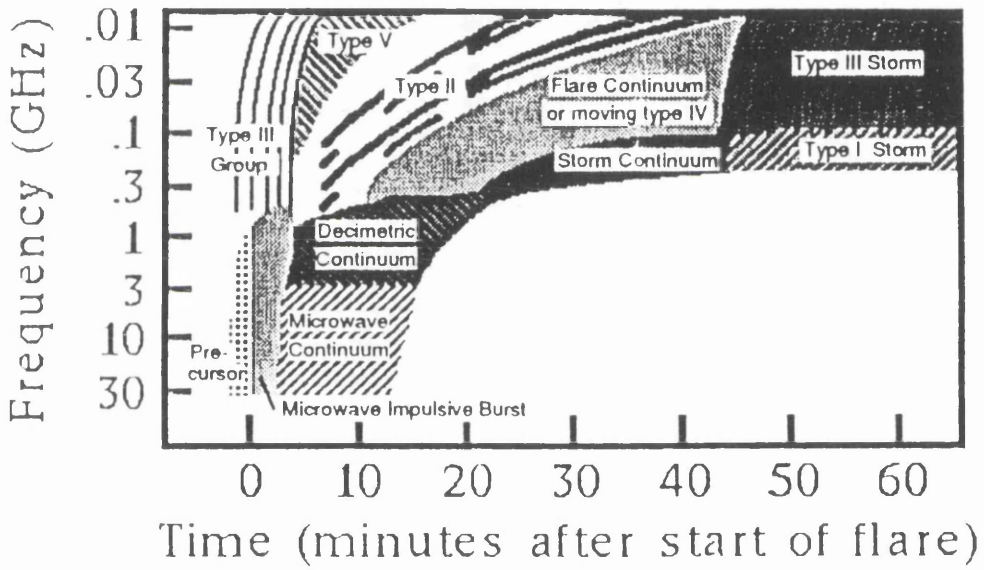

Figure 1.3: The radio spectrum of a flare

microwaves to a few kHz. There is a component of Type IV bursts the so called moving, observed at 10-100 MHz. Their emission lasts a few tens of minutes as the source moves outward from the corona to a few solar radii.

- Type III bursts are the most common. Their frequencies range from a few tenths of kHz to hundreds of MHz. The highest frequencies of Type III bursts are caused by oscillation in the low corona and the lowest by oscillations in the interplanetary space near 1 AU. Type II I bursts are generated by streams of mildly relativistic elect that propagates through the solar corona and excite plasma emission (Langmuir waves). The frequency decreases as they move outwards from the corona. Some are closely correlated to the impulsive phase of the flare and there is sometimes a good time correlation with Hard X-ray bursts. Most of them occur without the presence of a flare.

- Type V bursts are continuum emission which are sometimes observed after Type III bursts. They might be associated with very intense particle beams.

Millimeter-interferometer observations of flares are used to study the MeV electrons accelerated in flares. This is an important observation especially for small and moderate flares that don't produce observable γ rays. In a large number of flares, the impulsive phase emission at millimeter wavelengths consists of a rapid rise, sharp peak, and exponential decay. It is thought to be produced from the gyromotion of MeV electrons in the coronal magnetic field (White, 1994).

1.3.3 Soft X-rays

The emission of flares in X-rays is usually divided into two components, a non-thermal one in hard X-rays, with photon energy above 20 KeV and a thermal one in soft X-rays, with photon energy below 20 KeV. The range of soft X-rays lie between 1 and 10 Åand it consists of Bremsstrahlung (free-free) continuum, bound-free continuum and spectral lines, typically due to highly ionised species of metals such as Ca^{18+} and Fe^{24+}. Thermal electrons are possibly responsible for flare emissions with temperature around 10^7 K. The highly ionised state of this hot plasma combined with the strong magnetic fields restrict transport of energy or mass across field lines. As a result the soft X-ray flare appears composed of energetically isolated flux tubes of enhanced temperature and density.

Soft X-ray lines provide a valuable diagnostic of conditions (temperature, density, velocity) in flaring atmospheres. In a typical flare the soft X-rays manifest three phases: a preflare stage of gradual, weak brightening, an impulsive phase of rapidly increasing flux and brightness, and a main phase when the emission gradually decreases. It is during the impulsive phase that the temperature and emission measure of the soft X-ray plasma increase most rapidly and the temperature reaches 10^7 K. The emission measure usually reaches its highest value at the end of the impulsive phase and some times can continue to increase during the main phase as well.

The mechanism that is invoked to explain the increase in coronal emission measure is chromospheric evaporation. Antonucci et al (1982) found blueshifted components of emission lines Ca XIX and Fe XXV, which indicate the upward motion of soft X-ray emitting material. Fisher, Canfield and McClymont (1984) showed that the velocity amplitudes corresponding to these blueshifted components are consistent with chromospheric evaporation (see also Feldman (1994) for an opinion against chromospheric evaporation). The emission lines of the highly ionised species are very broad during the impulsive phase which suggests that there are turbulent motions of several hundred kilometres per second (Phillips 1986). The rise time of the soft X-ray flare leads to information about energy input and fall times are simply related to cooling mechanisms.

1.3.4 Hard X-Rays

First observations of solar flare hard X-rays came from balloon-borne and rocket-borne experiments and they already showed the close time coincidence between hard X-ray and microwave bursts (Peterson and Winckler, 1959, Chubb et al. 1966). Later instruments include the Hard X-ray Imaging Spectrometer (HXIS) and the Hard X-ray Burst Spectrometer (HXRBS) on the SMM satellite (review by Dennis 1985) and lately the HXT on Yohkoh satellite (Kosugi 1994). The impulsive hard X-ray burst time profile exhibits one or more spikes, which can last a few tens of seconds (e.g. Kane and Anderson, 1970 and Hoyng et al. 1976). Better time resolution though has shown that the hard X-ray bursts can fluctuate much faster than that and timescales down to a few tens of ms have been suggested (e.g. Kiplinger et al. 1983). An example of very fast variations is given in fig. (1.4) (Dennis, 1985). Although such variations are not a common phenomenon, they are used to invoke upper limits to the timescales of the acceleration mechanisms. (See also

Brown, Loran, and MacKinnon 1985, who discuss their statistical reality.)

'The principal theoretical flare problem is that of sufficiently rapid primary energy release' as Brown, Smith, and Spicer (1981) put it. Hard X-rays are observed with such intensities that, given the standard interpretation of them as collisional bremsstrahlung from high energy electrons in the flare plasma, energy release rates as high as 10^{30} ergs/sec are required to accelerate the emitting electrons during the impulsive phase. Such energy release rates are extremely challenging theoretically given the magnetic field strengths and configurations believed to exist in the corona. It is for this reason that increasing emphasis is being placed on observations of impulsive phase phenomena at all wavelengths where such evidence is found.

The spectra of hard X-ray bursts have most often been described by a power law i.e. the X-ray intensity $I(\epsilon)$ at photon energy ϵ is

$$I(\epsilon) \sim \epsilon^{-\gamma} \tag{1.1}$$

where γ is a positive number. Some bursts are best fit by a thermal type spectrum. The spectrum of the burst can change with time (usually a soft-hard-soft pattern) (Hoyng et al. 1986). The determination of the spectrum of the particles that produce the hard X-rays depends on the temperature and density of the plasma distribution with which the particles are interacting and also on the model assumed. From the events recorded on SMM instruments Dennis (1985) gives a review of the statistical properties observed. First, the 152-158 day periodicity, which was initially noticed by Rieger et al (1985). Second, the differential spectrum obtained from all events recorded with HXRBS (Hard X-Ray Burst Spectrometer) above $\sim$ 30 keV between launch and the beginning of 1985, can be well represented by an expression of the form

$$N(P) = 110P^{-1.8} \text{ Flares (counts s}^{-1} \text{ day)}^{-1}, \tag{1.2}$$

where N(P) is the rate of flares detected with peak rate P above background measured with HXRBS as the sum of the rate of all channels. And third, the value of γ was found to range from $\sim$ 3 to 8.

There are also important questions such as the directivity of the bursts and their polarization. Any directivity of the hard X-ray bursts could be a key diagnostic of the electron population that is believed to produce them. This is because bremsstrahlung is emitted preferentially in the direction of the incident electron (see Dennis and Schwartz 1989). This

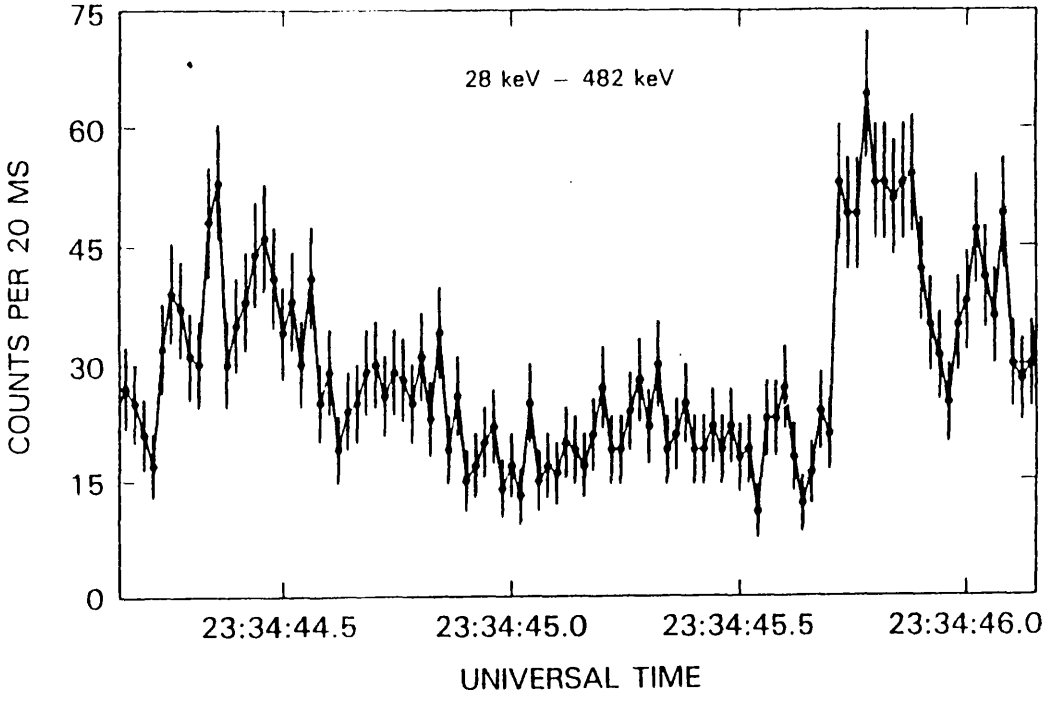

Figure 1.4: Two seconds of HXRBS memory data showing very rapid X-ray variations in a solar flare which occurred on June 6, 1980. The counting rate is plotted at a time resolution of 20 ms per point with 1 σ statistical error bars.

is true for relativistic electrons. For non-relativistic electrons the radiation is isotropic (see Brown (1975) for discussion).

1.3.5 Gamma Rays and High Energy Particles

A typical flare gamma ray line spectrum consists of several prompt nuclear de-excitation lines from elements of the solar atmosphere (Fe, Mg, Ne, Si, C, O) with energies mostly between about 1 and 7 MeV. This line spectrum is superimposed on a continuum made of the same kinetically broadened de-excitation lines and of a bremsstrahlung component extending above 1MeV. For a fraction of events this last component has been detected above 10 MeV and for an even smaller number to a few hundred MeV (Ramaty and Murphy 1987).

The hard X-ray and γ-ray continuum is believed to be electron-ion bremsstrahlung, the γ-ray lines and neutrons result from nuclear interactions, the microwaves are most probably gyrosynchrotron emission, and the longer wavelength radio emission is plasma wave emission of various types. All of these emissions are produced before the accelerated particles lose their energy to the solar atmosphere, and, consequently, they contain the greatest amount of information available about how the particles were accelerated.

Spacecraft observations of high energy particles in space manifest the acceleration processes on the Sun, provided that we understand their propagation from the Sun. The fraction of particles detected at the earth depends strongly on their initial position on the Sun. Since the transverse particle diffusion across the magnetic field is small in interplanetary space, the particles essentially propagate along magnetic field lines. So, strong particle events should be observed when the flare region is at the foot of the magnetic field line that directly connects the earth to the Sun (Svestka 1976).

Neutrons can be produced in the photosphere from proton-proton (p-p), proton α-particle (p-α), and α particle -α particle (α-α) reactions. A fraction of the neutrons produced during solar flares can escape and are detected at the Earth before they decay. The neutrons arrive at the Earth minutes after the γ rays photons. Because neutrons don't interact with the interplanetary magnetic field, what we see at the Earth is close to what is produced at the Sun. It is difficult though to know what we see. The time-dependent neutron flux at the Earth depends on the accelerated particle energy spectrum and angular distribution on the Sun.

The calculation of the neutron energy spectra is model dependent (Ramaty and Murphy, 1987). The neutrons that remain at the Sun can either decay or can be captured by nuclei. The dominant capture reactions are $^1H(n,\gamma)^2H$ and $^3He(n,p)^3H$, and they take place predominantly in the photosphere. The ^1H capture produces the 2.223 MeV line which is attenuated at the limb. This is because the neutrons must thermalize before capture, and this process takes place in the low photosphere. Observations of this line can set constrains on the $^3He/H$ ratio because it affected by the capture on ^3He (Ramaty and Murphy, 1987). The line is very narrow and the width results from thermal broadening in the photosphere.

Positrons result from the decay of radioactive β^+ emitting nuclei (e.g., ^{11}C, ^{13}N, ^{15}O, ^{19}Ne), de-excitation of nuclei (^{16}O,^{40}Ca), and decay of π^+ mesons, all of which are produced from the interaction of accelerated protons and heavy nuclei with the ambient plasma. Relativistic electrons can also produce positrons by pair production. Positrons resulting from the β^+ emitting nuclei have typical energies of $\sim$1 MeV, while positrons resulting from the pion decay have energies of $\sim$ 30 MeV. Direct annihilation produces two 0.511 MeV γ rays per positron. The number of 0.511 MeV photons escaping from the Sun depends on several factors but it doesn't seem to be limb darkened. The width of the 0.511 MeV line depends on the temperature the density and the degree of ionization (Ramaty and Murphy, 1987 and references therein).

The bulk of the observed γ ray emission between 4-7 MeV result from nuclear de-excitation lines (Forrest, 1983). The angular distribution of the emission is nearly isotropic (Ramaty, 1986). The decay of π mesons leads to the production of broad band gamma ray emission extending to high energies ($\geq$ 100 MeV).

From the analysis of electromagnetic radiations and energetic particles observed in flares, some authors suggest that not all particles are accelerated to their final energies at the same time. There appears to be a first phase acceleration which produces mostly nonrelativistic electrons and a second phase acceleration which accelerates ions and electrons to relativistic energies. It is not clear whether these two phases are manifestations of different acceleration mechanisms or whether they are due to the evolution in space and time of the same mechanism modified by different energy loss and particle transport processes.

The hypothesis of different acceleration process competes with the suggestion that, because of the different environment in which the gradual flares occur, the accelerated particle

distributions evolve in a different way than during impulsive events. Maybe electrons are more effectively trapped during gradual flares (Dennis 1988).

A way to learn the temporal evolution of an acceleration process is by the observed time dependence of gamma ray fluxes. The 2.223 MeV line is delayed because of the finite capture time of the neutrons in the photosphere (Wang and Ramaty, 1974) and the 0.511 MeV line is delayed mostly because of the finite lifetimes of the various positron emitting nuclei. Bremsstrahlung, most nuclear line emission, and π^o decay emission, are produced essentially instantaneously at the time of the interaction of the particles. So, they can be used as indicators of the time dependence of the acceleration and interaction processes.

The temporal relationship between the fluxes in the different energy ranges gives indications on the relationship between ion and electron acceleration, and acceleration of different ions. Delays and coincidence between different channels have been observed. For example, in the 1982, February 8 flare the maxima in the energy bands from 0.04 to 25 MeV are simultaneous to within ~2 seconds (Kane et al 1986). This means that electrons and ions are accelerated to tens of MeV energies in less than 2 seconds. In the 1982, June 3 flare the flux above 100 MeV and the flux from 4.1 to 6.4 MeV peak simultaneously to within $\sim$ 16 seconds. This suggests that the acceleration time of protons from tens of MeV to a GeV is less than 16 s.

Energetics

The most direct diagnostics of high energy particles on the Sun are hard X-ray and gamma ray emission. Typical values of the number of nonthermal electrons involved in the production of hard X-ray emission are of the order $10^{36} - 10^{37}$ electrons above 25 KeV for impulsive flares and greater than 10^{38} electrons for long duration gradual events (Bruggman et al. 1993). The energy content then in the nonthermal electrons ($\geq$ 25 KeV) is thus of the order of 10^{30} ergs for impulsive flares , up to 10^{31} ergs for gradual flares and so represents a large fraction of the total flare energy. Hoyng et al. (1976) gave 10^{39} electrons above 25 keV and up to 10^{32} ergs for gradual flares.

Gamma ray observations have shown that energetic ions can be produced very promptly, within a few seconds of the nonrelativistic electrons (Chupp et al. 1982). So, they are not a signature of second phase acceleration as was thought before the launch of the SMM.

The total numbers of protons inferred from gamma ray line observations depend on the

abundances in the proton interaction region, but typical values lie in the range of $10^{30}-10^{33}$ protons above 30 MeV. These protons are energetically insignificant in the flare as a whole but lower energy ones have almost no radiative signatures and could be energetically significant (MacKinnon 1989).

1.3.6 Site of Energy Release

From Skylab, Howard and Svestka (1977) observed in soft X-rays a complex of activity. The basic components of the activity were interconnected sets of magnetic field lines, which retained their identity during the life of the active region. However the visibility of individual loops in these connections was greatly variable and typically shorter than one day. Each brightening of a coronal loop in X-rays seemed to be related to a variation in the photospheric magnetic field near its footpoint. Only loops (rarely visible) connecting active regions with remnants of old fields can be seen in about the same shape for many days. The interconnecting X-ray loops do not connect sunspots.

The flare occurrence and the loop brightening seem to be two independent consequences of a common triggering action, that is emerging of new flux. In an old active region, growing and brightening of X-ray loops can be seen quite often without any association with a flare event. Thus the absence of any flare in the chromosphere does not necessarily mean that the overlying coronal active region is quiet and inactive. The final decay of this complex of activity was accompanied by the penetration of a coronal hole into the region where the complex existed before.

Currently, there is no direct way to determine the magnetic field strength and configuration in the corona, only the photospheric and chromospheric fields being measured from the Zeeman splitting of emission lines from various partially-ionised atoms generally at temperatures much less than 10^6 K. These photospheric fields can be extrapolated into the corona assuming either a potential field or a 'force-free' field, neither of which is appropriate fo a flare situation.

Observations show that a flare is most likely to occur in an active region where the magnetic shear is the greatest, thus implying that there is considerable twist in the magnetic field lines of the loop. So, it may well be that the flare energy is derived from the dissipation of the poloidal component of the field in the loop produced by a current along the loop. Such theories though are very speculative because the uncertainty in measurements of the

total magnetic field in an active region is generally greater than or of the same order as the energy released in the flare. Thus, while definite before-to-after magnetic changes have been detected in a few flares (e.g., Moore et al., 1984), in no case has it been shown that the observed change quantitatively accounts for the flare energy (Moore, 1988).
There is hope that future microwave observations made with high spatial resolution at many frequencies can provide a means of determining magnetic field strengths in the corona and transition zone.

1.4 Possible Solar Flare Classification Schemes

Solar flares are frequently classified as single loop, compact type and Hα two ribbon type, these types most probably being the extremes of a wide distribution. A feeling one gets by looking at different flares at different wavelengths is that no two flares are alike, in their signatures anyway. So, the classification schemes that appear in the literature are likely to fall into the trap of adjusting the classification to the flare model desired. Here I will try to give some general guidelines of classification specially from the high energy emission that I am interested in.
Before observations in X-rays were obtainable, flares were classified by their optical appearance, usually in Hα emission line. So, the area of the solar surface that brightened was measured and flares were classified according to their size. Later, measurements of intensity were included also. When Skylab data became available, Pallavicini et al. (1977) classified flares into a) compact flare loops, b) point like flares and c) large, diffuse flare loop systems from their appearance in X-rays. Since then a lot of in-between cases have been observed.
The Hinotori satellite was in operation from February 1981 to October 1982. It made observations in soft and hard X-rays and gamma rays, though hard X-ray imaging was possible only in relatively intense flares. In most flares hard X-ray sources are in the corona $10^4 km$ or more above the solar surface. If the flare takes place in a magnetic loop the brightest location of the soft X-rays is near the top of the loop or all the loop brighten. Hinotori found that Hard X-ray sources show a variety of forms.
After the Hinotori observations, flares were classified by Tanaka (1983) into three types.

- Type A (Hot Thermal Flares). These flares produce a superhot component of temperature 3-4 10^7 K, that emits hard X-rays in the range E < 40 keV and strong Fe XXVI lines. The hard X-ray time profile shows a gradual rise and fall similar to the soft X-ray profile. The hard X-ray source is compact (< 5000 Km). The spectrum is soft (γ is 7-8). Radio emission is weak.

- Type B (Impulsive Flares). These show typical impulsive hard X-ray bursts consisting of rapidly varying spikes emitted from the low corona, including the loop footpoints. The spectral index γ is 3-7. The later phase of some flares evolves to a more gradual time profile with softer spectrum (γ 5-8) and to a more compact source structure located at a higher altitude.

- Type C (Gradual Hard Flares) These flares show a long-lived (>30 min) burst with a broad peak or peaks showing no impulsive variation. The source is located high in the corona (h > 4 $\times 10^9$ cm) and can be identified with large extended loops. The spectrum is very hard, is well characterised by a power law ($\gamma \sim$ 2.5-4), and shows systematic hardening with time. Microwave emission is very strong.

A more recent classification scheme, combining Hinotori and Solar Maximum Mission (SMM) results was introduced by Bai and Sturrock (1989).

From their X-ray appearance solar flares have been divided into two classes. As we know, flare associated hard X-ray and radio emission usually lasts between tens of seconds and several hours. Based on the different durations of these emissions two extreme cases of flares have been distinguished: impulsive and gradual (or extended) hard X-rays/radio bursts (Bai and Dennis 1985).

Gradual hard X-ray and radio bursts flares are characterized by their long duration, smooth time profiles, time delays between peaks at different hard X-ray energies and microwaves and radiation from extended sources in the low and middle corona.

The distinction between impulsive and gradual hard X-rays/radio bursts flares is not always evident. Nakajima (1983), using microwave imaging and hard X-ray spectral observations, showed that gradual and impulsive signatures may occur simultaneously, but at different location. This underlines the influence of the environment where the emission is produced on the temporal and spectral evolution of the radiation and serves as a warning against the generality of classification schemes.

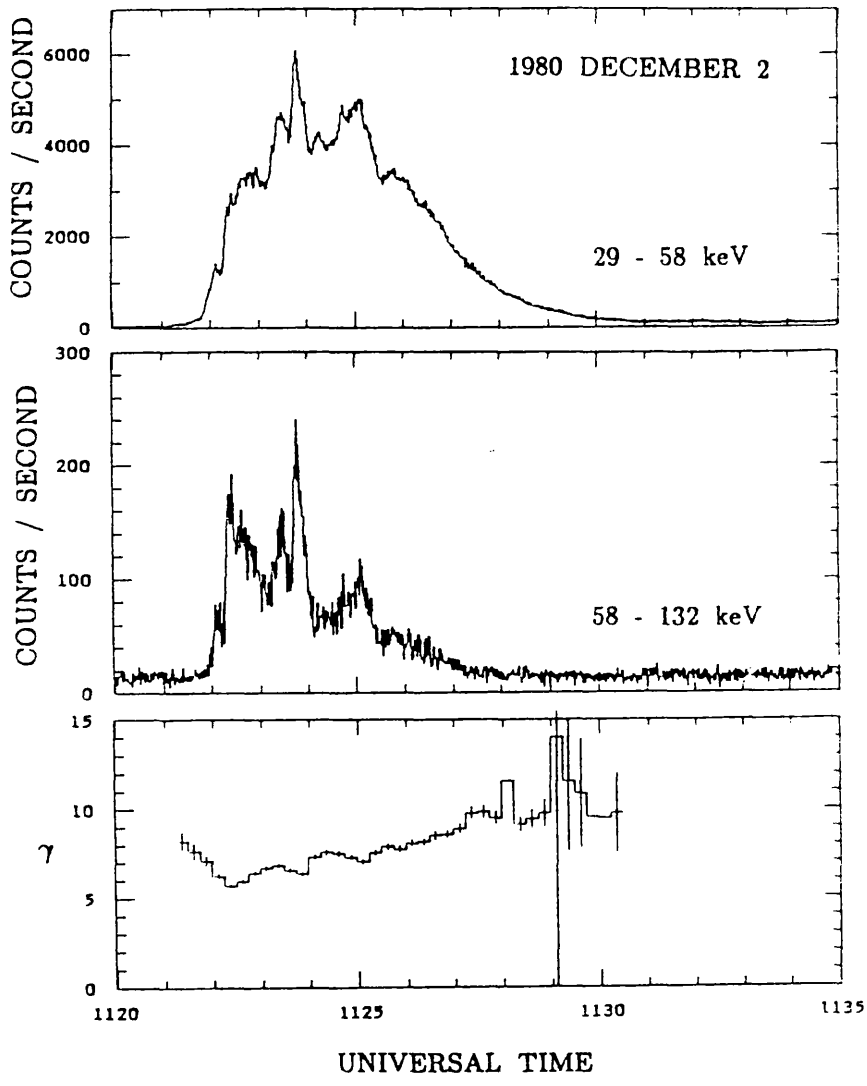

Figure 1.5: HXRBS time profiles and spectral evolution of the thermal Hard X-ray flare on 2 December 1980. The time profile of the 29-59 keV range is gradual, with some contribution from a spiky nonthermal component. That of 58-132 keV is more spiky. For power law fits, the spectral indices are large. For thermal fits, the temperature is about 6×10^7 K. Both pure power law fits and pure thermal fits result in large χ^2 values, which indicates that the X rays might be a combination of thermal and nonthermal emissions (Bai and Sturrock 1989).

The differences between the two classes of flares, impulsive and gradual, are not only of timescale or morphology (Cane et al. 1986). The energetic particles observed in space from impulsive events exhibit abundance enhancements (Reames 1990) and these flares are also called ^{3}He-rich events because they were originally identified by a ^{3}He/^{4}He ratio of 0.1-10 which is a huge increase over the coronal value of $\sim 5 \times 10^{-4}$. These events are also characterized by enhanced Fe/C and ^{4}He/H ratios, are associated with 2-100 keV electron acceleration and type III radio bursts, and possess impulsive hard X-ray and gamma ray emission. Gradual Flares have large proton fluxes, are associated with Type II radio emission, produce coronal mass ejections, have small ^{4}He/H ratios, and do not exhibit ^{3}He/^{4}He or Fe/C enhancements. One interpretation of these observations (Lin 1987) is that the particles from impulsive flares originate in the region of primary energy release and that particles from gradual flares are accelerated by a coronal or interplanetary shock.

1.5 Solar Observations from *YOHKOH*

The Yohkoh satellite has as its primary scientific objective the understanding of solar flares. It has two instruments that observe in soft X-rays: the SXT (Soft X-ray Telescope) and BCS (Bragg Crystal Spectrometer). The soft X-ray radiation as we know is principally emitted by thermal radiation processes. Yohkoh has observed the evolution of hot plasmas in the corona both in flares and outside flares. It also carries two types of instruments dedicated to the study of high energy aspects of solar flares, the Hard X-ray Telescope (HXT) and the hard X-ray and γ ray spectrometers.

The Soft X-Ray telescope (SXT) on board the Yohkoh satellite has obtained a very large quantity of images of active regions throwing new light on the geometry of flare occurrence. From these data one realises that active regions evolve constantly. Loop structures often show sudden brightenings and drastic changes, which one would like to explain as results of reconnection events. Loops with initially complicated structures, develop to more simplified loops (parallel loops sometimes). There are strong suggestions (Cheng and Acton 1994) that magnetic connections change in a way that two originally unrelated loops appear related, that is when simultaneous brightenings appear at two distant footpoints. The interaction of crossing loops leads to the relaxation of the originally stressed fields

and their disappearance, thus the reconfiguration of the magnetic field topology. After the interaction these loops could fade away (possibly drained of their hot material) and other loops initially not populated by plasma are then filled with heated gas and so become visible. A very interesting result is that there are a few events where the hard X-ray and microwave emission is present but no thermal (soft X-ray) component is present (Yaji et al. 1994). Hudson (1994) gives a summary of interesting results and discoveries of Yohkoh both in flares and outside flares.

Energy-dependent structure of hard X-ray flare sources is clearly detected. In lower energies one can see the whole flaring loop, and as one goes to higher energies, hard X-ray emissions tend to concentrate at the loop footpoints. The source varies impulsively which means that spikes are seen on the total flux. But in the impulsive phase of several limb flares, in addition to the double footpoints a hard X-Ray source is found above the soft X-ray loop, at an altitude of more than 10^4 km above the photosphere. The source is weaker than the footpoints but is definitely of impulsive nature, as it is inferred from the temperature and the emission measure needed in order to be of thermal origin. This is a very important result. It is thought that we probably observe an acceleration site (Masuda 1994).

A highly dynamic nature of the solar corona is revealed. Large-scale changes in coronal structures are seen much more frequently than anticipated from the Skylab observations with lower time resolution. On the smaller end of the size spectrum, active regions and X-ray bright points show frequent brightenings, which might well be the soft X-ray counterpart of hard X-ray microflares. Whether this burst energy release associated with the microflares can account for the heating of the corona is an important issue under investigation.

Everyone that has watched the movies from the SXT, has been amazed by the complexity of the structures observed in the corona. When the resolution increases, more fine structure can be observed.

1.5.1 A Cartoon

A few cartoons of flare models are shown here. The first one Fig. (1.6) shows the emission produced during a flare. In Fig. (1.7) we see the emerging flux mechanism of Heyvaerts et al. (1977) for a small flare (a single loop flare). In Fig. (1.8) is the generally accepted

scenario for two-ribbon flares (Priest, 1982).

1.6 Noise Storms

When the Sun is observed in metre and decameter wavelengths long-lasting solar radio emission consisting of thousands of shortlived spikes superimposed on a slowly varying continuum is seen. This type of storm which is usually called noise storm lasts from hours to days, and this long duration is one way of distinguishing this kind of emission from other solar radio emission. Noise storms are usually observed above sunspots with large magnetic fields (see e.g. McLean and Labrum, 1985).

Storms consist of numerous short lived bursts, so it is plausible to assume that each of these bursts corresponds to an acceleration event. The acceleration should persist for a long time in a small volume in the corona. Type I bursts is believed to be some form of fundamental plasma frequency. Melrose (1980) developed a Type I emission theory based on the assumptions that, the emission mechanism is fundamental plasma emission and is due to coalescence of Langmuir waves with low-frequency waves (ion-sound or lower-hybrid waves), and the exciting agency for the Langmuir waves is a population of energetic particles trapped in a closed magnetic structure over an active region. The source of the electrons that produce the noise storms is unspecified.

1.7 Flare emission from stars

Stellar radio flares are defined as variable radio emission from stellar mass objects which is possibly produced by explosive releases of magnetic energy. Such flares have been found in the following stars: late-type main-sequence stars (dMe and dKe stars), detached, semi-detached and contact close binaries (RS CVn, Algol-type and W UMa-type stars, respectively), X-ray binaries, pre-main-sequence stars (T Tauri and protostars), magnetic Ap/Bp stars, and late-type giants and supergiants.

Some X-ray binaries show radio jets. In the case of SS433 the jets consist of individual knots travelling at constant speed of 0.26 c along a precessing axis. These knots attain their maximum radio brightness at a distance of a few 10^{15} cm from the nucleus, and subsequently fade away on a time scale of days as the knots travel outwards. The radio spectral index is always between -0.6 and -0.8 and indicates optically thin synchrotron

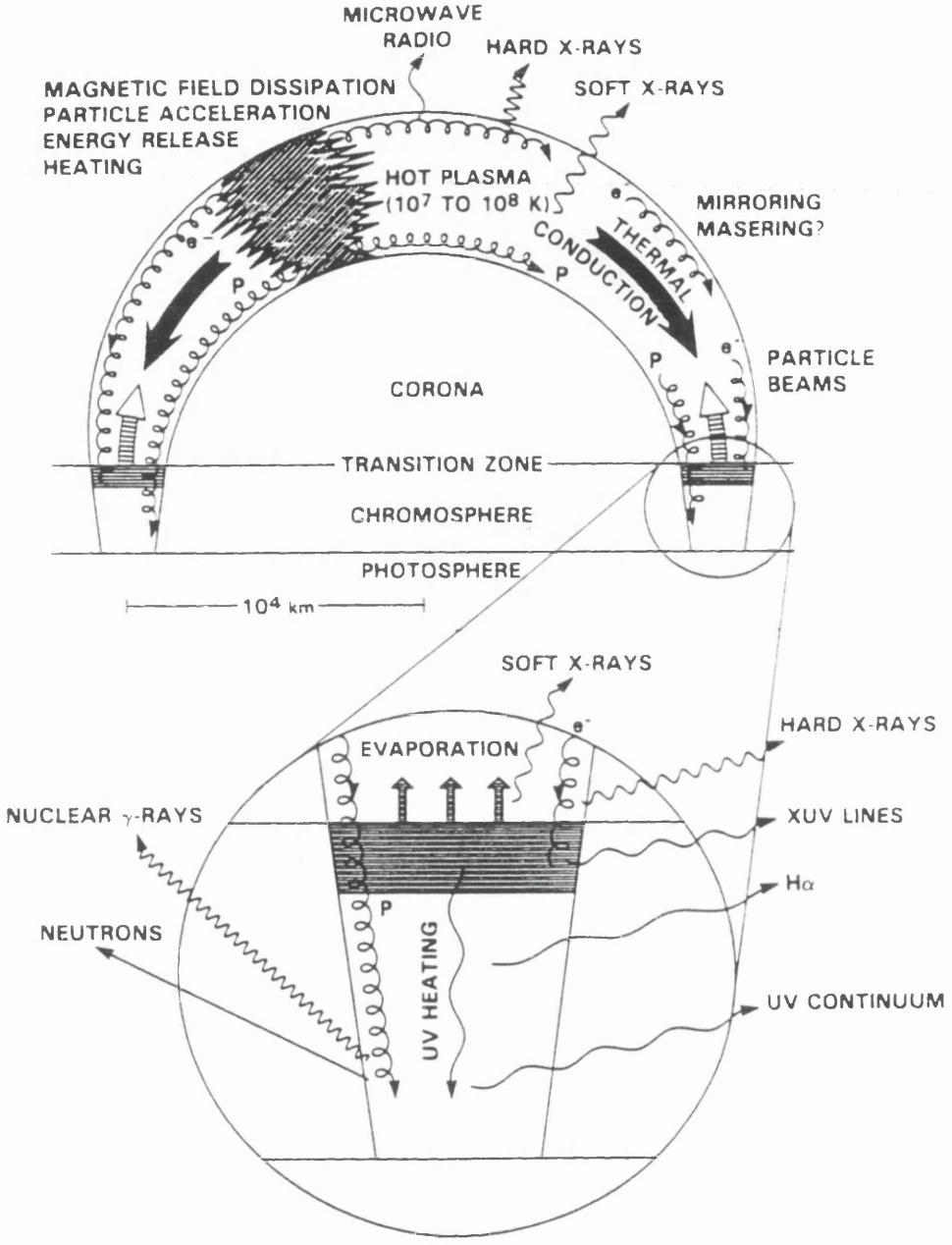

Figure 1.6: Schematic diagram of a simple flare showing some of the physical processes that are believed to occur and where in the solar atmosphere different emissions are thought to originate (Dennis and Schwartz 1989).

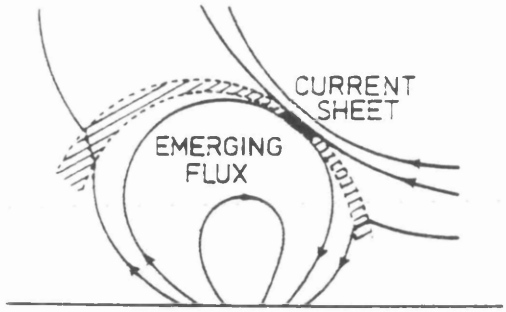

(a) Preflare Heating

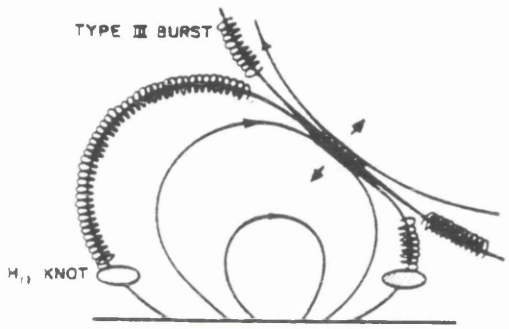

(b) Impulsive Phase

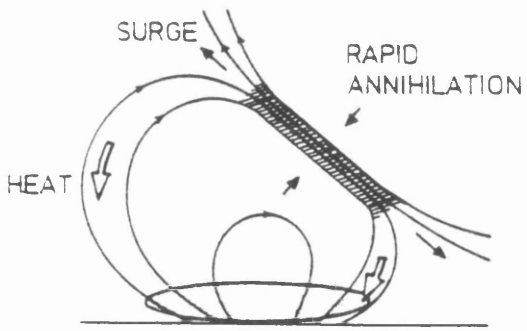

(c) Main Phase

Figure 1.7: The emerging flux mechanism of Heyvaerts et al. (1977) for a small flare (a single loop flare). (a) Preflare phase. the emerging flux reconnects with the overlying field. Shoch waves (dashed) radiate from a small current sheet and heat the plasma as it passes through them into the shaded region. (b) Impulsive phase. Electric field accelerates particles, which escaping along the field lines produce microwave bursts, hard X-rays and possibly $H\alpha$ knots. (c) Flash and main phases. Heat and particles are conducted down to the lower chromoshpere, where they produce the $H\alpha$ flare.

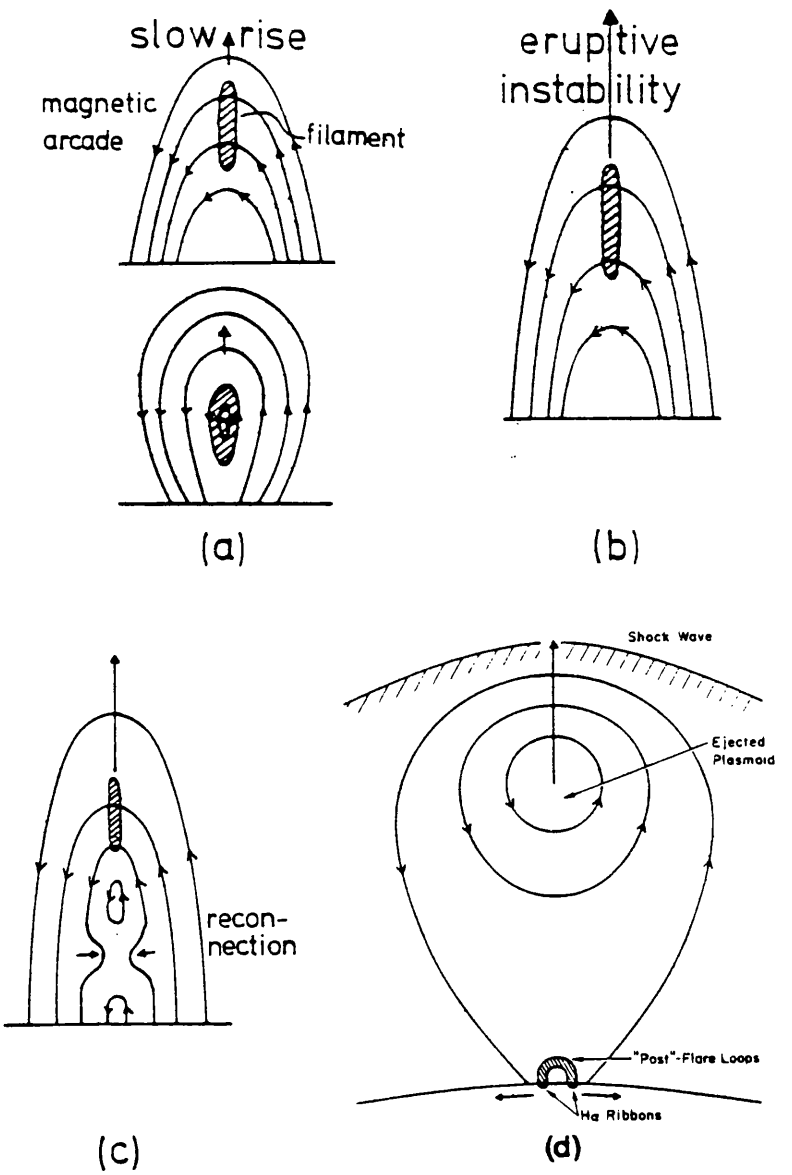

Figure 1.8: Two-ribbon flare. The overall magnetic behaviour in a two-ribbon flare, as seen in a section through the magnetic arcade. (a) Slow preflare rise of a filament, emerging flux or the initial stages of an MHD instability. The surrounding field may just be sheared (upper diagram) or it may contain a magnetic island so that the filament lies along a flux tube (lower diagram). (b) Eruptive instability of a magnetic arcade and filament. (c) Field lines below the filament are stretched out until reconnection can start. (d) As reconnection proceeds, 'post'-flare loops rise and $H\alpha$ ribbons move apart.

emission (Kuijpers, 1989).

RS CVn type binaries are probably the most common kind of radio detected stars. Their radio emission is intense, highly variable, and often circularly polarised. They are moderately close binary stars with periods 1-30 days. One star is usually G type or later. Some have variable visible and UV emission, and dark areas (maybe sunspots) covering much of the star. They most probably have intense magnetic fields, which are induced by tidally enforced rapid rotation. For many systems the fields of the two stars probably interact in the intervening medium (Uchida and Sakurai, 1983).

Magnetic fields in the sun are typically measured from the difference in absorption line profiles obtained in opposite circular polarizations from magnetically sensitive transitions. This method has failed for stars due to cancellation effects. Robinson (1980) proposed that the average magnitude of the stellar photospheric magnetic field could be derived from a careful study in unpolarised light of the enhanced Zeeman broadening of a magnetically sensitive line compared with another spectral line very similar in shape and formation, but with smaller magnetic sensitivity. Since Zeeman broadening increases with the square of the wavelength, infrared lines should have more pronounced broadening.

1.8 Emission From SS433

SS433 was first recognised as an optical object and later it was found that it shows variable emission in radio waves and X-rays. Also it shows strong emission lines in some unexpected wavelengths. Emission lines from hydrogen and helium exhibit very large Doppler shifts both red- and blue-shifted which move symmetrically around a central position in a period of 164 days. A second period of 13 days is also observed.

SS433 is thought to be a binary system the first companion being an early type star and the second a compact object ie neutron star or black hole. An extended and thick accretion disk is thought to exist around the compact object. W50 is thought to come from the supernova explosion that created the compact object of the binary system. The system must be a close binary. The second period of thirteen days in the data is thought to be the orbital period of the binary system

The most popular model for the understanding of the behaviour of this object assumes the existence of two oppositely directed relativistic beams coming out of this object. The

derived velocity of the beams is about 0.26c. The observed period of 164 days is believed to be the precession period of the relativistic beams. The kinetic luminosity of the beams is more than 10^{39} erg/sec which means that the mass loss rate is more than 10^{-6} solar masses per year. The early type star has a wind of speed $u_w = 500$ Km/sec.
There is a strong Hα luminosity of 10^{35} erg/sec within 10^{15} cm from SS433. The optical spectrum of SS433 shows Balmer, Paschen, Brackett and HeI lines but it doesn't show any HeII in the jets. So the temperature of the optical emitting area must be about 10^4 K. Since the forbidden lines are missing the density of the jets must be more than $10^7/\text{cm}^3$. Since the lines are so narrow the cone half-angle of the jets must be less than 0.03 rad.

1.8.1 Radiative instability in the jets of SS433

Work on wind collisional heating and radiation cooling processes in the jets of SS433 is presented here as well. The fact that the transient 'bullet' phenomenon and major variability seen in the optical spectrum of SS433 are essentially absent in X-ray data from the 'inner' jets seems to preclude their being 'true' bullets (i.e. comprising intermittent large mass ejections). In Brown et al (1994) we have demonstrated that the density conditions in the jets of SS433 are such that small variations in the jet density, angle, filling factor, or wind density, can cause the wind heated jets to switch between hot and hot/cool regimes. Because of radiative instability the inner jet is not allowed to cool down to optical temperatures so the optical jets vanish with negligible change in the inner X-ray jet (for jet parameters see Brown et al 1991).

Chapter 2

Magnetic Reconnection and Particle Acceleration

2.1 Introduction

Magnetic reconnection is one possible mechanism for conversion of magnetic energy. As such, is one possible mechanism by which energy may be released in the flare process. Magnetic fields containing X-type neutral points are probable configurations for magnetic reconnection. Reconnection taking place in such X-type neutral points, is an important ingredient in the open magnetosphere model (Dungey 1961). Dungey (1953) showed that the MHD equations could be solved at a magnetic neutral point which was also a stagnation point of the flow assuming that the conductivity was infinite and ignoring pressure gradients.

A major question is whether magnetic reconnection can proceed quickly enough to explain the observed rapidity of energy release in solar flares. Energy should be released in tens of seconds. The mechanism should give rise to fast particles, up to relativistic energies in timescales of seconds. A large proportion of the magnetic energy must go into these particles, and enough of them should be produced to account for the observed signatures. These requirements do not just apply to reconnection, but to any proposed flare model. Since in astrophysical plasmas the magnetic Reynolds number is very big ($R_m \simeq 10^8$ or higher for solar flares, $R_m \simeq 10^{11}$ for the solar wind and the magnetosphere) a change in the magnetic field such as discussed by magnetic reconnection would not be possible. Each plasma would flow in its own configuration, and wherever plasmas with different

magnetic topologies met (eg the solar wind and the earth's magnetosphere) the boundary layers would remain unchanged. This is of course true but not quite. When the magnetic Reynolds number is defined the size of the region in consideration is used. However, the size at the region where two distinct (magnetically) plasma populations approach can be very small. This will allow diffusion to take place and plasma to flow across the boundary layers causing release of the magnetic energy of the plasma.

2.2 Magnetic energy

Magnetic fields arise as a result of electric charges in motion; that is currents. Magnetic energy storage arises when a current system, driven by electromotive forces -i.e. voltage- does work against the voltages included by the build-up of the current system itself. The work is stored in the magnetic field associated with the currents and can be regained by allowing the current to decay. To maintain the stored magnetic energy the system must have the ability to create new magnetic energy or to permit its transport in the system at a rate greater than the rate of transformation of magnetic energy into other forms of energy.

2.2.1 Magnetic energy storage and conversion in the solar atmosphere

The problem of storage and conversion of magnetic energy on the Sun has been investigated primarily in the context of solar flares but also in the context of coronal heating. We expect stars to be hottest in the center and progressively cooler at larger and larger radii. It is generally agreed that the source of energy by which the solar corona is heated to temperatures 100 times the temperature at photosphere level is ultimately the convective motion of the very dense plasma in the photosphere. However, it is still uncertain what the mechanisms are by which that energy is first transmitted to the corona, and then dissipated to provide the necessary heating (Heyvaerts 1985). The corona though is much hotter than the underlying chromosphere and photosphere. The original view was that the corona is heated by acoustic waves propagating from the photosphere. Recent estimates have excluded this idea and have led to the conclusion that magnetic activity is responsible for the high coronal temperatures. The storage of energy in this magnetic field can be thought of as a slow process where the field evolves through a sequence of force-free

configurations, each time ending in a higher energy state (Low, 1982).

Magnetic flux tubes with trapped plasma are the most likely configuration for magnetic energy conversion. In fact, active and passive processes from the magnetic field point of view, clearly correspond to phenomena taking place perpendicular and parallel to the flux tubes respectively.

Today, in general, we do not have enough detailed, simultaneously obtained information about small scale structures or dynamics to distinguish between many possibly similar interactions and configurations. We still lack good resolution of the 3D plasma, velocity and magnetic field profiles on 100-1000 Km spatial scales.

2.2.2 Form of the magnetic field

As we said the place where the magnetic energy is converted into other forms of energy, lies close to neutral points. In a first approximation the magnetic field of bipolar sunspot groups in the chromosphere may be regarded as a magnetic dipole field. Neutral points arise if two or more such groups are present at places where the magnetic fields of individual spot pairs have opposite directions. A neutral point can arise for example between two parallel directed currents. Suppose that the magnetic field is given by (Syrovatskii, 1981)

$$\underline{B}(x,y) = \nabla \times [A(x,y)\hat{e}_z]. \tag{2.1}$$

This describes a 2-D configuration in which

$$\nabla \cdot \underline{B} = 0 \tag{2.2}$$

is automatically satisfied. We can rewrite $A(x,y)$ in the form

$$A(x,y) = \alpha_{11}x^2 + \alpha_{22}y^2. \tag{2.3}$$

It is clear that three different types of singular lines are possible, depending on the values of the coefficients α_{11} and α_{22}.

1. A singular line of O type, if $\alpha_{11} \cdot \alpha_{22} < 0$. In this case, the transverse magnetic field lines take the form of ellipses, an encircling singular line, while the real field lines take the form of spirals coiling around the singular line.

2. A singular line of X type, if $\alpha_{11} \cdot \alpha_{22} > 0$. In this case the transverse field has a null point of X type at the singular line, and the singular line is the intersection

of two surfaces, dividing the vicinity of the singular line into topologically different regions. The field lines in every region cannot be transformed by a continuous small deformation into field lines of any of the other regions.

3. Singular lines of shear type, if $\alpha_{11} \cdot \alpha_{22} = 0$. In this case, the transverse field lines are all parallel, and the vector $\underline{B}(x, y)$ smoothly changes in magnitude and reverses when crossing the singular line. Lines of this type are typical for the shear magnetic field. In such a field the field lines lie on parallel magnetic surfaces and change direction smoothly from one surface to another.

For a discussion of 3-D magnetic field reconnection see Lau and Finn (1990, 1991).

2.3 MHD Equations

In conducting liquids or dense ionized gases the collision frequency of different species (electrons, ions) is sufficiently high for a wide range of frequencies of an applied electric field so that Ohm's law in its simple form is valid $\underline{j} = \sigma \underline{E}$ where $\underline{E} = \underline{E}' + \underline{v} x \underline{B}$ ($\underline{E}'$ is the electric field when the plasma is at rest. $\underline{v}$ is the plasma bulk flow velocity.)
Under the action of applied fields the electrons and ions move in such a way that apart from a high frequency jitter, there is no separation of charge. Electric fields arise from motion of the fluid which causes a current flow, or as a result of time-varying magnetic fields or charge distribution external to the fluid. The mechanical motion of the system can then be described in terms of a single conducting fluid with the usual hydrodynamic variables of density, velocity and pressure. At low frequencies the displacement current is ignored. This approximation is then called the magnetohydrodynamic (MHD) approximation.
The Equations of Magnetohydrodynamics are the following: First, Maxwell's equations (here in CGS units):

$$\nabla \times \underline{B} = \frac{4\pi}{c} \underline{j} \tag{2.4}$$

$$\nabla \times \underline{E} = -\frac{1}{c} \frac{\partial \underline{B}}{\partial t} \tag{2.5}$$

$$\nabla \cdot \underline{B} = 0 \tag{2.6}$$

$$\nabla \cdot \underline{E} = 4\pi\rho \tag{2.7}$$

where ρ and $\underline{j}$ are the change and the current density. Then the momentum equation,

where several force terms can be included

$$\rho \frac{d\underline{\mathrm{p}}}{dt} = force\ density. \tag{2.8}$$

The generalized Ohm's law

$$\frac{m_e}{ne^2}\frac{\partial \underline{\mathrm{j}}}{\partial t} = \underline{\mathrm{E}} + \underline{\mathrm{v}} \times \underline{\mathrm{B}} - \eta \underline{\mathrm{j}} \tag{2.9}$$

where an inertial term has been included, the pressure gradient and the Hall effect are omitted. Ohm's law is a rigorous consequence of the Boltzmann equation. An equation of state for the gas closes this set of equations.

Equation (2.8) has on the right hand side, the Lorentz (magnetic) force, the effect of the electric field, pressure term, collisions term. For an extensive discussion of the equations of MHD see Priest (1982).

The MHD approximation has two special cases: the kinematic and strong field approximation. We have the kinematic approximation when the evolution of relatively weak magnetic fields is controlled by flows controlled by non-magnetic forces (this is thought to be important in the photosphere and convection zone of the Sun) and the strong field approximation when the magnetic field is strong enough to control the plasma motion (corona). Strong field conditions exist in stellar and planetary atmospheres. This approach usually implies a given magnetic field and its time evolution; the induction equation that we now discuss, gives the velocity field.

Induction Equation

The so-called induction equation governs the evolution of magnetic fields in the MHD regime. Many important conclusions can be derived from it. It may be derived as follows. We start with Maxwell's equations, Ampere's law (where we neglect the displacement current term $(1/c)\partial \underline{\mathrm{E}}/\partial t$, one can do that if one assumes that the fluid velocities are much smaller than the speed of light and low frequency oscillations of the electric field compared to timescales of the system (Jackson, 1965)), Faraday's law together with Ohm's law,

$$\nabla \times \underline{\mathrm{B}} = \frac{4\pi}{c}\underline{\mathrm{j}} \tag{2.10}$$

$$\nabla \times \underline{\mathrm{E}} = -\frac{1}{c}\frac{\partial \underline{\mathrm{B}}}{\partial t} \tag{2.11}$$

$$\underline{\mathrm{E}} = -\frac{\underline{\mathrm{v}} \times \underline{\mathrm{B}}}{c} + \eta \underline{\mathrm{j}}. \tag{2.12}$$

Substituting $\underline{E}$ in Faraday's law from Ohm's law gives

$$\frac{\partial \underline{B}}{\partial t} = \nabla \times (\underline{v} \times \underline{B}) - c\nabla \times (\eta \underline{j}) \tag{2.13}$$

and eliminating $\underline{j}$ between this and Ampere's law, we get

$$\frac{\partial \underline{B}}{\partial t} = \nabla \times (\underline{v} \times \underline{B}) - \frac{\eta c^2}{4\pi}\nabla \times (\nabla \times \underline{B}) - \frac{c^2}{4\pi}\nabla\eta \times (\nabla \times \underline{B}). \tag{2.14}$$

Things become simpler if we assume that the resistivity is uniform at least in the area we are interested in. By using the following vector identity

$$\nabla \times (\nabla \times \underline{B}) = \nabla(\nabla \cdot \underline{B}) - \nabla^2 \underline{B} \tag{2.15}$$

and Gauss's law for the magnetic field

$$\nabla \cdot \underline{B} = 0 \tag{2.16}$$

we get the induction equation

$$\frac{\partial \underline{B}}{\partial t} = \nabla \times (\underline{u} \times \underline{B}) + \frac{\eta c^2}{4\pi}\nabla^2 \underline{B}. \tag{2.17}$$

We will try to understand this equation by considering the magnetic flux enclosed by a contour C

$$\Phi = \int\int_S \underline{B} \cdot d\mathbf{S}, \tag{2.18}$$

where S is a surface bounded by the contour C. Let's assume that the contour C moves with the plasma, after some time dt the contour will be displaced to C'. Any change in the magnetic flux through this contour will be due either to time variation of $\underline{B}$ during dt or due to flux that was lost through the boundary defined from the movement of C (see figure (2.1)). An element $d\mathbf{l}$ is defining and area $d\mathbf{S} = d\mathbf{l} \times \underline{v}dt$ as it moves. The change in the magnetic flux will then be

$$d\Phi = \int\int_S \frac{\partial \underline{B}}{\partial t} \cdot d\mathbf{S}dt - \oint_C \underline{B} \cdot (d\mathbf{l} \times \underline{v}dt). \tag{2.19}$$

Using some vector identities and Stokes's theorem in the second term of the right hand side, we have

$$\frac{d\Phi}{dt} = \int\int_S [\frac{\partial \underline{B}}{\partial t} - \nabla \times (\underline{v} \times \underline{B})] \cdot d\mathbf{S}. \tag{2.20}$$

So, if the plasma is perfectly conducting ($\eta = 0$) the magnetic flux through the contour C is constant in time. This is called the 'frozen in' condition in a plasma.

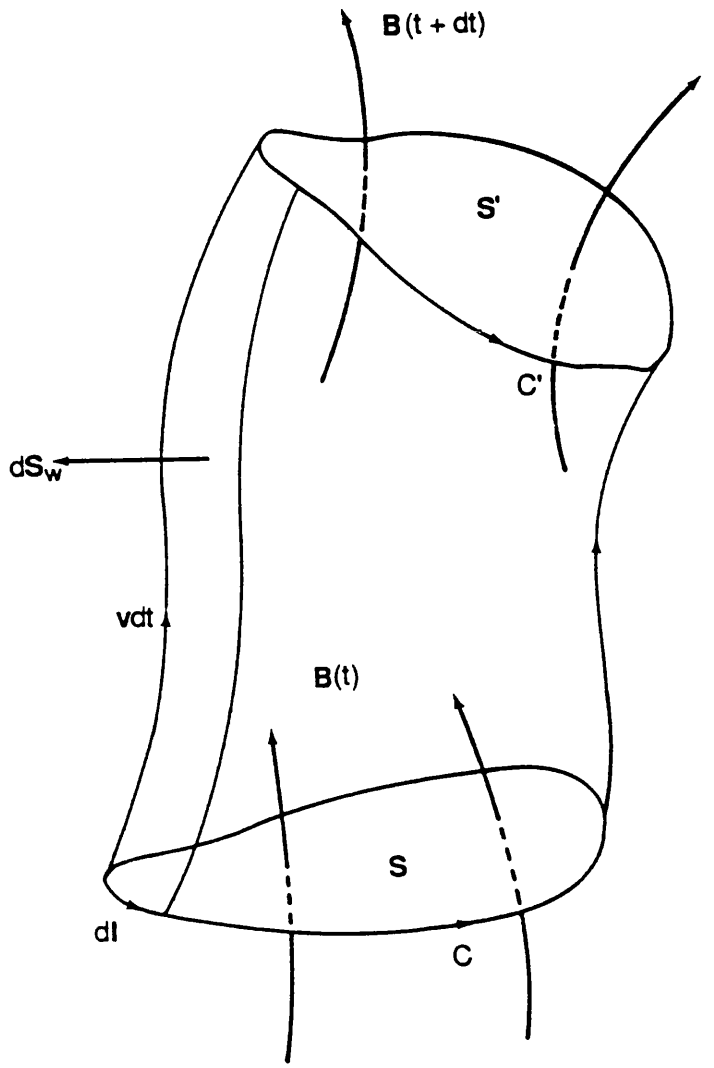

Figure 2.1: A surface S bounded by a contour C and moving with the plasma. After a small time interval dt, the surface has deformed to S', bounded by C'. the difference in the magnetic flux through S' from that through S arises from two causes: a change in the strength of B and the escape of flux through the walls defined by the fluid streamlines. The area vector $d\mathbf{S}$ for the wall element shown is given by $d\mathbf{l} \times \mathbf{v}dt$.

2.4 Magnetic Reconnection

Magnetic reconnection is a phenomenon of considerable importance in solar system plasmas. In the large scale magnetic fields of the solar corona, magnetic reconnection results in flares and in the smaller scale magnetic fields maybe in coronal heating which leads to the outflow of the solar wind. Reconnection in the magnetotail of the Earth's magnetosphere can cause large scale magnetic reconfiguration, which is associated with auroral substorms. Also, reconnection in laboratory plasmas can cause major disruption to the plasma confinement (Cowley 1985).
The process may also play an important role in astrophysical plasmas in systems such as accretion disks and generally in current sheets formed in interstellar and intergalactic space (Kuijpers 1993).

Definition

Magnetic field line merging, or reconnection, is the process whereby plasma flows across a surface that separates regions containing topologically different magnetic field lines (Vasyliunas (1975)). The magnitude of the plasma flow is a measure of the merging rate. The magnetic merging process enables the magnetic field to act as an energy source for the plasma. A more recent discussion by Schindler et al. (1988) gives as definition the 'Breakdown of magnetic connection due to a localised nonidealness' for general magnetic reconnection. This allows a finite B to remain after the reconnection (see also Axford 1984).

2.4.1 Main features

The basic principles behind magnetic reconnection can be understood by looking at the induction equation and the form of the Lorentz force

$$\frac{\partial \underline{B}}{\partial t} = \nabla \times (\underline{u} \times \underline{B}) + \eta \nabla^2 \underline{B} \tag{2.21}$$

where η is the magnetic diffusivity. This equation describes how the magnetic field changes in time due to the effects of transport by the plasma flow and diffusion. The ratio of the two terms in the r.h.s. of this equation is the magnetic Reynolds number

$$R_m = \frac{uL}{\eta} \tag{2.22}$$

which is very large for most astrophysical plasmas because the length scales for changes in the magnetic field are large. For example, R_m is 10^8 for the solar flare problem and 10^{11} for magnetospheric phenomena. So, the magnetic field lines are "frozen-in" to the fluid which means that the magnetic field lines are convected along with the flow or the magnetic flux tubes are moving and carrying with them the plasma they contain. Which of the two is applicable in a particular situation depends on whether there is a kinematic or a strong field approximation.

The Lorentz force (or magnetic force) which is perpendicular to the magnetic field (so any plasma acceleration parallel to the magnetic field must be caused by other forces) is given by

$$F_L = \underline{j} \times \underline{B} \tag{2.23}$$

and when we substitute in $\underline{j}$ from Ampere's Law

$$\frac{4\pi}{c}\underline{j} \times \underline{B} = \nabla \times \underline{B} \times \underline{B} = (\underline{B} \cdot \nabla)\underline{B} - \nabla(\frac{B^2}{2}). \tag{2.24}$$

The first term on the right hand side represents the effect of magnetic tension parallel to the magnetic field of magnitude B^2 per unit area. The second term represents the effect of magnetic pressure.

In regions of high magnetic field gradient (which could mean the encounter of two distinct plasma populations), however the length scale L is very small and so the second term in the induction equation can become important and the field can diffuse rapidly through the plasma on a time scale

$$\tau = \frac{L^2}{\eta}, \tag{2.25}$$

where η is the resistivity of the medium which though generally small in astrophysical plasmas (values of 10^{-18} are not unheard of) can locally acquire an important value, particularly through anomalous resistivity in turbulence (eg Papadopoulos 1976). One can picture the field lines diffusing through the plasma down field gradients, in such a way as to reduce the gradients. The plasma and the velocity field are no longer coupled. This not only alters the topology of the field, but also releases a great amount of magnetic energy since the tension in the newly reconnected field lines accelerates the plasma away from the reconnection site at approximately the Alfvén speed

$$u_A = \frac{B}{(4\pi\rho)^{\frac{1}{2}}}. \tag{2.26}$$

So, depending on the value of Reynolds number one can have convection of the magnetic field with the flow or diffusion of the magnetic field lines through the flow, or an intermediate situation if the magnetic Reynolds number gets some intermediate values. In most astrophysical plasmas $R_m \gg 1$ prevails so that different magnetically plasma populations won't interact unless something else happens. For example two different plasma populations are the solar wind and earth's magnetosphere (or any other planetary magnetosphere). These two meet in the interplanetary medium and they reach an equilibrium state where both populations remain separate. They should remain separate in this way for ever if the 'frozen-in' condition stands. But in such a close approach the length scale for consideration in the induction equation is not the same as before but reduces significantly. So, diffusion phenomena in a localised small region are important and this is why magnetic reconnection is an important mechanism (Jardine 1991).

The coupling of the plasma flow and the transport of magnetic flux arises from the equation of the electric field, as discussed before

$$\underline{E} + \frac{\underline{v} \times \underline{B}}{c} \simeq 0 \tag{2.27}$$

where $\underline{v}$ is the bulk flow velocity of the plasma, i.e. the particle momentum flux density divided by the mass density. Equation (2.27) is expected to be approximately true in most cosmical plasmas. It implies that any plasma flow across magnetic field lines is associated with an electric field. In particular, a plasma flow across the separatrix is associated with an electric field lying in the separatrix surface at right angles to $\underline{B}$. So, that such an electric field occurs is thus an alternate way of stating that magnetic merging is occurring. At the intersection of the two branches of the separatrix, the component of $\underline{v} \times \underline{B}$ along the X line becomes zero. Then (2.27) becomes inapplicable, since several terms have been neglected at the right hand side on the ground of them being small in comparison with $\underline{v} \times \underline{B}$. One of these terms is the effect of finite resistivity, whose inclusion changes (2.27) to the ordinary Ohm's law. So, when one is sufficiently close to the neutral line

$$\underline{E} = \eta \underline{j}. \tag{2.28}$$

Thus $\underline{E}$ is related to the plasma flow across the separatrix. Hence for a given magnetic configuration the electric field along the X line is proportional to the merging rate.

2.4.2 Spontaneous and Driven Reconnection

A distinction often made in the literature is that between spontaneous and driven reconnection. Spontaneous reconnection is said to occur when a system whose external parameters are only slowly changing becomes unstable giving rise to reconnection with a rate that is not controlled from outside. Driven reconnection refers to an open system where plasma and magnetic field are injected and extracted, and the reconnection rate is determined in this way. Biskamp (1986) argues that the distinction is overemphasised and that the basic mechanism is the same. The second one permits higher resolution of the reconnection region, which is regarded as a small section of a spontaneously reconnecting one.

2.4.3 Current Sheets

One candidate topology, that has received considerable attention, where reconnection might happen is a magnetic field with an X-type neutral point.

$$\underline{\mathrm{B}} = B_o(y\hat{x} + x\hat{y} + B_z\hat{z}) \tag{2.29}$$

(see 2.2.2). Usually B_z is considered to be very small or is completely ignored, so a two dimensional system with a well defined x-type neutral line is considered. Dungey (1953) discussed the possibility of 'discharges' occurring close to a neutral point like this which would result in particle acceleration. The possibility of particles in a small region reaching very high energies by absorbing energy from a large surrounding region is of more interest than the moderate heating of the material in a large region. The growth of the current density is opposed by the electromagnetic forces everywhere in a magnetic field except near a neutral point. In the neutral point a small initial perturbation will lead to the formation of a discharge that cannot be balanced by the electromagnetic forces.

A current sheet may be defined as a non-propagating boundary between two plasmas, with the dominant magnetic field component tangential to the boundary. The tangential field components are arbitrary in magnitude and direction, subject only to the conditions that the total pressure be continuous

$$p_2 + \frac{B_2^2}{8\pi} = p_1 + \frac{B_1^2}{8\pi}. \tag{2.30}$$

If the sheet is curved significantly, additional magnetic tension terms need to be included.

A current sheet (Fig. 2.2) is rather like a shock wave, in the sense that it may be regarded as a discontinuity separating two regions where the equations of ideal MHD hold. Also its width and the details of its interior are determined by diffusive processes. However, the similarity ends there. Unlike shocks, current sheets do not propagate. They diffuse away in time and jets of plasma come out of their ends at Alfvenic speeds.

As we said an X-type neutral point in a magnetic configuration tends to be locally unstable, provided that the sources of the field are free to move (Dungey, 1953). Let us consider the equilibrium current free field

$$B_x = y, \quad B_y = x. \tag{2.31}$$

The field strength increases with distance from the origin, so the hyperbolae are situated closer and closer together. Any element of plasma, such as the one shown near the x-axis experiences a magnetic tension due to the outwardly curving field lines. This force acts outwards from the origin and is balanced by a magnetic pressure force, which acts inwards because the magnetic field strength weakens as one approaches the origin. If the field becomes distorted to the form

$$B_x = y, \quad B_y = \alpha^2 x, \tag{2.32}$$

where $\alpha^2 > 1$, and the hyperbolae change to

$$y^2 - \alpha^2 x^2 = constant \tag{2.33}$$

then the separatrices close up like a pair of scissors. On the x-axis the field lines are closer together so that the magnetic pressure has increased. But they also have smaller curvature than before, so that the magnetic tension has increased less than the pressure. The forces don't balance anymore and the X-type point collapses to a current sheet (Priest, 1981).

2.5 Modelling of Magnetic Reconnection

There are two paths to reconnection theory which have been developed almost independently in the past: the MHD approach which is directly applicable to collisional solar coronal plasmas, and the single particle motion in model electromagnetic fields approach

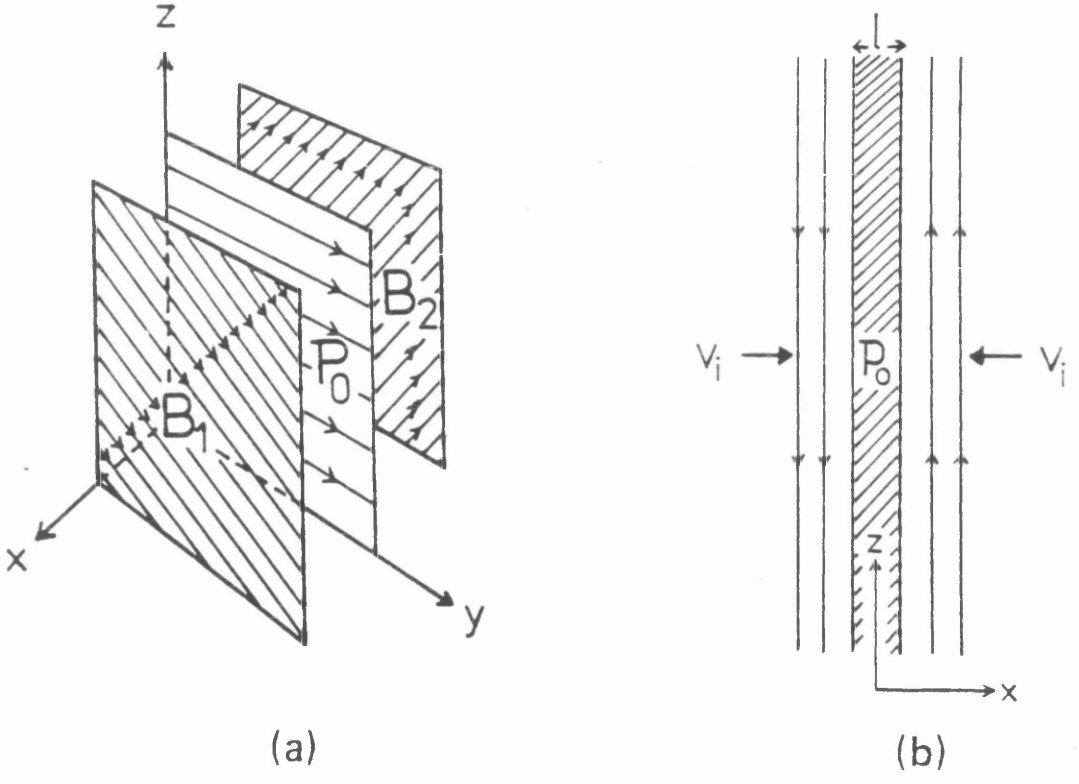

Figure 2.2: a) A current sheet across which the magnetic field rotates from B_1 to B_2. b) A neutral current sheet, in whose centre the magnetic field vanishes and the plasma pressure is p_0.

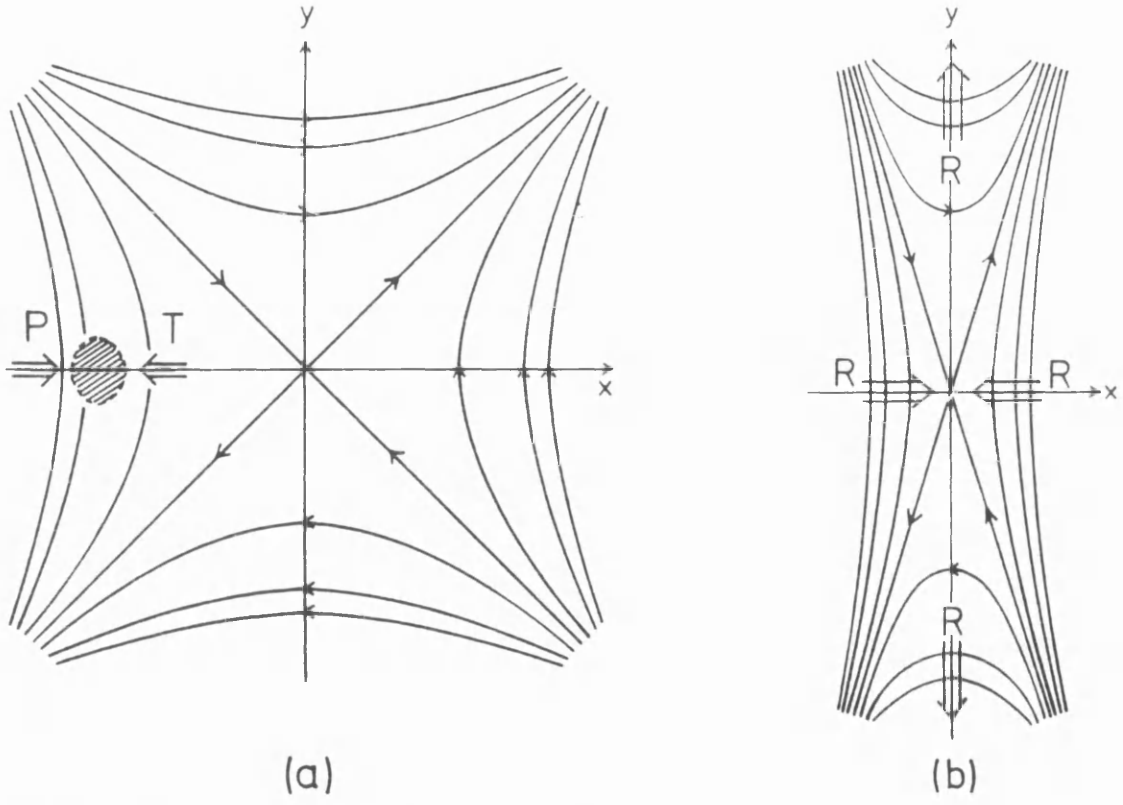

Figure 2.3: The magnetic field lines near an X-type neutral point a) in equilibrium with no current and b) away from equilibrium with a uniform current

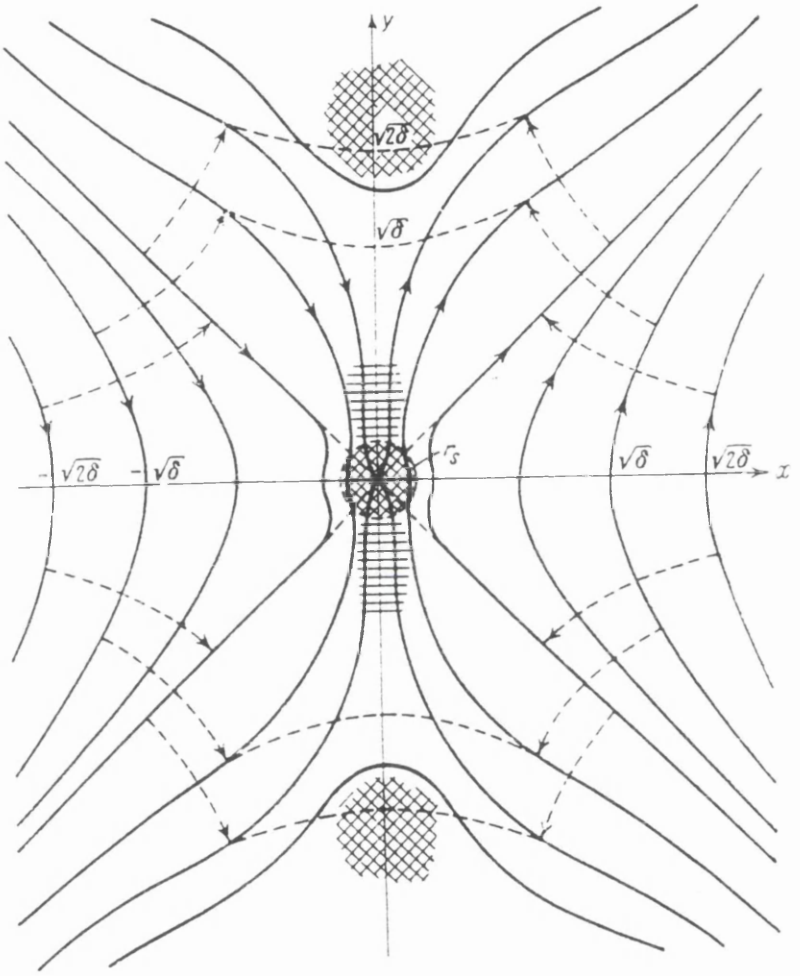

Figure 2.4: The formation of a current sheet from a configuration initially containing an X-type neutral point in Syrovatskii's flare model. The sources of the field have moved a distance δ and cause the field lines at large distances ($r > r_s$) to move as indicated by the arrowed, dashed lines. Close to the neutral point the field lines are greatly distorted so as to form a current sheet, since no reconnection is allowed. Two regions (cross-hatched) of compressed plasma are formed on the y-axis and one near the neutral point. The plasma in the rest of the sheet is rarefied, as shown by the horizontal shading (From Syrovatskii, 1966).

which is applicable to collision free solar wind and magnetospheric plasmas and maybe in the high corona.

The hydromagnetic models often make the simplifying assumption that the plasma flow is incompressible, which is equivalent to the assumption that $\beta \gg 1$, i.e. the plasma pressure is much bigger than the magnetic pressure.

On the other hand, single particle models often neglect the thermal speed in the velocities of the incoming (to the reversal field region) plasma particles; this is equivalent to assuming that $\beta \ll 1$. Within the reversal region β is of the order one.

2.5.1 Hydromagnetic Models

In the paragraphs to follow I discuss specific hydromagnetic models of magnetic reconnection that have been important in the development of the understanding of this phenomenon.

Parker-Sweet Model

This was the first model for how reconnection might take place (Sweet, 1958, Parker, 1963). Their system is two dimensional and steady state and the inflow magnetic fields are antiparallel and of equal strength. The plasma is assumed to be incompressible and the density of the medium uniform everywhere. The plasma flows in towards the current sheet in both sides with V_i and flows out parallel to the current sheet with velocity V_o (see fig. 2.5). The half width of the current sheet is calculated by assuming that there is a balance between the inflow magnetic flux and the flux annihilated in the current sheet due to diffusion. $VB_o \simeq B_o/(\mu_o \sigma l)$ which gives

$$l \simeq \frac{1}{\mu_o \sigma V} \tag{2.34}$$

They also assume that the width of the current sheet has the same value for all the length L and by using the conservation of mass they get (the density is thought to be constant)

$$V_o l = V_i L \tag{2.35}$$

All the reconnection rate determines is how much plasma is accelerated to the inflow Alfven speed per unit time.

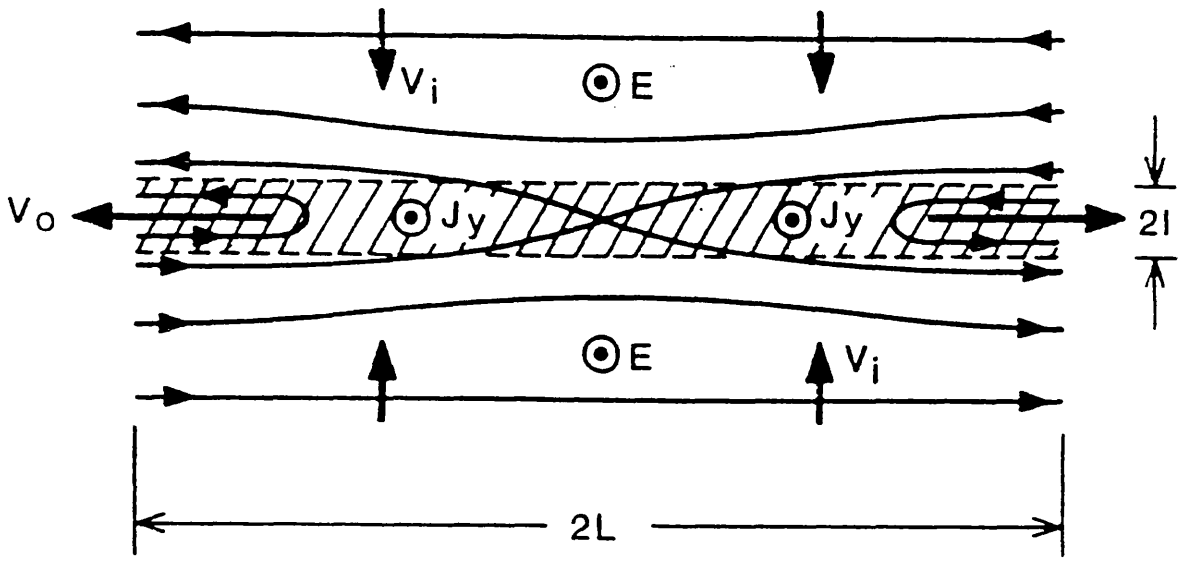

Figure 2.5: Sketch of the field and flow configuration (solid lines and arrows respectively) assumed in the Sweet-Parker Model. The current sheet (diffusion region) shown hatched, has the small half-width l set by the scale of diffusion over its whole half-length L, the latter being assumed to be equal to the scale size of the system (Cowley, 1985).

When the inflow speed is calculated they get

$$V_i \simeq \frac{V_{Ai}}{\sqrt{R_m}} \tag{2.36}$$

which means that reconnection proceeds very slowly in this model and cannot account for the timescales of energy release in solar flares since $R_m \sim 10^8$ or bigger in the solar flare problem. The reason that reconnection proceeds slowly in this model is that the plasma can flow into the boundary region from a large area, but is allowed to leave only from a very narrow area.

Petschek's Model

A very significant contribution to the understanding of magnetic reconnection came from Petschek (1964). He realised that an MHD slow mode compressional wave could also be used to decrease the magnetic field strength and increase the plasma energy.
The slow wave speed in the incompressible limit is

$$V_w = \frac{B_{nom}}{\sqrt{4\pi\rho}} \tag{2.37}$$

where B_{nom} is the magnetic field component normal to the wave front.
The configuration Petschek proposed is shown in figure(2.6). He pointed out that since material is ejected symmetrically along the X-axis, the origin must be a fluid stagnation point. Two waves (slow mode shocks) are standing in the plasma flow on both sides of the neutral line and they confine the plasma outflow regions. The diffusion region is now much smaller than the one proposed in the Parker-Sweet model. The width is the same but the length of the diffusion region is not comparable to the size of the system anymore. This happens if we allow the inflow velocity of the plasma to be comparable to the Alfvén speed. This can be seen from the continuity equation

$$L^\star \simeq \frac{V_{Ai}}{V_i} l \tag{2.38}$$

where one assumes incompressible flow and outflow speed of the size of the Alfvén speed. Thus, if the inflow speed is much less than V_{Ai} the length of the diffusion region is much larger than its width as it was assumed in the Parker-Sweet model. But if the inflow speed is comparable to the Alfvén speed then the length of the current sheet is much reduced.
A slow shock is an oblique shock, where the magnetic field has components both parallel and perpendicular to the shock front (Fig. 2.7) The basic property of a slow shock is that

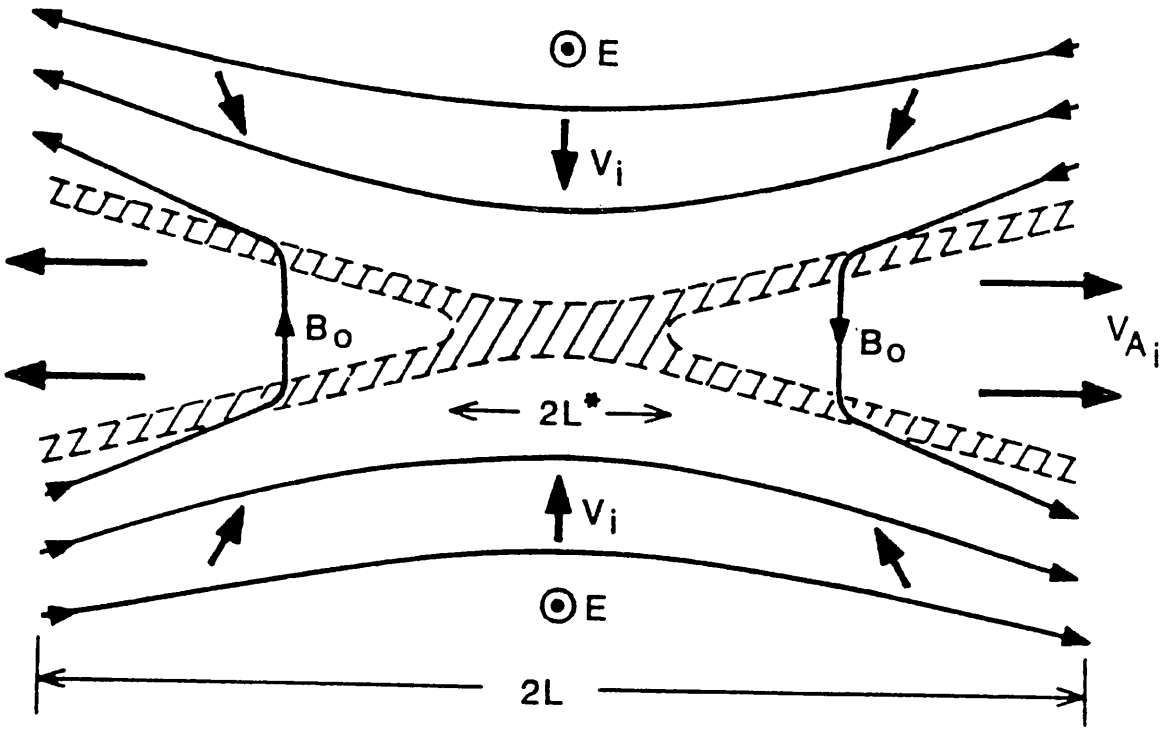

Figure 2.6: Sketch of the magnetic field and plasma flow configuration (solid lines and arrows respectively) in the Petschek reconnection solution. A small central diffusion region of length L^* surrounding the neutral line bifurcates into two standing wave current sheets in the downstream flow (current carrying regions are shown hatched). Most of the inflowing plasma is accelearted to flow rapidly ($\simeq V_{Ai}$) along the boundary between the two inflow regions as it crosses these standing waves (Cowley, 1985).

the magnetic field is refracted towards the shock normal and its strength reduces as the shock front passes by.

In this model the magnetic merging can be regarded as the collision of two jets of plasma carrying oppositely directed magnetic fields. In the vicinity of the neutral line they approach each other at a speed, that no matter how small, is still bigger that the MHD slow wave and hence their collision is expected to give rise to slow shocks. Since slow shocks cannot propagate perpendicular to the magnetic field, they must remain attached to the diffusion region.

In Petschek's model reconnection can occur at any rate, with the outflow region responding to accommodate variations in the plasma inflow. So, the reconnection can take place at any rate up to an upper limit. The plasma outflow is not confined in a small region but takes place in an expanding 'scissors' area whose angle will change as the inflow velocity is changing. Detailed treatment (see Vasyliunas 1975) shows that the upper limit on the inflow velocity is

$$V_{i_{max}} = \frac{\pi}{8} \frac{V_{Ai}}{\ln R_m}. \tag{2.39}$$

Since the maximum rate depends only logarithmically on the Reynolds number it is much faster than the Parker-Sweet one. This also determines the term 'fast reconnection'. In 'fast reconnection' the global energy dissipation rate depends only logarithmically on the plasma resistivity. One problem with this mechanism is whether fast particles can be generated in numbers and energy range observed during flares.

Sonnerup's Model

Sonnerup's (1970) model for reconnection discuss what happens in the convection region but did not discuss what happens in the diffusion region. The diffusion region is absent in his model. The solution which assumes an incompressible plasma, is constructed from regions of uniform magnetic field and plasma velocity separated by the plane wave discontinuities standing in the plasma flow. The condition for the existence of these waves are the same as in Petschek's model, and their angles are determined by the requirement that both the magnetic field and the fluid velocity are rotated by ninety degrees between the inflow and outflow regions. In order to succeed in this at least two standing waves are necessary in each quadrant of the solution.

If solutions in the wave model of reconnection as discussed by Petschek exist over a wide

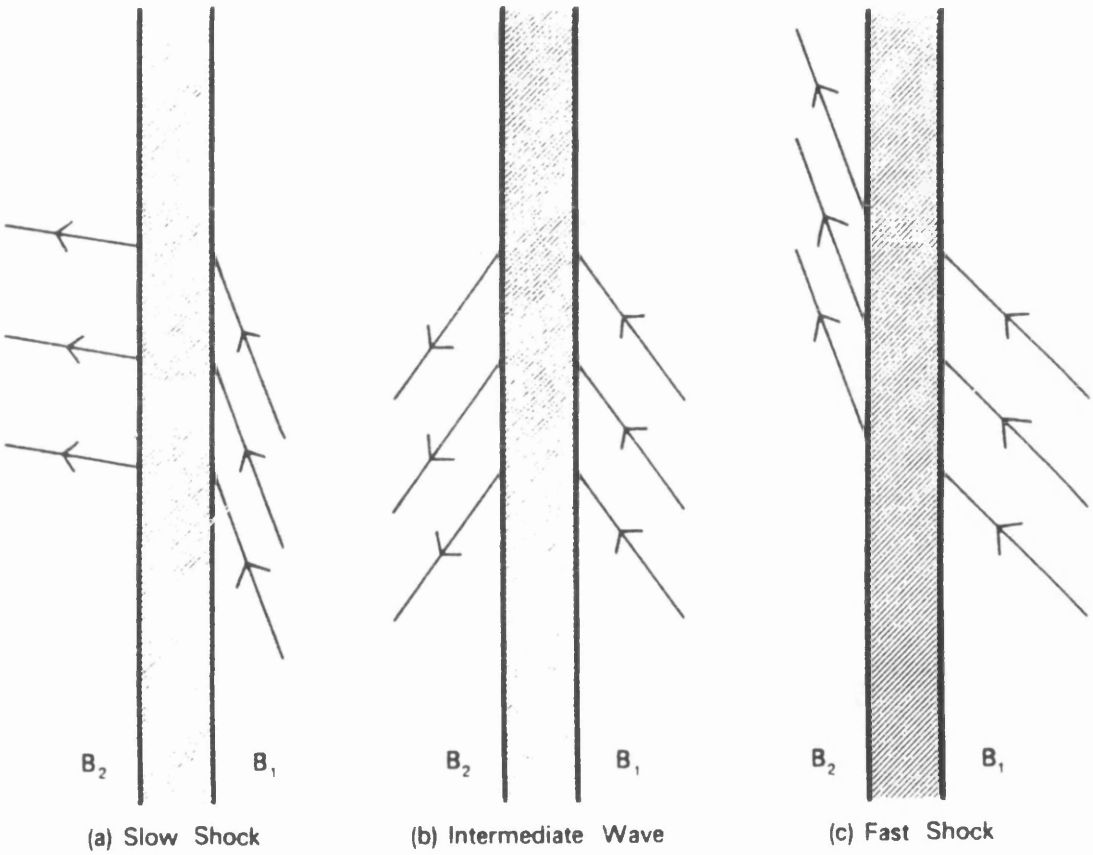

Figure 2.7: The change in magnetic field direction that are caused by the three types of oblique wave (Priest, 1982). The axis are set up in a frame of reference moving with the shock. Subscripts 1,2 denote respectively the values ahead of and behind the front.

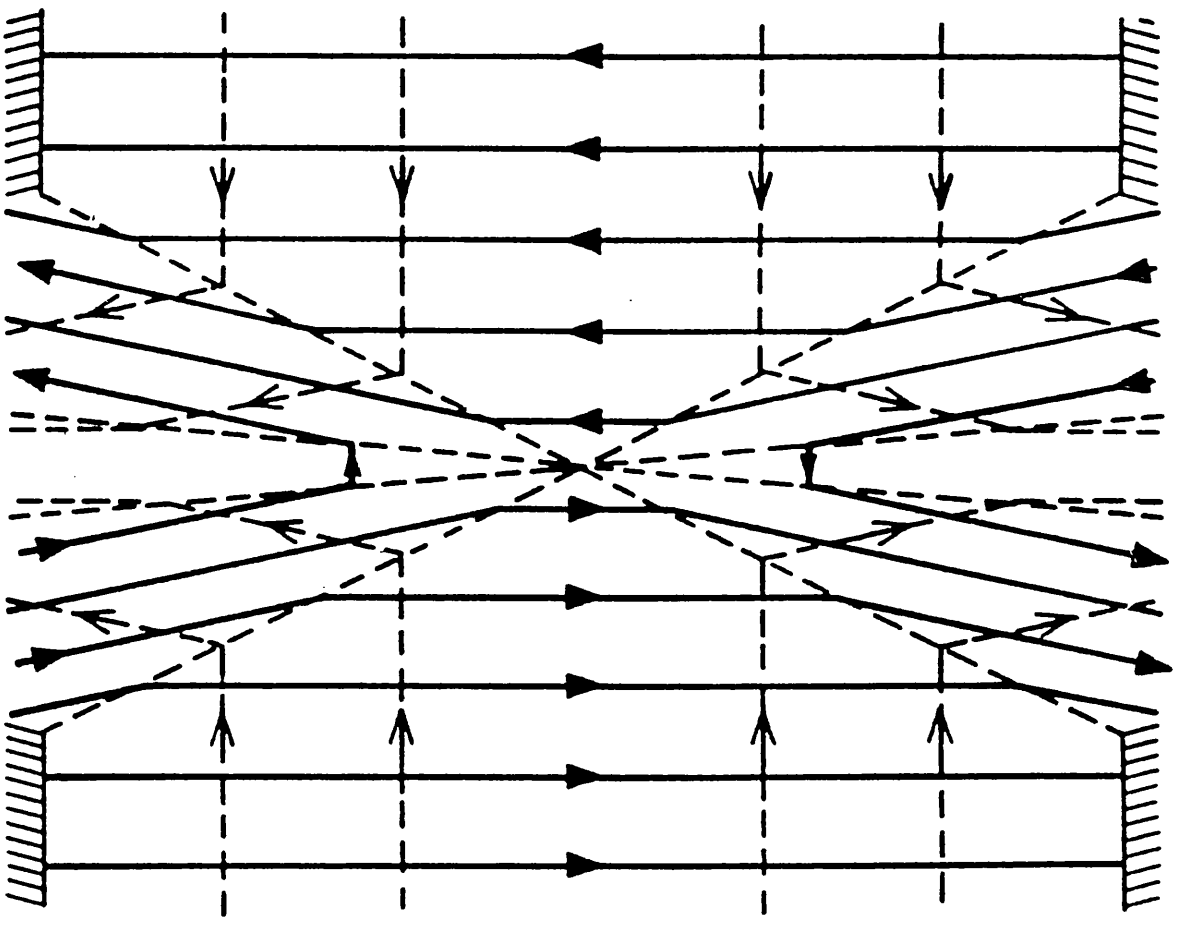

Figure 2.8: Sonnerup's Model. Magnetic field lines are shown by solid lines, streamlines by long-dashed lines and the standing waves by short dashed lines. The inflow may be considered to take place between plane parallel walls (shown hatched), while the outflow takes place through gaps in the walls. The outer waves originate at the gap edges, and the width of the gaps determines the inflow (and reconnection) rate. The central diffusion region is not represented.

range of inflow speeds (reconnection rates), then what actually determines the reconnection rate in any given situation. An answer to this question is that the overall reconnection rate is determined by the external boundary conditions of the physical system. This does not preclude the possibility that more local conditions could influence the system over shorted timescales.

Recent Developments

Forbes and Priest (1987) discuss the role of boundary conditions in both analytical and numerical solutions of steadily driven reconnection. According to this work a lot of the contradictory results in steadily driven reconnection are due to particular boundary conditions. Many puzzling questions have been raised by numerical experiments on reconnection, because these experiments don't always agree with the behaviour predicted by Petschek. Often the central current sheet is much longer that the Petschek analysis predicts, and the inflow towards the X line diverges rather than converges. Also the pressure variations in the inflow can be many orders of magnitude larger than those in the Petschek model. Lee and Fu (1986) and Priest and Forbes (1986) recognised that much of the unusual behaviour in the numerical experiments of reconnection is due to boundary conditions.

As was originally noted by Vasyliunas (1975), the behaviour of a reconnection solution depends strongly on whether the boundary conditions give rise to a slow-mode or a fast-mode expansion in the inflow region. Forbes and Priest (1987) show that many of the numerical experiments have boundary conditions which produce a slow-mode expansion in the inflow region rather than a fast-mode expansion. Since the fast mode expansion is an essential feature of the Petschek solution, it is not too surprising that these numerical experiments do not behave like the Petschek solution.

Syrovatskii's Model

The concept of current sheets originally discussed in the Parker-Sweet model was subsequently investigated by Syrovatskii (1971, 1981). He envisaged a mechanism that would involve the dynamics of individual particles which would affect the process of magnetic reconnection. This process is called dynamic magnetic reconnection. The X-type neutral point leaves equilibrium and relaxes to a current sheet. That happens since the boundary

is free to move. The solutions are exponential growing.

If the assumption of magnetohydrodynamics is violated in the nonadiabatic region then the medium will not admit the current density necessary for quasistationary conservation of field gradients. An electric induction field will appear, which will have two important consequences. First, the field **E** is not directly associated with the plasma displacements and can appear in a coordinate system fixed relative to the plasma. This would imply the destruction of the freezing-in property, which is fundamental for MHD, and leads to the condition that an electric field is absent in coordinates based on the conducting medium. The violation of the freezing-in property implies the possibility of lines of force slipping relative to the medium, closing up, and so on. In this case the process is not associated with Joule dissipation, and may operate in a collisionless plasma.

Second, the electric field is directed along the current **j**, and thus it will perform positive work on the charged particles, increasing their energy. It is this process that will be capable of converting magnetic energy into kinetic energy of the particles, the distinctive dissipation that it is called dynamic dissipation. Its distinction from Joule dissipation is primarily that in the case of dynamic dissipation there is no simple proportionality between the current density **j** and the intensity of the electric field **E**. If the criterion is violated the current density will reach saturation and the field energy will be expended in increasing the total energy $\epsilon = \sqrt{(m^2c^4 + c^2p^2)}$ of the particles. Particle acceleration will proceed along the null lines.

Craig and McClymont approach to Petschek's model

In an attempt to understand Petschek's mechanism Craig and McClymont (1991, 1993), have presented a linear model of magnetic reconnection that gives the right timescales. A serious problem with Petschek's mechanism is the matching to the solution in the diffusion region, which is treated very approximately by Petschek. Craig and McClymont (1991, 1993) develop a linear theory for the dissipation of the free energy of the magnetic field in small disturbances imposed on the potential field of an X-type neutral point.

They study a closed system, with no magnetic flux or plasma entering or leaving the volume. The perturbation of the vector potential is set constant on the boundary, which means that the current and the Lorentz force vanish there. Only the $m = 0$ azimuthal modes correspond to topological reconnection, all other modes are current free. The

reconnection process is oscillatory. What this means is that a current sheet is formed due to the perturbation that after a few oscillations relaxes to the initial potential field (see Fig (2.9)). The reconnection rate scales as $(\ln \eta)^2$, so the reconnection is 'fast'. Detailed discussion of this model is presented in Chapter 4.

2.5.2 Collisionless Models

I am going to discuss now reconnection in plasmas that are collision free, that is that the mean free path for particles' collisions (or close encounters) is bigger than the size of the system. Here single particle motion in electromagnetic fields is considered. The electromagnetic fields should be appropriate to reconnection and self-consistency conditions should be applied. Certain effective conductivities may become important whenever scale lengths of the the system consider are small compared to the mean free path.

Dungey first (1953) described single particle field motion in an X-type field geometry with an electric field along the X-line.

In the absence of collisions (classical) two mechanisms have been proposed to limit the current close to the neutral line, anomalous resistivity and particle inertia. Anomalous resistivity results as strongly localised current close to an X-line builds up and goes unstable. The finite time that a particle spends in the weak magnetic field region limits the maximum velocity that it can acquire. In this case energy is carried out of the system by accelerated particles. In this work we will be discussing the role of particle inertia in determining and controlling the rate of the reconnection.

Burkhart et al. (1991) present the results of an analytic and numerical investigation of the structure of the X line during steady magnetic reconnection in collisionless plasma. To obtain a self-consistent description of steady collisionless reconnection one needs to consider the feedback effect of the accelerated particles on the initial vacuum magnetic field, which is a nonlinear problem. Their simplifying assumptions are the following: i) two dimensional (2-D) magnetic field of X-type geometry, ii) invariance of the system in the direction of the inductive electric field, iii) small temperature of the injected particles. They assume a highly elongated current carrying dissipation region with a strongly deformed magnetic field in the vicinity of the neutral line, and they calculate the ion trajectories inside the dissipation region. Knowing these trajectories, they close the system of equations, and so obtain scaling relations for nonlinear collisionless reconnection.

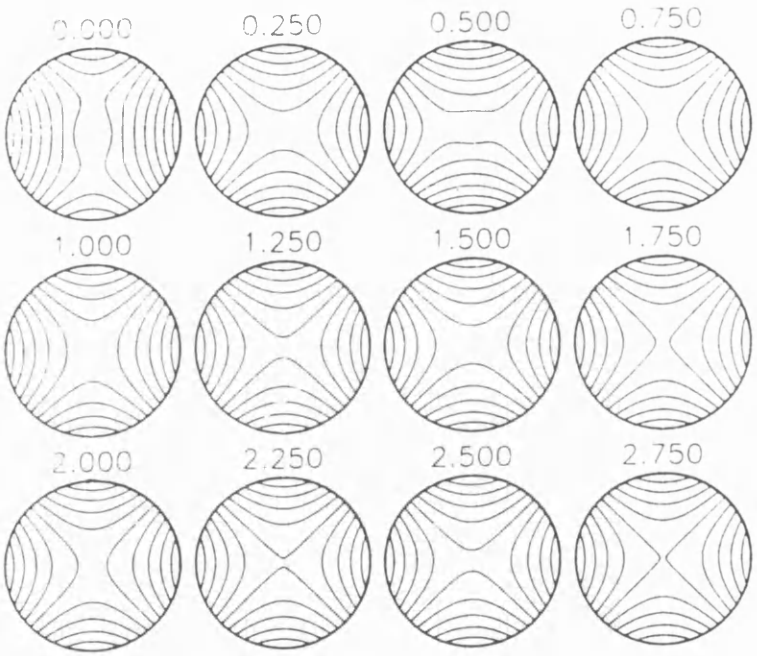

Figure 2.9: Evolution of field lines in the fundamental (m=0, n=0) mode for $\eta = 10^{-3}$ (the inverse magnetic Reynolds number). The number above each plot, $\omega t/2\pi$, gives the phase of the oscillation. Three complete cycles are shown, during which the amplitude of the perturbation decreases by a factor of 60. Note that during the oscillation the field lines reconnect as they pass through the origin, so resistivity is essential for this mode. The initial vertical 'current sheet' begins reconnecting, and the inertia of the flowing plasma carries the system past the equilibrium configuration, till a weaker horizontal 'current sheet' is formed at phase=1/2. A much weaker vertical 'current sheet' returns at the end of the first cycle. After three cycles, the system is very close to its equilibrium neutral point configuration.

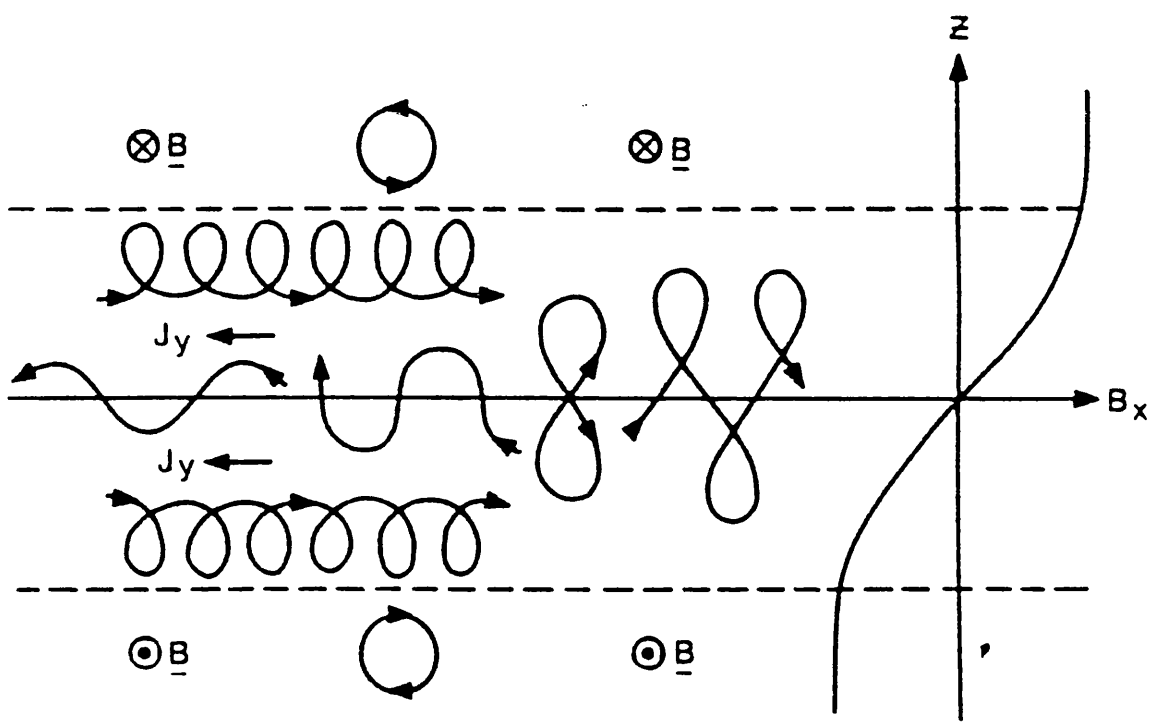

Figure 2.10: Sketch of ion trajectories in a magnetic neutral sheet system with zero electric field. The variation of the field strength is shown on the right and the dashed lines indicate the boundaries of the current layer. The horizontal solid line is the neutral sheet.

Harris Model

An exact solution of the Vlasov equations was found by Harris (1962) which describes a layer of plasma confined between two regions of oppositely directed magnetic field. The electrons and ions have Maxwellian distributions on the plane where the magnetic field vanishes.

When the simplest magnetic field configuration containing a field reversal area is considered with no electric field imposed then the trajectories for ions look like the ones in figure (2.10). The orbits for electrons are obtained if the direction of motion is reversed. In the vicinity of the neutral sheet the field varies approximately linearly with 'z' due to a uniform current, before becoming constant with distance away from the current sheet. Outside the neutral sheet the particle orbits are circular (in projection). But when the particles enter the field gradient area things change. From the drift theory we know that a gradient in the magnetic field gives rise to drift motion. This drift motion is adiabatic. If however the particle's orbit crosses the neutral line then a snake like orbit is observed and the particle starts moving along the neutral line, having an oscillatory motion. Electrons and ions drift into opposite directions. So, a current is set up in which both electrons and ions contribute. When no electric field is present an equilibrium will be set up. To have an equilibrium, two conditions must exist. First the amplitude of the particle oscillation should be the same so that charge neutrality exists. The second is that their amplitude must match the thickness of the current sheet. Once this particle population is set up it will carry this current indefinitely, provided that the current sheet is infinite. There is no field annihilation and no conversion of energy between the plasma and the field taking place here.

Speiser's Orbits

Speiser (1965) discussed particle trajectories in simple linear current sheets. In the simplest case of a current sheet, with the magnetic field given by

$$\underline{\mathrm{B}} = -B\frac{x}{d}\hat{y} \tag{2.40}$$

and the electric field given by

$$\underline{\mathrm{E}} = -a\hat{z}, \tag{2.41}$$

particles of both charges, enter the reversal region and they oscillate in between the oppositely directed magnetic field regions. They can thus increase their energy indefinitely. He then added a small perpendicular magnetic field of the form

$$\underline{\mathrm{B}} = -B(\eta\hat{x} - \frac{x}{d}\hat{y}) \tag{2.42}$$

where η is assumed to be a small quantity, which caused particles to leave the reversal region after a few oscillations. Ions and electrons move in opposite directions both contributing to the current.

Speiser (1970) qualitatively analyses Ohm's law including both inertial and collisional terms and calculates the effective conductivity. Ohm's law is approximated by

$$\frac{m}{ne^2}\frac{\partial \underline{\mathrm{j}}}{\partial t} = \underline{\mathrm{E}} - \frac{\underline{\mathrm{j}}}{\sigma_c} \tag{2.43}$$

where σ_c is the collisional conductivity. The effective conductivity is equal to the collisional conductivity when we consider times much bigger that the collision time. If on the other hand we consider times much smaller than the collision time then the conductivity becomes arbitrarily small, depending on the lifetime of a particle in the system. Consequently, the inertial term in Ohm's law which is usually ignored in MHD become important. The same argument stands for the characteristic distance as well.

2.5.3 Resistive Instabilities

Resistive instabilities are different from MHD modes in that finite resistivity is required to produce them. The treatment of resistive instabilities is in general more complex than the MHD ones, because the resulting differential equations are fourth order, and the important modes are spatially localised an a small neighbourhood centered around the singular surface $\mathbf{k} \cdot \mathbf{B} = 0$, or result from modes which are singular in the absence of dissipation. The significance of the singular surface derives from the fact that when the resistivity is finite, the plasma is completely detached from the magnetic field in a small region around the singular surface. Such an effect enables the system to go from states of high potential energy to states of neighbouring lower potential energy, which are not accessible without dissipation. In particular the energy realised when going from the higher potential state to the lower potential state thermalizes the magnetic field and generates directed kinetic energy.

The general development of the theory of resistive instabilities began with the work of Furth, Killeen and Rosenbluth (1963). Resistive instabilities such as the tearing mode instability lead to the formation of several X-type neutral points which have magnetic 'islands' in between. Configurations like this help to carry material away from the reconnection region at a substantial rate which increases the reconnection rate. Spicer (1976, 1977) pointed out that the reconnection regions in the presence of the tearing instability may overlap and so increase the number of X-type neutral points. The tearing-mode instability develops on a timescale which is typically the geometrical mean $(\tau_d \tau_A)^{1/2}$ of the diffusion time τ_d and the Alfven travel time τ_A.

2.6 Particle Acceleration

2.6.1 Observational Evidence for Accelerated Particles

Because in situ measurements are not possible, the existence of fast particles in solar flares must be inferred from their consequences. These are electromagnetic, continuum and line radiation, over the whole spectrum from radio to gamma rays, and fast particles detected in the interplanetary medium. From these observations one must infer the spatial, spectral and temporal characteristics of the particles. The detection of fast particles in space is usually done by measuring energy spectra over some range, pitch angle distributions of the particles and mass distributions.

A major problem of relating the particle observational data to the spectrum of the fast particles at the sun, or determining the timing of the acceleration process, is the propagation effects. There may be strong interactions involved, such as MHD turbulence in the solar wind and even acceleration existing in the interplanetary medium. The spectrum observed at the satellite depends also on time, being harder at the beginning of the observation when the faster particles have arrived. It also depends on the magnetic connection, that is if there are magnetic field lines connecting the satellite with the flaring part of the corona. Also effects of propagation, storage and release in the corona are of great importance.

Proton energy spectra at 1 AU when the observations are done at maximum particle intensity, under good magnetic connection conditions, usually show a power law shape from 20 MeV to 80 MeV with a spectral index between 2.5 and 3.7 (Heyvaerts, 1981).

Steeper spectra are observed when the magnetic connection is not good, which could result from an energy dependence of particle escape from the corona.

2.6.2 Particle Acceleration Mechanisms

Any viable acceleration mechanism should be able to account for the timescales of electron and proton acceleration, their energy spectra, the total numbers or ratios of accelerated particles and it must be able to give a large fraction of the flare energy in the form of accelerated particles. As we have already mentioned, what gives energy to accelerated particles is the magnetic field, through some induced electric field developed in some (resistive) MHD process (Heyvaerts 1981).

The acceleration mechanism must operate on a timescale of seconds to produce electrons with energies in excess of 10-20 keV, possibly with a power-law spectrum, at a rate of up to $10^{37}s^{-1}$. It must convert the available magnetic energy into these fast particles with an efficiency up to 50%. It must probably lie in the corona and it must be able to produce MeV ions, or there must be a related mechanism that can do that.

Another view is that the acceleration mechanism must energize in bulk more than 10^{38} electrons to a relaxed (possibly Maxwellian) distribution with temperature $\geq 10^8$ K.

Essentially all acceleration mechanisms rely on electric fields. These can be produced inductively either over an extended region in the reconnection process, or locally in the fluctuations associated with various sorts of plasma oscillations. For reviews on particle acceleration see Heyvaerts, (1981), Forman et al. (1986) and for a link with impulsive phenomena see MacKinnon (1986).

Diffusive Shock Acceleration

A first order Fermi process functions in diffuse shock acceleration. Essentially one has a shock moving along the magnetic field. The fraction of particles that move fast enough can cross and recross the shock front, thus gaining energy (Kuijpers, 1993). A different shock acceleration mechanism relies on the 'grad B' drift of a charged particle along the shock front for a shock moving perpendicular to the magnetic field. Particles with cyclotron radii larger than the shock front thickness gain enough energy by the electric field at the shock. This is called the shock drift acceleration (Decker 1988).

Stochastic Acceleration

Stochastic acceleration of particles in turbulent fields is defined as the process that causes particles to change their energy in a random way with many increases and decreases that lead finally to acceleration. Stochastic acceleration of ions can result from Alfven waves with wavelengths of the order of the ion gyroradius. Furthermore, for resonant scattering, ions have to be moving with velocity equal to or larger than the Alfven speed and electrons must have $u > 43V_A$ to scatter from whistlers (Melrose, 1974). The characteristic spectra obtained from such a mechanism can fit the observational data (see Ramaty and Murphy, 1987). Ambrosiano et al. (1989) found that particles can be accelerated to high energies from turbulent reconnecting magnetic fields (Vlahos 1989).

Electric fields Acceleration

As we know direct electric fields can accelerate particles. Such fields are associated with magnetic reconnection in the vicinity of neutral points and current sheets (Syrovatskii, 1981). Particle acceleration is possible also when the electric field is parallel to the magnetic field (Colgate, 1978). Parallel electric fields arise from the interruption (due to plasma instabilities) of the parallel currents associated with twisted magnetic flux tubes and from the formation of double layers (Alfvén and Carlquist (1966), Spicer (1982)).
D.C. (or at least slowly varying) electric fields will be produced inductively during the reconnection process. But what is the response of a plasma to an imposed electric field? This depends on the magnitude of the electric field. Collisions of the plasma electrons will oppose acceleration from the electric field. Only those electrons for which this 'frictional' force is smaller than the force from the electric field will be accelerated. The magnitude of the 'frictional' force falls off with increasing velocity. So for any specified value of the electric field there will be a critical value of electron velocity above which electrons are freely accelerated out of the bulk of the plasma. The field for which this critical velocity equals the thermal velocity is called the Dreicer field (Dreicer, 1959), E_D and is given by

$$E_D = \frac{e \ln \Lambda}{\lambda_D^2} \tag{2.44}$$

where e is the electronic charge (e.s.u.), Λ is the Coulomb logarithm and λ_D is the Debye length (cm). For $E > E_D$, collisions cannot maintain a steady state, and the bulk of the plasma will runaway. For $E < E_D$ some fraction of electrons in the tail of the distribution

is accelerated out of the bulk. This fraction is approximately

$$\frac{n_r}{n} = \frac{1}{2}\exp\{-\frac{1}{2}[(\frac{E_D}{E})^{1/2} - \frac{E}{E_D}]^2\} \tag{2.45}$$

where n is the density of the bulk plasma, and n_r is the density of runaway electrons. The fraction of runaway electrons falls off with decreasing E roughly as $\exp(\frac{E_D}{2E})$.

2.6.3 Evolution of Particle Distributions

In the kinetic theory of plasmas the properties of particles are described by distribution functions whose evolution is determined by kinetic equations. Many different modes of waves can be created in a plasma. If these waves are weakly damped waves then the kinetic equations of the plasma can be averaged over these fluctuations. One finds the averaged kinetic equations then, which are sometimes called quasilinear equations.

Consider a distribution of particles of species α (where α is e for electrons and i for ions) with charge q_α and mass m_α. The distribution of particles can be described in terms of the density of representative points for particles in the 6-dimensional $\underline{x} - \underline{p}$ phase space, where $\underline{x}$ is the position vector and $\underline{p}$ is the momentum of the particle. A kinetic theory description of a plasma is based on a set of kinetic equations that describes how the distribution functions evolves due to wave-particle and particle-particle interactions.

The Vlasov Equation

The basic equations of the kinetic theory of plasmas are called the *Vlasov Equations.* They are the following:

- A set of equations which is formally identical to a set of Boltzmann equations for each species of particles:

$$\{\frac{\partial}{\partial t} + \underline{u}\cdot\frac{\partial}{\partial \underline{x}} + q_\alpha[\underline{E}(\underline{x},t) + \underline{u}\times\underline{B}(\underline{x},t)]\cdot\frac{\partial}{\partial \underline{p}}\}f_\alpha(\underline{x},\underline{p},t) = \frac{df_\alpha(\underline{x},\underline{p},t)}{dt}|_{coll} \tag{2.46}$$

  where $f_\alpha(\underline{x},\underline{p},t)$ is the single particle distribution function for species α. The right hand side is the effect due to collisions so in a collisionless plasma it is neglected.

- A pair of equations giving the charge and current density in terms of the single particle distribution functions:

$$\rho(\underline{x},t) = \sum_\alpha q_\alpha \int f_\alpha(\underline{x},\underline{p},t)d^3\underline{x}, \tag{2.47}$$

$$\underline{J}(\underline{x},t) = \sum_\alpha q_\alpha \int f_\alpha(\underline{x},\underline{p},t)\underline{u}d^3\underline{x} \tag{2.48}$$

where the sum is over all species of particle.

- Maxwell's equations here in CGS units:

$$\nabla \times \underline{B} = \frac{4\pi}{c}\underline{j} \tag{2.49}$$

$$\nabla \times \underline{E} = -\frac{1}{c}\frac{\partial \underline{B}}{\partial t} \tag{2.50}$$

$$\nabla \cdot \underline{B} = 0 \tag{2.51}$$

$$\nabla \cdot \underline{E} = 4\pi\rho. \tag{2.52}$$

The source terms ρ and $\underline{j}$ are identified with those in previous equations. In the Vlasov equations $\underline{B}$ and $\underline{E}$ are the self-consistent fields, which are functionals of the distribution functions. Despite its apparent simplicity, the this set of equations is a set of nonlinear, coupled, integro-differential equations for the distribution functions $f_\alpha(\underline{x}, \underline{p}, t)$.

The Vlasov equation conserves particles, and the probability remains constant. The Vlasov equation has a wide variety of stationary states. That is there are many solutions $f_{\alpha 0}$ that satisfy $\partial f_{\alpha o}/\partial t = 0$. These states are often called meta equilibria, since they are only equilibria on a timescale short compared with collision time. A stationary state must satisfy

$$\{\underline{u} \cdot \frac{\partial}{\partial \underline{x}} + q_\alpha \underline{x}[\underline{E} + \underline{u} \times \underline{B}] \cdot \frac{\partial}{\partial \underline{p}}\} f_{\alpha 0}(\underline{x}, \underline{p}) = 0. \tag{2.53}$$

A procedure for generating a general solution of (2.53) is found by defining $\underline{x}'(t')$, $\underline{u}'(t')$ as the orbit of a particle of charge q, mass m, in the field $\underline{E}$, $\underline{B}$, with the orbit $(\underline{x}', \underline{u}')$ intersecting the point in phase space $(\underline{x}, \underline{u})$ at time $t' = t$.If $a(\underline{x}', \underline{u}')$, $b(\underline{x}', \underline{u}')$, ..., are constants of the motion of the particle, they satisfy

$$\frac{da}{dt'} = \underline{u}' \cdot \frac{\partial a}{\partial \underline{x}'} + \frac{\partial \underline{u}'}{\partial t'} \cdot \frac{\partial a}{\partial \underline{u}'} = 0 \tag{2.54}$$

$$\frac{db}{dt'} = \underline{u}' \cdot \frac{\partial b}{\partial \underline{x}'} + \frac{\partial \underline{u}'}{\partial t'} \cdot \frac{\partial b}{\partial \underline{u}'} = 0. \tag{2.55}$$

Then any function

$$f_{\alpha 0} = f_{\alpha 0}[a(\underline{x}', \underline{u}'), b(\underline{x}', \underline{u}'), ...] \tag{2.56}$$

satisfies (2.53) at $t' = t$, and thus any function

$$f_{\alpha 0} = f_{\alpha 0}[a(\underline{x}, \underline{u}), b(\underline{x}, \underline{u}), ...] \tag{2.57}$$

of the constants of the motion of a particle is also a stationary-state distribution for an assembly of particles, according to the Vlasov equation. In many cases, the distribution

f_α is controlled by external fields and the constants of motion for a particle in these fields can be used to construct stationary states.

The entropy is constant in a Vlasov plasma. This is consistent with the fact that the Vlasov equation neglects the process (binary collisions) which causes statistical systems to increase their entropy and evolve toward a Maxwell-Boltzmann distribution.

2.6.4 Calculations of Particle Energy Spectrum

Attempts have been made to calculate the energy spectrum of particles accelerated in neutral sheets. In the absence of stochastic processes such as Coulomb collisions or wave-particle interactions, the phase space distribution function satisfies Liouville's theorem. The density of particles in phase space is constant on phase space trajectories. Therefore given the initial distribution of injected particles and solutions of particle orbits, the momentum distribution function of particles leaving the acceleration region can be calculated (Friedman, 1969; Bulanov and Sasarov, 1976; Bulanov 1980). Friedman (1969) presented a numerical study of particle trajectories in a Petshek field configuration, with a constant electric field which gives an exponential energy distribution for the accelerated particles. The particles are distributed randomly around the x-line with a thermal velocity distribution.

Bulanov and Sasarov (1976) solve the equations of motion approximately in the region where particles are not magnetised. They use that to estimate approximately the time that a particle will spend close to the neutral point area before it is expelled. The energy that particles gain in a magnetic field containing an X-type neutral point depends on how close to the neutral point they start (so if they start at the neutral point they gain an infinite amount of energy). They find that when the initial distribution of particles is uniform in space, the spectrum is exponential in energy or in a fractional power of the energy.

Bruhwiler and Zweibel (1992) study particle trajectories near a magnetic X-line when a strong component of the magnetic field along the X-line is present. When they compare their results with those of Bulanov and Sasarov (1976), they find that the characteristic energy of accelerated particles scales very differently with the physical parameters of the problem. Both distributions have an exponential spectrum, but the Bulanov and Sasarov (1976) spectrum is slightly harder energy spectrum than Bruhwiler and Zweibel (1992)

spectrum.

Matthaeus et al (1984) analyse particle orbits in MHD fields which evolve and reconnect in the presence of finite amplitude fluctuations. As they point out, the short time that particles spend near an X-type neutral point is viewed as a limitation of this configuration for accelerating charged particles. They find however that turbulent fluctuations appearing near the reconnection zone can trap test particles in the strong electric field region for long enough times to produce significant acceleration.

2.7 Orbits

The motion of charged particles is an essential ingredient of fully understanding plasma properties in a collisionless environment. In systems where the charged particle Larmor radii are much smaller than any spatial length scales, the particle motion can be approximated by adiabatic invariance theory. Adiabatic invariance may also be applicable if the time variation of the system is sufficiently slow relative to the gyroperiod. If the Larmor radii are much greater than any spatial length scales one may be able to assume unmagnetised particle motion. However, if the Larmor radii and spatial length scale are comparable, then the particle motion is difficult to analyse. If in addition particle-particle or wave-particle interactions exist (generally referred to as collisions) then the complexity of the particle motion is further increased. Particle motion (even without collisions) is particularly complex if the system of interest consists of both adiabatic and non-adiabatic regions.

A different approach is to consider families of orbits and phase space topology of the system rather than individual orbits. Chen and Palmadeso (1986) showed that there are only two global constants of motion in the magnetotail geometry and that particle motion is not integrable. Using the Poincare surface of section technique, they found that the phase space is divided into disjoint regions occupied by dynamically distinct classes of orbits. Based on the partitioning of phase space they proposed a process called 'differential memory', which can significantly influence the time evolution of plasma distributions. This process arises from the property that different phase space regions are characterised by widely separated time scales, so that the respective phase space regions can retain memory of the existing population of particles for different lengths of time. The time scales referred

to here are the accessibility time, the time for orbits far away from the mid plane to reach various regions of the phase space. The dynamical system is chaotic in the sense that the outgoing conditions exhibit sensitive dependence on the incoming conditions (Chen 1992).

Chaotic properties

Martin (1986) used the Lyapunov characteristic exponents (LCEs) to show that orbits passing near an X-line are chaotic. In particular Martin (1986) suggested that chaotic particle motions can serve as effective dissipation ("chaotic resistivity") in a collisionless environment. In that case estimates of the Lyapunov exponent (which measures the rate at which nearby orbits diverge) may provide a chaotic dissipation time-scale. This is because the LCE measures the time it takes for the system to randomize and therefore may play a similar role to the collisional frequency in a collisional plasma. Doxas et al. (1990) used $\mathbf{J}.\mathbf{E}$ (calculated numerically) to study the effects of collisionless chaotic conductivity. They calculated the power transfer ($\mathbf{J}.\mathbf{E}$) for groups of test particles and they argued that irreversible heating occurs as a result of chaotic particle motion. They had a uniform electric field imposed in collisionless conditions. The characterisation "chaotic scattering" requires specific demonstration. One must first define suitable asymptotic initial and final states which are regular and then show that the final states sensitively depend on the initial states. See Eckhardt (1988) for a brief review of chaotic scattering. For an extensive discussion of nonlinear dynamics of particles in magnetic reconnection see Chen (1992).

Chapter 3

Model for Particle Acceleration in Dynamic Magnetic Reconnection

3.1 Introduction

A considerable number of studies of particle acceleration in collisionless reconnection by the test particle approach exist. In most of these studies the electric and magnetic fields are specified and do not depend upon the particle response (e.g. Martin, 1986, Burkhart et al. 1990, 1991). The test particle approach can be justified in a number of situations relevant to collisionless reconnection. First, if the plasma density is low enough, then the current carried by the particles will have a negligible effect on the magnetic field. Also, the test particle approach can be justified for a collisionless tail of particles even when there is a collisional background plasma whose response determines the reconnecting fields. A recent test particle study focussing on the particle density and current density of the electron and ion species and the relationship with the driving electric field was done by Burkhart et al. (1990) and was later generalised to include self-consistent effects by Burkhart et al. (1991).

Under the assumption that a 'DC' electric field accelerates particles, Martens (1988) discuss the acceleration of particles in the solar corona, arguing that this is completely collisionless. This is justified by the fact that the mean free paths of protons and electrons in the solar corona are (for energies E_p and E_e)

$$\lambda_{p,e} = \frac{E_{p,e}^2}{n_p \pi e^4 (\ln \Lambda)^2} \sim 10^{10-11}\,\mathrm{cm} \tag{3.1}$$

where n_p is the proton density and is $10^{10}\,\mathrm{cm}^{-3}$, and $\ln \Lambda$ (~ 20) is the Coulomb logarithm. He uses observational indications for the electric field present in the current sheet such as given by Kopp and Poletto (1986) and estimates the acceleration lengths (of the order 10^4 cm for electrons of 30 kev and 10^5 cm for protons of 200 keV) to be much smaller than the mean free path.

One should have strong electric fields in order to accelerate particles. The existence of strong electric fields of order 10^2 Volts/cm in flares has been widely recognised from studies of Stark broadening of high Balmer lines in flares. Reports of values as high as 7×10^2 Volts/cm exist (see Foukal et al. 1986, for references and different interpretations of the line broadening). Kopp and Poletto (1986) calculate an electric field of $10 - 10^2$ Volt/cm from the observed lateral velocity of the Hα ribbons and the photospheric line of-sight magnetic field. Foukal et al. (1987) find an upper limit to the electric field of 5-10 Volts/cm.

In this chapter I present the results of a non self-consistent calculation for collisionless magnetic reconnection. We start with the assumption of electric and magnetic fields, so this is not necessarily self-consistent. The magnetic field is one containing an X-type neutral point. Two cases of imposed electric fields are considered, one constant and the other time-varying. We calculate the particle orbits in these fields and the energy distributions that result. In the following chapters we use the linear analysis of dynamic magnetic reconnection of Craig and McClymont (1991), to calculate the electromagnetic fields present. Then we calculate the motion of particles in these electromagnetic fields.

Recall the gist of eg the Craig and McClymont (1991) linear description of dynamic reconnection. A disturbance propagating from the boundary of the system behaves like an MHD wave, travelling with the local Alfven speed, until it reaches the neutral point. In the dissipation region surrounding the neutral point resistivity becomes important. The wave resembles a 'diffusive' disturbance as it propagates across the neutral point, and the electric field associated with it becomes significant. When the electric field is significant, particles can get a net acceleration.

Since we will be considering the particle acceleration consequences of a linear, reconnective disturbance, we may pick our test particles from an isotropic, homogeneous distribution. In

other words, we consider the influence of a linear disturbance on particles drawn from the background distribution. This is in contrast to particle studies of nonlinear reconnection, where consistency demands consideration of the motion of particles into the dissipation region. In most studies particles are injected in two opposite quadrupoles of the X-point and they subsequently are driven, by the $\underline{E} \times \underline{B}$ drift due to an imposed constant electric field, to cross from the nonadiabatic region or miss it depending on their initial conditions. The obvious problem with the 2-D X-type neutral point is the size of the system in the Z-direction. If a particle is somehow trapped around the nonadiabatic region then it can get accelerated for ever. We understand that this is an important problem, but consider a full 3-D treatment to be beyond the scope of the present work.

3.2 Equations of motion

We adopt an idealised magnetic field containing an X-type neutral point:

$$\underline{B} = \frac{B_o}{D}(y\hat{x} + x\hat{y}). \tag{3.2}$$

The current density vanishes for this field configuration. The field lines are the solutions of the $\frac{dx}{dy} = \frac{y}{x}$ which are hyperbolae $y^2 - x^2 = const.$ No B_z component of the magnetic field is included. The x-line (neutral line) lies along the z-axis. The field modulus is

$$|\underline{B}| = B_o \frac{r}{D} \tag{3.3}$$

where $x^2 + y^2 = r^2$.

Note that this configuration has no natural scale length. Requiring the field to have a value of 10^2 gauss at a typical active region distance of 10^9 cm from the neutral point, fixes only $B_o/D = 10^{-7}$ gauss cm^{-1}. We are free to use other considerations to fix one of B_o and D independently, as we do below in introducing dimensionless variables.

An electric field is imposed in the z direction and is restricted to the neutral point area. We will consider the effects on particle acceleration from two forms of electric field imposed on the X-type neutral point. First, we will consider a constant electric field and second, a time varying electric field.

The equations that we solve numerically are the relativistic (particles are expected to acquired relativistic velocities) equations of motion in the observer's reference frame:

$$\frac{d\underline{r}}{dt} = \frac{\underline{p}}{m\gamma} \tag{3.4}$$

$$\frac{d\underline{p}}{dt} = -q(\underline{E} + \frac{1}{c}(\underline{u} \times \underline{B})) \tag{3.5}$$

3.2.1 Dimensionless parameters and equations

We will normalize distances to D and times to the gyroperiod at $r = D$. We denote this timescale by τ_p and τ_e for electrons and protons respectively. As noted above, D is as yet undetermined. It turns out to be convenient in this relativistic calculation to choose D such that velocities are normalised to the speed of light. This has the consequence that D takes different values D_e and D_p for electrons and protons respectively, such that

$$D_p = (\frac{m_p}{m_e})^{\frac{1}{2}} D_e. \tag{3.6}$$

Specifically, with $B_o/D = 10^{-7}$, we find $D_e = 1.3 \times 10^5$ cm and $D_p = 5.6 \times 10^6$ cm. With our choices of $\underline{E}$ and $\underline{B}$ the Lorentz equations (3) and (4) become in dimensionless units:

$$\begin{aligned}
\frac{d\bar{x}}{d\bar{t}} &= \bar{u}_x = \frac{\bar{p}_x}{\gamma} \\
\frac{d\bar{y}}{d\bar{t}} &= \bar{u}_y = \frac{\bar{p}_y}{\gamma} \\
\frac{d\bar{z}}{d\bar{t}} &= \bar{u}_z = \frac{\bar{p}_z}{\gamma} \\
\frac{d\bar{p}_x}{d\bar{t}} &= -\epsilon \bar{x} \bar{u}_z \\
\frac{d\bar{p}_y}{d\bar{t}} &= \epsilon \bar{y} \bar{u}_z \\
\frac{d\bar{p}_z}{d\bar{t}} &= \bar{E}_o + \epsilon(\bar{x}\bar{u}_x + \bar{y}\bar{u}_y)
\end{aligned} \tag{3.7}$$

where $\gamma = (1 + {p_x}^2 + {p_y}^2 + {p_z}^2)^{\frac{1}{2}}$ and $\epsilon = +1$ for protons, $\epsilon = -1$ for electrons. E_o is the true value of the electric field and $\bar{E}_o = E_o D_i / B_o D$ is the dimensionless electric field, the suffix i is e for electrons and p for protons. The kinetic energy of the particles in dimensionless units is $E_{kin} = \gamma - 1$. Equations (3.7), with appropriate initial conditions describe the motion of a particle.

3.2.2 Characteristic timescale

The maximum velocity that a particle can acquire in a collisionless plasma during magnetic reconnection can be estimated by the characteristic lifetime of the particle in the

nonadiabatic region. In all these calculations the particle crosses the neutral point area once or is not trapped in that region for times bigger than the characteristic timescale. The usual way to estimate the characteristic timescale is first estimating the effectively unmagnetised region as a region of size

$$\Delta_i \sim \frac{u_i}{\Omega_i(\Delta_i)} \tag{3.8}$$

where u_i is the particles velocity of the i species and $\Omega_i(\Delta_i)$ is the gyrofrequency at the location Δ_i (Sonnerup, 1971). Near the X-line, $\Omega_i(\Delta_i) \simeq \Omega_i'\Delta_i$, where the prime denotes a derivative that can be evaluated along x or y, because of the symmetry. So,

$$\Delta_i \sim (\frac{u_{thi}}{\Omega_i'})^{1/2} \tag{3.9}$$

which is the geometric mean of the Larmor radius in the asymptotic magnetic field and the characteristic magnetic scale length. Within a region, Δ_p and Δ_e of the X-line, the protons and electrons are effectively unmagnetised and decouple from the magnetic field. The characteristic lifetime t_i of particles in the unmagnetised region Δ_{xi} is simply given by

$$t_i \sim \frac{\Delta_{xi}}{u_{thi}} \sim (\frac{d\Omega_i}{dx} u_{thi})^{-1/2} \tag{3.10}$$

It has been suggested that this lifetime in the unmagnetised region can be regarded as an effective collision time for electrons and protons in a collisionless plasma (Rusbridge, 1971, Galeev et al. 1978).

We call the radius of the unmagnetised region the 'adiabaticity radius'. Inside this radius is where the electric field becomes significant.

3.2.3 Parameters, Initial Conditions

We start the integration of particle orbits at t=0 and with the particles positioned randomly in a box with the following size

$$-1.0 \leq \quad x0 \quad \leq 1.0 \tag{3.11}$$

$$-1.0 \leq \quad y0 \quad \leq 1.0 \tag{3.12}$$

$$z0 \quad = 0.0. \tag{3.13}$$

The initial velocities of the particles are picked randomly from a Maxwellian distribution of temperature $5 \times 10^6 K$, a typical coronal value. This corresponds to initial thermal energy of 0.65 keV.

We consider only small values for $\bar{E}_o$, corresponding to the passage of a disturbance in the linear regime (cf Craig and McClymont). Values of 0.01 or 0.001 are used in the actual calculation. The value 0.001 corresponds to electric field $= 5.88 \times 10^{-4}$ statvolt/cm. These are moderate values for the electric fields present in the solar atmosphere (see Foukal et al. 1986).

The electric field becomes significant where non-adiabatic motion of particles results in inertial resistivity. A rough indication of the size of the region is thus given by the 'adiabaticity' radius r_{ad} (MacKinnon and Petkaki, 1995 and 3.2.2), the distance from the neutral point at which the Larmor radius equals the magnetic field scale length. For $r > r_{ad}$, particles move adiabatically. The 'adiabaticity' radius depends on the particle mass and velocity perpendicular to the magnetic field, $u_\perp$, and is given by

$$r_{ad} = (\frac{mcDu_\perp}{eB_o})^{\frac{1}{2}}. \tag{3.14}$$

(In a sense this definition is circular, in that $u_\perp$ must be evaluated at r_{ad}, but it suffices for order of magnitude.) Note the mass dependence of r_{ad}. Specifically, for electrons and protons of the same energy, the electron gyroradius is $(\frac{m_e}{m_p})^{\frac{1}{2}}$ smaller than the proton gyroradius. We use the gyroradius of a thermal proton as a guide to the size of the dissipation region. In practice we take this to be 10 times r_{ad} for a thermal proton, recognising that non-thermal particles will also contribute to inertial resistivity. So, the adiabaticity radius for protons is of the order 2×10^5 cm. The adiabaticity radius is much smaller than the proton mean free path in the corona. During the time that the particle moves close to the neutral line, collisions are unlikely. In fact the total size of system that we consider is smaller or of the order of the mean free path expected in the corona for protons of 200 keV. So, during the time that the particles cross the neutral point and get accelerated, they don't collide with other particles.

The total real time of the integration corresponds to 0.05 seconds for electrons and 1 s for protons. Since the timestep for electrons is $(\frac{m_p}{m_e})^{\frac{1}{2}}$ times smaller for electrons than for protons, $(\frac{m_p}{m_e})^{\frac{1}{2}}$ times more steps are needed to achieve the same real time. This makes the calculation very long. Approximate methods of calculating the orbits of electrons should be used. For example, when an electron is moving along the separatrices then its motion is adiabatic and the guiding centre approximation might be used. The problem with this is that changing to the guiding center calculation one loses phase information.

Conditions for adiabatic motion

A usual criterion for the particle's motion to be considered adiabatic when the magnetic field is constant in time is that its gyroradius be much smaller than the scale length of the magnetic field

$$\rho_g \ll \frac{\mid B \mid}{\mid \nabla B \mid}. \tag{3.15}$$

Since the magnetic field discussed here has $\mid B \mid = r$ and $\mid \nabla B \mid = 1$ then in order for the motion of a particle to be adiabatic its gyroradius should be much smaller than its distance from the neutral point.

One interesting thing to see here is the distribution of initial conditions (positions and velocities) of particles that gain energies versus those that don't gain energies. We discuss briefly here some results that are presented later in this chapter. That is the calculation with the time-varying electric field (see sec. 3.4). The protons that then gain most energy lie initially inside the nonadiabatic region and along the separatrices. Few of the rest increase their initial energy significantly and those that do have initial gyroradii that bring them inside the nonadiabatic region. In Figures (3.1) and (3.2) we show these distributions. The total number of particles present is 6000. In Fig. (3.2) we see that some of the particles that don't gain energy lie along the separatrices. This is because all the final distributions of protons for the different frequencies for the electric field have been included. The same pattern is not observed for electrons. This is because of the way the electrons are ejected. They all feel the presence of the electric field when the calculation starts.

3.2.4 Numerical Method and tests

Due to the complexity of the orbits, their calculation cannot be done analytically. For integrating the ordinary differential equations (ODEs) describing the motion of the particles, we use the Bulirsch-Stoer method. This is a well known method for obtaining high accuracy solutions for ODEs with minimal computational effort (Press et al., 1992). A single Bulirsch- Stoer step takes the integration from x to a point $x + H$ where H is the step attempted. It uses the modified midpoint method to advance a vector of dependent variables $y(x)$ from a point x to a point $x + H$ by a sequence of n substeps each having size $h = H/n$. So, this single step which is quite large consists of many (tens or hundreds)

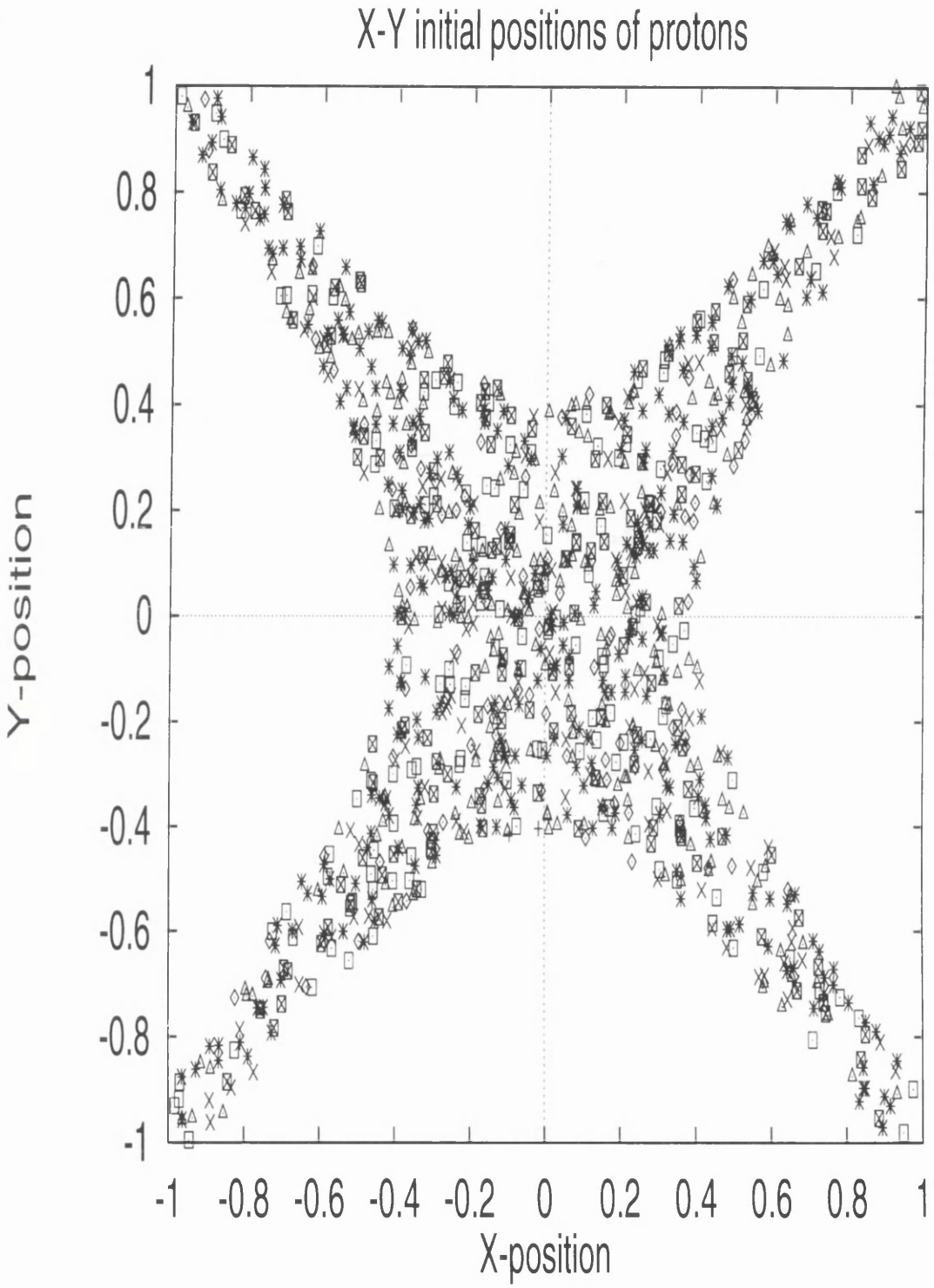

Figure 3.1: Initial positions of protons that increase their energy more than 10% during their motion in the electromagnetic fields discussed here. Their initial spatial distribution is very distinctive along the separatrices and the nonadiabatic region. For more information on the proton motions and energies see section 3.4.

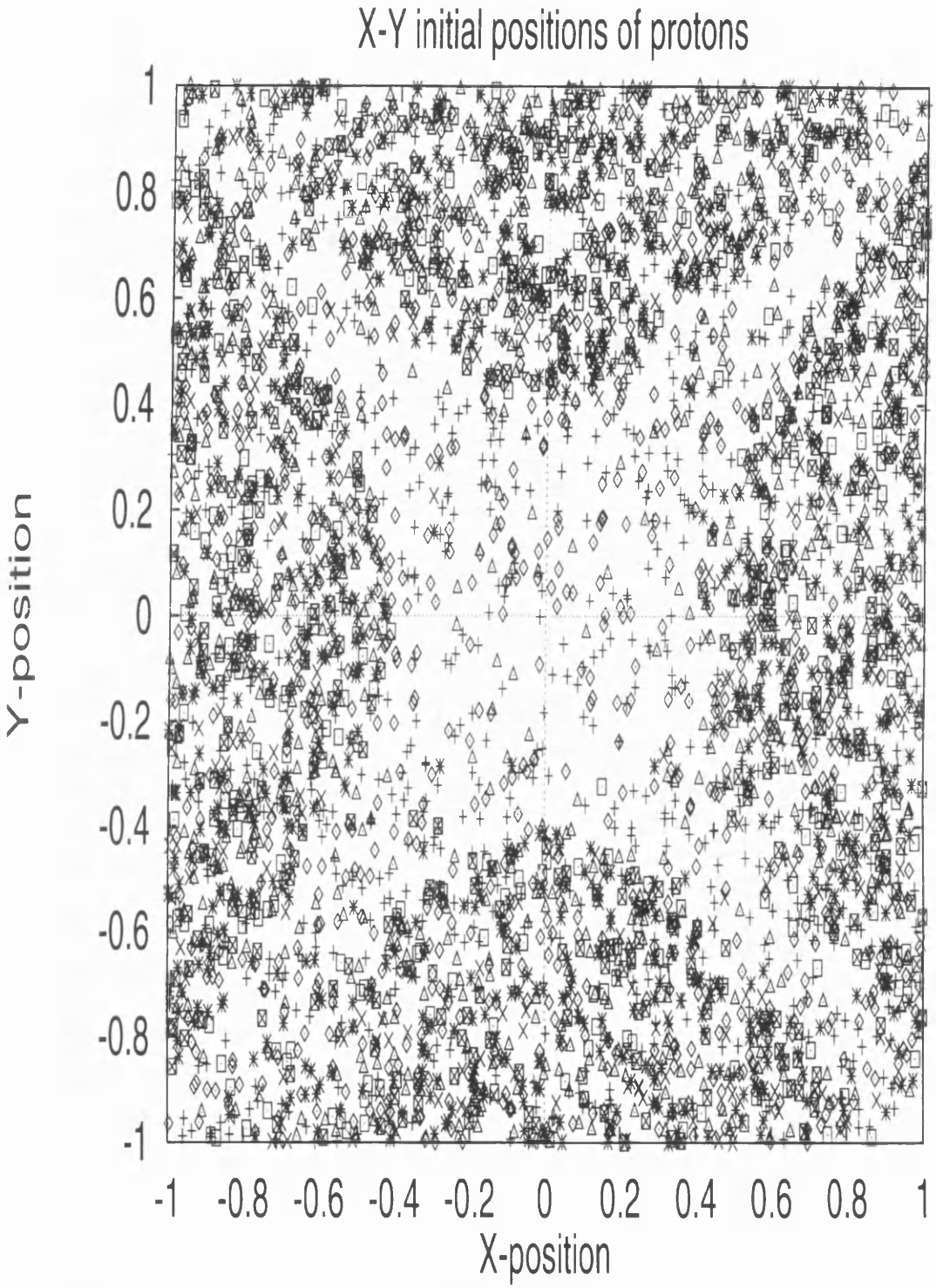

Figure 3.2: Initial positions of protons that do not increase their energy more than 10% during their motion in the electromagnetic fields discussed here. Their initial spatial distribution is very distinctive away the separatrices and the nonadiabatic region. For more information on the proton motions and energies (see section 3.4).

substeps which are finally extrapolated to zero (see Stoer and Bulirsch (1980)).

The method contains three key ideas. The first is Richardson's deferred approach to the limit. Consider the final answer of a numerical calculation as itself being an analytic function of an adjustable parameter like the stepsize h. That analytic function can be probed by performing the calculation with various values of h, none of them being necessarily small enough to give the accuracy that we want. When we know enough about the function, we fit it to some analytic form. Then we can evaluate the function at $h = 0$.

The second idea has to do with what kind of fitting function to use. Bulirsh and Stoer first recognised the strength of the rational function extrapolation in the Richardson's deferred approach to the limit. Rational function fits can remain good approximations to analytic functions even after the various terms in powers of h all have comparable magnitudes.

The third idea is the use of the modified midpoint method where the error function is strictly even, allowing the rational function or polynomial approximation to be in terms of the variable h^2 instead of just h.

The important issue for discussion here is the energy conservation. When no electric field is present the energy of the particles should be conserved. That is very easy to see from the equation of motion. Taking the dot product of both sides with the particle's velocity we have

$$\underline{u} \cdot m\frac{d\underline{u}}{dt} = -q\underline{u} \cdot \underline{E} + \frac{q}{c}\underline{u} \cdot (\underline{u} \times \underline{B}) \tag{3.16}$$

which gives

$$\frac{1}{2}m\frac{du^2}{dt} = -q\underline{u} \cdot \underline{E} \tag{3.17}$$

the second term in the right hand side being equal to zero. When no electric field is present the kinetic energy should be conserved. I have done several testing runs of the integration routine to see if energy is conserved when no electric field is present. For different accuracies of the integration routine I have calculated the initial and final energy of the particles. They should be identical if no error comes into the calculation. But since the calculation is numerical, I checked if the error was small.

In fig. (3.3) and (3.4) I have plotted the final energy of 1000 protons versus the absolute error ($\Delta\epsilon = E_{final} - E_{initial}$) for different accuracies of the integration routine. $\Delta\epsilon$ is multiplied by 10^6 for plotting reasons. From these graphs one can see that the absolute error is small.

In fig. (3.5) and (3.6) I have plotted the final energy of 1000 protons versus normalised error ($\Delta\epsilon/E_{initial} = (E_{final} - E_{initial})/E_{initial}$) for different accuracies of the integration routine. The normalised error is always small and decreases as the accuracy of the integration routine increases.

Another important question here is how different do individual orbits look when the accuracy of the calculation is changed. When the orbits don't leave the adiabatic region then they are identical over the integration time in consideration. When multiple crossings from the adiabatic region take place then the orbits diverge in time. In the example shown here, the orbits look identical for the first half of the integration time and diverge after that (see fig. (3.7) and (3.8)). Even if we increase the accuracy of the integration routine by a few orders of magnitude, orbits crossing the neutral point area several times will not be exactly the same. Also, very high accuracy would make the integration routine too time consuming to be useful. I refer once more to the discussion by Martin (1986) on the properties of X-type neutral points.

High accuracy of the integration routine is not necessary however, because here we are interested mainly in the energy distribution coming out of the system rather than in single orbits. When I plot the initial energy distribution over the final energy distributions (final meaning after integration time of 1 sec, that is 5360 timesteps), they look almost identical. Very small changes can be seen, that are not significant. The shape of the distribution does not change (see fig. (3.9) and (3.10)). Also statistical analysis of the results does not give significant differences (see fig. (3.11)). Thus, while individual orbits may not be correctly calculated, statistical properties of the distribution of test particles are adequately given.

3.3 Steady State Reconnection

We start by calculating the energy distributions that result when a constant electric field is imposed on a magnetic field containing an X-type neutral point. Calculations like the one that follows have been done before e.g. Martin (1986), Burkhart et al 1990. Martin (1986) studied the behaviour of particle orbits close to an X-type neutral point. He observes that when the particle has access to the neutral point the motion is erratic as shown by numerical integrating particle orbits. The system of equations is nonintegrable, so the motion could be chaotic. Questions we want to ask here are: i) what do individual

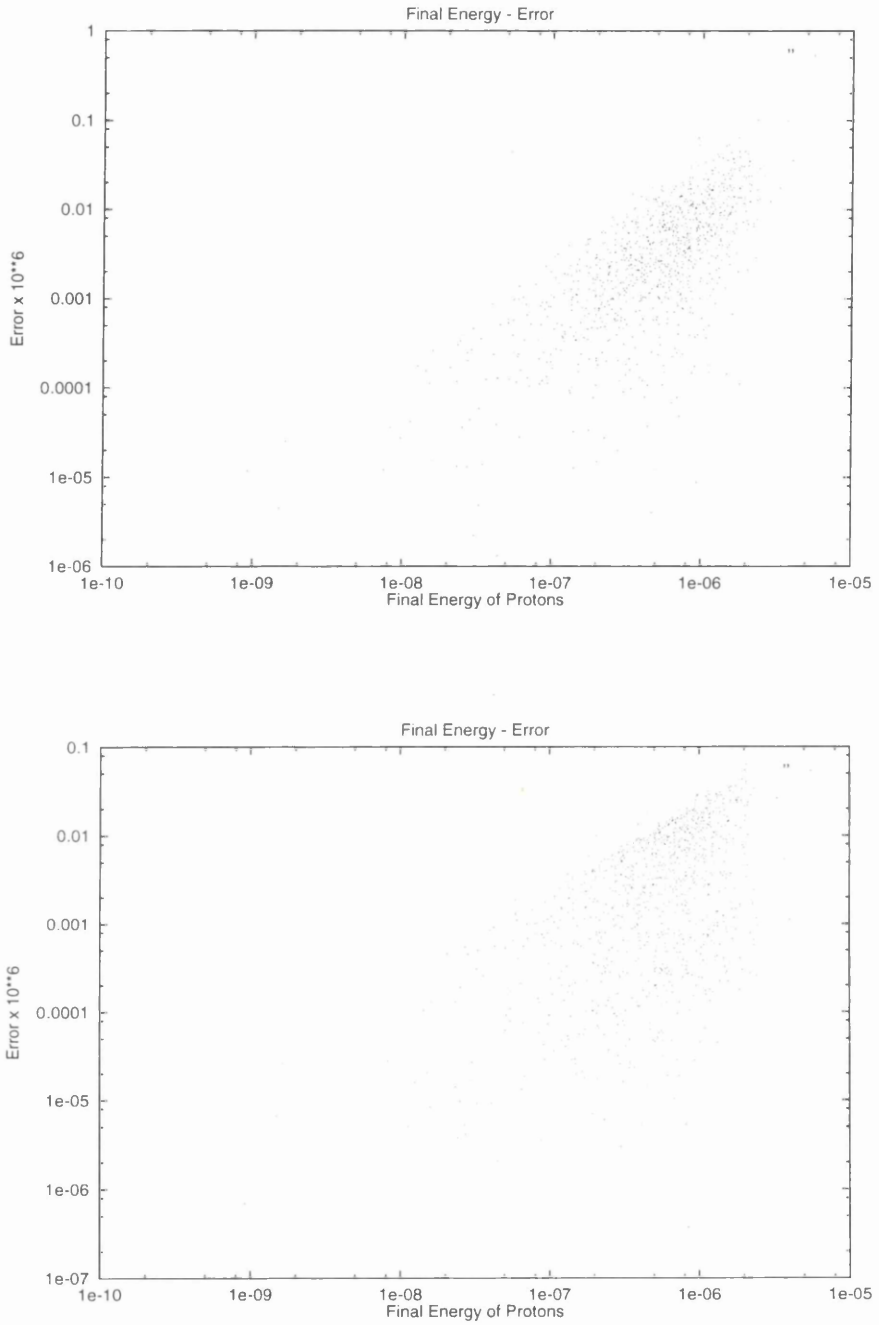

Figure 3.3: Final energy versus absolute error of 1000 protons after 5360 timesteps with zero electric field. Top diagram is for 10^{-5} accuracy and the bottom for 10^{-6} accuracy.

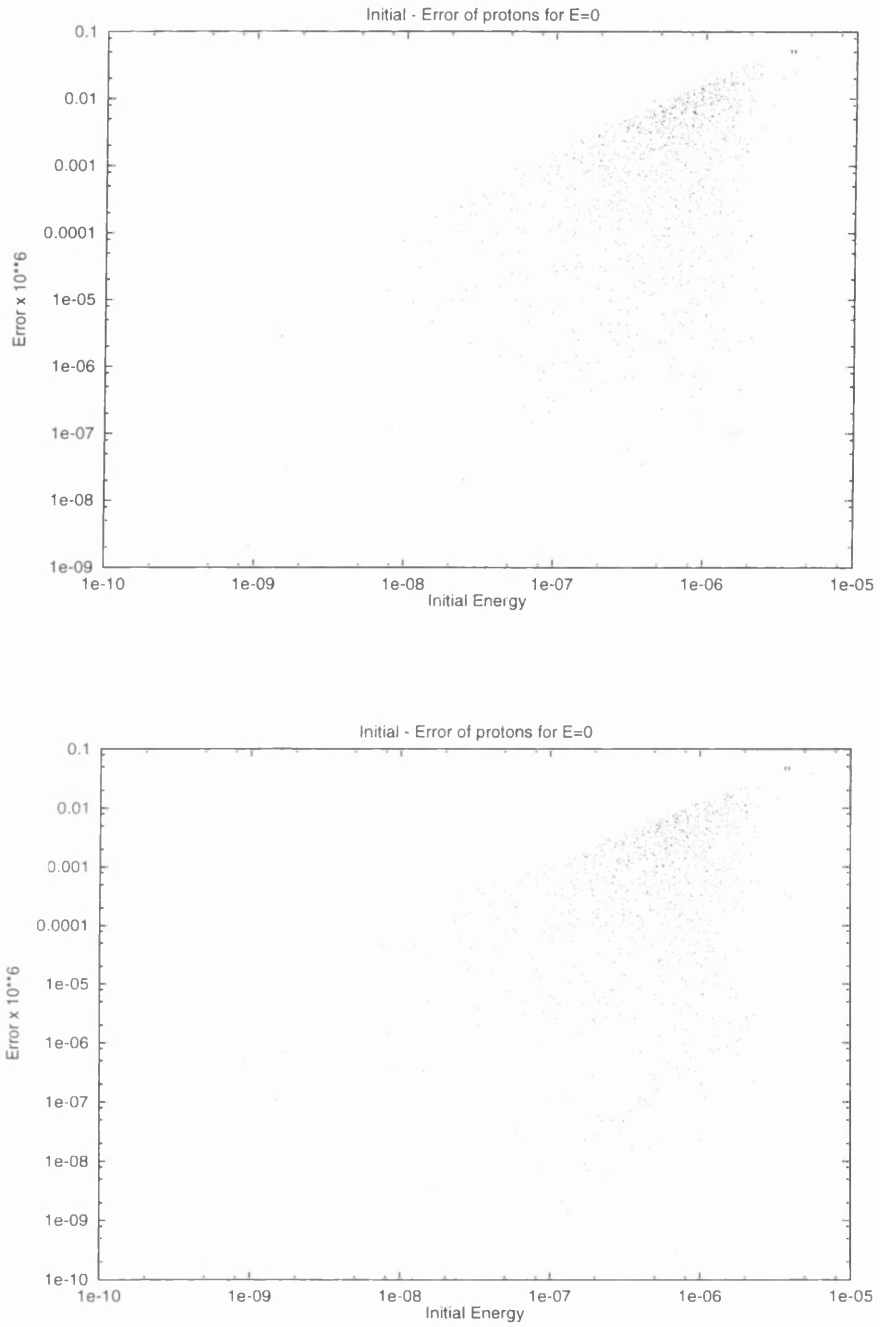

Figure 3.4: Final energy versus absolute error of 1000 protons after 5360 timesteps with zero electric field. Top diagram is for 10^{-8} accuracy and the bottom for 10^{-10} accuracy.

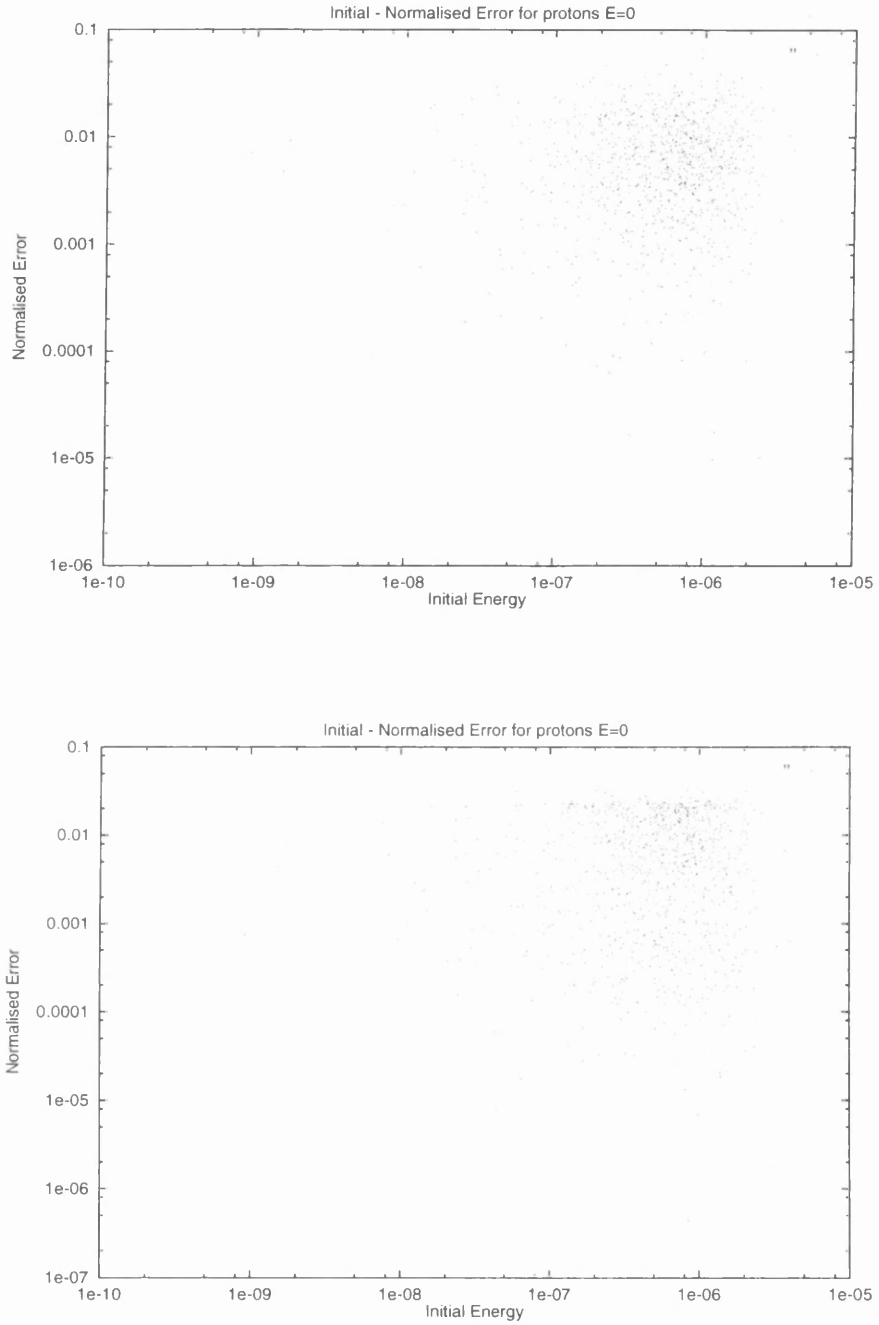

Figure 3.5: Final energy versus normalised error of 1000 protons after 5360 timesteps with zero electric field. Top diagram is for 10^{-5} accuracy and the bottom for 10^{-6} accuracy.

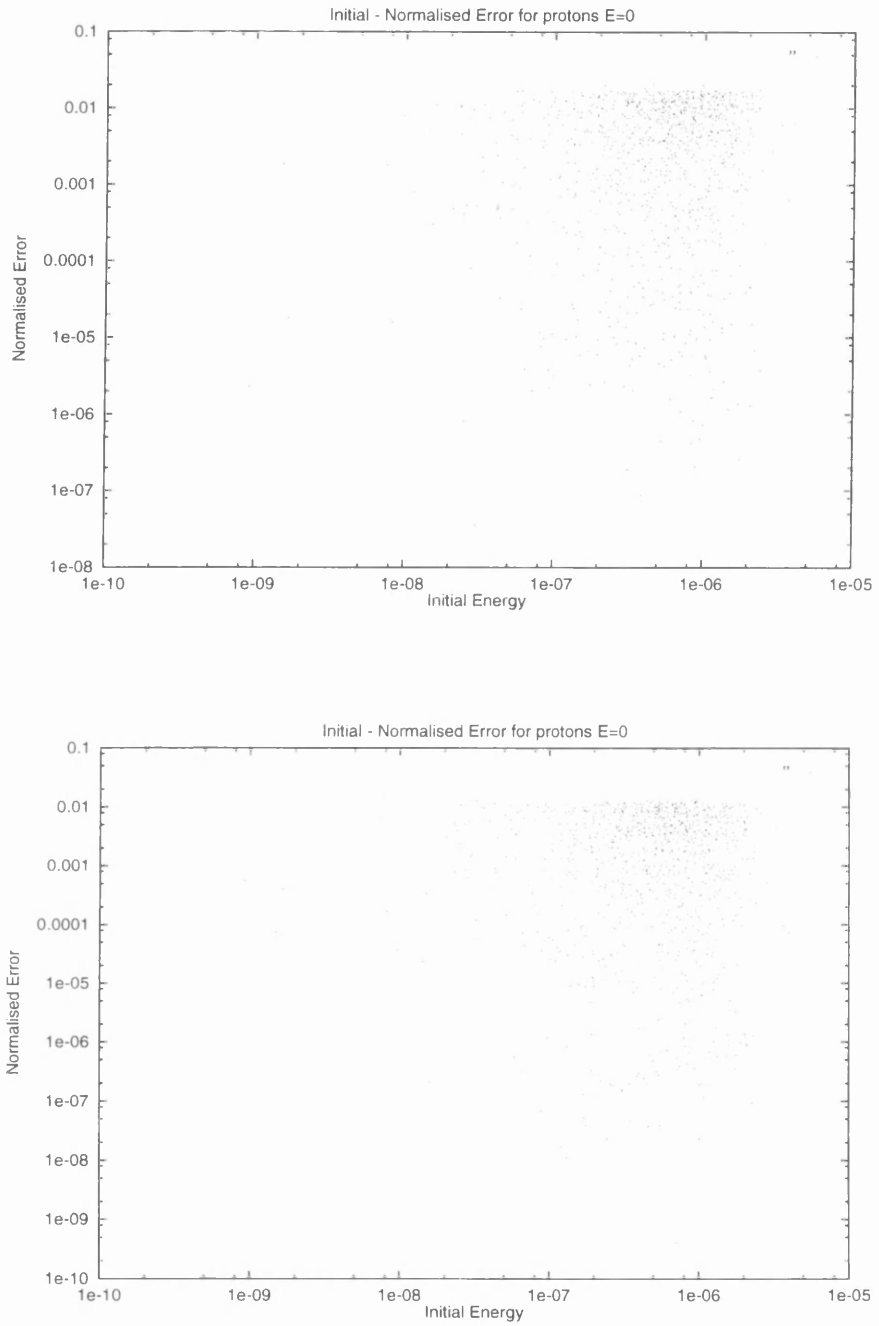

Figure 3.6: Final energy versus normalised error of 1000 protons after 5360 timesteps with zero electric field. Top diagram is for 10^{-8} accuracy and the bottom for 10^{-10} accuracy.

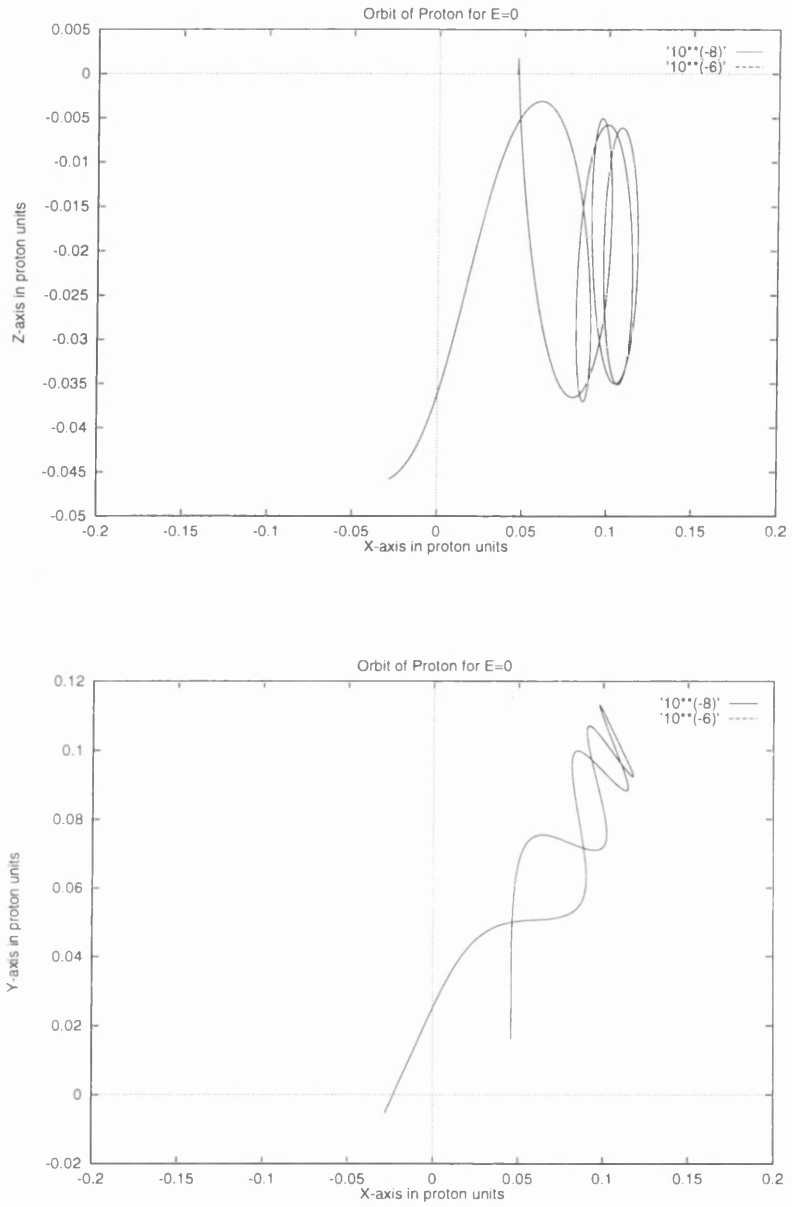

Figure 3.7: Orbit of a proton in an X-type magnetic field with E=0. The initial part of the orbit is shown here, before the particle crosses the neutral point area. For two different accuracies of the integration routine (10^{-8} and 10^{-6}) the orbits are identical. The orbits lie on top of each other.

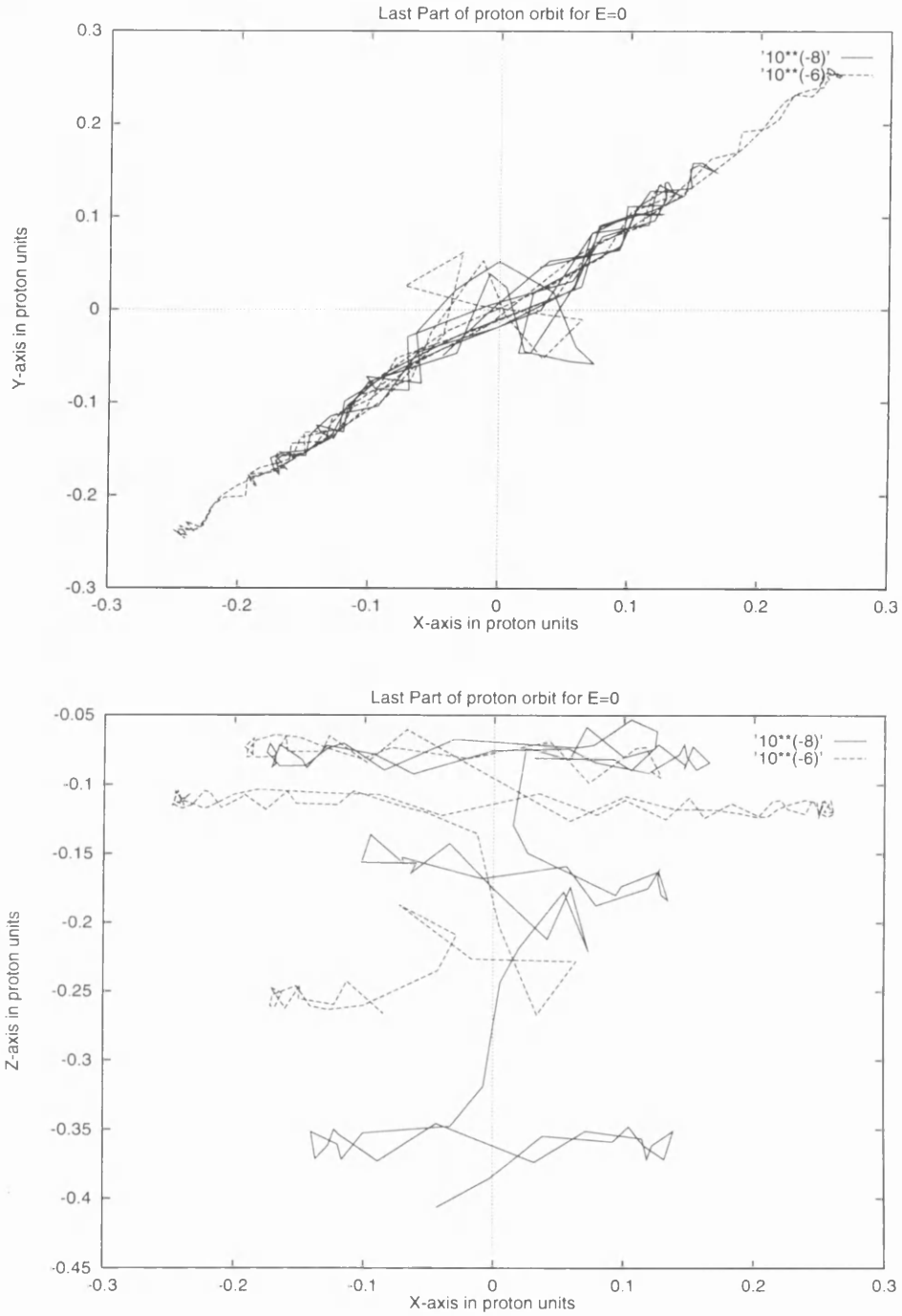

Figure 3.8: Orbit of a proton in an X-type magnetic field with E=0. The part of the orbit shown here, is the continiuation of fig. (3.7). For two different accuracies of the integration routine (10^{-8} and 10^{-6}) the orbits are not identical.

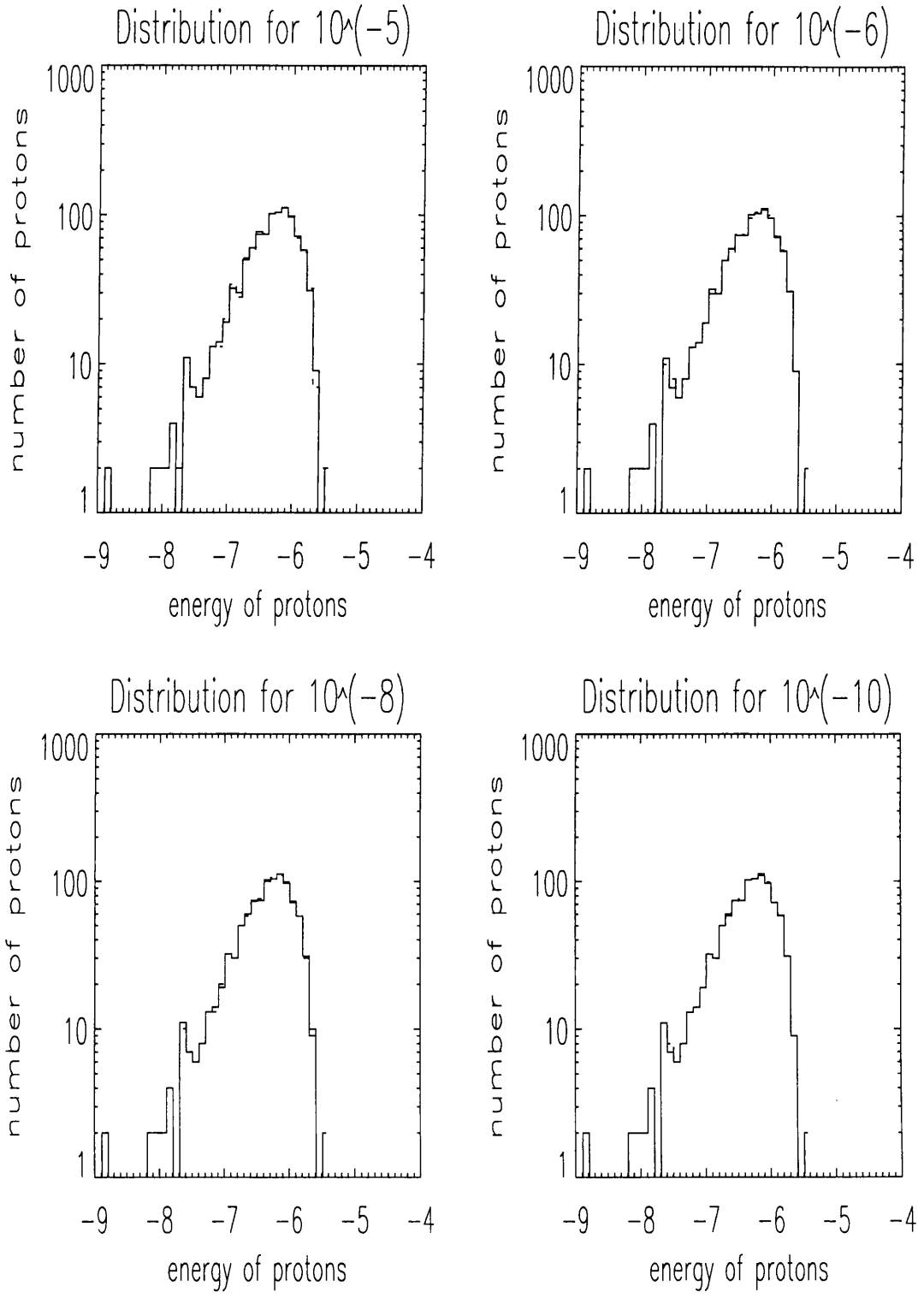

Figure 3.9: Histograms of the energy of protons for different accuracies when the electric field is zero. Every graph contains two distributions, the initial maxwellian distribution and the distribution after integration time of 5360 timesteps. The distributions lie almost on top of each other.

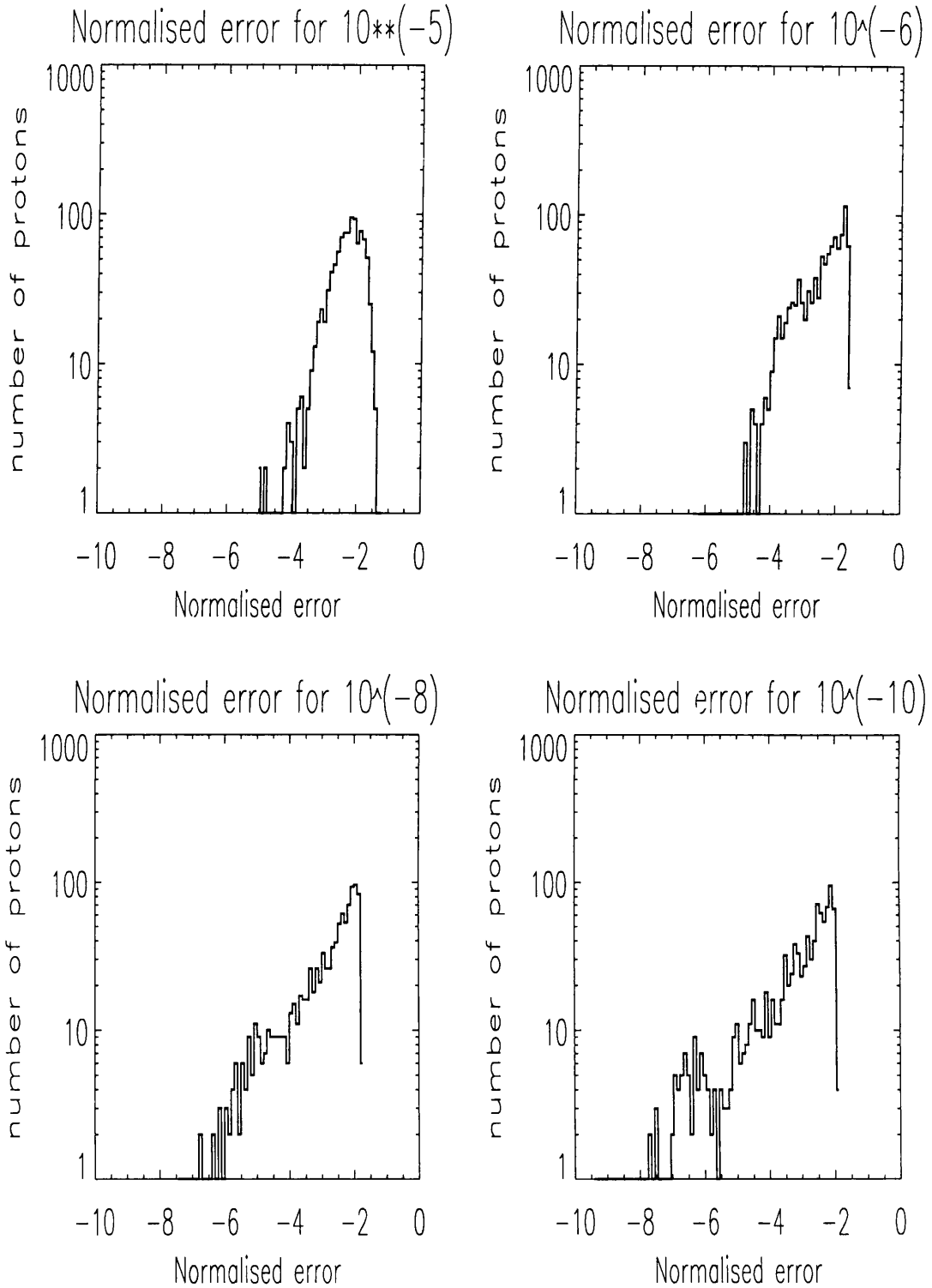

Figure 3.10: Histograms of the normalised error in the energy of protons for different accuracies when the electric field is zero. The integration time is 5360 timesteps. The error is generally reduced with increasing accuracy of the integration routine.

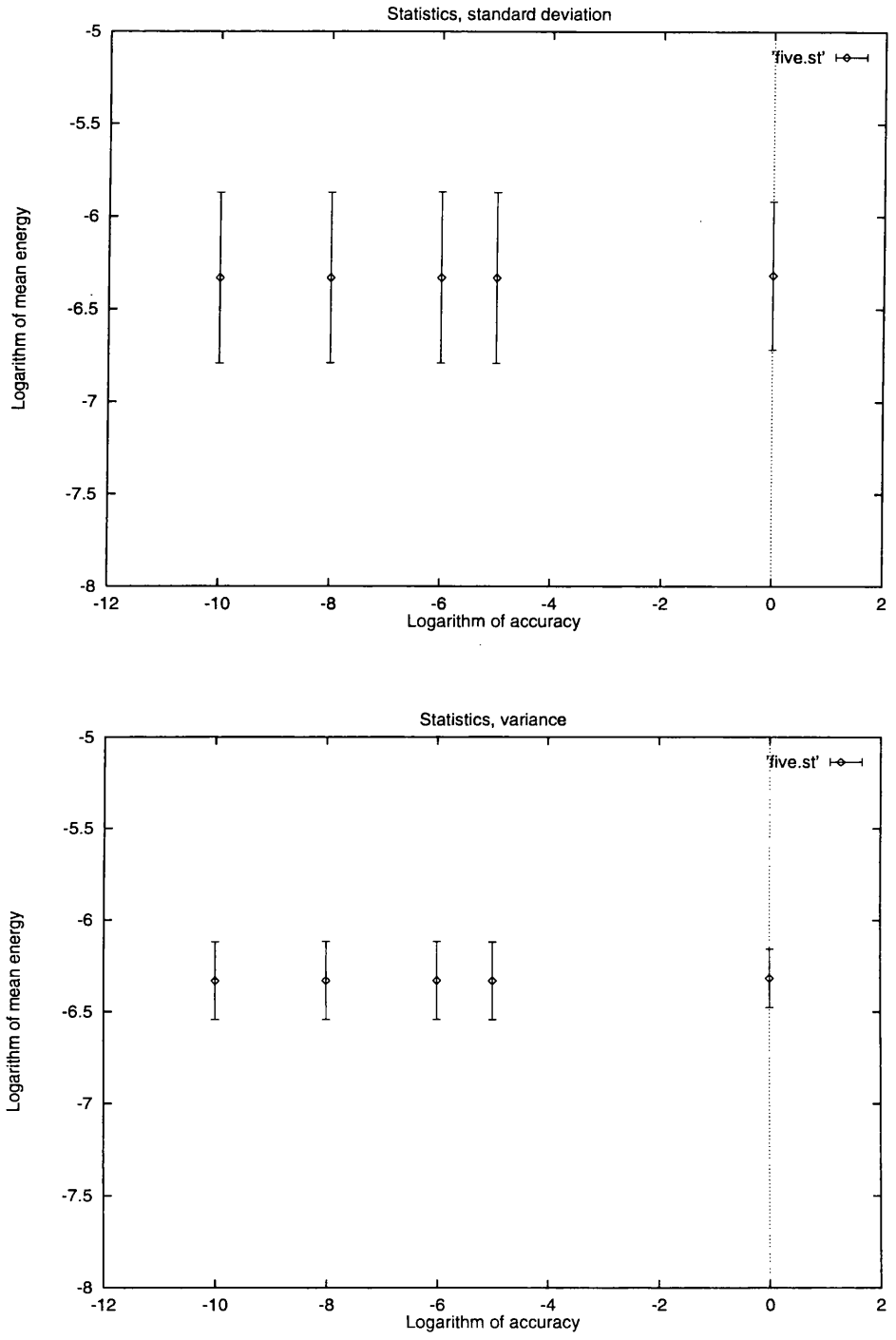

Figure 3.11: Logarithm of mean energy versus logarithm of accuracy when the electric field is zero. In the top diagram the error bars are standard deviation and in the bottom one are variance.

particle orbits look like in the present magnetic configuration, ii) how are they different from previous calculated ones, iii) what do the energy distributions look like and iv) what does this imply for the mechanism discussed. We are going to try to answer these questions in the following sections. The difference from previous calculations is that we restrict the electric field close to the neutral point. The particles are not carried into the nonadiabatic region by some flow velocity, in the case of single particle dynamics by the $\underline{\mathrm{E}} \times \underline{\mathrm{B}}$ drift. The particles have initial thermal velocities of the order of those that is expected in the solar corona. So, many different initial conditions for the particles are tried.
A constant ad hoc electric field is applied

$$\underline{\mathrm{E}} = E_o \hat{z} f(x, y) \tag{3.18}$$

where $f(x, y)$ restricts $\underline{\mathrm{E}}$ to a region of width d surrounding the neutral point, and E_o, and d are treated as free parameters. We take

$$f(x, y) = H(d - |x|)H(d - |y|) \tag{3.19}$$

where, H is the Heaviside function.

3.3.1 Typical Orbits

Each orbit that I have calculated is different from every other because of the many different initial conditions tried but also because of the diffusive properties of the X-type neutral point (see discussion in section (3.2.4). In fig. (3.12) we see part of the orbit of an electron in the magnetic field containing an X-type neutral point with a constant electric field imposed. The electron starts close to the neutral point and drifts outside the nonadiabatic region due to $\underline{\mathrm{E}} \times \underline{\mathrm{B}}$ drift. There is a net acceleration during this part of the motion. The electric field is restricted in an box of side 34 of electron units (see eq. (3.14) and the discussion that follows), so is present in all of the area shown in fig. (3.12).
In fig. (3.13) we show part of the orbit of a proton in the model magnetic and electric field discussed in the previous section. After mirroring a few times in relative magnetic gradients the proton starts moving on field lines that get closer and closer to the separatrices. This particular one will eventually mirror and return the neutral point. The electric field is restricted to a box of side 0.8 (in proton units) around the neutral point (see eq. (3.14) and the discussion that follows).

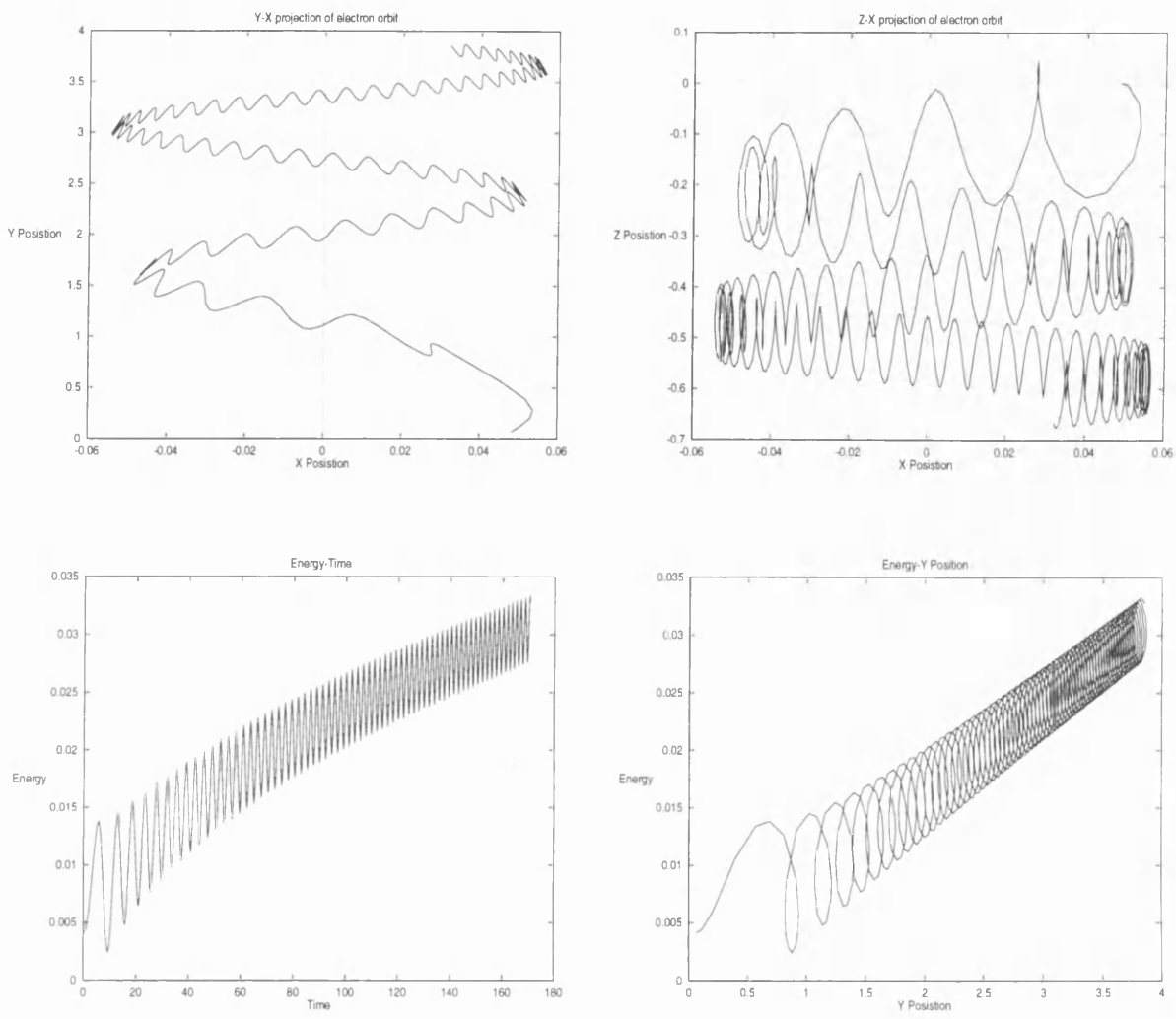

Figure 3.12: Orbit of an electron in constant electric field. The magnitude of the electric field is 0.001. The projection in the X-Y plane and X-Z plane are shown on the top graphs. The lower graphs show the variation of the electron's energy with time and y-position. The electric field is restricted to a box of side 34 (in electron units) around the neutral point.

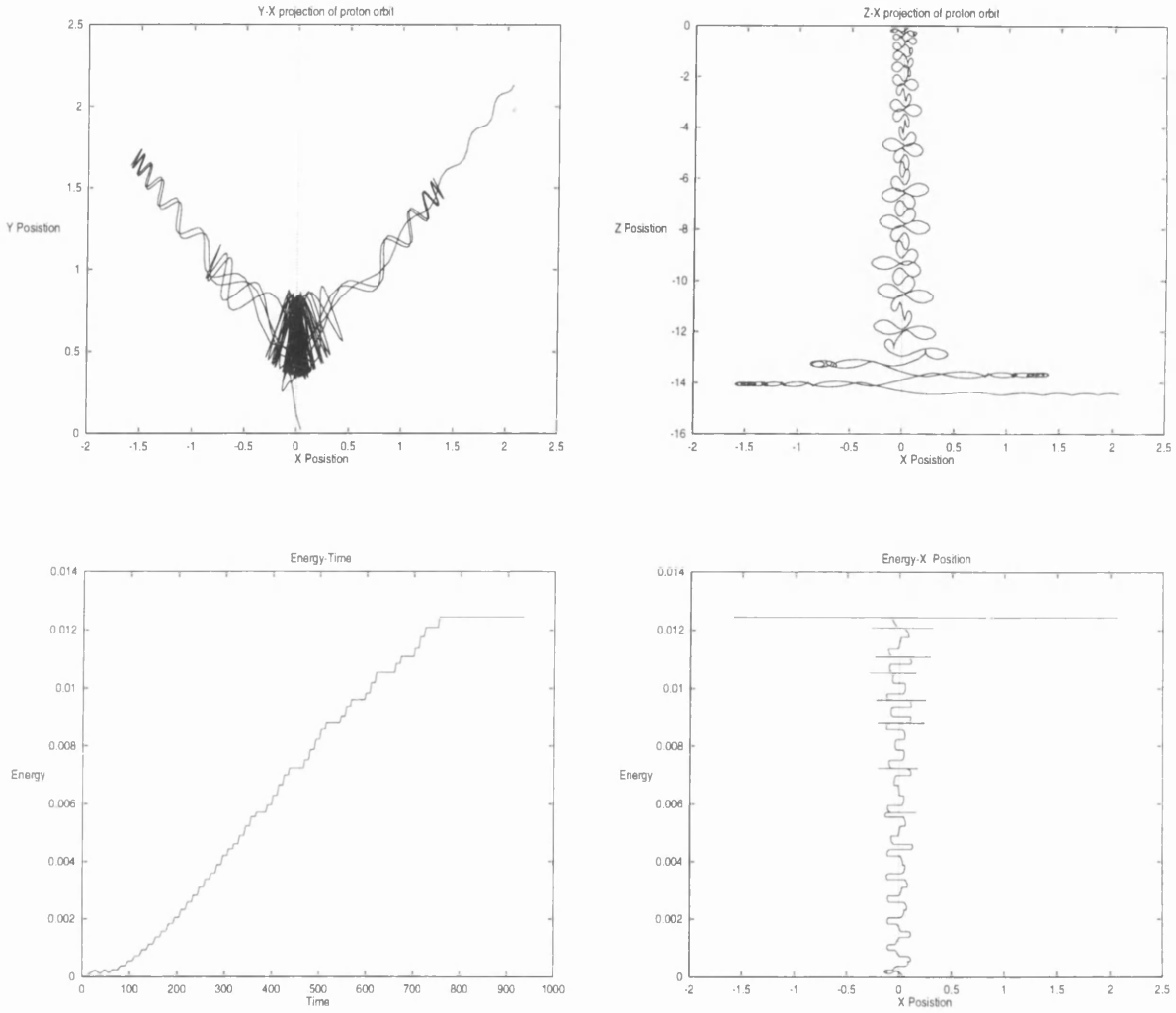

Figure 3.13: Orbit of an proton in constant electric field. The magnitude of the electric field is 0.001. The projection in the X-Y plane and X-Z plane are shown on the top graphs. The lower graphs show the variation of the proton's energy with time and y-position. The electric field is restricted in an box of side 0.8 (in proton units) around the neutral point.

3.3.2 Energy Distributions

In the constant electric field case only the distributions for protons have been calculated. The reason for that was the appearance of an instability in the numerical routine in the boundary between the area where the electric field is applied and where the electric field is zero. In future work, the reasons for this instability will be investigated and methods to remove it will be considered. Preliminary investigations have shown that the abrupt switch-off of the electric field is probably causing this problem.

Starting with a number of protons randomly distributed around the X-type neutral point area, I calculated the distribution resulting after the particle orbits are followed for 5360 timesteps (which is 1 sec). This is a time that is relatively easy to achieve computationally but also gives a feeling about the efficiency of the mechanism. The following values for the electric field magnitude have been used, i) $E_o = 0.01$, ii) $E_o = 0.001$, and iii) $E_o = 0.0001$. In fig. (3.14) we see these distributions along with the initial energy distribution.

In table (3.1) we see the percentage of the final distribution that gets accelerated for different values of the magnitude of the constant electric field. I calculate the percentage of particle for which

$$\frac{E_{final} - E_{initial}}{E_{initial}} \geq constant \tag{3.20}$$

where *constant* takes the values 1, 10 and 100. In column one we see the percentage of the final distribution that doubles its initial energy. In column two we see the percentage of the final distribution that increases its initial energy by 10 times and in column three the percentage of the final distribution that increases its initial energy by 100 times. In column four we see the percentage of the final distribution that attains energies greater than 1MeV. When $E_o = 0.01$ then the highest energy aquired by protons is 160 MeV. When $E_o = 0.001$ then the highest energy aquired by protons is 19 MeV. In both cases about 30 % of the final distribution is acquiring energies higher than 1MeV. When $E_o = 0.0001$ then the highest energy acquired is 5 MeV. 6 % of the final distribution has energies above 1 MeV.

In fig. (3.15) we see the initial energy distribution of 1042 protons and their final distribution, for E=0.001. In histogram iii) we see the initial distribution of those protons that gain more then 10% energy and in histogram iv) we see the final energy distribution of those protons that gain more than 10% energy. So, one can see that the particles that get accelerated come from all parts of the initial Maxwellian, not only from the tail. The

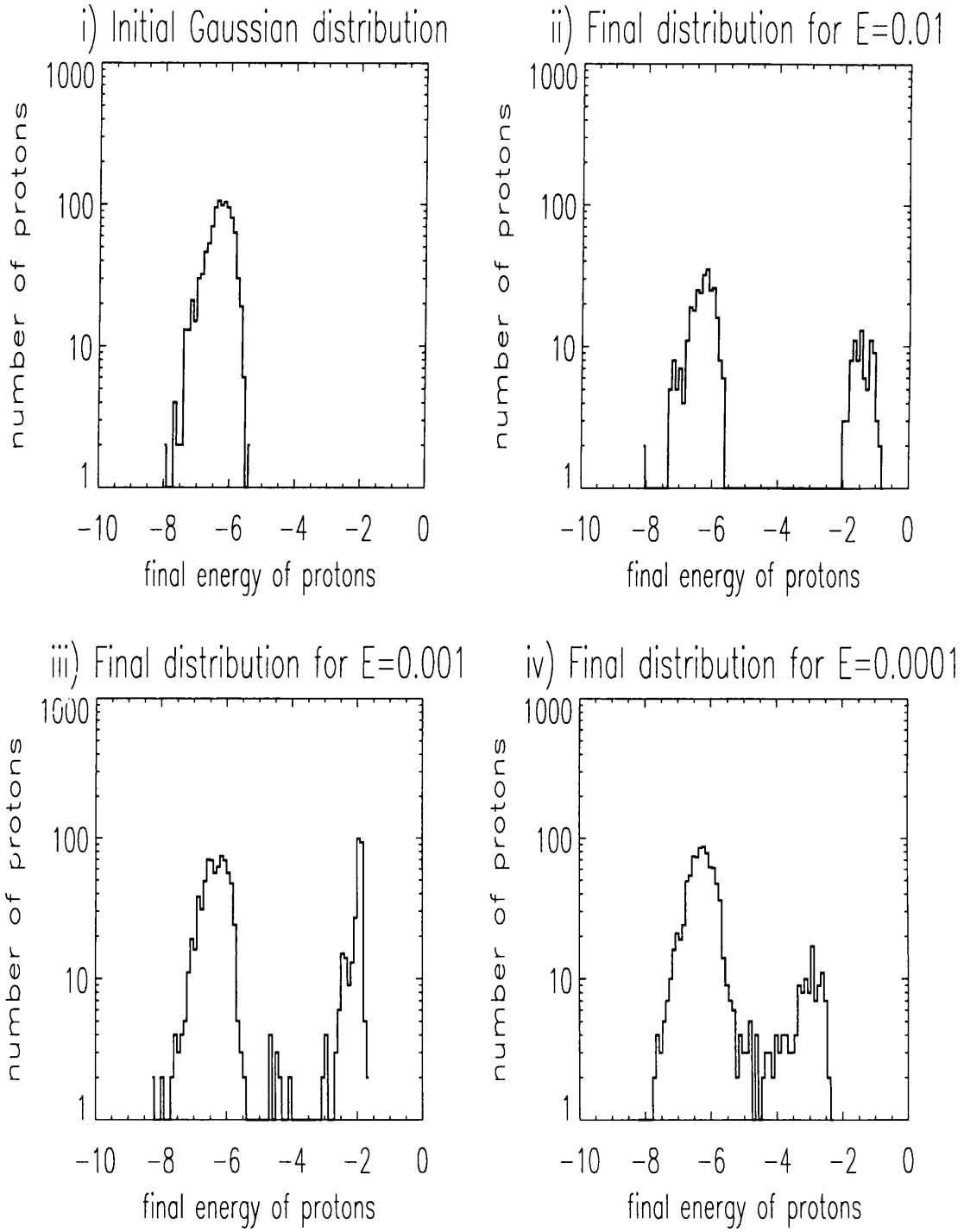

Figure 3.14: Final energy distributions for protons for constant electric field. Histogram i) shows the initial Maxwellian distribution. Histograms ii) to iv) show the final distribution of protons for decreasing value of the electric field. In ii) there are 547 protons, in iii) 1042 and in iv) 1004. Total integration time for all the distributions is 5360 timesteps.

Magnitude	1	10	100	> 1 MeV
0.01	27 %	27 %	27 %	27 %
0.001	30 %	30 %	29 %	28 %
0.0001	22 %	15 %	12 %	6 %

Table 3.1: Percentage of accelerated protons after 5360 timesteps in constant electric field

same is true for the distributions produced for the other two values of the electric field.

3.3.3 Discussion of the results

When a constant electric field is imposed on an X-type neutral point in an area around the neutral point, then the initial maxwellian distribution of protons injected inside this area, results in distributions like those in fig. (3.14). These distributions are not power laws as previously was thought, see e.g. Bulanov and Sasarov (1976) and Bruhwiler and Zweibel (1992). In both of these calculations the particles are assumed to cross the neutral point only once.

The initial distribution splits into two distinct parts after the particle orbits have been calculated for 1 second. The lowest energy one comprises the protons that don't get accelerated significantly. The highest energy component comprises the protons that are affected by the presence of the electric field (see table (3.1)). Protons are able to cross the neutral point area a number of times depending on their initial conditions. So, they encounter the electric field more than once and we have a Fermi type acceleration. More detailed discussion of this effect is presented in the next section.

3.4 Model for Particle Acceleration in Dynamic Reconnection

We are going to examine now the consequences for particle acceleration when a sinusoidal, ad hoc electric field is applied on an X-type neutral point. The form of the electric field is the following

$$\underline{\mathrm{E}} = E_o \sin(\omega t)\hat{z} f(x, y) \tag{3.21}$$

where $f(x, y)$ again restricts $\underline{\mathrm{E}}$ to the nonadiabatic region surrounding the neutral point, as discussed in section (3.2.3).

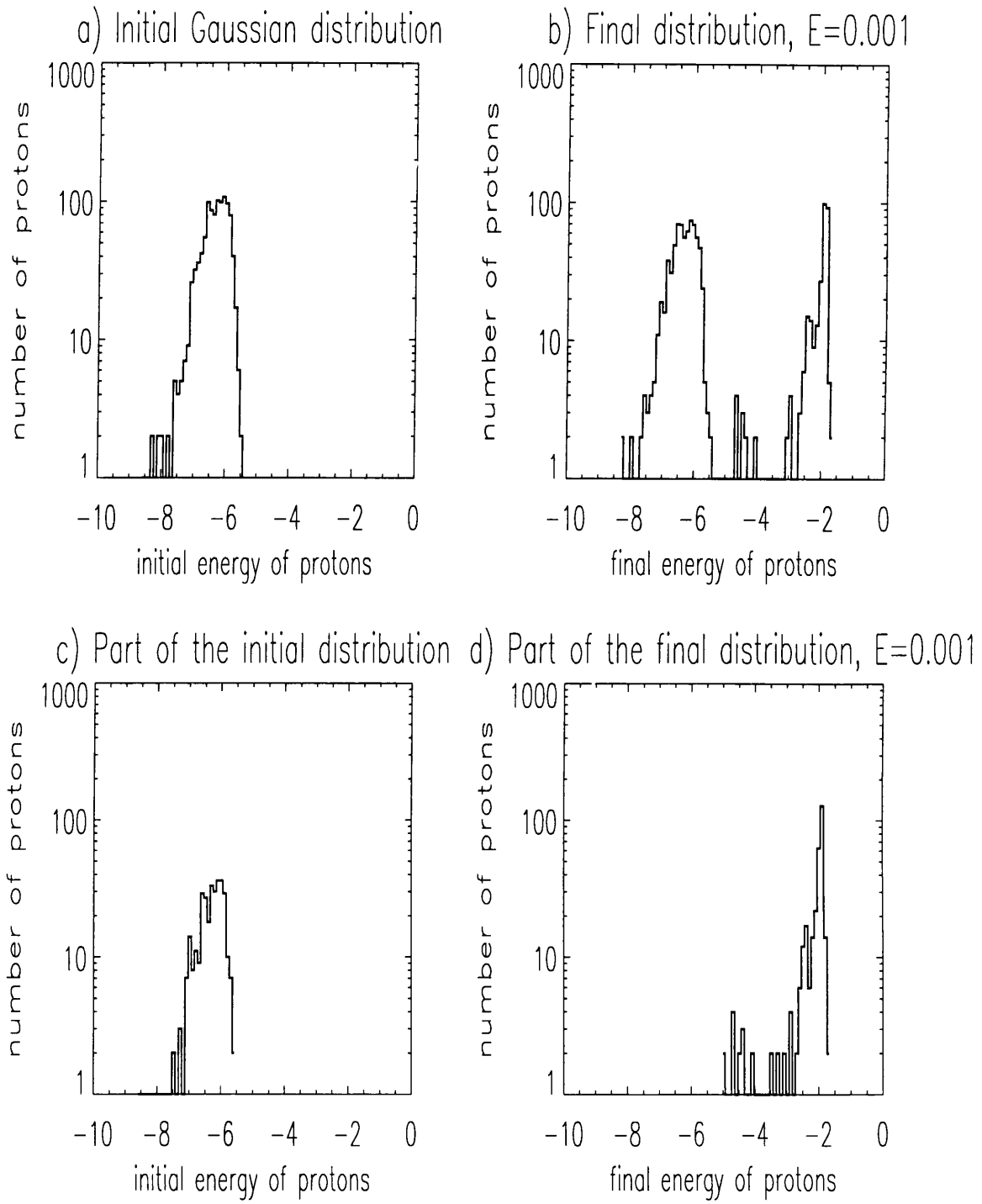

Figure 3.15: Final energy distributions for protons for constant electric field. Histogram i) shows the initial Maxwellian distribution. Histograms ii) shows the final distribution of 1042 protons for E=0.001. Total integration time for all the distributions is 5360 timesteps. In iii) we see the initial distribution of those protons that gain more then 10% energy and in iv) we see the final energy distribution of those protons that gain more than 10% energy.

The dimensionless equations of motion that we integrate numerically are the following.

$$\frac{d\bar{x}}{d\bar{t}} = \bar{u}_x = \frac{\bar{p}_x}{\gamma} \tag{3.22}$$

$$\frac{d\bar{y}}{d\bar{t}} = \bar{u}_y = \frac{\bar{p}_y}{\gamma} \tag{3.23}$$

$$\frac{d\bar{z}}{d\bar{t}} = \bar{u}_z = \frac{\bar{p}_z}{\gamma} \tag{3.24}$$

$$\frac{d\bar{p}_x}{d\bar{t}} = -\epsilon\bar{x}\bar{u}_z \tag{3.25}$$

$$\frac{d\bar{p}_y}{d\bar{t}} = \epsilon\bar{y}\bar{u}_z \tag{3.26}$$

$$\frac{d\bar{p}_z}{d\bar{t}} = \epsilon(\bar{x}\bar{u}_x - \bar{y}\bar{u}_y) + \epsilon\bar{E}_o\sin(\omega\bar{t}) \tag{3.27}$$

where $\bar{E}_o = E_o D_i / B_o D$ and the suffix i is e for electrons and p for protons.
The free parameter here is the frequency of oscillation of the electric field which we denote by ω. We take values of ω such that $1/1000 < \omega < 500$.

3.4.1 Comment on the numerical method

To check the numerical method I have done the following test. I have integrated the trajectories of 1000 protons for 5360 timesteps and for frequency of the electric field $\omega = 1$, for different accuracies of the integration routine. As I mentioned before individual orbits change but the final distribution keeps the same shape, as one can see in fig. (3.16). The accuracies tried are (corresponding to the histograms in fig. (3.16)) ii) 10^{-5}, iii) 10^{-6}, iv) 10^{-7}, v) 10^{-8}, and vi) 10^{-9}.

3.4.2 Orbits

The orbits are shown here in projection on the X-Y plane and superimposed on the magnetic field lines (Fig. 3.17). Away from the neutral point area the particles start moving closer and closer to the separatrices. They actually move more and more strictly along particular field lines, but all field lines tend to the separatrices as the distance from the neutral point becomes very large. The gyroradius becomes smaller and smaller as the particle moves away from the neutral point. The mirroring effects are clear once more. The complexity of the orbit close to the neutral point area is clear, too.
In figure 3.18 we see two orbits. The top one is the orbit of a proton that was obtained when the frequency of the electric field applied in the non-adiabatic area was $\omega = 10^2$,

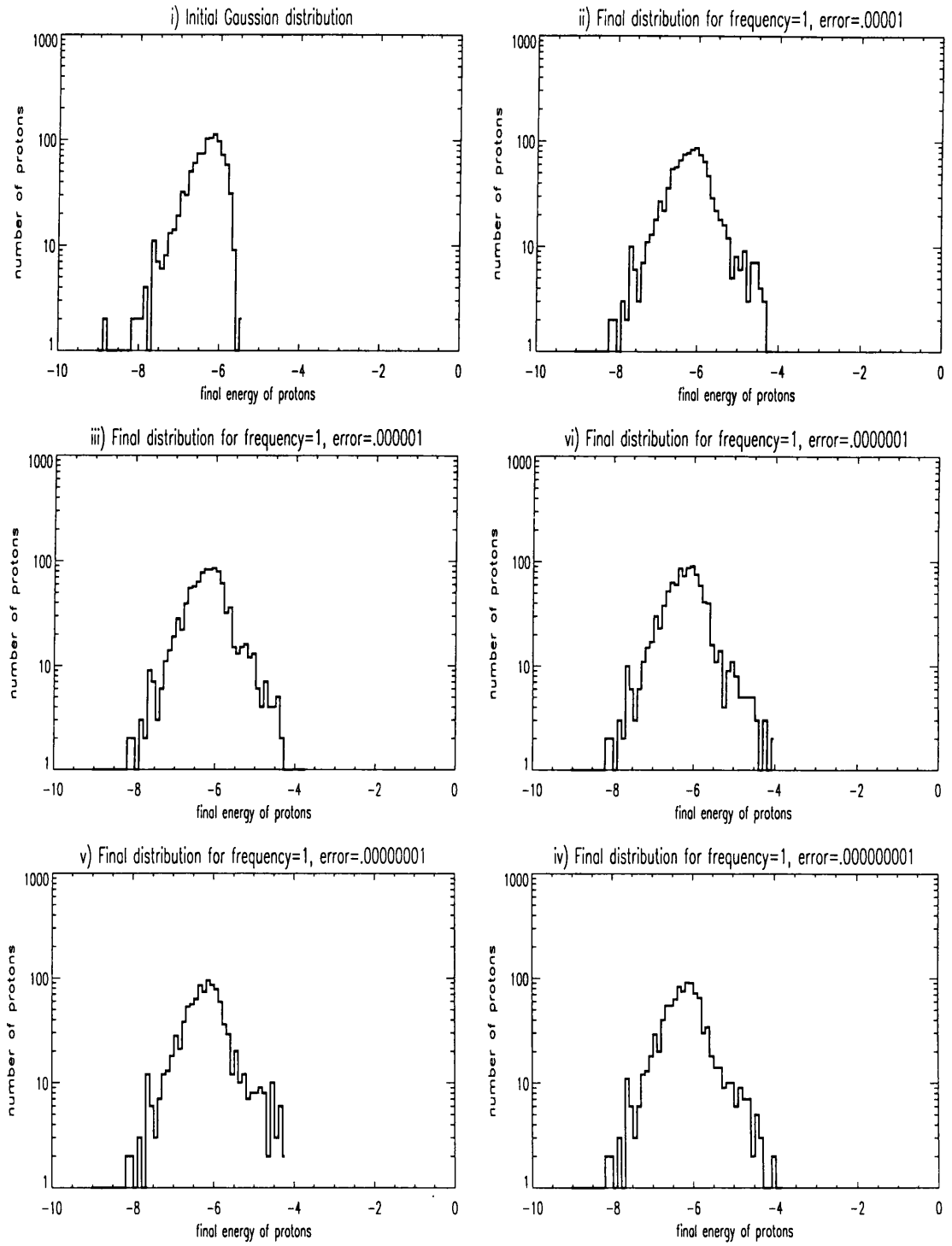

Figure 3.16: Final energy distributions for protons for frequency=1 of the electric field. Histogram i) shows the initial Maxwellian distribution. Histograms ii) to iv) show the final distribution of 1000 protons for increasing accuracy of the integration routine. Total integration time for all the distributions is 5360 timesteps.

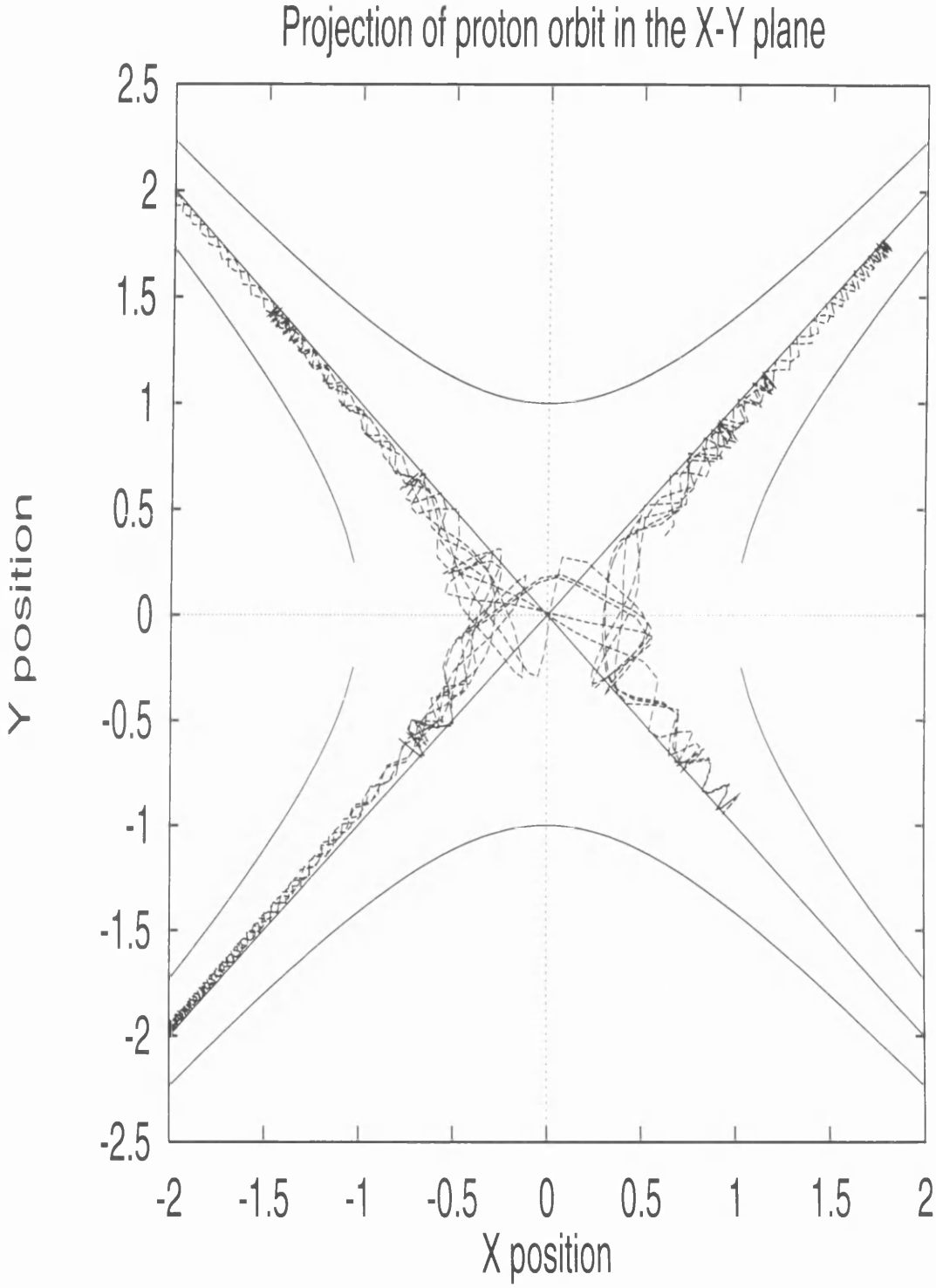

Figure 3.17: Proton orbit in time-varying Electric field with frequency 1/10. The projection in the X-Y plane is shown here. Field lines of the X-type magnetic field are also plotted.

a slowly varying field. The proton crosses the non-adiabatic area several times mostly increasing its energy. After an integration time of about 1 second its initial energy has increased by a few hundred thousand times. In this graph only the part of the proton's orbit close to the neutral point is visible. The particle actually goes a long distance (up to 120 dimensionless distance units for this one) but mirrors and so crosses and recrosses the neutral point. Sometimes when a particle goes on such an expedition it doesn't come back but leaves the box of integration, and so is lost from the system. Only particles with large energy gains can escape, the rest are trapped at least in this collisionless calculation. The second orbit in figure 3.18 is an orbit of a particle that doesn't gain any energy (its energy doesn't increase within the limits of accuracy of our calculation). The reason is that it is positioned initially away for the non-adiabatic region and also its initial energy is small so that its gyroradius doesn't cross the neutral area. Of course between the two examples are several intermediate situations.

3.4.3 Magnetic Moment

The modulus of the component of the particle's velocity parallel to the magnetic field is

$$u_{||} = \frac{\underline{u} \cdot \underline{B}}{\mid B \mid}. \tag{3.28}$$

So in dimensionless units

$$u_{||} = \frac{u_x y + u_y x}{r} \tag{3.29}$$

where $r = \sqrt{(x^2 + y^2)}$ is the modulus of the magnetic field in dimensionless units. The modulus of the perpendicular component to the magnetic field of the particle's velocity is given by

$$\mid \underline{u}_{\perp} \mid = \frac{\mid \underline{u} \times \underline{B} \mid}{\mid B \mid}. \tag{3.30}$$

The modulus of the perpendicular velocity is given by

$${u_{\perp}}^2 = \frac{(x u_x - y u_y)^2}{r^2} + {u_z}^2. \tag{3.31}$$

The magnetic moment is a quantity that is constant when the motion of the particle is adiabatic (see for example Chen 1984) and is given in dimensionless units by

$$\mu = \frac{{u_{\perp}}^2}{\mid B \mid}. \tag{3.32}$$

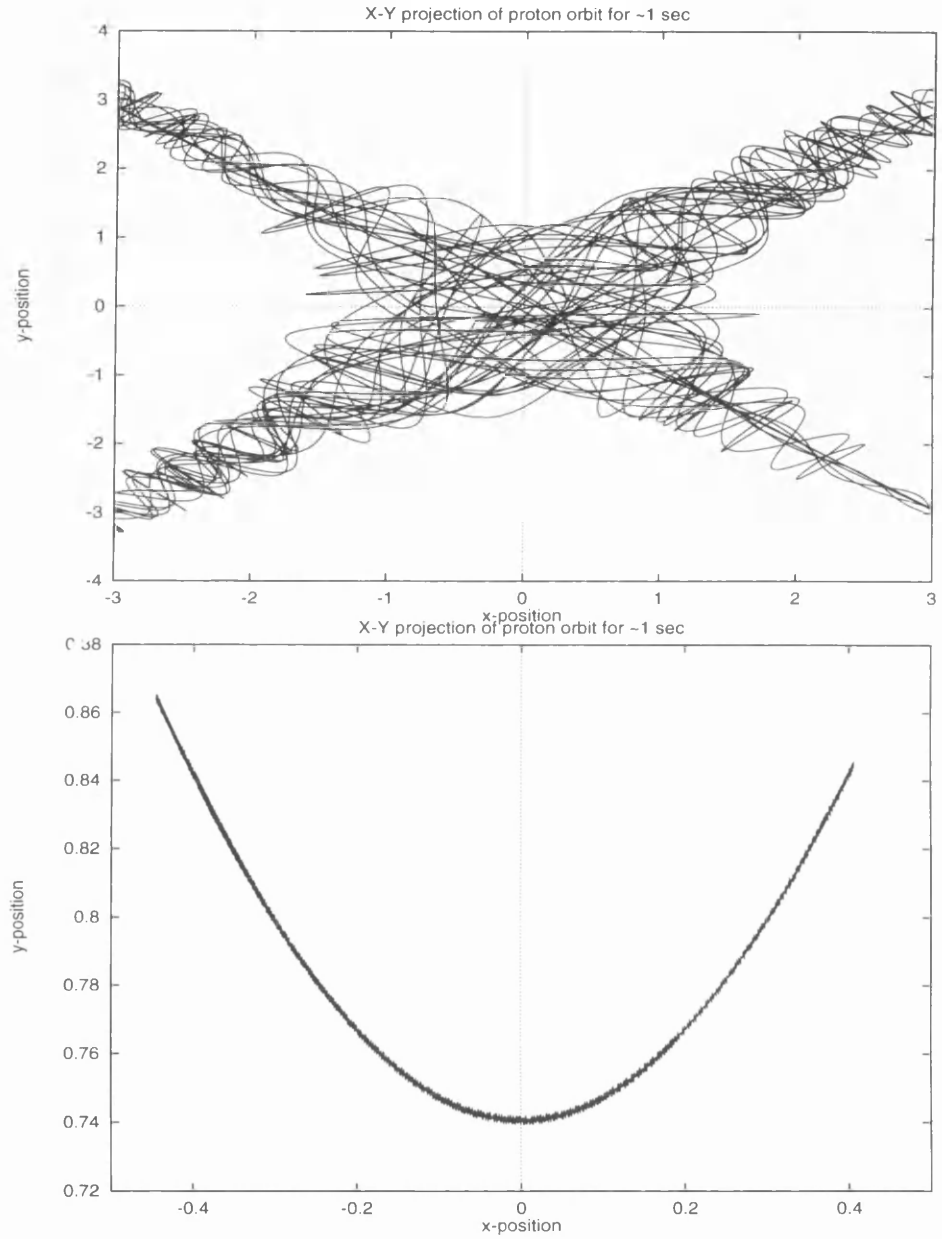

Figure 3.18: Proton orbit projection in the $x - y$ plane after time = 1 sec in the presense of a time-varying electric field with $\omega = 10^2$.

We have calculated the evolution of magnetic moment for several particles with different initial conditions. In fig. (3.19) we see the orbit of proton in the X-type magnetic field with no electric field present. The orbit has adiabatic and nonadiabatic behaviour. The energy of the particle is conserved. The magnetic moment though is nearly conserved when the particle moves along separtices. In fig. (3.20) we see the orbit of a proton that stays adiabatic during all of its orbit. The reason for that is that its orbit does not cross from the nonadiabatic region. It magnetic moment is conserved. In fig. (3.21) we see the orbit of a proton in time varying electric field that has both adiabatic and nonadiabatic parts. Every time the particle crosses from the neutral point area the magnetic moment is not conserved, but is changing. Such study of the magnetic moment shows clearly the episodes of adiabatic and non-adiabatic behaviour.

3.4.4 Properties of the Acceleration Mechanism

The kinetic energy of the particle is calculated after the end of a specific time along with final positions and velocities. Recall that the unit of energy here is the rest mass energy (mc^2) of the particles. For electric field fluctuation frequencies in a certain range we find that the energy distributions have two peaks (see figure 3.30). The protons that gain the most energy lie there. We observe that the particles that gain the most energy are the ones that initially are positioned close to the separatrices of the hyperbolae $y^2 - x^2 = const$ and close to the neutral point; these are the particles whose trajectories are most likely to take them through the non-adiabatic region.

The particles in our calculation spend a short period of time close to the neutral point but they get trapped in the magnetic configuration and cross the neutral point a number of times (see figure 3.18). Thus multiple encounters with the neutral point, which do not take place in steady reconnection with the electric field present everywhere, result in a Fermi-type acceleration. This occurs indepedently of the time-dependence of the electric field and has been noted also in section (3.3.3) A similar phenomenon has been noted for a multiple neutral point configuration by Kliem (1994).

The amount of acceleration that particles get depends on the time they spend close to the neutral point (see 3.2.2). The crossing time of a particle from the nonadiabatic region is given in rough estimation, by

$$t_{cr} \sim \frac{2r_{ad}}{u_{x,y}} \sim \frac{2r_{ad}}{u_{th}} \tag{3.33}$$

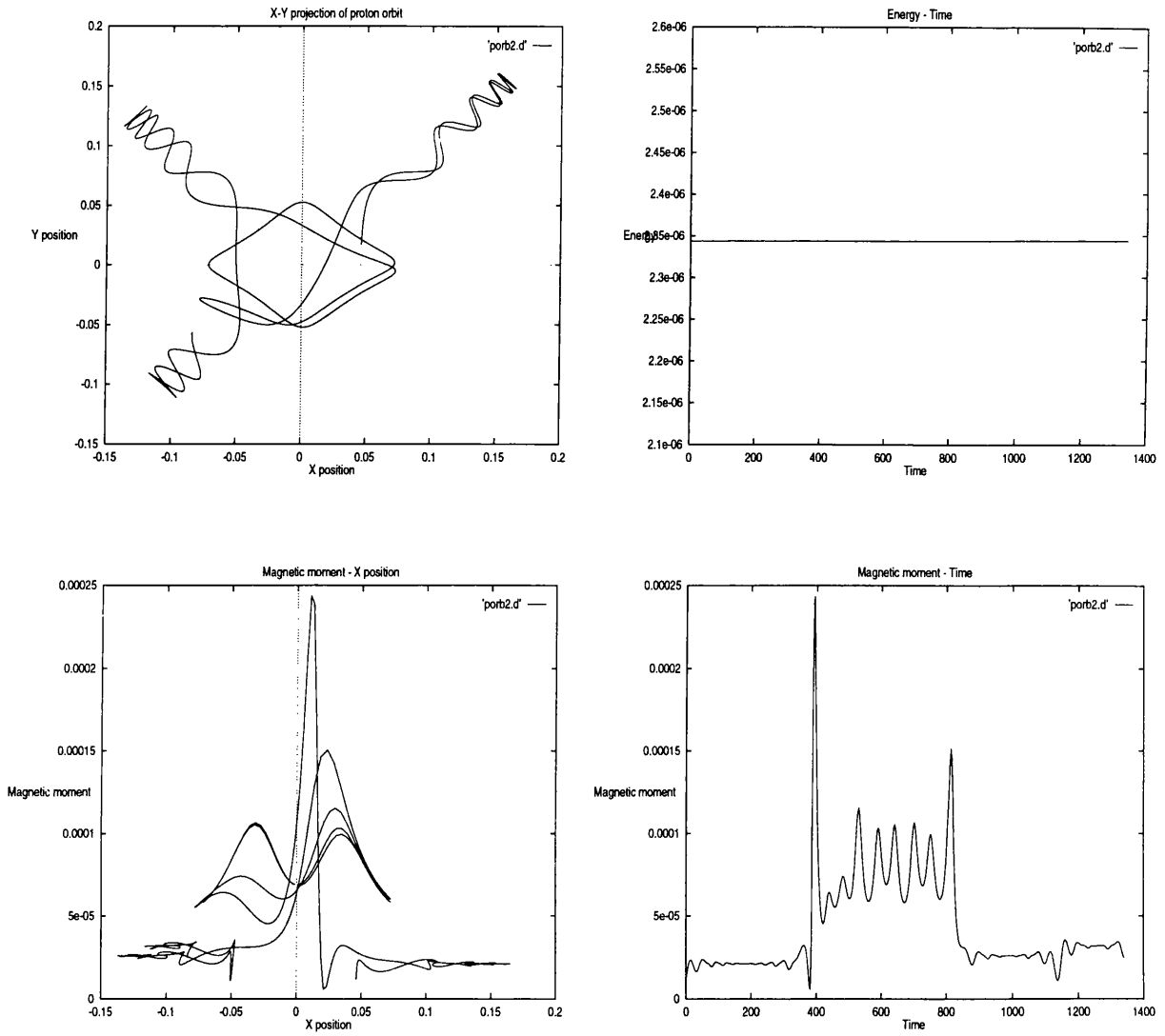

Figure 3.19: Orbit of a proton in the X-type magnetic field with no electric field present. The orbit has adiabatic and nonadiabatic behaviour. The energy of the particle is conserved. The evolution of its magnetic moment both in time and in space are very interesting.

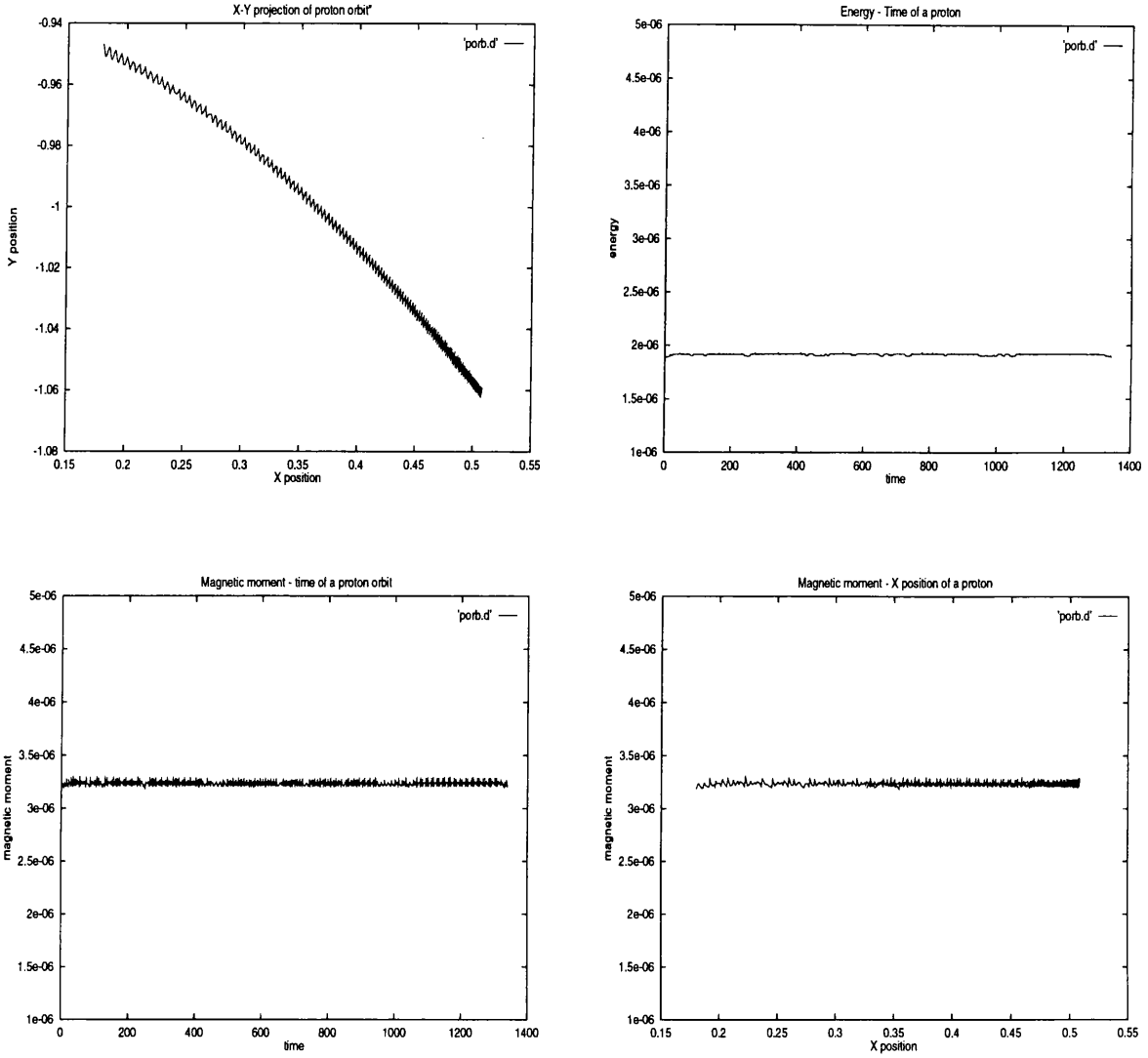

Figure 3.20: Orbit of a proton in the X-type magnetic field with time varying electric field present. The orbit stays adiabatic, since the particle is far enough from the neutral point region and the gyroradius is small compared to the scale length of the magnetic field. The energy of the particle is conserved.

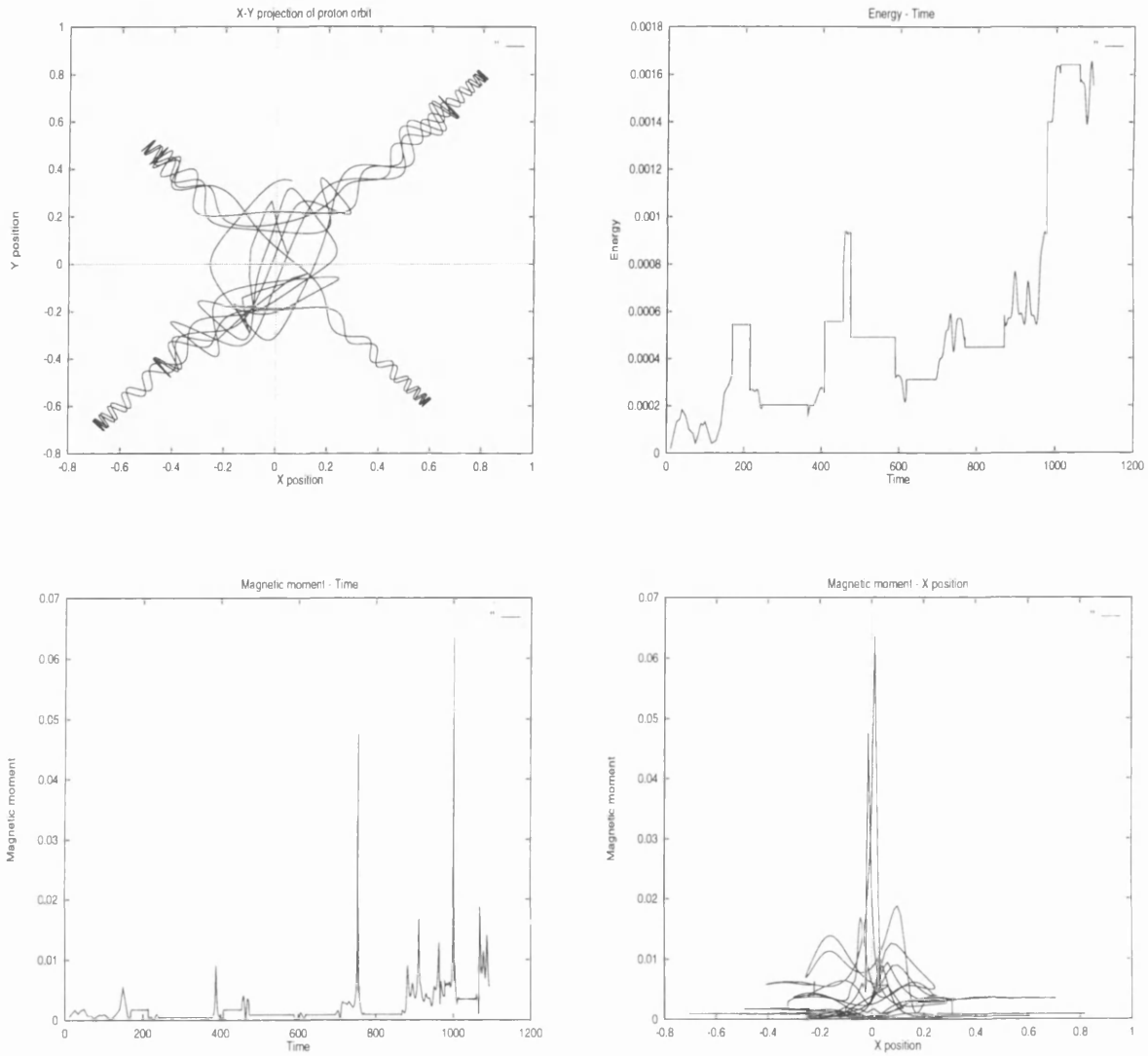

Figure 3.21: Orbit of a proton in the X-type magnetic field with time varying electric field present. The orbit stays adiabatic away from the neutral point. Near to the neutral point nonadiabatic behaviour is clearly demonstrated. The particle's energy is not conserved.

where $u_{x,y}$ is the velocity projection in the x-y plane. This is assumed to be roughly equal to the thermal velocity. So,

$$t_{cr} \sim (\frac{2.828cD}{eB_o})^{1/2} \frac{m_i^{3/4}}{E^{1/4}}. \tag{3.34}$$

It turns out that particles with the same energy satisfy

$$t_{cr_p} = t_{cr_e}(\frac{m_e}{m_p})^{\frac{3}{4}} = 280 t_{cr_e} \tag{3.35}$$

where t_{cr_p} is the proton crossing time and t_{cr_e} is the electron crossing time. The crossing time is the time that the particle needs to cross the non-adiabatic region (see Sec. 3). One would expect that in order to get particles effectively accelerated (or decelerated since the sign of the electric field is not constant) we need $t_E \gg t_{cr}$ where t_E is the period of fluctuation of the electric field.

Protons gain most energy from the most slowly varying electric field (see figure 3.30) as expected. For frequencies greater than $\omega = 1$ their initial energy distribution does not change significantly in the time scale of the integration ($1sec$ for protons). The electrons on the other hand seem to gain most energy when $10 \leq \omega \leq 500$ (see figure 3.27) which is close to ${\tau_e}^{-1}$ and the electron crossing time.

So, the presence of relatively low frequency electric fields in the adiabatic region does not seem to increase the energy of electrons significantly at least not in the time of our calculation. From the way we pick our initial conditions the electrons start closer to the neutral point. But since the true area where the electric field is applied, for both species is calculated from the proton adiabatic radius, electrons see an area much larger than their adiabaticity radius where the electric field is present. Some of them start their motion outside the adiabaticity radius and their motion is immediately adiabatic. In this case the presence of the electric field does not increase their energy. They move with the $\underline{E} \times \underline{B}$ drift. They bounce between two points of the magnetic field (see Fig. 3.22), and they don't recross the nonadiabatic region.

3.4.5 Energy Distributions

As we have already said the kinetic energy of the particles here is given in terms of their rest mass energy $E_{kin} = \gamma - 1$. The rest mass energy for protons is 939 MeV and for electrons 0.511 MeV. It is now obvious from fig. (3.30) that protons acquire very high energies.

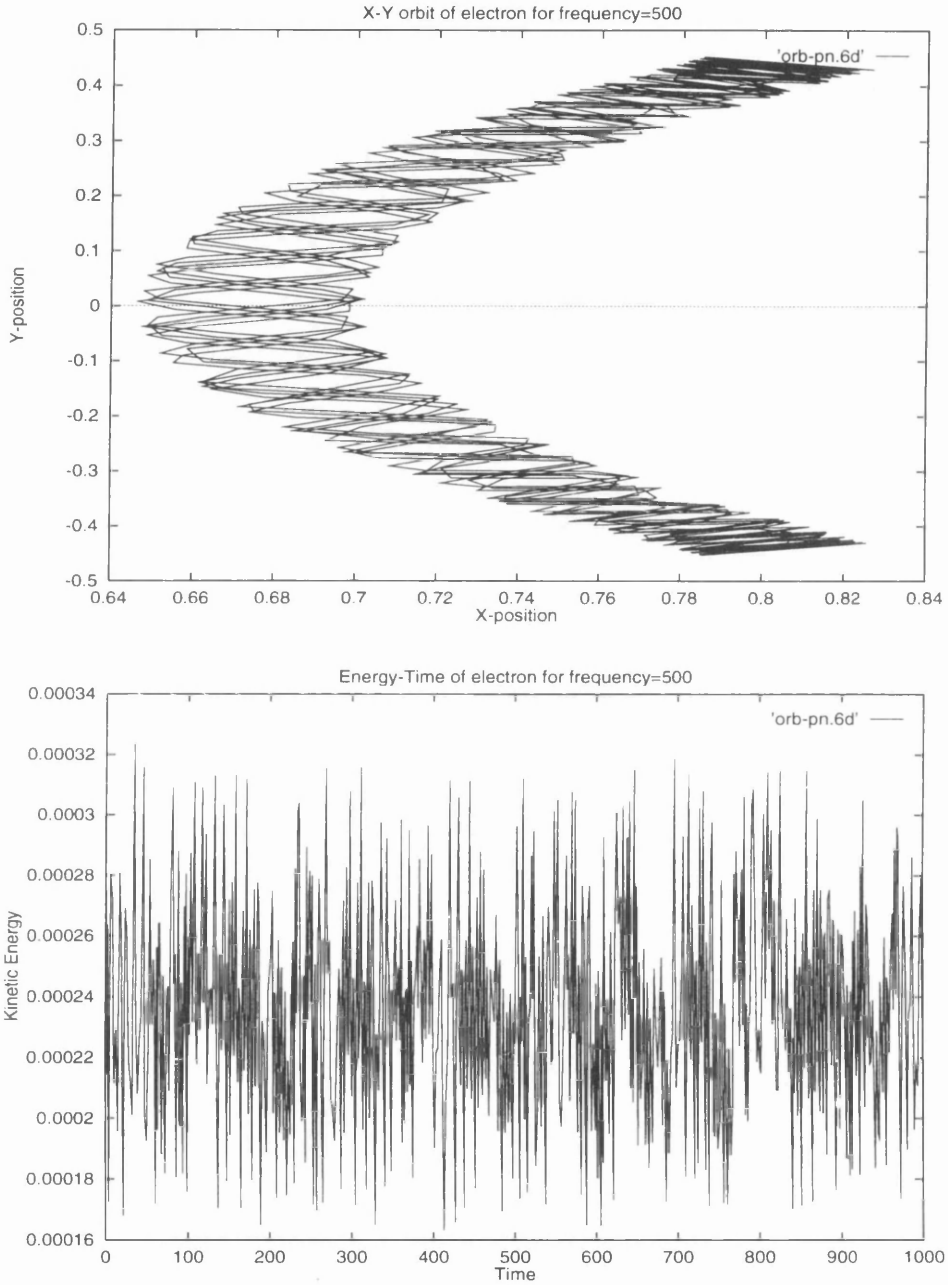

Figure 3.22: Projection of the orbit of an adiabatic electron. The electric field frequency is 500.

In fig. (3.23) we see the initial energy distribution of 1042 protons and their final distribution, for E=0.001 and frequency=1/100. In histogram iii) we see the initial distribution of those protons that gain more then 10% energy and in histogram iv) we see the final energy distribution of those protons that gain more than 10% energy. So, one can see that the particles that get accelerated come from all parts of the initial Maxwellian, not only from the tail. The same is true for the distributions produced for the other frequencies of the electric field (see fig. (3.24)).

In Fig. 3.25 we see the mean values of the final distributions of protons for different frequencies of the electric field. In the top graph only the energies of the particles that increase their initial energy by more than 10%, are present. The mean energy increases when the frequency of the electric field decreases. In the bottom graph the mean final energies of the whole distribution are presented.

As we said before due to computational limitations the integration time for electrons is only 11500 timesteps. With $B_o = 100$ gauss, this corresponds to 0.05 seconds. The distributions that result are significantly different from the initial maxwellian as can be seen in fig. (3.26).

When the calculation is done for 1/20th of a second for protons also we see that the change in the initial distribution is not as significant as the one in the electron distribution (fig. 3.28). The evolution of the proton distribution is more significant after 1/10th of a second and 1 second integration time (fig. 3.29 and 3.30 respectively). In other words our results suggest that, when the frequency is suitable, electrons are more rapidly accelerated than protons. Clearly, this might have observable consequences, but numerical limitations prevent us from more extensive investigation.

In fig. (3.31) I plotted the mean value of the final distributions versus the frequency of the electric field for the three different integration times. I repeated the same calculation and analysis for $E_o = 0.01$. In fig. (3.32) we see the final distributions of protons for different values of the frequency of the electric field and $E_o = 0.01$. In fig. (3.33) the results for $E_o = 0.01$ and $E_o = 0.001$ are compared.

In tables (3.2), (3.3) and (3.4) we see the percentage of the final distribution that gets accelerated for different values of the frequency of the electric field and for magnitude 0.001. I calculate the percentage of particles for which

$$\frac{E_{final} - E_{initial}}{E_{initial}} \geq constant \tag{3.36}$$

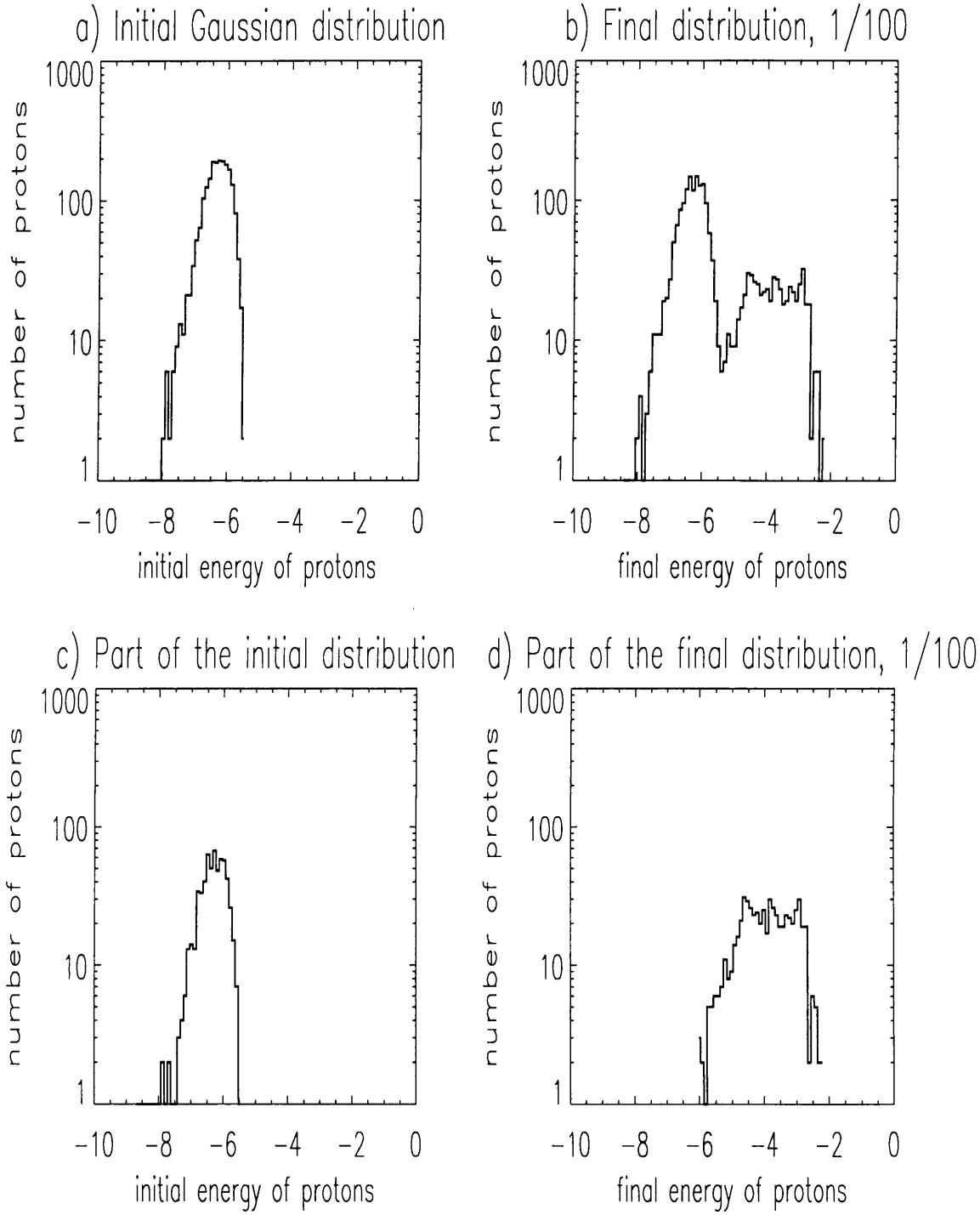

Figure 3.23: Final energy distributions for protons for time-varying electric field. Histogram i) shows the initial Maxwellian distribution. Histograms ii) shows the final distribution of 2000 protons for E=0.001 and frequency=1/100. Total integration time for all the distributions is 5360 timesteps. In iii) we see the initial distribution of those protons that gain more then 10% energy and in iv) we see the final energy distribution of those protons that gain more than 10% energy.

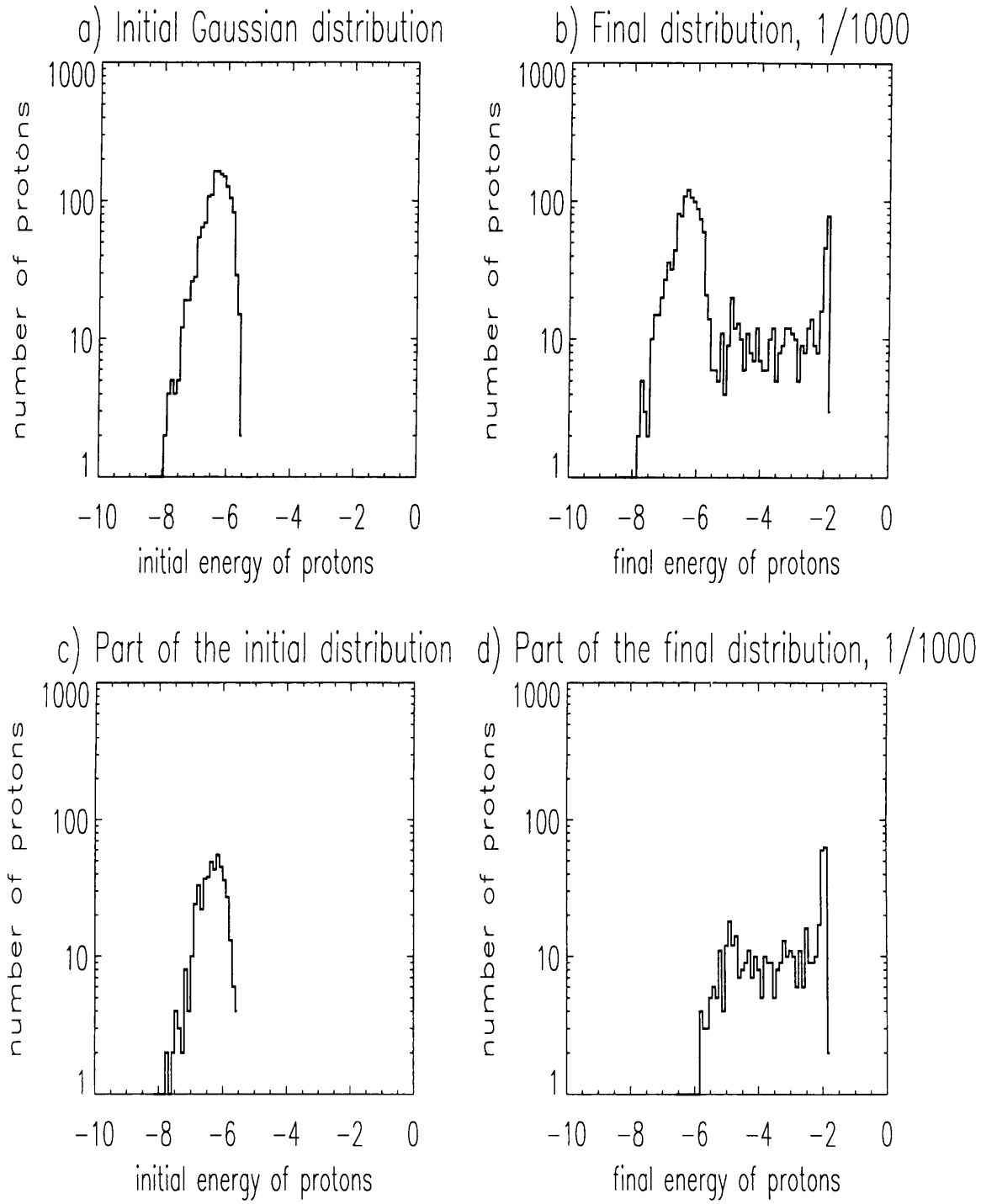

Figure 3.24: Final energy distributions for protons for constant electric field. Histogram i) shows the initial Maxwellian distribution. Histograms ii) shows the final distribution of 2000 protons for E=0.001 and frequency=1/1000. Total integration time for all the distributions is 5360 timesteps. In iii) we see the initial distribution of those protons that gain more then 10% energy and in iv) we see the final energy distribution of those protons that gain more than 10% energy.

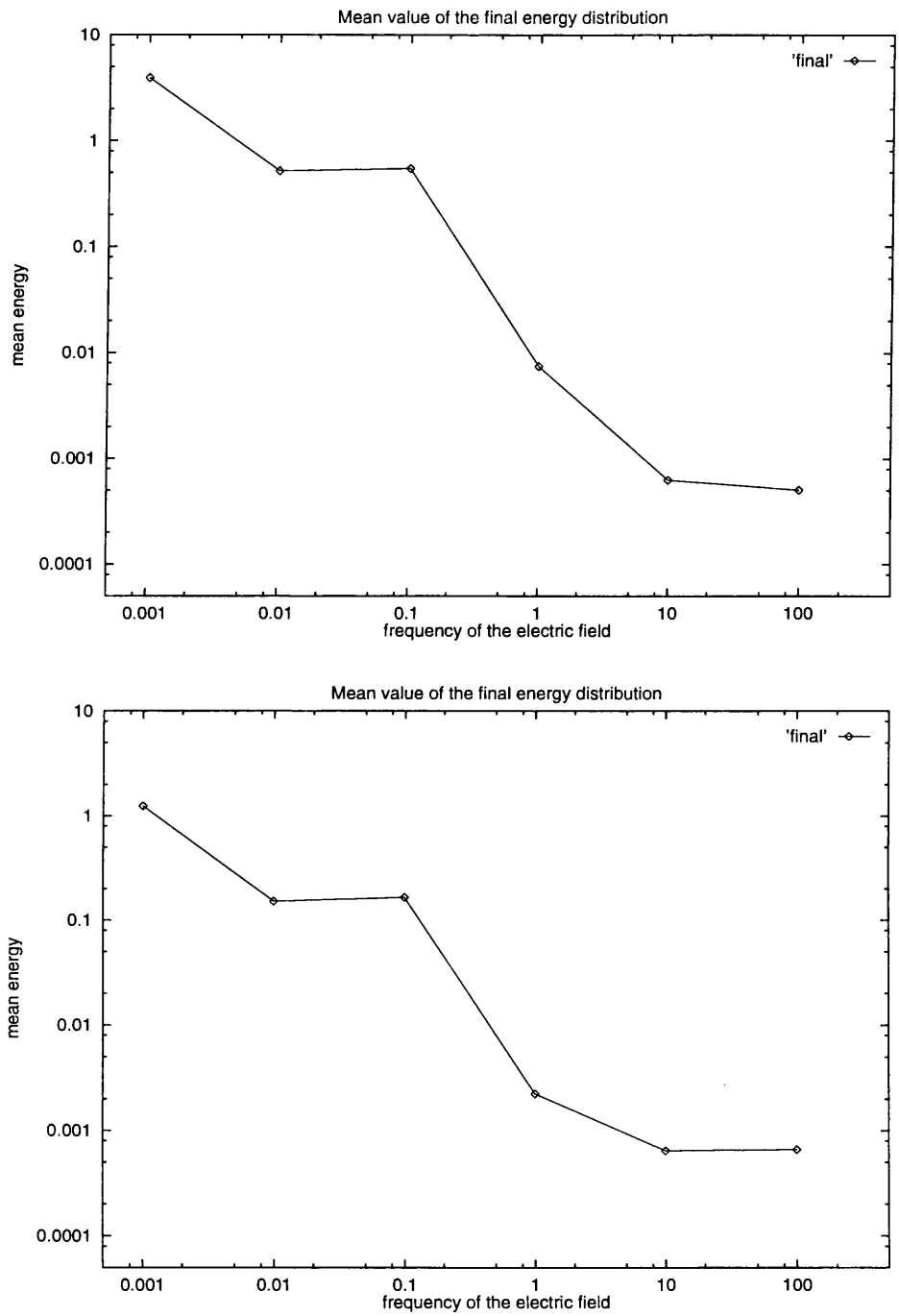

Figure 3.25: Mean final energy versus the frequency of the electric field. On the top graph only the protons that their energy changes more than 10 % are present. In the bottom graph all the prorotns are present The mean energy of the distribution increases as the frequency decreases. The magnitude of the electric field is 0.001.

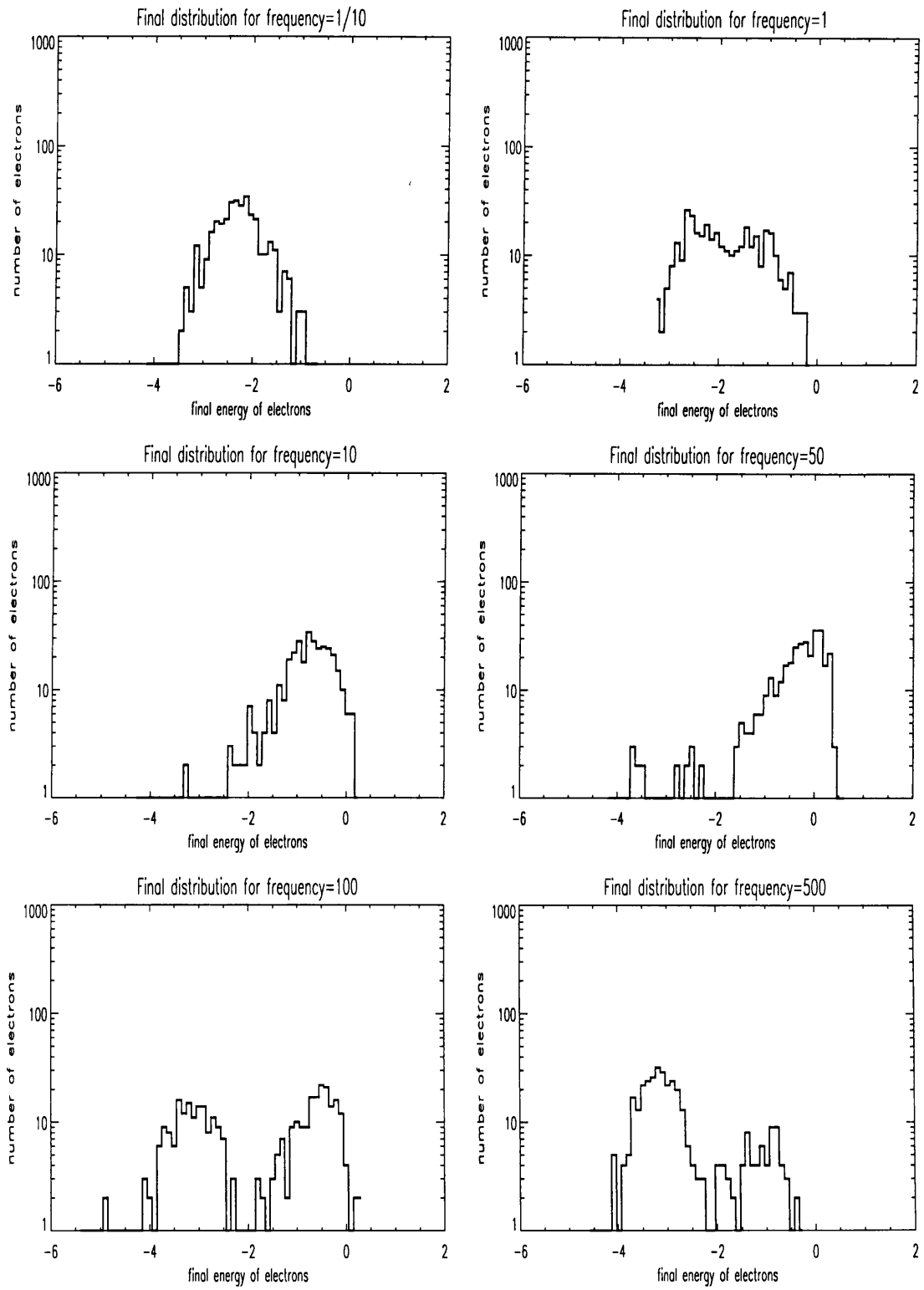

Figure 3.26: Final distributions of 350 electrons, for different frequncies of the electric field. All the distributions are taken after integration time of $\sim 1/20$ of a second assuming that $B_o = 100$ gauss. The magnitude of the electric field is 0.001.

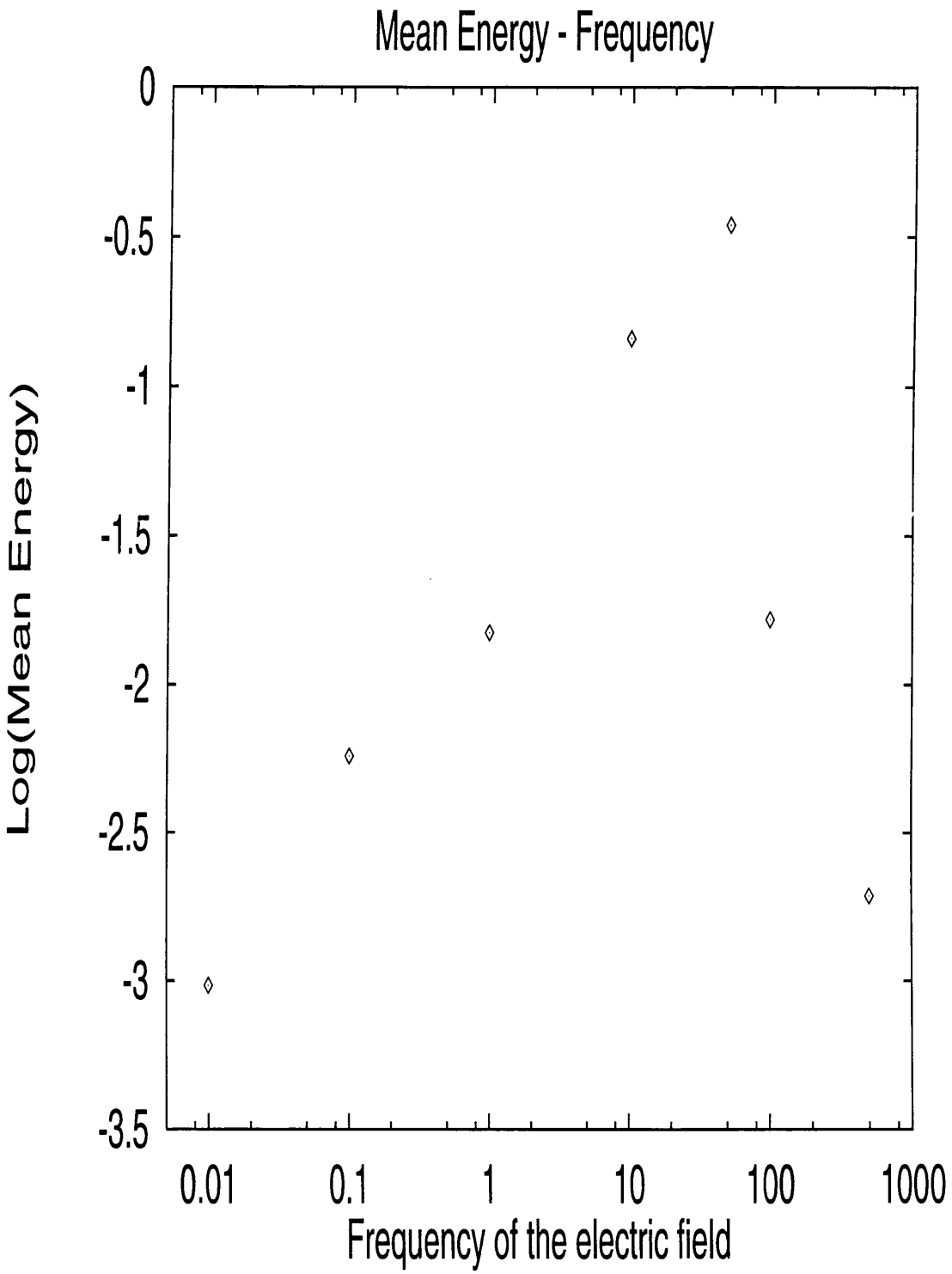

Figure 3.27: Diagram of the logarithm of mean energy of the final distributions of electrons versus the frequency of the electric field. All the distributions are taken after integration time of $\sim 1/20$ of a second. The magnitude of the electric field is 0.001. The value 0.01 is used to show the mean energy of the initial distribution of electrons.

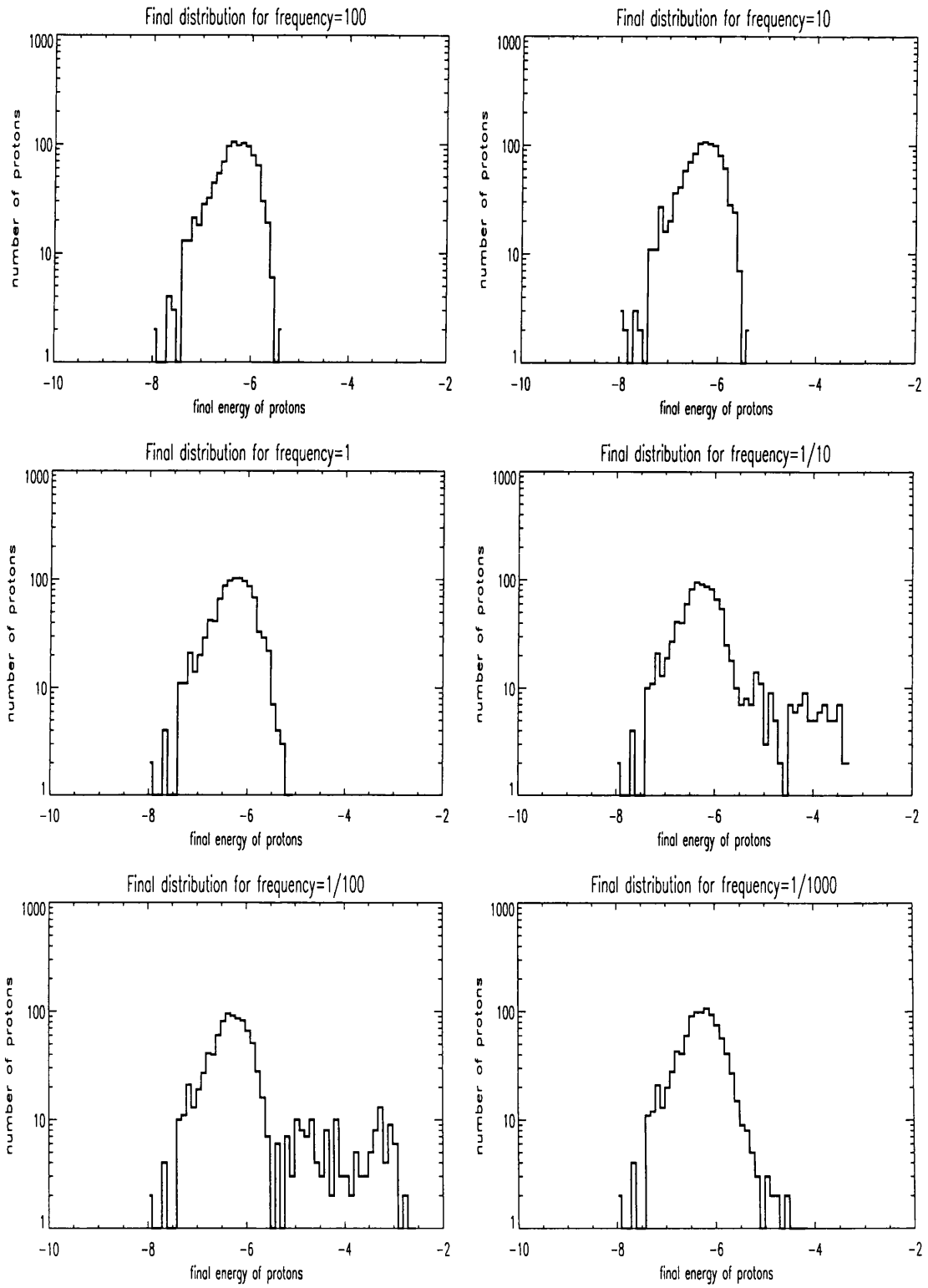

Figure 3.28: Final distributions of protons, for different values of the electric field. All the distributions are taken after 268 timesteps. The magnitude of the electric field is 0.001.

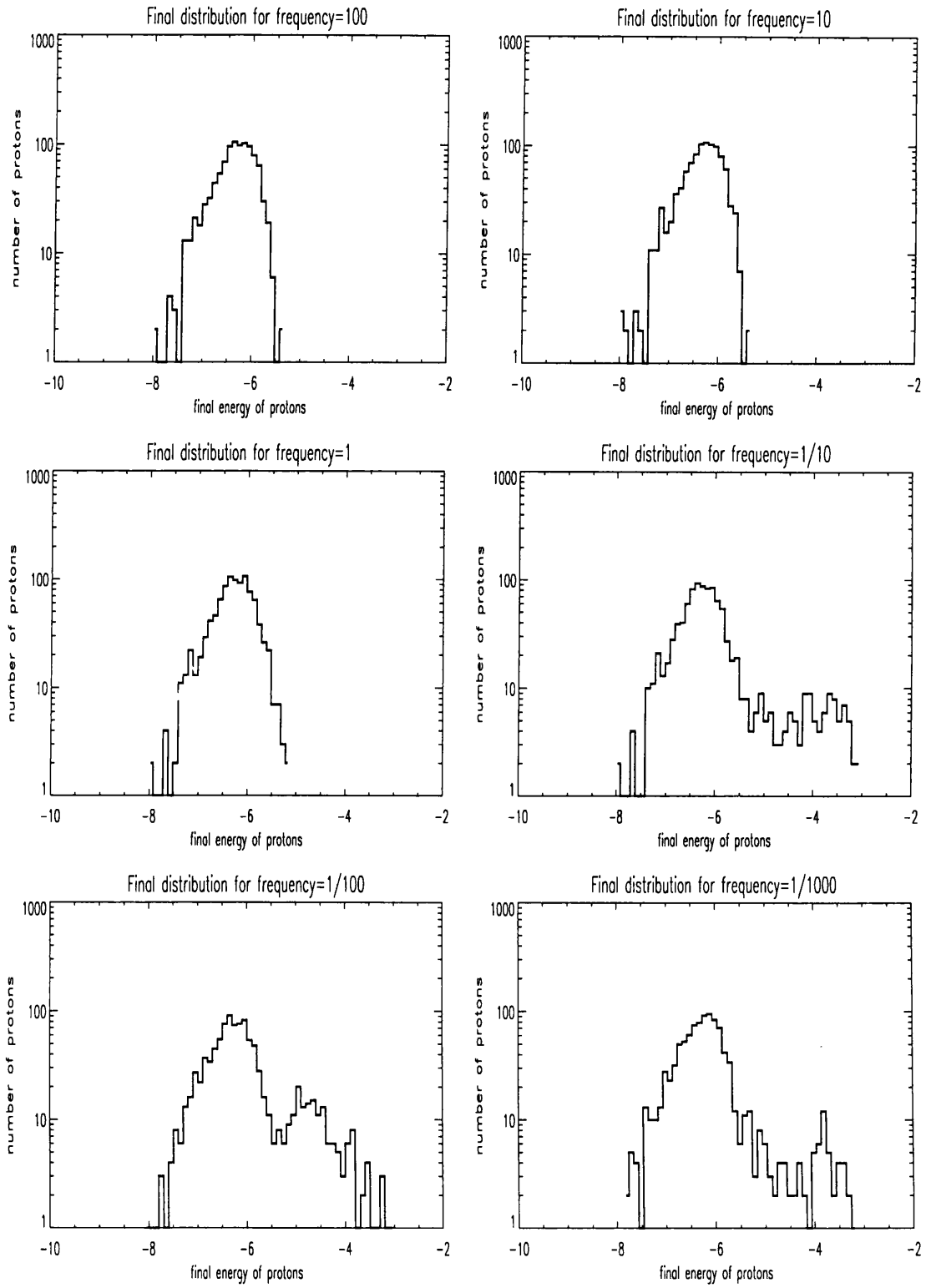

Figure 3.29: Final distributions of protons, for different values of the electric field. All the distributions are taken after 536 timesteps. The magnitude of the electric field is 0.001.

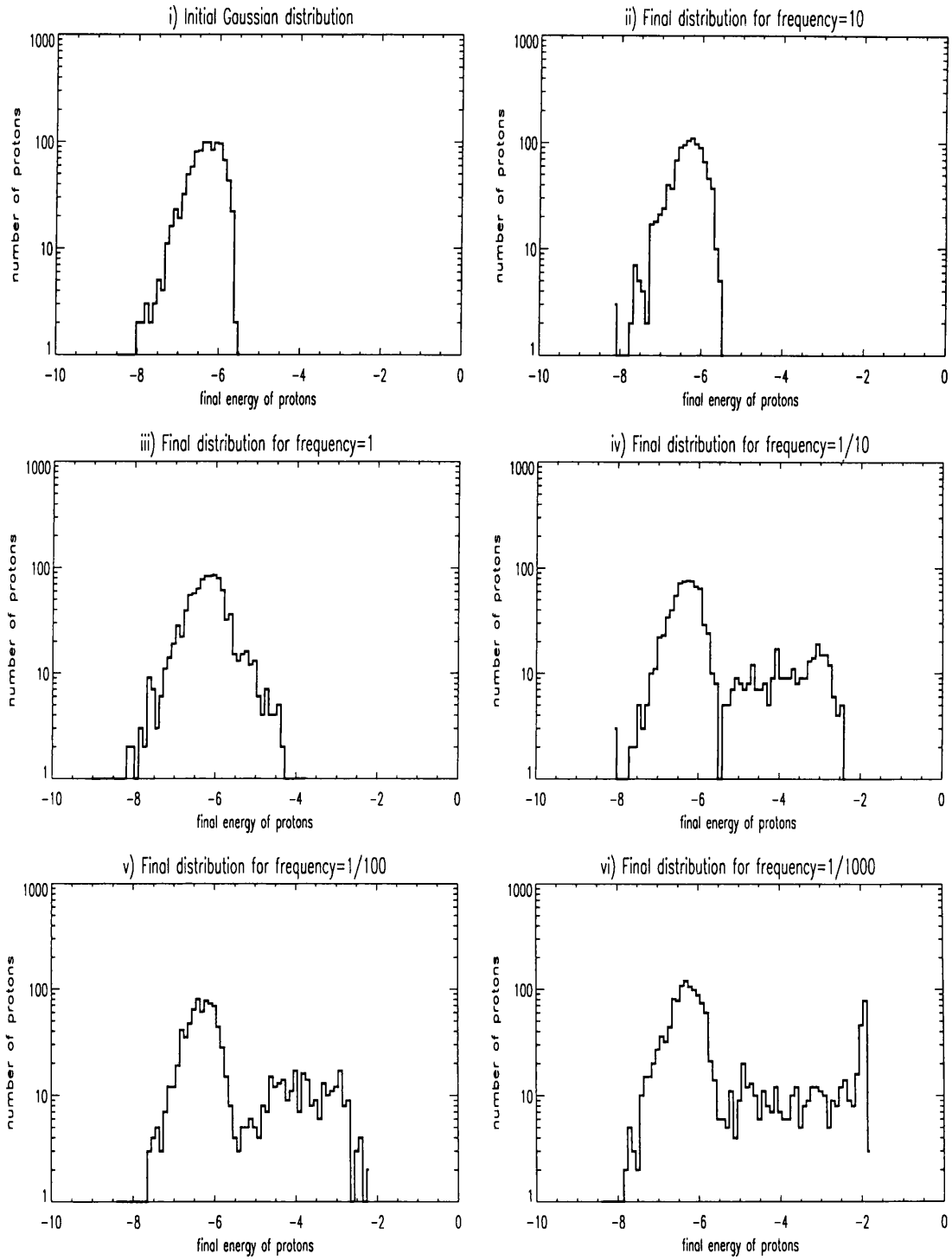

Figure 3.30: Final proton distributions for different frequencies of the electric field. In i) the initial gaussian distribution is shown. The magnitude of the electric field is 0.001. The total integration time is 5360.

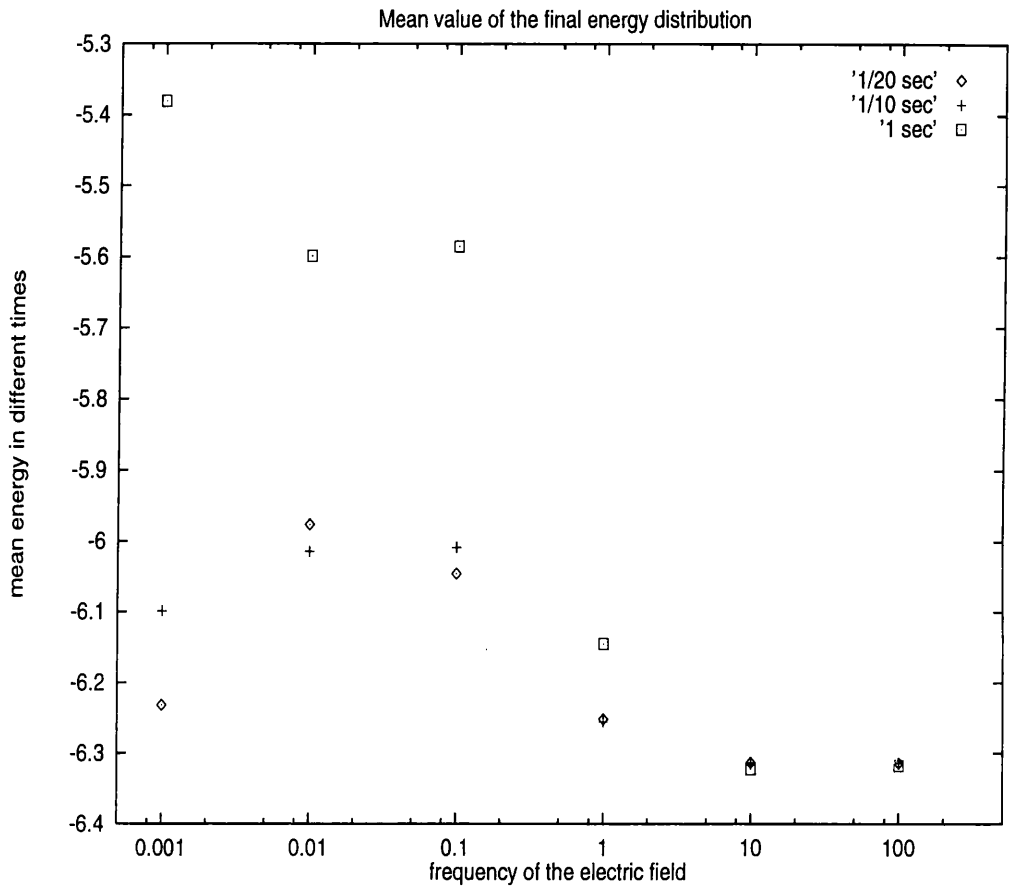

Figure 3.31: The mean value of the energy distributions for protons is plotted for different values of the frequency of the electric field, and for different integration times. Denoted with: a) diamont are the distributions after integration time of $\sim$ 1/20 sec, b) cross are the distributions after integration time $\sim$ 1/10 sec, and c) square are the distributions after 1 sec. The magnitude of the electric field is 0.001. Frequency 0.0001 represents the case with no electric field.

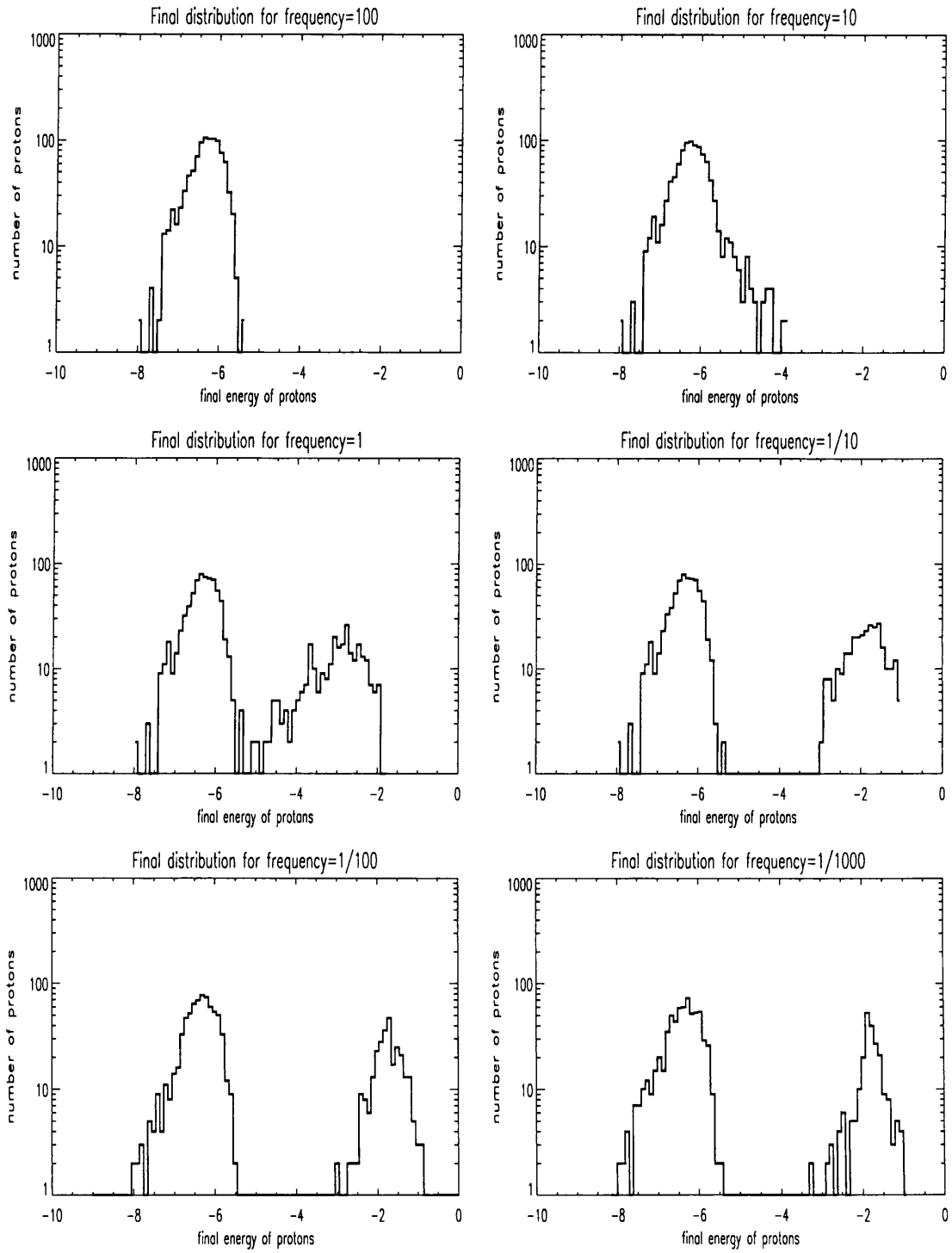

Figure 3.32: Final proton distributions for different frequencies of the electric field. The magnitude of the electric field is 0.01. The total integration time is 5360.

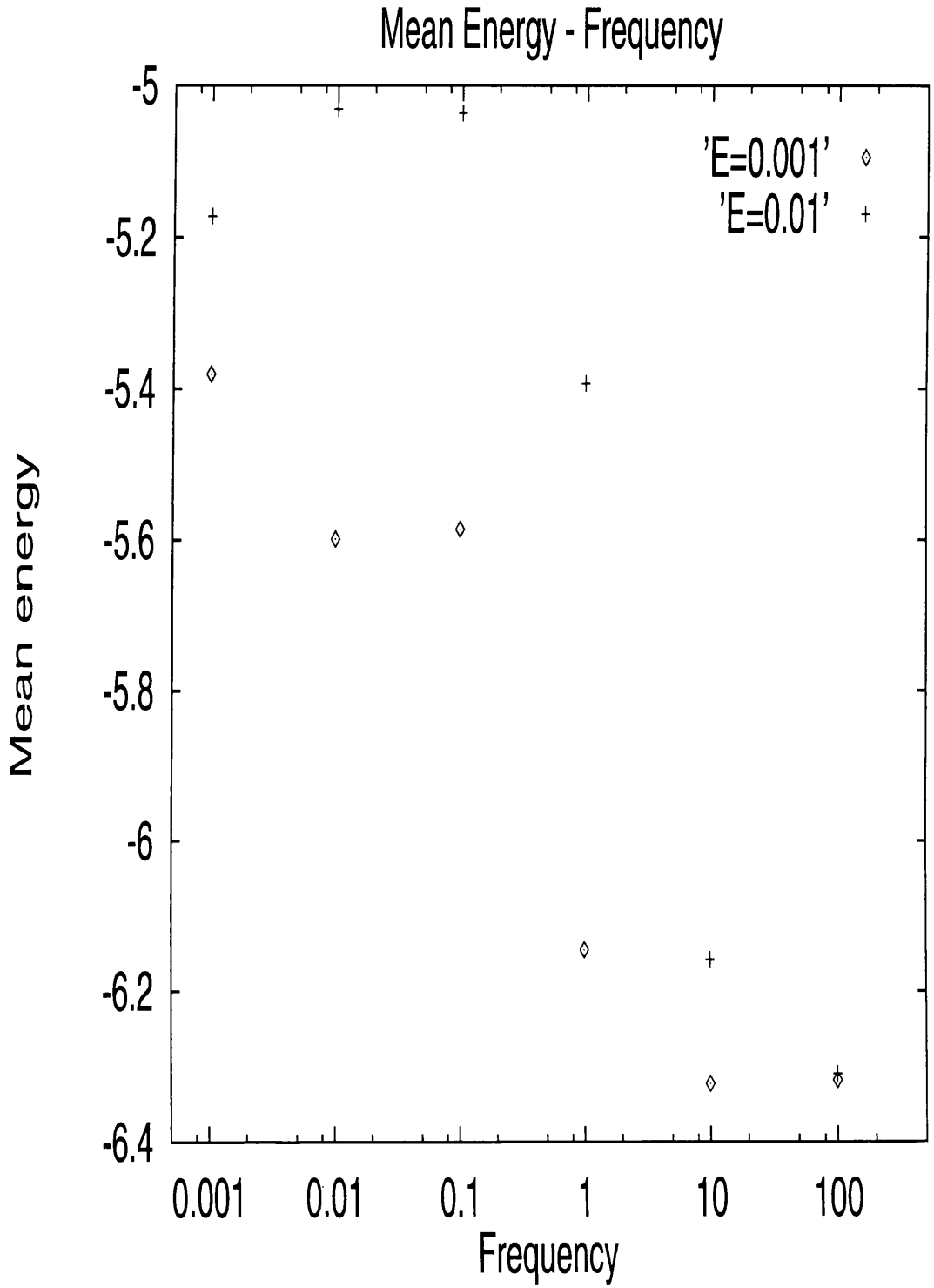

Figure 3.33: Mean energy of the final proton distributions for different frequencies of the electric field. The magnitude of the electric field is 0.01 and 0.001. The total integration time is 5360.

where *constant* is , 1, 10 and 100. In column one we see the percentage of the final distribution that doubles its initial energy. In column two we see the percentage of the final distribution that increases its initial energy by 10 times and in column three the percentage of the final distribution that increases its initial energy by 100 times. In column four we see the percentage of the final distribution that has energy greater than 1MeV for protons and 20 KeV for electrons. The highest energies for each distribution are shown in column five.

So, the initial distribution of electrons seems to get accelerated to hard X-ray producing energies in less than 1/20th of a second in the presence of a time varying electric field. When the frequency of the electric field is 50 then 90 % of the initial gaussian acquires energies bigger then 20 KeV and the highest energy observed is 1.65 MeV. On the other hand proton distributions get accelerated to γ-ray producing energies in less than 1 sec. For frequency of the electric field 1/1000 15 % of the initial gaussian gets to energy bigger that 1 MeV. The highest energy observed is 15.5 MeV.

Frequency	1	10	100	> 20keV	MeV
1/10	86 %	26 %	2.4 %	7.1 %	0.14
1	89 %	56 %	12.3 %	32 %	0.38
10	98 %	92 %	67 %	86 %	0.9
50	97 %	94 %	86 %	90 %	1.65
100	69 %	54 %	41 %	51 %	1.15
500	25 %	19 %	6 %	16 %	0.27

Table 3.2: Percentage of accelerated electrons after 0.05 seconds

Frequency	1	10	100	> 1 MeV	MeV
1/1000	30 %	29 %	22 %	15 %	15.5
1/100	30 %	28 %	20 %	5 %	7.0
1/10	30 %	27 %	20 %	6 %	5.0
1	20 %	8 %	1 %	0 %	0.18
10	0.4 %	0 %	0 %	0 %	0.0038
100	0 %	0 %	0 %	0 %	0.0047

Table 3.3: Percentage of accelerated protons after 1 second

3.4.6 Radiation Losses

For a given particle velocity the power radiated is proportional to m^{-2}, so radiation losses are more important for electrons than for protons. For an isotropic distribution of electron

Frequency	1	10	100	> 1 MeV
1/1000	10 %	2.2 %	0.3 %	0 %
1/100	15 %	13.6 %	8.6 %	1.1 %
1/10	15.2 %	11.3 %	6.1 %	0 %
1	8.7 %	1.2 %	0 %	0 %
10	0 %	0 %	0 %	0 %
100	0 %	0 %	0 %	0 %

Table 3.4: Percentage of accelerated protons after 0.05 seconds

velocities, the synchrotron radiation losses are given

$$P = \frac{4}{9} r_o{}^2 c B^2 \gamma^2 \beta^2 = 1.1 \times 10^{-15} B^2 \gamma^2 \beta^2 \text{ erg/sec} \tag{3.37}$$

where $r_o = e^2/m_e c^2$ is the classical electron radius and $\beta = u/c$ (Tucker 1975). So the lifetime of a 10 MeV electron (much higher energy than the ones calculated here) in a 100 gauss magnetic field, is $\sim$ 3000 seconds, much longer than the times considered in our calculation. So, our conclusion is that we can ignore synchrotron radiation losses. Bremsstrahlung losses are even less important.

3.5 Conclusions and Discussion

In this work we investigate the likely particle acceleration consequences of dynamic, collisionless reconnection. We have shown that protons and electrons may gain relativistic energies in times $< 1s$; for plausible (small) electric field amplitudes and active region magnetic fields. Later in this thesis we will attempt to tie this approach self-consistently to an MHD description of the passage of a wave. Before discussing some consequences of this, we note some limitations of our calculation. First, this is a test particle approach. Particles do not interact with each other, nor do they influence the background field. In particular, the particle distribution including the accelerated component may well be unstable to growth of various sorts of waves. Obviously such wave growth would influence the motion of particles, but we neglect this possibility. We neglect also radiation losses. In the solar corona this is not a serious neglect (even for 10 MeV electrons the radiative energy loss time is $\sim$ 3000 seconds), but elsewhere in the cosmos it could become significant.

In the presence of a spatially uniform magnetic field, no particles would gain energy in the spatially uniform, temporally oscillating electric field we have invoked here. The finite width of the nonadiabatic region allows particles to gain or lose some energy randomly

before returning to adiabatic motion. Together with repeated encounters with the dissipation region, the consequence of mirrorings in the extended configuration, this results in a Fermi-type, 'stochastic' acceleration. It is important to emphasize that this takes place for purely geometrical reasons, without any resonant interaction of wave and particle. There is no threshold for this sort of acceleration, unlike resonant interaction with low-frequency, MHD waves. The necessity for protons particularly to have threshold energies of around 25 KeV is a well known difficulty when such mechanisms are invoked (eg Forman et al., 1986). Our results indicate that low-frequency waves may themselves perform the 'first-step' acceleration, if they propagate in a coronal structure including a neutral point. This may occur independently of, or simultaneously with, the resonant cascade scenario of Miller and Vinas (1993). Possible difficulties with the number of pre-accelerated particles may be obviated if many neutral points are present (cf Kliem, 1994), although such a situation obviously needs separate investigation.

We note the effectiveness of acceleration of various species varies according to the frequency of oscillation invoked. In particular, electron energies are maximized when $10 \leq \omega \leq 500$ and proton energies for frequencies less than $\omega = 1$. This finding might bear on the apparent variation of electron/proton ratios in flares (Murphy and Ramaty 1987) and the phenomenon of 'electron-only' flares (Rieger, 1989). More definitive statements will need a proper treatment involving a more realistic wave.

It seems that electrons, when they are accelerated, are accelerated more rapidly than protons, although numerical limitations prevented us from further investigating this possibility.

Svestka and Hick (1986) present an event with a correlation between the hard X-ray variation and radio noise storm variation. This could mean that the same population of electrons is causing them both. This population could result from small scale reconnection events in the corona after the main phase of a flare (in the case of the observation referenced here several hours after the flare), with fast particles possibly produced as in this chapter. In the solar corona neutral points or sheets must join smoothly on to their surroundings. As a result, if electrons start to move adiabatically at quite low field strength, they may face an 'uphill battle' trying to proceed to the wider corona. Non- to mildly- relativistic electrons accelerated at a neutral point will possibly encounter very large mirror ratios, which will contain them in the corona. We suggest that this may offer an explanation of coronal

hard X-ray sources (Hudson 1978, Tsuneta at al 1984), addressing both acceleration and effective containment. We investigate this possibility in MacKinnon and Petkaki (1995).

Chapter 4

Analytical and Numerical Evaluation of an MHD Disturbance in an X-type Neutral Point

In this chapter we formally derive an analytical description for the time and space dependence of a linear incompressible, azimuthally symmetric disturbance propagating in a medium with a neutral point. We use this description to study the detailed form and behaviour of reconnective eigenfunctions, as a preliminary to addressing particle orbits. In the next chapter we study particle orbits in the presence of such a disturbance, and consider the fast particle distributions produced and the timescales involved. The description of the disturbance involves an arbitrary scalar resistivity, and the Chapter 6 attempts its self-consistent evaluation.

4.1 Background and Assumptions

In the previous chapter we studied charged particle orbits in a general way, in prescribed electromagnetic fields. Here we are going to use the analysis of Craig and McClymont to study the consequences for particle orbits from the relaxation of a perturbed potential magnetic field containing an X-type neutral point. Because of the azimuthal symmetry

of the system being considered it is convenient to use a cylindrical system of coordinates. The magnetic field is as before 2-D and the field lines are anchored at the boundary. In the equations of MHD we ignore gas pressure and viscosity. The resistivity of the medium is assumed constant and the mass density uniform. In the first instance we assume that such a scalar resistivity adequately describes the collisionless 'inertial' resistivity operating at the neutral point.

In deriving the expression for the magnetic disturbance we follow Craig and McClymont (1991) and Craig (1994) fairly closely, major differences being: recasting of the problem in our set of dimensionless variables, for consistency with the integration of the particle orbits, and some slight restriction on the possible modes of interest, with the consequence that the final, hypergeometric function form of the solution is always exact (cf. Craig, 1994). Also there is a heavier emphasis here than in other work on numerically evaluating the eigenfunctions.

4.2 Formulation of Equations

As we said the formula that gives the equilibrium magnetic field containing an X-type neutral point is

$$\underline{\mathrm{B}} = \frac{B_o}{D}(y\hat{x} + x\hat{y}). \tag{4.1}$$

The calculations that we want to do are easier in cylindrical coordinates. It will turn out that it is easier for example to use the method of separation of variables.

In polar coordinates we have:

$$x = r\cos\phi \tag{4.2}$$

$$y = r\sin\phi \tag{4.3}$$

and also

$$\hat{r} = \cos\phi\hat{x} + \sin\phi\hat{y} \tag{4.4}$$

$$\hat{\phi} = -\sin\phi\hat{x} + \cos\phi\hat{y}. \tag{4.5}$$

So in cylindrical coordinates

$$\underline{\mathrm{B}} = \frac{B_o}{D}r(sin2\phi\hat{r} + \cos 2\phi\hat{\phi}). \tag{4.6}$$

The magnetic field can be given by the curl of a vector potential

$$\underline{\mathrm{B}} = \frac{B_o}{D}\nabla \times \underline{\mathrm{A}} \tag{4.7}$$

where $\underline{\mathrm{A}} = \Psi\hat{z}$ because our system is essentially a 2-D one, z being an ignorable coordinate. One can easily prove that the potential giving the field (4.6) is

$$\Psi = -\frac{r^2}{2}\cos 2\phi + \nabla\psi \tag{4.8}$$

where ψ is a scalar potential. So, the magnetic field is

$$\underline{\mathrm{B}} = \frac{B_o}{D}\nabla \times \Psi\hat{z}. \tag{4.9}$$

I am going to use the vector potential to rewrite the induction equation and the momentum equation. First we make these two equations dimensionless. The induction equation is:

$$\frac{\partial \underline{\mathrm{B}}}{\partial t} = \nabla \times (\underline{\mathrm{u}} \times \underline{\mathrm{B}}) + \frac{c^2}{4\pi\sigma}\nabla^2\underline{\mathrm{B}}. \tag{4.10}$$

The quantity

$$\eta = \frac{c^2}{4\pi\sigma} \tag{4.11}$$

we call here the resistivity of the medium (usually the resistivity is defined as $\eta = 1/\sigma$). σ is the conductivity of the medium. The velocity is again normalized to the speed of light *for consistency with the previous calculations.* The normalization of distance and time is so that $c = d_p/\tau_p$ (please see chapter 3). As before a tilde above a quantity means that it is normalised. So, the induction equation becomes

$$\frac{\partial \tilde{B}}{\partial \tilde{t}} = \nabla \times (\tilde{u} \times \tilde{B}) + \frac{\eta}{cd_p}\nabla^2\tilde{B}. \tag{4.12}$$

The quantity

$$\tilde{\eta} = \frac{\eta}{cd_p} \tag{4.13}$$

is the dimensionless resistivity which is something like the magnetic Reynolds number only the velocity is the speed of light and the size of the region is our distance unit. We will get back to this later.

We substitute in eq. (4.12) the magnetic field in the form of eq. (4.9). After using the following vector identities

$$\mathbf{A} \times (\mathbf{B} \times \mathbf{C}) = (\mathbf{A} \cdot \mathbf{C})\mathbf{B} - (\mathbf{A} \cdot \mathbf{B})\mathbf{C} \tag{4.14}$$

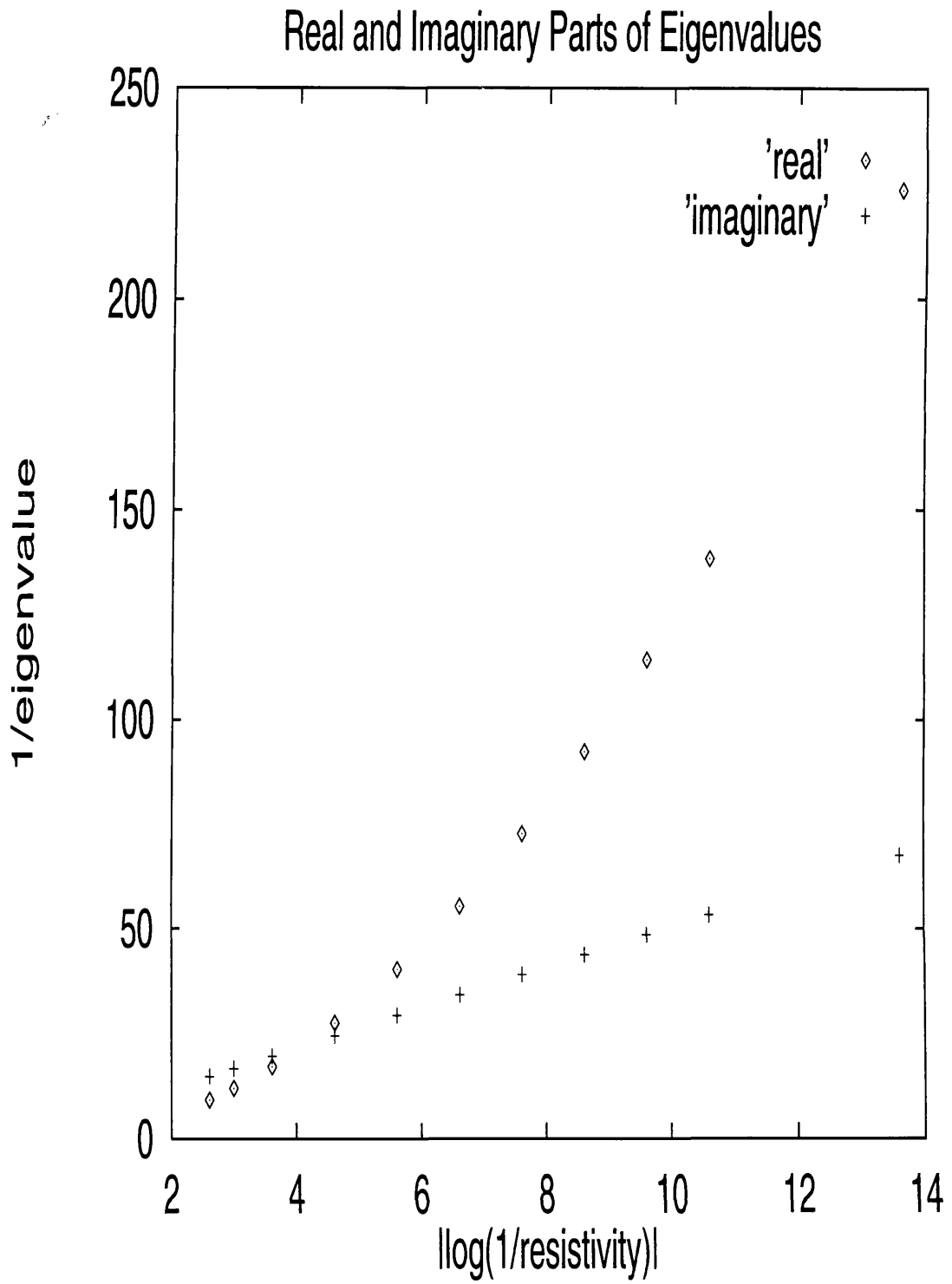

Figure 4.1: Plot of the $1/\kappa$ (i.e. 'damping time') and $1/\omega$ (i.e. frequency) versus $\mid 1/\log \eta \mid$ for n=0.

and

$$\nabla \times \nabla\phi = 0, \tag{4.15}$$

the fact that Ψ has only a **z**-component, and after integration over a surface **S** we get the following equation

$$\frac{\partial \Psi}{\partial t} + \tilde{u} \cdot \nabla\Psi = \tilde{\eta}\nabla^2\Psi \tag{4.16}$$

where a potential function that is added in the right hand side of eq. (4.16) is ignored. By using the Lagrangian time derivative eq. (4.16) becomes

$$\frac{D\Psi}{Dt} = \tilde{\eta}\nabla^2\Psi. \tag{4.17}$$

The fluid momentum equation in the absence of an electric field is

$$\rho\frac{d\underline{u}}{dt} = \frac{1}{c}\underline{j} \times \underline{B}. \tag{4.18}$$

This equation in dimensionless variables gives

$$\frac{d\tilde{u}}{d\tilde{t}} = \mathcal{A}\nabla \times \tilde{B} \times \tilde{B} \tag{4.19}$$

where the constant $\mathcal{A}$ is

$$\mathcal{A} = \frac{{u_A}^2}{c^2}\frac{{d_p}^2}{D^2}. \tag{4.20}$$

Here u_A is the Alfvén velocity at the boundary of the system. Typically we take $B_o = 100$ gauss and the number density $n = 10^{10}cm^{-3}$ (see also chapter (6).

The current density is given by

$$\underline{j} = \frac{c}{4\pi}\nabla \times \underline{B} \tag{4.21}$$

and after substituting (4.9) it becomes in dimensionless form

$$\tilde{j} = \nabla \times \tilde{B} = -\nabla^2\Psi\hat{z}. \tag{4.22}$$

So the right hand side of eq. (4.19) becomes

$$\nabla \times \tilde{B} \times \tilde{B} = -\nabla^2\Psi\nabla\Psi. \tag{4.23}$$

So the dimensionless equation of motion after inserting the vector potential becomes

$$\frac{D\tilde{u}}{D\tilde{t}} = -\mathcal{A}\nabla^2\Psi\nabla\Psi. \tag{4.24}$$

We are going now to make a linear expansion of equations (4.17) and (4.24). Let's assume that

$$\Psi = \Psi_o + \Psi_1 \tag{4.25}$$

where Ψ_1 is a first order term. We do the same with the fluid velocity u,

$$u = u_o + u_1 \tag{4.26}$$

only here we know that the system starts from equilibrium so that $u_o = 0$. By using the following facts

$$\frac{\partial \Psi_o}{\partial t} = 0 \tag{4.27}$$

$$\nabla^2 \Psi_o = 0, \tag{4.28}$$

ignoring second order terms and writing out fully the Lagrangian derivative we get from eq. (4.17)

$$\frac{\partial \Psi_1}{\partial t} + (u_1 \cdot \nabla)\Psi_o = \tilde{\eta}\nabla^2 \Psi_1. \tag{4.29}$$

Now we take the time derivative of eq. (4.29) which gives

$$\frac{\partial^2 \Psi_1}{\partial t^2} + (\dot{u_1} \cdot \nabla)\Psi_o = \tilde{\eta}\nabla^2 \dot{\Psi}_1. \tag{4.30}$$

We go back now to eq. (4.24) and write out fully the Lagrangian derivative in the left hand side

$$\frac{\partial \tilde{u}}{\partial \tilde{t}} + (\tilde{u} \cdot \nabla)\tilde{u} = -\mathcal{A}\nabla^2 \Psi \nabla \Psi. \tag{4.31}$$

But we have

$$\tilde{u} = \tilde{u}_1 \tag{4.32}$$

and if we make a linear expansion of eq. (4.31) we get

$$\frac{\partial \tilde{u}_1}{\partial \tilde{t}} = -\mathcal{A}\nabla^2 \Psi_1 \nabla \Psi_o. \tag{4.33}$$

So now combining eq. (4.30) and (4.33) we get

$$\frac{\partial^2 \Psi_1}{\partial t^2} - (\mathcal{A}\nabla^2 \Psi_1 \nabla \Psi_o \cdot \nabla)\Psi_o = \tilde{\eta}\nabla^2 \dot{\Psi}_1. \tag{4.34}$$

Obviously

$$(\nabla \Psi_o \cdot \nabla)\Psi_o = |\nabla \Psi_o|^2, \tag{4.35}$$

so eq. (4.34) with eq. (4.35) gives

$$\frac{\partial^2\Psi}{\partial t^2} - \tilde{\eta}\nabla^2\dot{\Psi} = \mathcal{A}|\nabla\Psi_o|^2\nabla^2\Psi. \tag{4.36}$$

Now

$$|\nabla\Psi_o|^2 = \tilde{r}^2 \tag{4.37}$$

so, the final equation which we will be trying to find solutions to is

$$\frac{\partial^2\Psi}{\partial t^2} - \tilde{\eta}\nabla^2\dot{\Psi} = \mathcal{A}\tilde{r}^2\nabla^2\Psi, \tag{4.38}$$

where we have dropped the suffix 1 and Ψ will denote the perturbed potential from now on.

4.2.1 Solutions

I am going to look for solutions of eq. (4.38) of the following form

$$\Psi = e^{\lambda t}f(r)e^{im\phi}, \tag{4.39}$$

where we have dropped tildes from dimensionless quantities $t = \tilde{t}, \lambda$ is complex, $f(r)$ is complex and m is integer. We are going to insert this solution to eq. (4.38). We have

$$\ddot{\Psi} = \lambda^2 e^{\lambda t}f(r)e^{im\phi}, \tag{4.40}$$

$$\nabla^2\dot{\Psi} = (\frac{1}{r}\frac{\partial f}{\partial r} + \frac{\partial^2 f}{\partial r^2})\lambda e^{\lambda t}e^{im\phi} - \frac{m^2}{r^2}\lambda e^{\lambda t}f(r)e^{im\phi}, \tag{4.41}$$

and

$$\nabla^2\Psi = (\frac{1}{r}\frac{\partial f}{\partial r} + \frac{\partial^2 f}{\partial r^2})e^{\lambda t}e^{im\phi} - \frac{m^2}{r^2}e^{\lambda t}f(r)e^{im\phi}. \tag{4.42}$$

Combining eq. (4.40), (4.41), and (4.42) the following terms cancel

$$e^{\lambda t}e^{im\phi} \tag{4.43}$$

and we get after a bit of algebra

$$r^2(\frac{1}{r}\frac{df}{dr} + \frac{d^2 f}{dr^2}) = (\frac{\lambda^2 r^2}{\mathcal{A}r^2 + \tilde{\eta}\lambda} + m^2)f(r). \tag{4.44}$$

For $m = 0$ eq. (4.44) becomes

$$r(rf')' = (\frac{\lambda^2}{\mathcal{A} + \frac{\tilde{\eta}\lambda}{r^2}})f(r). \tag{4.45}$$

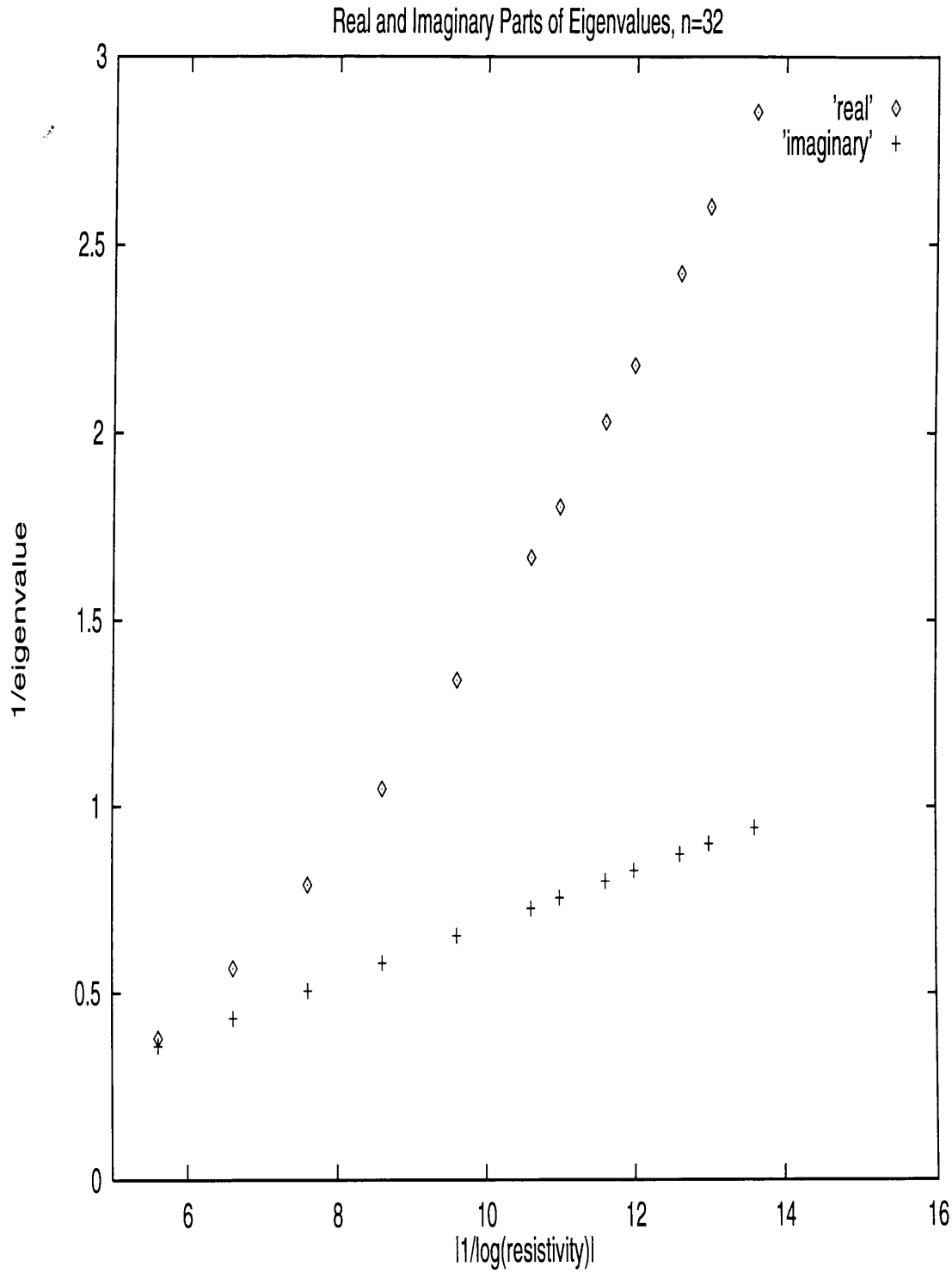

Figure 4.2: Plot of the $1/\kappa$ (i.e. damping time) and $1/\omega$ (i.e. frequency) versus $\mid 1/\log \eta \mid$ for n=32.

This equation governs the evolution of the radial component of the solution. Putting $m = 0$ we concentrate on those solutions that have no azimuthal dependence (because the ones with azimuthal dependence are not "reconnective" modes (Craig and McClymont 1991, 1993)). I am going to make the following change of variable

$$\frac{\mathcal{A}r^2}{\tilde{\eta}\lambda} = -z \tag{4.46}$$

where z is a complex variable. So, we have

$$\frac{df}{dr} = \frac{df}{dz}\frac{dz}{dr} = -\frac{2\mathcal{A}r}{\tilde{\eta}\lambda}\frac{df}{dz} \tag{4.47}$$

and

$$\frac{d^2f}{dr^2} = \frac{d^2f}{dz^2}(\frac{dz}{dr})^2 + \frac{df}{dz}\frac{d^2z}{dr^2} = \frac{d^2f}{dz^2}\frac{4\mathcal{A}^2r^2}{\tilde{\eta}^2\lambda^2} - \frac{2\mathcal{A}}{\tilde{\eta}\lambda}\frac{df}{dz}. \tag{4.48}$$

Combining eq. (4.47) and (4.48) we get

$$z(1-z)\frac{d^2f}{dz^2} + (1-z)\frac{df}{dz} = -\frac{\lambda^2}{4\mathcal{A}}f(z) \tag{4.49}$$

which has the same form as

$$z(1-z)\frac{d^2f}{dz^2} + (c-(\alpha+\beta+1)z)\frac{df}{dz} = \alpha\beta f(z) \tag{4.50}$$

which is the general form of the hypergeometric equation. By comparing (4.49) and (4.50) we see that

$$c = 1 \tag{4.51}$$

and

$$\alpha + \beta + 1 = 1 \tag{4.52}$$

so that

$$\alpha = -\beta. \tag{4.53}$$

Also by comparing the right hand side of eq. (4.49) and (4.50) we see that

$$\alpha\beta = -\frac{\lambda^2}{4\mathcal{A}}. \tag{4.54}$$

In general we have complex numbers so,

$$\alpha = \rho + i\xi \tag{4.55}$$

$$\beta = -(\rho + i\xi) \tag{4.56}$$

$$\lambda = -\kappa + i\omega. \tag{4.57}$$

From the previous formulae it can be easily seen that

$$\alpha^2 = \frac{\lambda^2}{4\mathcal{A}} \tag{4.58}$$

so that

$$(\rho + i\xi)^2 = \frac{(-\kappa + i\omega)^2}{4\mathcal{A}}. \tag{4.59}$$

If we equate the real and imaginary parts of eq. (4.59) we get the following formulae for ρ, ξ, κ, and ω

$$\rho^2 - \xi^2 = \frac{\kappa^2 - \omega^2}{4\mathcal{A}} \tag{4.60}$$

$$\rho\xi = -\frac{\kappa\omega}{4\mathcal{A}}. \tag{4.61}$$

When these equations are solved for ρ and ξ we get

$$\alpha = -\frac{\kappa}{2\sqrt{\mathcal{A}}} + i\frac{\omega}{2\sqrt{\mathcal{A}}} \tag{4.62}$$

$$\beta = \frac{\kappa}{2\sqrt{\mathcal{A}}} - i\frac{\omega}{2\sqrt{\mathcal{A}}} \tag{4.63}$$

So the solution is ${}_2F_1(\alpha, \beta, c, z)$ with α, β, c and, z given by the previous equations. Henceforth we write

$$f(r) = {}_2F_1(\alpha, \beta, c, z(r)) = f_{Re}(r) + if_{Im}(r) \tag{4.64}$$

where f_{Re} and f_{Im} are real valued functions. At $r = 0$, the boundary condition, that f remains finite, is guaranted by the adopted ${}_2F_1$ form of the solution. At $r = 1$ the boundary condition

$$\Psi = 0 \tag{4.65}$$

determines the value of κ and ω.

4.3 Calculation of the resistivity

A very important physical quantity here is the resistivity. It is this that allows magnetic field lines to reconnect. We are assuming that the medium is collisionless. So, we cannot use the collisional resistivity as given for example by Spitzer (1962). Collisional resistivity depends only on the electron mass

$$\eta = \frac{m_e c^2 \nu}{n_e e^2} \tag{4.66}$$

where ν is the collision frequency.

In chapter (6) we attempt to find a value of resistivity by demanding consistency between single particle and MHD approaches. Here we are concerned only with the particle acceleration consequences of a reconnective disturbance, so we need only a rough estimate of the likely order of magnitude of the resistivity.

We estimate the resistivity in the following way. Instead of calculating the time between collisions we calculated the time a particle of 1 KeV takes to cross the neutral point once, i.e. to cross the adiabaticity area around the neutral point as given by eq. (3.33). From equations (4.11) and (4.13) and our form of making the physical quantities dimensionless, we see that

$$\tilde{\eta} = \frac{1}{4\pi\sigma\tau_p}. \tag{4.67}$$

Now σ is given by

$$\sigma = \frac{ne^2}{m_e}t \tag{4.68}$$

as proven by Speiser (1965), where t is the crossing time in the nonadiabatic region. We use these rough estimates to get an idea of the order of magnitude of the resistivity of the plasma in the reconnection region. If in the formula (4.68) we use the proton mass instead of the electron as Burkhart et al. (1990) do, then the value of the resistivity is much larger (m_p/m_e times larger). The way we estimated the resistivity here gives a serious underestimate of the value of the resistivity, as we will see later. This is because particles cross the neutral point area more than once.

Particle orbits' details will show that some of them get trapped around the neutral point, instead of just simply transversing it. The value of the resistivity that we get for 1 KeV proton (when the electron mass is used in (4.68)) is $\tilde{\eta} = 1.7 \times 10^{-14}$ in our dimensionless units. The value of the resistivity that we get for 1 KeV proton (when the proton mass is used in (4.68)) is $\tilde{\eta} = 3.1724 \times 10^{-11}$ in our dimensionless units. The value of the resistivity for 1 KeV electron is $\tilde{\eta} = 2.08 \times 10^{-10}$ in our dimensionless units.

4.4 Numerical Method

To calculate the eigenmodes using the hypergeometric function required very tedious numerical work. First of all one should evaluate the hypergeometric function. The hypergeometric function is defined by using the analytic continuation of the hypergeometric series

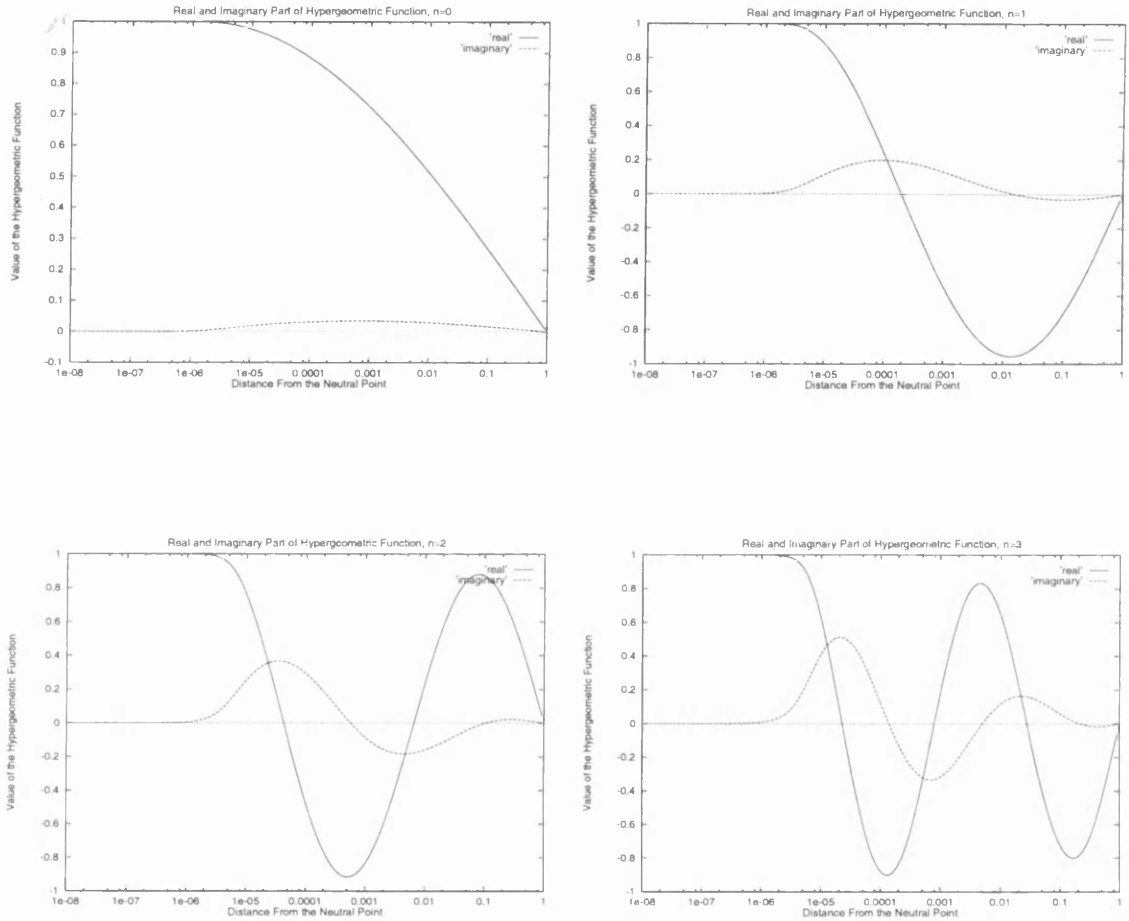

Figure 4.3: The hypergeometric function is shown for the first four eigenvalues for $\eta = 3.1724 \times 10^{-11}$. Both the real and the imaginary part of the hypergeometric function are shown for each eigenvalue. The boundary is at r=1.

(Abramovitz and Stegun, 1964),

$$
\begin{aligned}
{}_2F_1(\alpha,\beta,c,z) &= 1+\frac{\alpha\beta}{c}\frac{z}{1!}+\frac{\alpha(\alpha+1)\beta(\beta+1)}{c(c+1)}\frac{z^2}{2!}+\cdots \\
&\quad +\frac{\alpha(\alpha+1)\ldots(\alpha+j-1)\beta(\beta+1)\ldots(\beta+j-1)}{c(c+1)\ldots(c+j-1)}\frac{z^j}{j!}+\cdots
\end{aligned}
\tag{4.69}
$$

Then we need to find the values of κ and ω for which

$$
{}_2F_1(\alpha,\beta,c,z)=0 \tag{4.70}
$$

at the boundary with α, β and c given by (4.62), (4.63), and (4.51). Using some initial guess of those values one can find the eigenvalues of the hypergeometric function for different values of the resistivity. The value of the hypergeometric function has to be zero at the boundary ($r=1$) and equal to one at the centre ($r=0$). Since the hypergeometric function is complex, a system of two equations has to be solved to find the eigenvalues.

$$
\begin{aligned}
Re({}_2F_1(\alpha,\beta,c,z)) &= 0 \\
Im({}_2F_1(\alpha,\beta,c,z)) &= 0
\end{aligned}
\tag{4.71}
$$

where z is evaluated at $r=1$. We solve this system of equations by using Broyden's method as implemented by Press et al. (1992). This is a global method for solving systems of nonlinear equations when the analytic derivatives are not available. This method uses an approximation to the Jacobian. Such methods are also called secant methods since they reduce to the secant method in one dimension.

4.5 Behaviour of the Solution

Fundamental solutions of eq. 4.49 are those which are zero at the boundary. Assuming completeness, all other solutions can be constructed in terms of those (eg Roach 1982 and Craig and McClymont (1993) regarding completeness). The boundary is at distance

$$
r_b=\frac{D}{d_p}\simeq 178 \tag{4.72}
$$

in our dimensionless units. In most of the graphs that follow, though most distances are normalised to D the size of the system. The real part has the values $f_R(1)=0$ and $f_R(0)=1$. The imaginary part is $f_I(1)=0$ and $f_I(0)=0$. These are the boundary

conditions used to calculated the eigenvalues. Distance equal to 1 corresponds to the outer limit of the area in consideration and value equal to zero is the neutral point.

The graphs discussed in this section show the behaviour of the real and imaginary part of the hypergeometric function. For each value of the parameter η we get different eigenvalues. In figure (4.1) we have plotted the inverse of the real and imaginary part of the eigenvalues of the system. κ is the real part of the eigenvalue and is the dissipation term. ω is the imaginary part of the eigenvalue and is the oscillatory term. All the eigenvalues are for the fundamental (n=0), for different values of the resistivity η. As one can see from this graph there is a value of the resistivity beyond which dissipation effects dominate over the oscillatory behaviour. In figure (4.2) we see the same behaviour but for eigenvalues of order n=32.

In fig. (4.3) we see the hypergeometric function for the first four ($n = 0$ to $n = 3$) eigenvalues for $\eta = 3.1724 \times 10^{-11}$ (this is the value of the dimensionless resistivity). As n increases the eigenvalues get closer and closer together (see tables (4.1) and (4.2). Energy considerations will fix the amplitude of the disturbance (see chapter 6), which is a free parameter.

n	κ	ω
0	0.0072244	0.11774
1	0.02345	0.36797
2	0.04013	0.62336
3	0.05688	0.88031
14	0.25181	3.76103
15	0.27042	4.02792
22	0.40338	5.91417
28	0.52046	7.55169
32	0.59982	8.65208
33	0.61981	8.92812
34	0.63985	9.20459
35	0.65995	9.48138

Table 4.1: Eigenvalues of the hypergeometric function for $\eta = 3.1724 \times 10^{-11}$

In fig. (4.4) the hypergeometric function is plotted versus the distance from the neutral point, for the first four eigenvalues. The function is calculated for different resistivities. As the resistivity increases, so does the size of the diffusion region where dissipation is important. In figures (4.5) and (4.6) the hypergeometric function is plotted versus distance from the neutral point for higher eigenvalues (n=22, n=28, n=32 and n=50). Both the

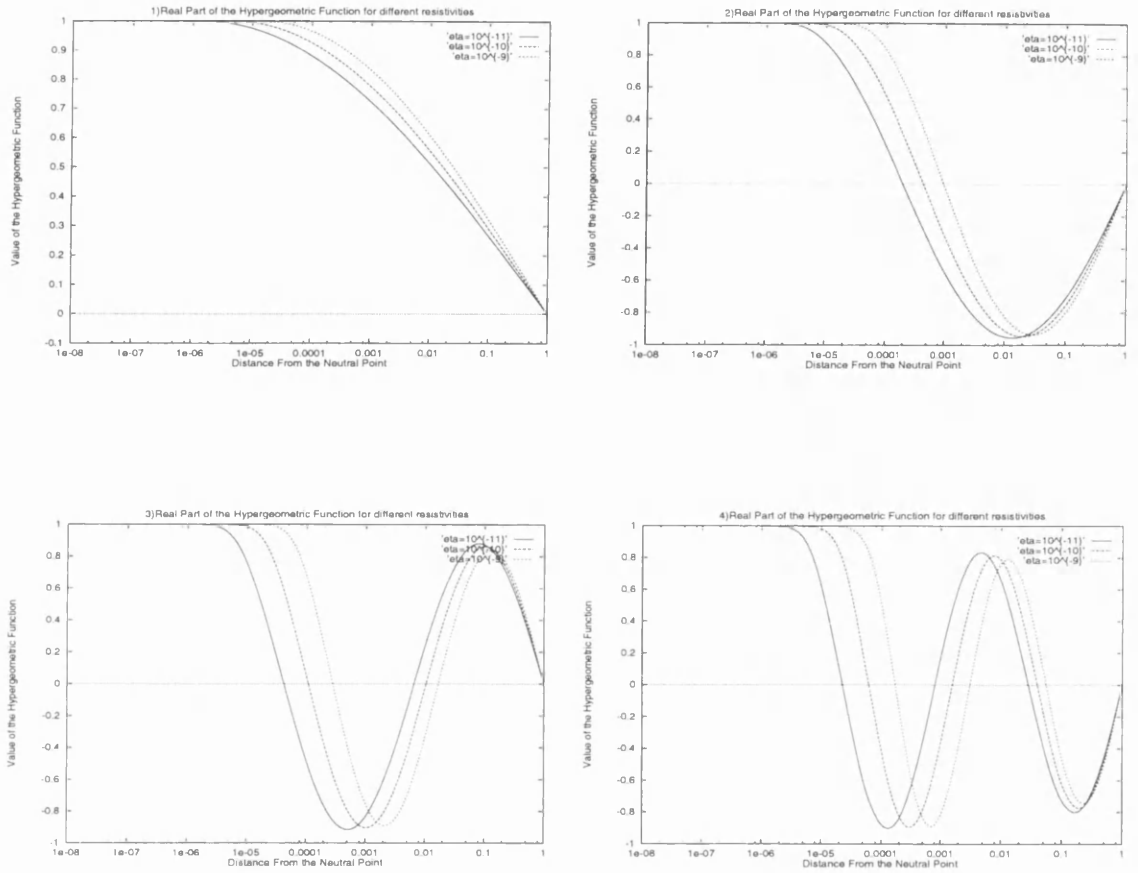

Figure 4.4: The hypergeometric function is shown for the first four eigenvalues for $\eta = 3.1724 \times 10^{-11}$ (eta=10(-11) curve), $\eta = 3.1724 \times 10^{-10}$ (eta=10(-10) curve), and $\eta = 3.1724 \times 10^{-9}$ (eta=10(-9) curve). The value of the resistivity is given in our dimensionless units. The real part of the hypergeometric function is shown here. As the resistivity increases so does the size of the diffusion region where dissipation is important. The boundary is at r=1. In graph 1) we the real part of the hypergeometric function for n=0, in graph 2) for n=1, in graph 3) for n=2, and for graph 4) for n=3.

n	κ	ω
0	0.01375	0.16104
1	0.07821	0.86674
4	0.14475	1.58624
15	0.55463	5.70483
20	0.75683	7.64675
24	0.88149	8.82694
26	0.96583	9.61923
27	1.00834	10.0169
31	1.22410	12.0195
32	1.26786	12.4226

Table 4.2: Eigenvalues of the hypergeometric function for $\eta = 3.1724 \times 10^{-8}$

real and the imaginary part are shown. As n increases the eigenvalues get closer and closer together.

In fig. (4.7) we plot the real part of the hypergeometric function against distance from the neutral point for resistivity values a) $\eta = 3.1724 \times 10^{-6}$ and b) $\eta = 3.1724 \times 10^{-7}$ and for n=32. As the resistivity increases one sees the increase in the magnitude of the spatial fluctuations and also the fact that the dissipation becomes important at a bigger distance from the neutral point.

4.6 Model Electric and Magnetic fields

Once the hypergeometric function is calculated we can use the eigenmodes to calculate the perturbation in the magnetic field and the induced electric field. First calculate the electric field from Faraday's law

$$\nabla \times \underline{\mathrm{E}} = -\frac{1}{c}\frac{\partial \underline{\mathrm{B}}_1}{\partial t} \tag{4.73}$$

where

$$\underline{\mathrm{B}}_1 = \nabla \times \Psi \hat{z}. \tag{4.74}$$

is the perturbation. After integration of the two sides of equation (4.74) the electric field reads

$$\underline{\mathrm{E}} = -\frac{1}{c}\frac{\partial \Psi}{\partial t}\hat{z} \tag{4.75}$$

and in dimensionless form

$$\tilde{E} = -\frac{B_o d_p}{E_o D}\frac{\partial \Psi}{\partial t}\hat{z}. \tag{4.76}$$

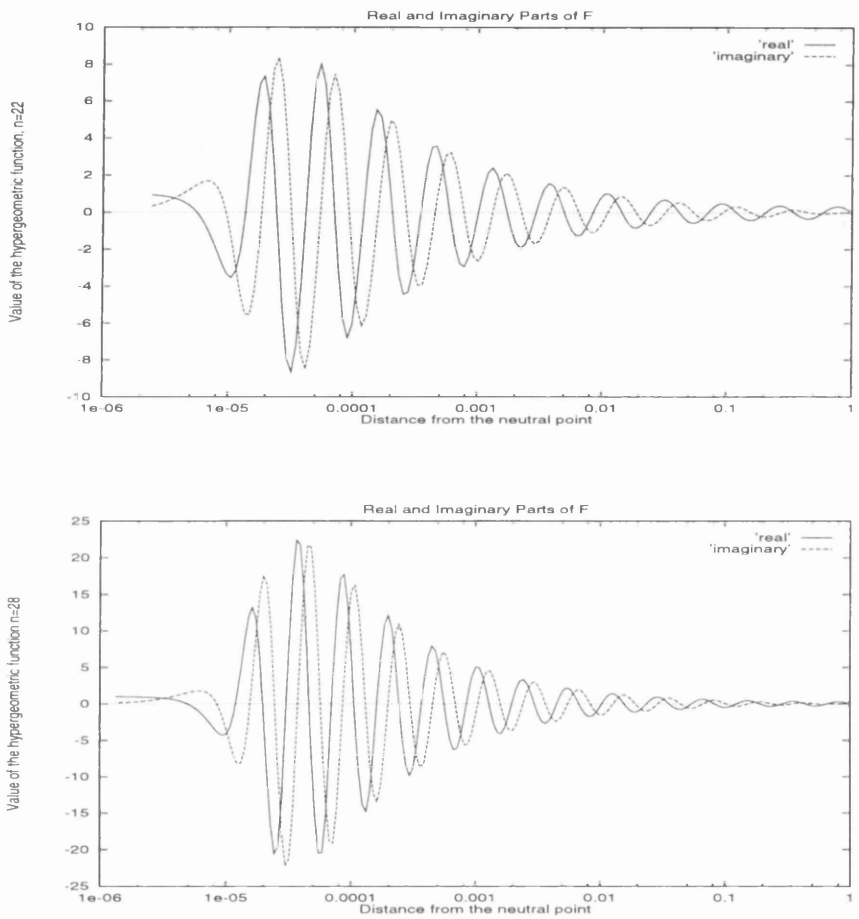

Figure 4.5: The eigenvalues of the hypergeometric function for $\eta = 3.1724 \times 10^{-11}$ n=22 (top) and n=28 (bottom). Both the real and imaginary part of the hypergeometric function are shown here. The boundary is at r=1.

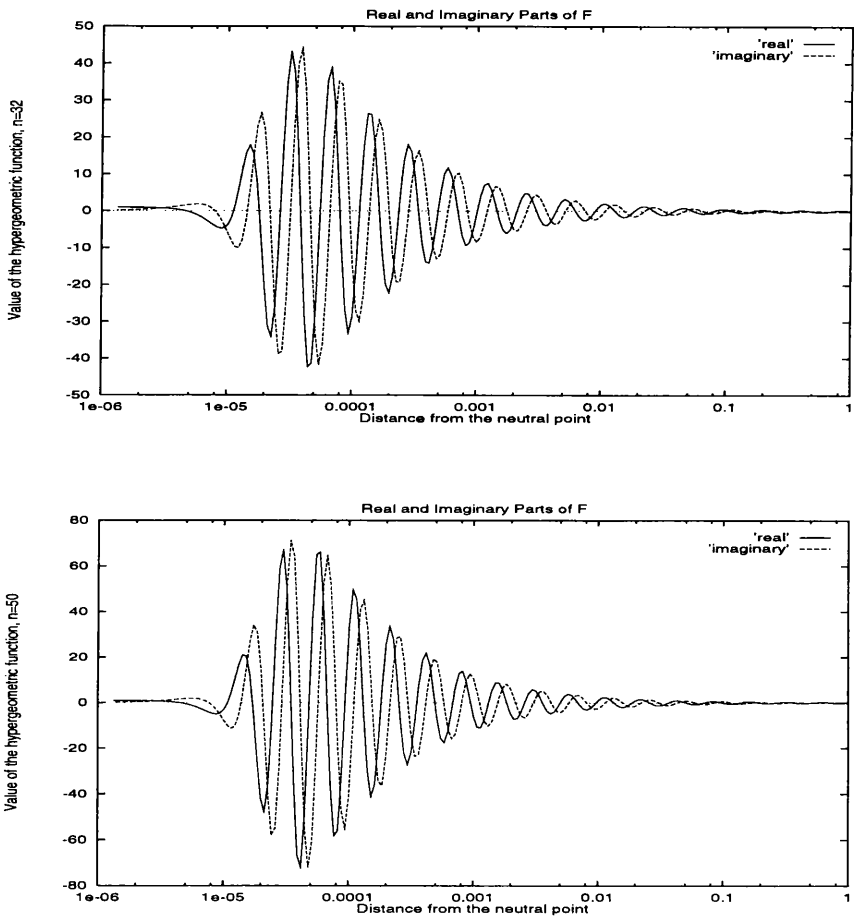

Figure 4.6: The eigenvalues of the hypergeometric function for $\eta = 3.1724 \times 10^{-11}$ n=32 (top) and n=50 (bottom) in our dimensionless units. The real and imaginary parts are shown here. The boundary is at r=1.

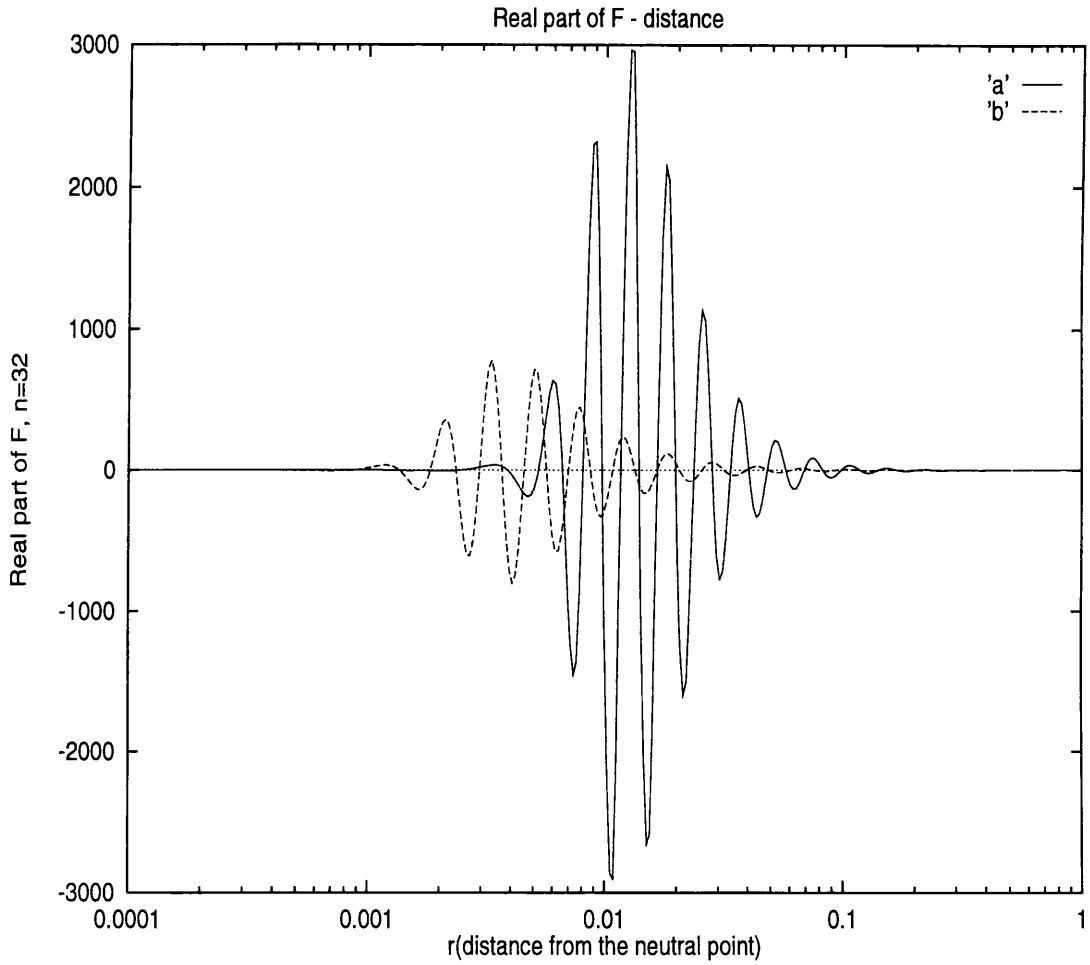

Figure 4.7: The values of the real part of the hypergeometric function for a) $\eta = 3.1724 \times 10^{-6}$ and b) $\eta = 3.1724 \times 10^{-7}$ for n=32. The boundary is at r=1.

A potential term should be added here but because of our initial conditions it is zero (no electric field present initially). So, an electric field is present in the Z direction whose form is given by

$$E_z = \frac{B_o d_p}{E_o D} \exp(-\kappa t)[\kappa(\cos(\omega t) f_{Re} - \sin(\omega t) f_{Im}) + \omega(\cos(\omega t) f_{Im} + \sin(\omega t) f_{Re})] \quad (4.77)$$

where $\Psi = \exp(\lambda t) f$ since we ignore the azimuthal dependence. Equation (4.77) is the real part only.

The components of the magnetic field perturbation are then given by

$$B_{1x} = -\frac{y}{2\eta} \exp(-\kappa t)[\kappa(\cos(\omega t) f'_{Re} - \sin(\omega t) f'_{Im}) + \omega(\sin(\omega t) f'_{Re} + \cos(\omega t) f'_{Im})] \quad (4.78)$$

and

$$B_{1y} = \frac{x}{2\eta} \exp(-\kappa t)[\kappa(\cos(\omega t) f'_{Re} - \sin(\omega t) f'_{Im}) + \omega(\sin(\omega t) f'_{Re} + \cos(\omega t) f'_{Im})] \quad (4.79)$$

In fig. (4.8) we see the temporal evolution of the magnetic field perturbation at two different spatial points, at r=0 (top) which is the neutral point and at r=1 (bottom) which is the boundary. The size of the magnetic field is reduced dramatically at r=1. So the magnitude of the magnetic field at r=1, has to be multiplied by 10^{12} for illustration purposes.

In fig. (4.9) we see the spatial evolution of the magnetic field perturbation for different phases during one period of oscillation. We see the magnetic field at T=0, T=1/4, T=1/2, T=3/4 and T=1, where T is the period of the oscillation.

In fig. (4.10) we see the magnetic field perturbation for $\eta = 3.1724 \times 10^{-11}$ and for eigenvalues n=0, n=3, n=15 and n=32.

In fig. (4.11) we see the spatial evolution of the electric field for $\eta = 3.1724 \times 10^{-11}$ and n=0, for different phases during one period of oscillation. We see the electric field at T=0, T=1/4, T=1/2, T=3/4 and T=1, where T is the period of the oscillation.

In fig. (4.12) we see the electric field for $\eta = 3.1724 \times 10^{-11}$ and for eigenvalues n=0, n=3, n=15 and n=32.

In chapter (5) we will see that the spatial structure of the magnetic and electric fields will complicate particle orbits beyond the 'simple', heuristic ones in chapter (3). In particular we will see that the magnetic perturbation tends to trap particles near the neutral point, enhancing the effective resistivity.

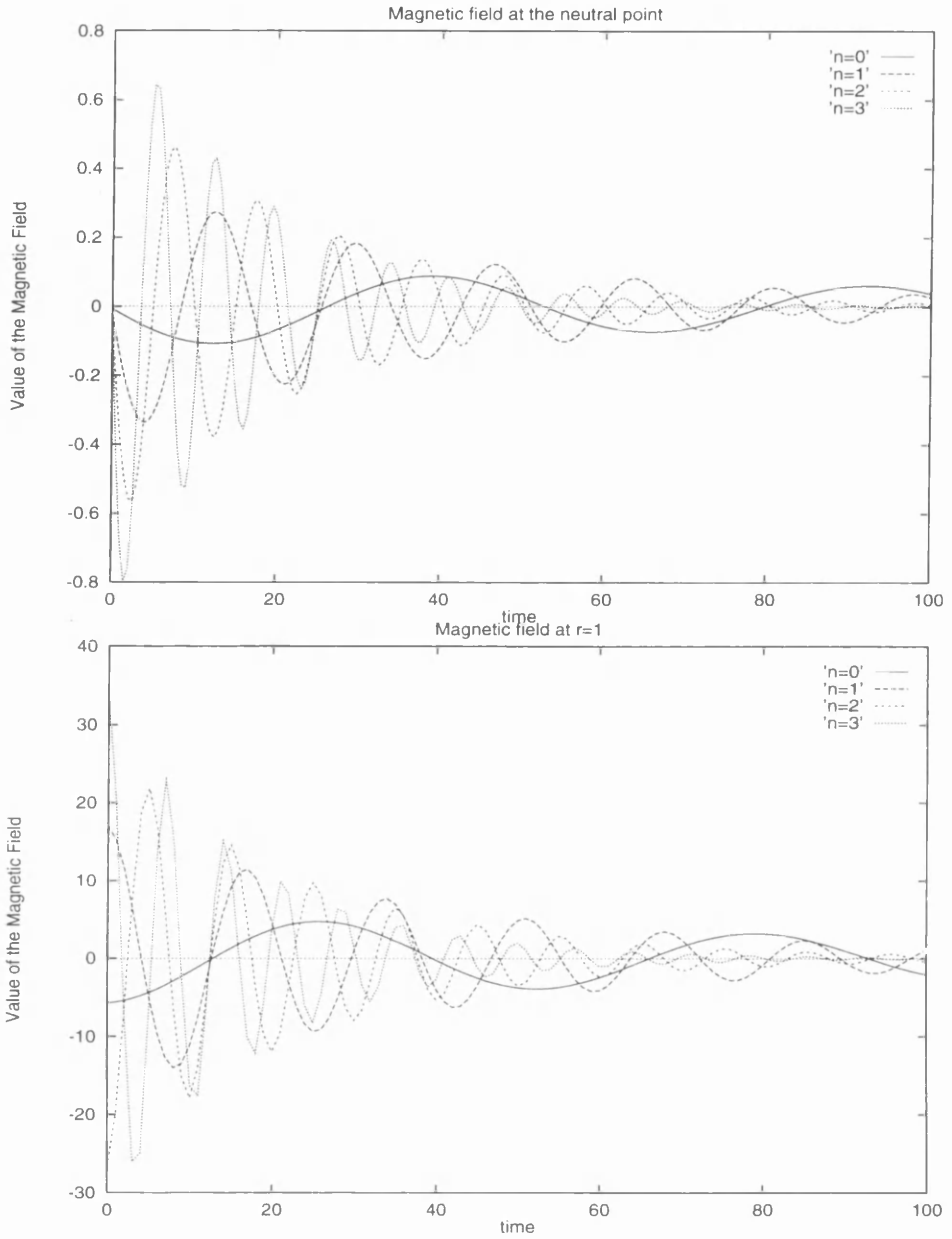

Figure 4.8: The time evolution of the magnetic field perturbation for $\eta = 3.1724 \times 10^{-11}$ and n=0,1,2,3 in our dimensionless units. The top graph is shows the behaviour of the magnetic field with time at r=0, the bottom at r=1. The values at r=1 are multiplied by 10^{12}. The perturbation amplitude decreases with time. This is due to the dissipation close to the neutral point.

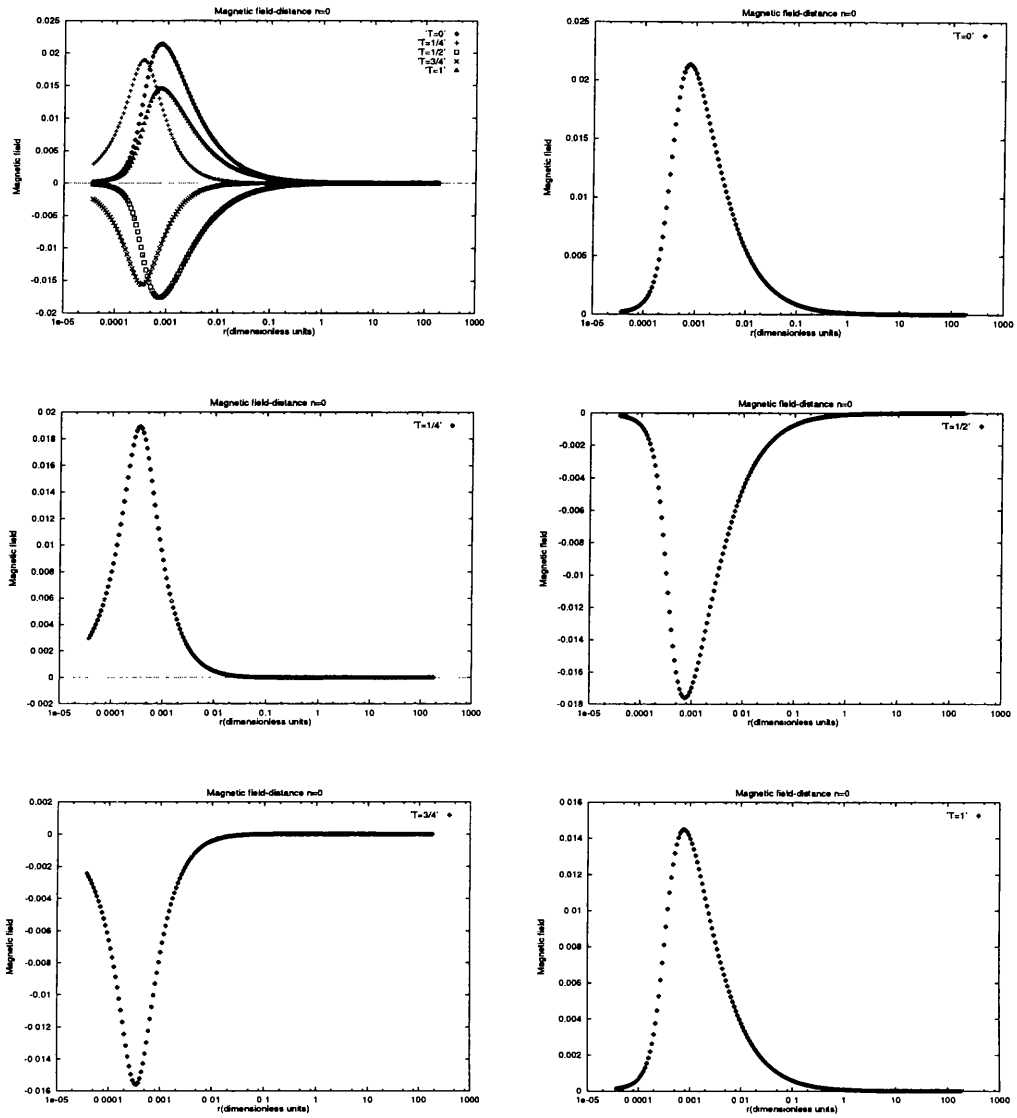

Figure 4.9: The spatial evolution of the magnetic field for $\eta = 3.1724 \times 10^{-11}$ and n=0. The distance is given in our dimensionless units. The magnetic field is shown in different phases. Its restriction to the vicinity of the neutral point, and also the damping effect can be seen. One period is shown, and times refer to phase of the period.

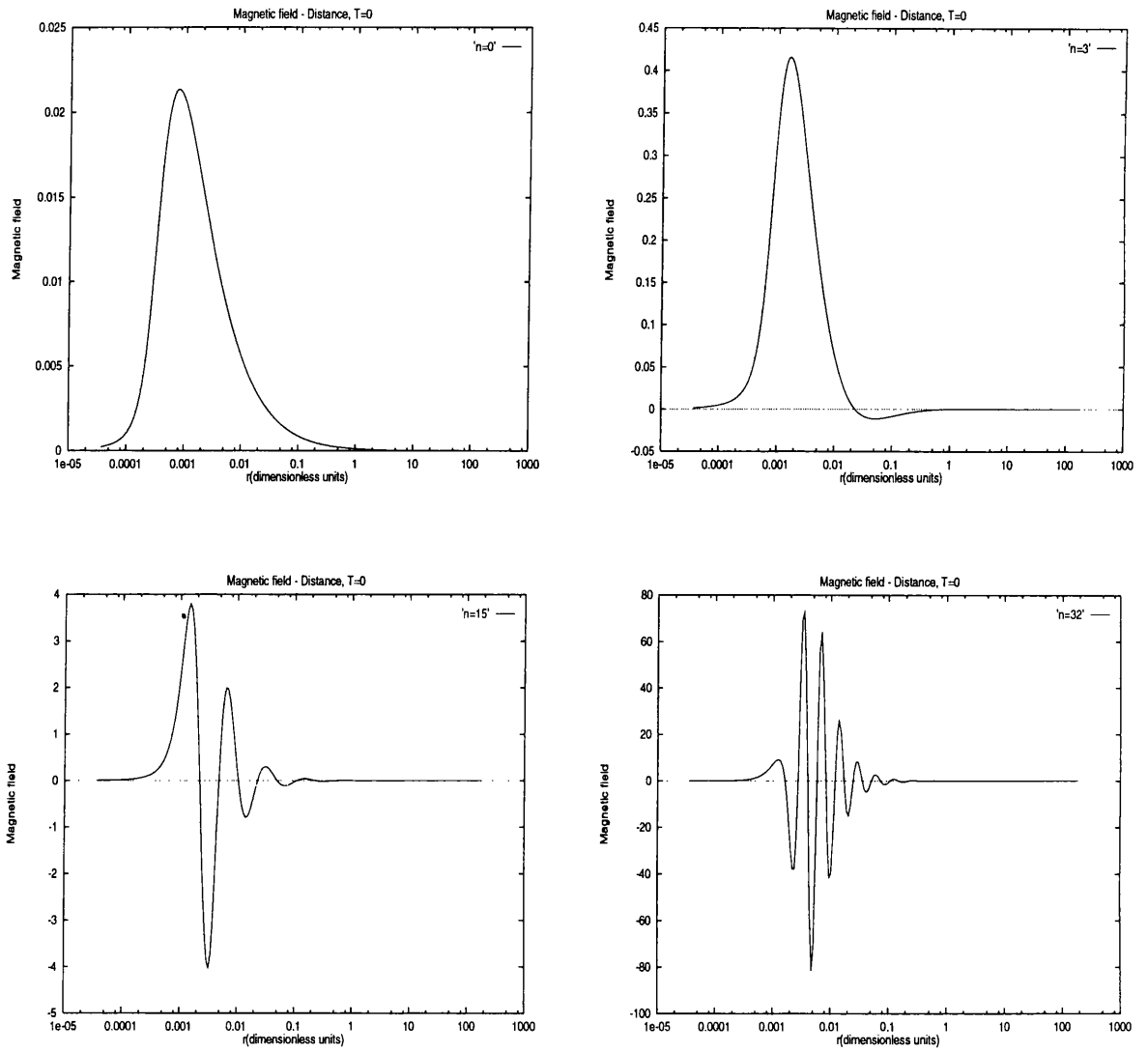

Figure 4.10: The spatial evolution of the magnetic field perturbation for $\eta = 3.1724 \times 10^{-11}$ and n=0, n=3, n=15 and n=32. The distance is given in our dimensionless units, so the boundary is at r=178. The restriction of the perturbation close to the neutral point can be seen.

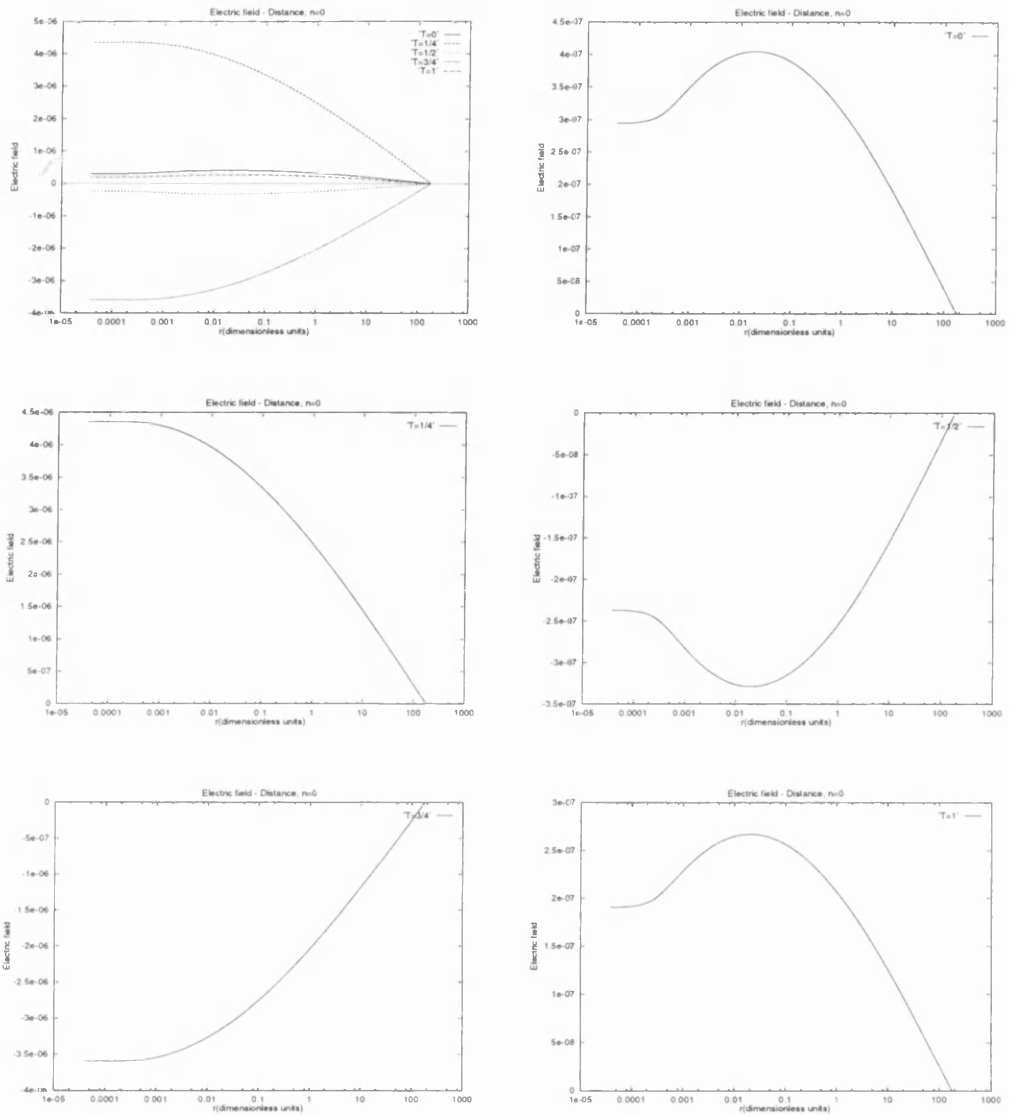

Figure 4.11: The spatial evolution of the electric field for $\eta = 3.1724 \times 10^{-11}$ and n=0. The distance is given in our dimensionless units, the boundary is at r=178. The electric field is shown in different phases. One can see the damping effect (the magnitude decreases with time). One period is shown, and times refer to phase of the period.

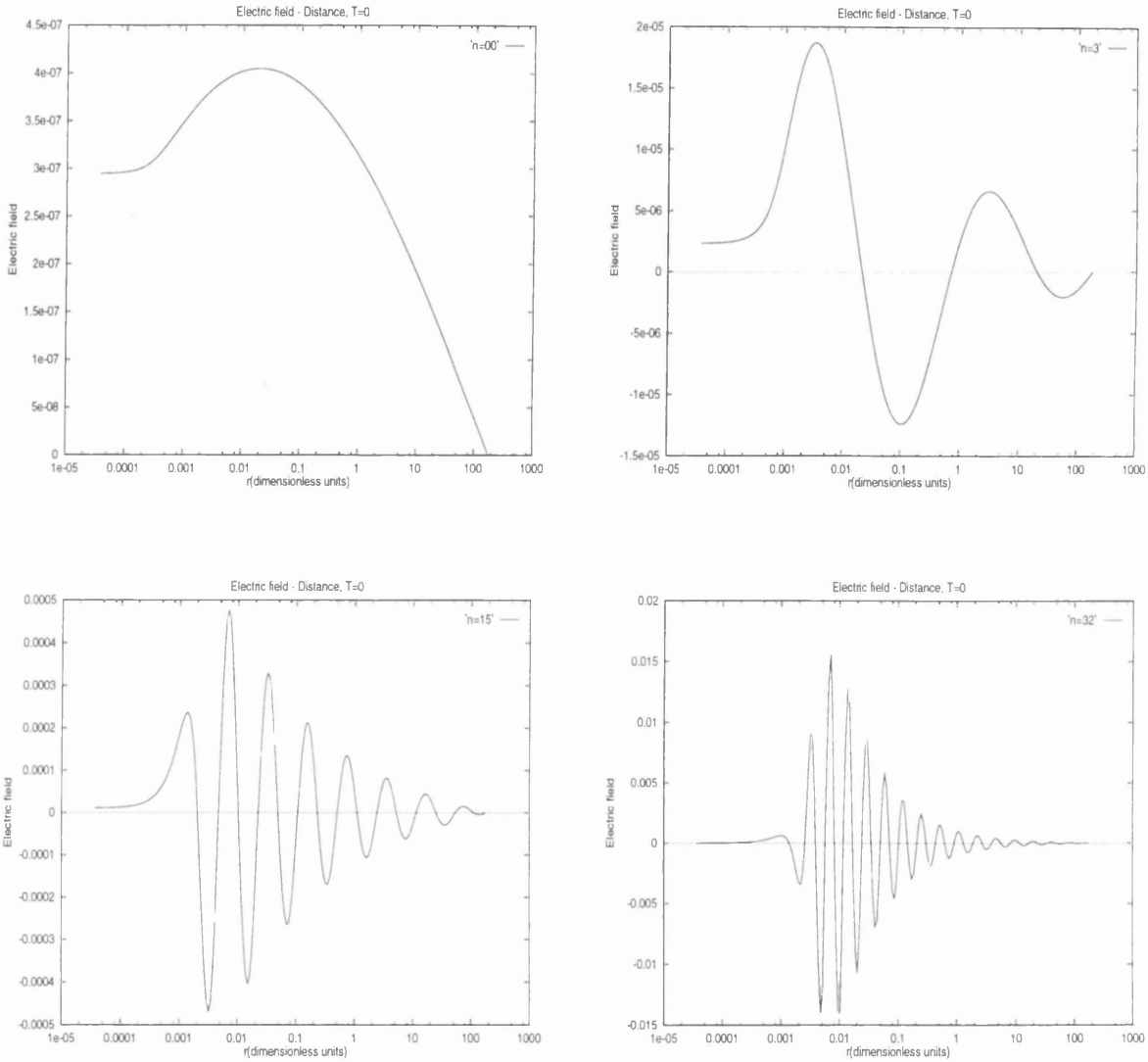

Figure 4.12: The spatial evolution of the electric field for $\eta = 3.1724 \times 10^{-11}$ and n=0, n=3, n=15 and n=32. The distance is given in our dimensionless units, so the boundary is at r=178.

4.7 Timescales

I am going to estimate the Alfvén wave travel time for the boundary to the diffusion region. Craig and McClymont (1991) give an estimate of the size of the diffusion region as

$$r_{diff} = a\eta^{1/2} \tag{4.80}$$

where a is of order unity and η is the resistivity and where the distance has been normalised to $D = 10^9$ cm. Then the crossing time is

$$t_A = \int_{r_{diff}}^{D} \frac{dr}{u_A} \tag{4.81}$$

where $u_A = B/\sqrt{(4\pi\rho)}$ is the Alfvén speed and $B = B_o r/D$ the magnitude of the magnetic field. So, the crossing time is

$$t_A = \sqrt{(4\pi\rho)}\frac{d}{B_o}[\ln D - \ln r_{diff}] \tag{4.82}$$

where r_{diff} is given in cm now. In table (4.3) we see the size of the diffusion region and the relevant crossing times for different values of the resistivity. The resistivity is given in our dimensionless units. Value of the dimensionless resistivity of 3.1724×10^{-11} corresponding to resistivity 7.436×10^{-14} sec. All the calculations of the resistivity and timescales are based on the assumption that the number density of the medium is 10^{10} protons cm^{-3}. When the density decreases so do the oscillation and decay times. All the calculations are done assuming $B_o = 100$ gauss at the boundary.

In table (4.4) we see the decay and oscillation times for different resistivities for n=0. As decay time I use the time for $\exp(-\kappa t) = 0.368$ (that is $t = 1/\kappa$). For $\eta = 3.1724 \times 10^{-4}$ the decay time is faster than the oscillation period. In fig. (4.5) we see the decay and oscillation times for different resistivities for n=32.

4.8 Conclusions and Discussion

In this chapter we calculated numerically the eigenmodes resulting from the Craig and McClymont (1991) analysis of an MHD disturbance in an X-type neutral point. Also, we calculated the electric field and the magnetic field perturbation resulting and showed their spatial and temporal structure. We showed the dependence of the solution on the value of the resistivity. In the chapter (5) we use the electromagnetic fields calculated here,

η	r_{diff} (cm)	t_A (sec)
3.1724×10^{-11}	4.94×10^3	56
3.1724×10^{-10}	1.56×10^4	50.7
3.1724×10^{-9}	4.94×10^4	45.4
3.1724×10^{-8}	1.56×10^5	40.13
3.1724×10^{-7}	4.94×10^5	34.85
3.1724×10^{-6}	1.56×10^6	29.6
3.1724×10^{-5}	4.94×10^6	24.3
3.1724×10^{-4}	1.56×10^7	19

Table 4.3: Alfvén crossing times for different resistivities.

η	$1/\kappa$ (sec)	$2\pi/\omega$ (sec)
3.1724×10^{-11}	634	244
3.1724×10^{-10}	523.5	222.5
3.1724×10^{-9}	423	200.6
3.1724×10^{-8}	333	178.6
3.1724×10^{-7}	253.6	156.6
3.1724×10^{-6}	184.5	134.4
3.1724×10^{-5}	126	112.2
3.1724×10^{-4}	78.5	90

Table 4.4: Decay and oscillation times for different resistivities for n=0.

to calculate particle orbits. We will find that the detailed structure of the eigenmodes produces new features of particle orbits.

η	$1/\kappa$ (sec)	$2\pi/\omega$ (sec)
3.1724×10^{-14}	13.9	4.4
3.1724×10^{-13}	11.9	4
3.1724×10^{-12}	10	3.8
3.1724×10^{-11}	7.64	3.5
3.1724×10^{-10}	6.14	2.84
3.1724×10^{-9}	4.8	2.65
3.1724×10^{-8}	3.6	2.3
3.1724×10^{-7}	2.6	2

Table 4.5: Decay and oscillation times for different resistivities for n=32.

Chapter 5

Particle Orbits in Reconnecting Electromagnetic Fields

The solar coronal magnetic field is constantly evolving either through equilibrium states or due to dynamic events. In the real solar corona, a superposition of several eigenfunctions will be present, as the magnetic structure responds to the various timescales on which the boundary is perturbed. In this and the next chapter we consider a more idealised problem. We use the eigenfunctions calculated in chapter 4 to study the particle acceleration consequences when a single eigenfunction is present. In this chapter we give examples of particle orbits in the presence of eigenfunctions, and describe generic features of particle behaviour.

5.1 Equations of motion

I am going to use the electromagnetic field calculated in the previous section to study particle trajectories. I want to see if the presence of the reconnective mode discussed in chapter (4) will change the particles energy significantly, and more specifically if it results in particle acceleration to energies that are observed during energetic phenomena in the Sun. As was discussed in chapters one and two during flares we observe hard X-ray bursts and γ continuum that are widely believed to result from electron-proton Bremsstrahlung and also γ ray lines from high energy (more than 10 MeV) protons.

To calculate the orbits we integrate the relativistic equations of motion as before using

the space- and time- dependent fields acquired in chapter (4). The system still has z-translation. The full six equations of motion to be integrated are the following (see (4.77), (4.78), and (4.79))

$$\begin{aligned}
\frac{d\bar{x}}{d\bar{t}} &= \bar{u}_x = \frac{\bar{p}_x}{\gamma} \\
\frac{d\bar{y}}{d\bar{t}} &= \bar{u}_y = \frac{\bar{p}_y}{\gamma} \\
\frac{d\bar{z}}{d\bar{t}} &= \bar{u}_z = \frac{\bar{p}_z}{\gamma} \\
\frac{d\bar{p}_x}{d\bar{t}} &= -\epsilon \bar{B}_y \bar{u}_z \\
\frac{d\bar{p}_y}{d\bar{t}} &= \epsilon \bar{B}_x \bar{u}_z \\
\frac{d\bar{p}_z}{d\bar{t}} &= \bar{E} + \epsilon(\bar{B}_y \bar{u}_x + \bar{B}_x \bar{u}_y)
\end{aligned} \tag{5.1}$$

where $\gamma = (1 + {p_x}^2 + {p_y}^2 + {p_z}^2)^{\frac{1}{2}}$ and $\epsilon = +1$ for protons, $\epsilon = -1$ for electrons. $\bar{B}_y$ and $\bar{B}_x$ are given by the following

$$\bar{B}_y = \bar{x}[1+A_o\frac{1}{2\eta}\exp(-\kappa t)[\kappa(\cos(\omega t)f'_{Re}-\sin(\omega t)f'_{Im})+\omega(\sin(\omega t)f'_{Re}+\cos(\omega t)f'_{Im})]] \tag{5.2}$$

and

$$\bar{B}_x = \bar{y}[1-A_o\frac{1}{2\eta}\exp(-\kappa t)[\kappa(\cos(\omega t)f'_{Re}-\sin(\omega t)f'_{Im})+\omega(\sin(\omega t)f'_{Re}+\cos(\omega t)f'_{Im})]] \tag{5.3}$$

where A_o is the amplitude of the perturbation. $\bar{E}$ is given by

$$\bar{E} = A_o[\exp(-\kappa t)[\kappa(\cos(\omega t)f_{Re} - \sin(\omega t)f_{Im}) + \omega(\cos(\omega t)f_{Im} + \sin(\omega t)f_{Re})]]. \tag{5.4}$$

We calculate the orbits for different values of the resistivity, different eigenmodes and different amplitudes.

5.1.1 Small B_z

Certain features of the particle orbits appear at first to be possibly an artifact of our pure 2-D treatment. A fully 3-D treatment is well beyond the scope of our present work. However some estimate of the effects of relaxing the 2-D assumption is possible via an ad hoc incorporation of a nonzero z-component of the magnetic field. So, a B_z component in the magnetic field is sometimes included in the equations of motion which become:

$$
\begin{aligned}
\frac{d\bar{x}}{d\bar{t}} &= \bar{u}_x = \frac{\bar{p}_x}{\gamma} \\
\frac{d\bar{y}}{d\bar{t}} &= \bar{u}_y = \frac{\bar{p}_y}{\gamma} \\
\frac{d\bar{z}}{d\bar{t}} &= \bar{u}_z = \frac{\bar{p}_z}{\gamma} \\
\frac{d\bar{p}_x}{d\bar{t}} &= -\epsilon \bar{B}_y \bar{u}_z + \bar{u}_y B_z \\
\frac{d\bar{p}_y}{d\bar{t}} &= \epsilon \bar{B}_x \bar{u}_z - \bar{u}_x B_z \\
\frac{d\bar{p}_z}{d\bar{t}} &= \bar{E} + \epsilon(\bar{B}_y \bar{u}_x + \bar{B}_x \bar{u}_y)
\end{aligned} \tag{5.5}
$$

5.2 Orbits in the reconnecting field

As we said before the amplitude of the perturbation discussed in chapter (4) is a free parameter. We fix the amplitude by energy considerations (see chapter 6). There is a dependence of the amount of energy that particles gain on the size of the amplitude of the perturbation. The orbits presented here are for different amplitudes. One common feature of these orbits is that the particles don't move very far away from the neutral point area during the integration time which is usually 1 second but can be 2 and 3 seconds. So, we have particles confined in the corona close to an area where they can get accelerated.

In fig. (5.1) we show the orbit of a proton in the electromagnetic field resulting from the analysis in chapter 4 when the resistivity is $\eta = 3.1724 \times 10^{-11}$ (which is the smallest value of the resistivity that we use) for the fundamental eigenvalue (n=0). After a brief nonadiabatic period close to the neutral point the particle starts drifting outside the nonadiabatic region ($\underline{E} \times \underline{B}$ drift). Figure (5.2) shows an orbit when the resistivity is $\eta = 3.1724 \times 10^{-11}$ and n=32. The particle's energy does not change significantly. The 'wobbling' of the orbit is due to the spatial structure of the eigenvalues (see fig. (4.10) and (4.12)). The complexity of the fields increases when the eigenvalue increases.

In fig. (5.3) we see the orbit of a nonadiabatic proton for $\eta = 3.1724 \times 10^{-7}$ and the fundamental eigenvalue, n=0. The particle is trapped in the neutral point region and is gaining energy very fast. When we integrate the orbit of a proton with exactly the same initial conditions but for $\eta = 3.1724 \times 10^{-6}$ and n=0, we don't get similar results. The particle is accelerated close to the neutral point but it is not trapped in the neutral point

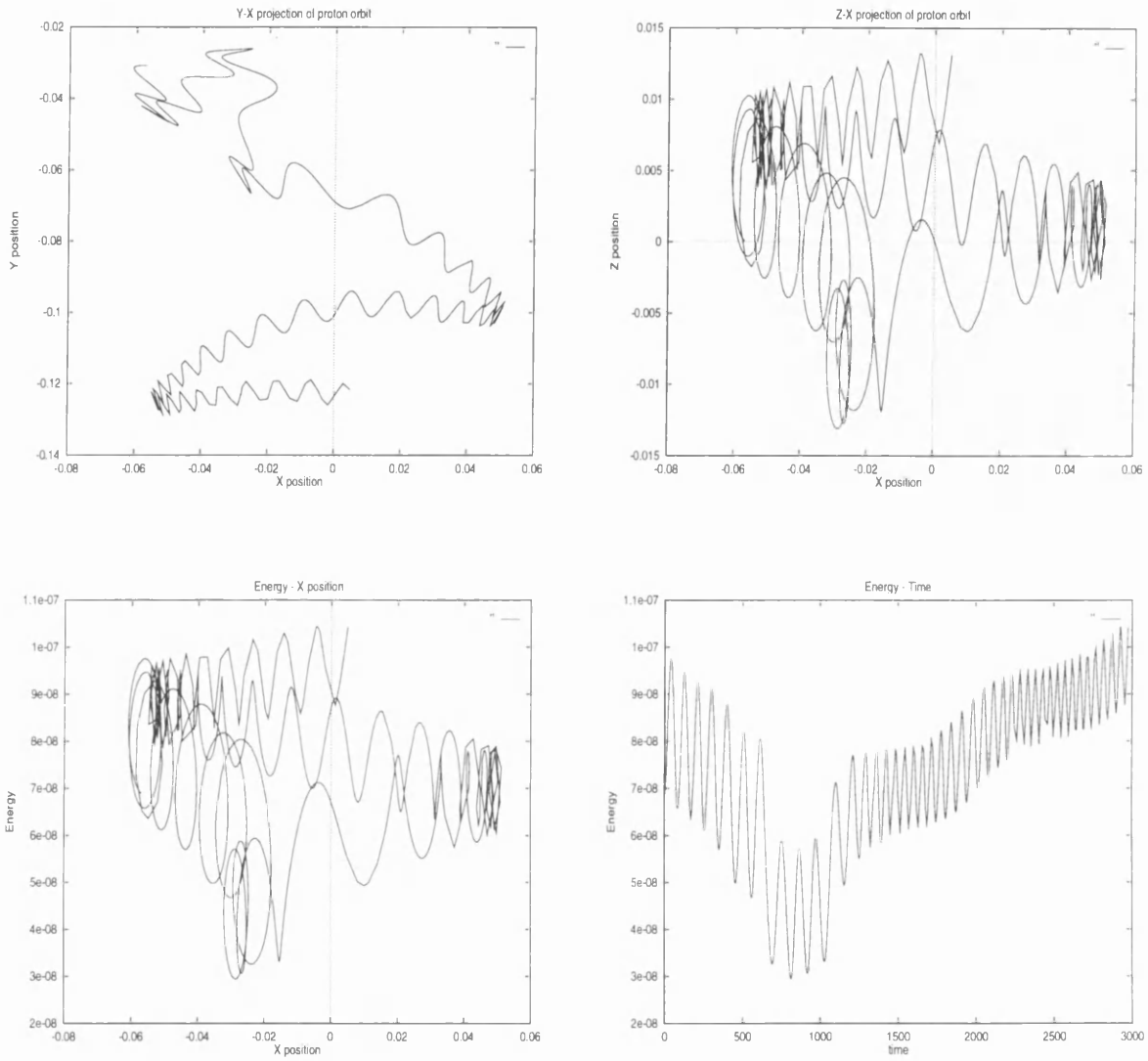

Figure 5.1: Orbit of a proton in the model electromagnetic field that results for $\eta = 3.1724 \times 10^{-11}$ and n=0. This particle gains some energy.

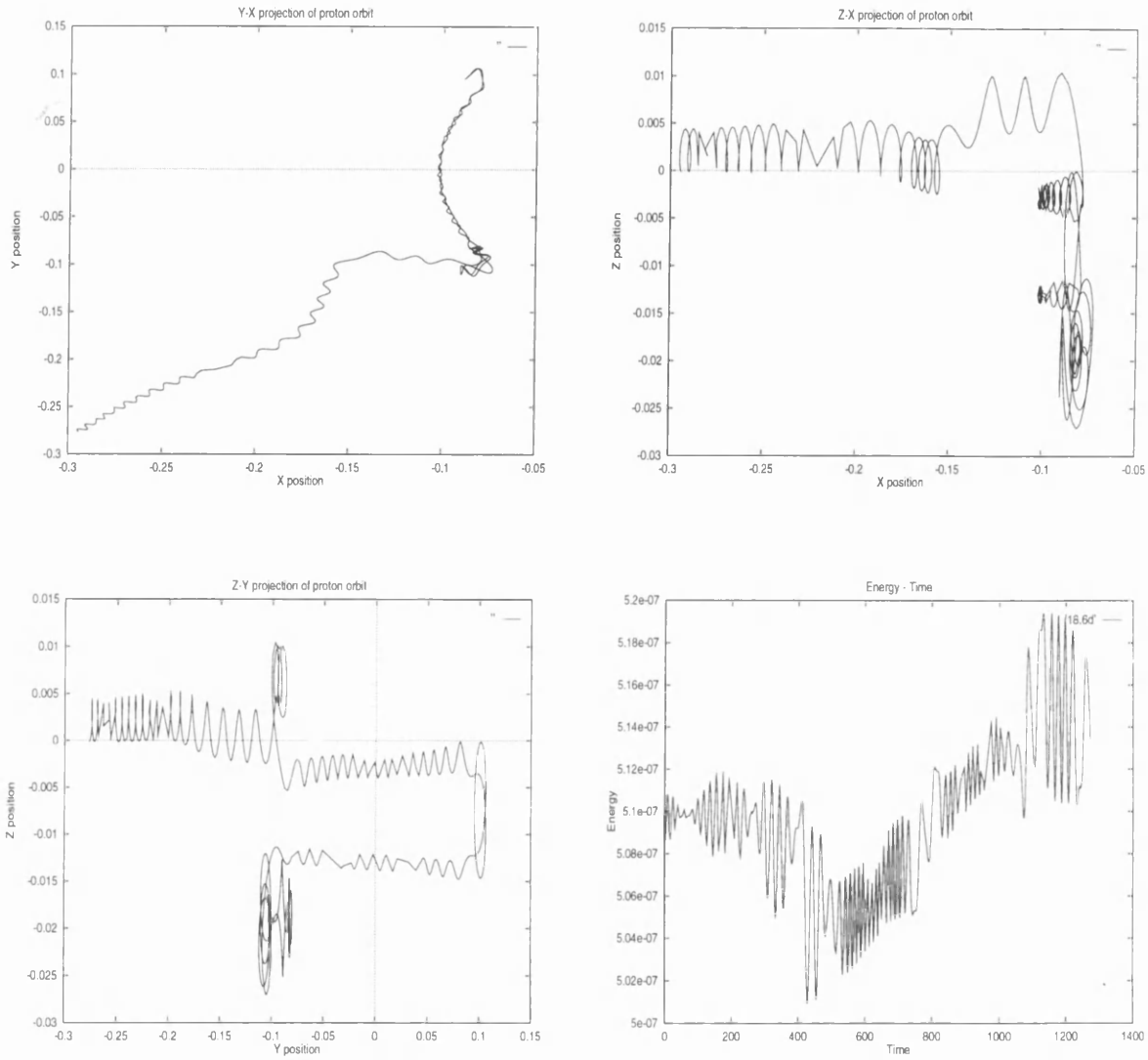

Figure 5.2: Orbit of a proton in the model electromagnetic field that results for $\eta = 3.1724 \times 10^{-11}$ and n=32. This particle energy doesn't change very much during the time shown here.

area as before. After a short period it is expelled.

The form of the electric and the magnetic field for resistivities $\eta = 3.1724 \times 10^{-7}$ and $\eta = 3.1724 \times 10^{-6}$ and n=0 is shown in fig. (5.4) and (5.5). The form of the magnetic field perturbation will help us understand the particle orbits. So, for the lower value of the resistivity $\eta = 3.1724 \times 10^{-7}$ the magnitude of the magnetic perturbation is bigger. One can see that from the form of magnetic perturbation in equations (5.2) and (5.3). The magnitude of the magnetic perturbation depends on the inverse of the resistivity. So, when the resistivity increases, the size of the dissipation region increases but the magnitude of the magnetic perturbation, which traps particles near the neutral point, decreases. The combined effect of the two results in particles being trapped at the neutral point area for values of the resistivity close to the value $\eta = 3.1724 \times 10^{-7}$. For smaller values of the resistivity fewer particles are trapped (see also discussion in chapter 6). Now, one has to consider the fact that for smaller values of the resistivity the electric field is smaller. So, the acceleration is smaller.

In fig. (5.6) we see the orbit of a proton in the model electromagnetic field that results for $\eta = 1.3006 \times 10^{-6}$, $\eta = 2.6012 \times 10^{-6}$, and n=0. All other conditions are kept the same (initial positions and velocities, and amplitude). The projection on the X-Y plane and X-Z plane are shown here. The orbits are very different. The one for $\eta = 1.3006 \times 10^{-6}$ ($\log \eta = 5.886$) shows the effect of trapping close to the neutral point and the one for $\eta = 2.6012 \times 10^{-6}$ ($\log \eta = 5.585$) shows no trapping.

In fig. (5.7) we see the energy versus x position and energy versus time for the particle discussed in (5.6). In fig. (5.8) we see the spatial evolution of the magnetic field perturbation for $\eta = 1.3006 \times 10^{-6}$, $\eta = 2.6012 \times 10^{-6}$, the two values of the resistivity discussed. It is clear that the change in the position of the magnetic perturbation maximum results in a dramatic decrease in the efficiency of trapping near the neutral point.

In fig. (5.9) we see the orbit of a proton in the electromagnetic field produced when $\eta = 3.1724 \times 10^{-6}$ for the fundamental eigenvalue n=0. This particle's orbit is adiabatic, its energy does not change significantly during the integration time.

5.2.1 Smaller Amplitude

We calculated some particle orbits for a smaller amplitude of the perturbation. The amplitude of the perturbation used here is a factor of $\sqrt{10}$ smaller than the previous ones

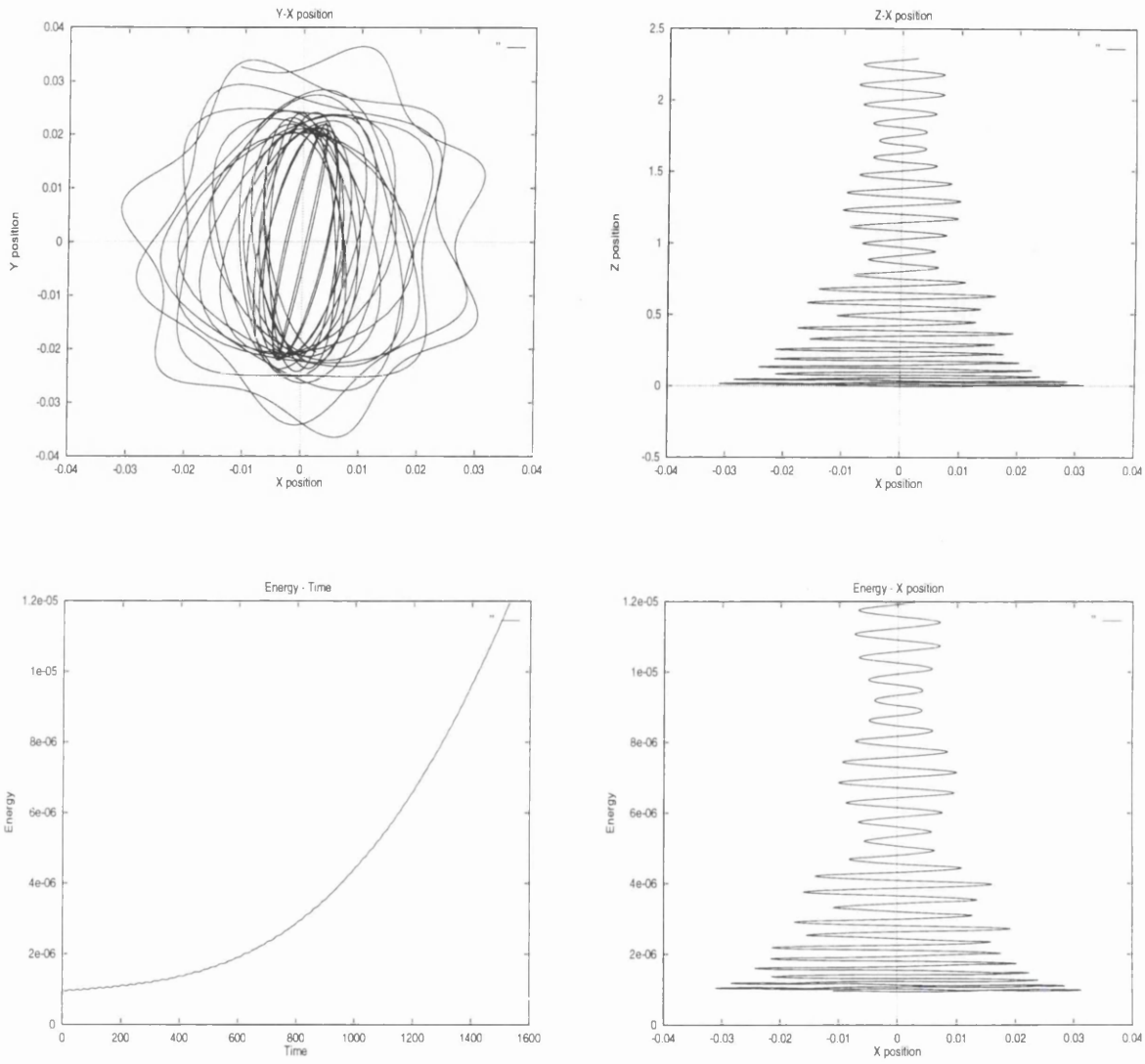

Figure 5.3: Orbit of a proton in the model electromagnetic field that results for $\eta = 3.1724 \times 10^{-7}$ and n=0.

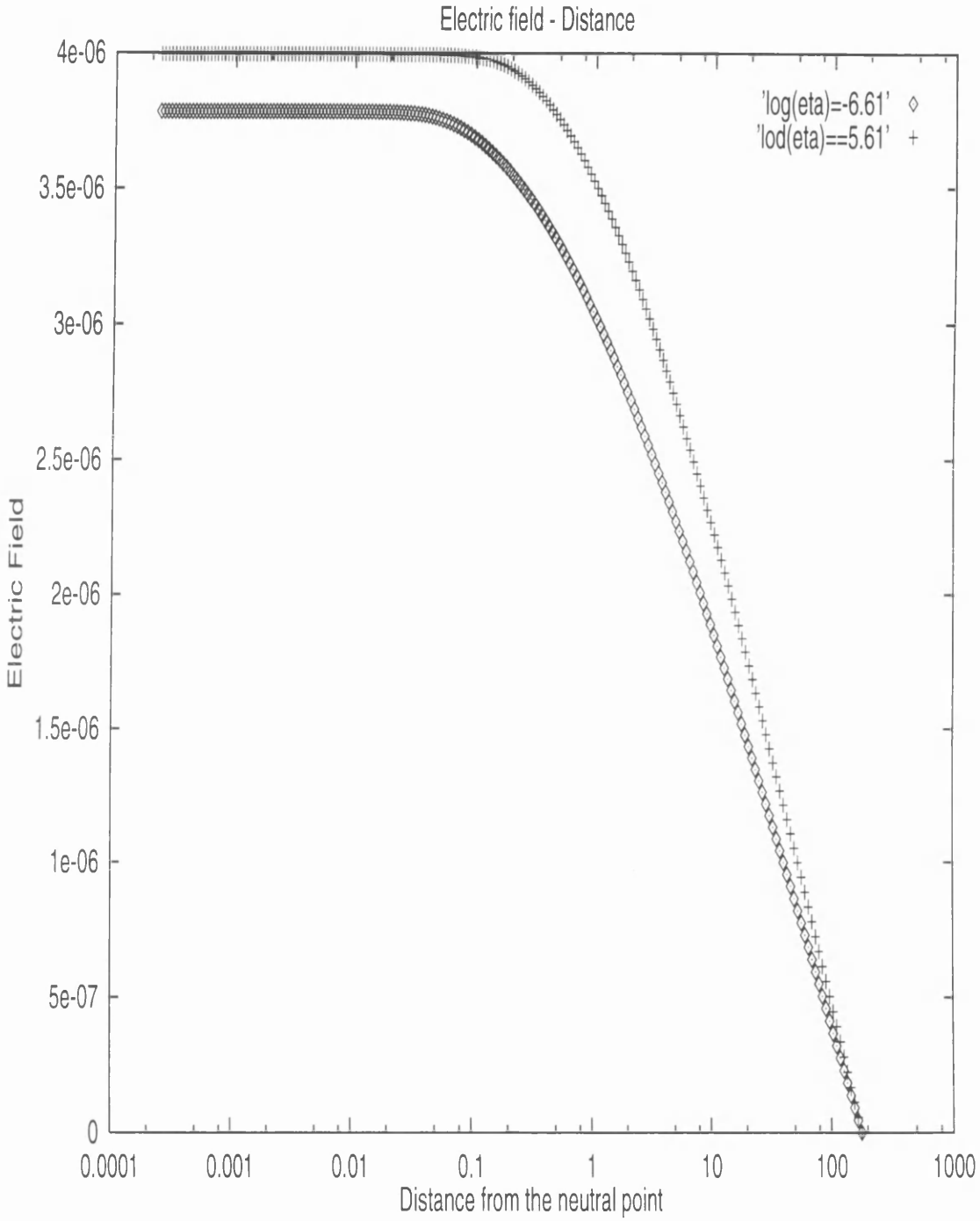

Figure 5.4: The spatial evolution of the electric field for $\eta = 3.1724 \times 10^{-7}$ and $\eta = 3.1724 \times 10^{-6}$ for eigenvalue n=0. The distance is given in our dimensionless units, the boundary is at r=178.

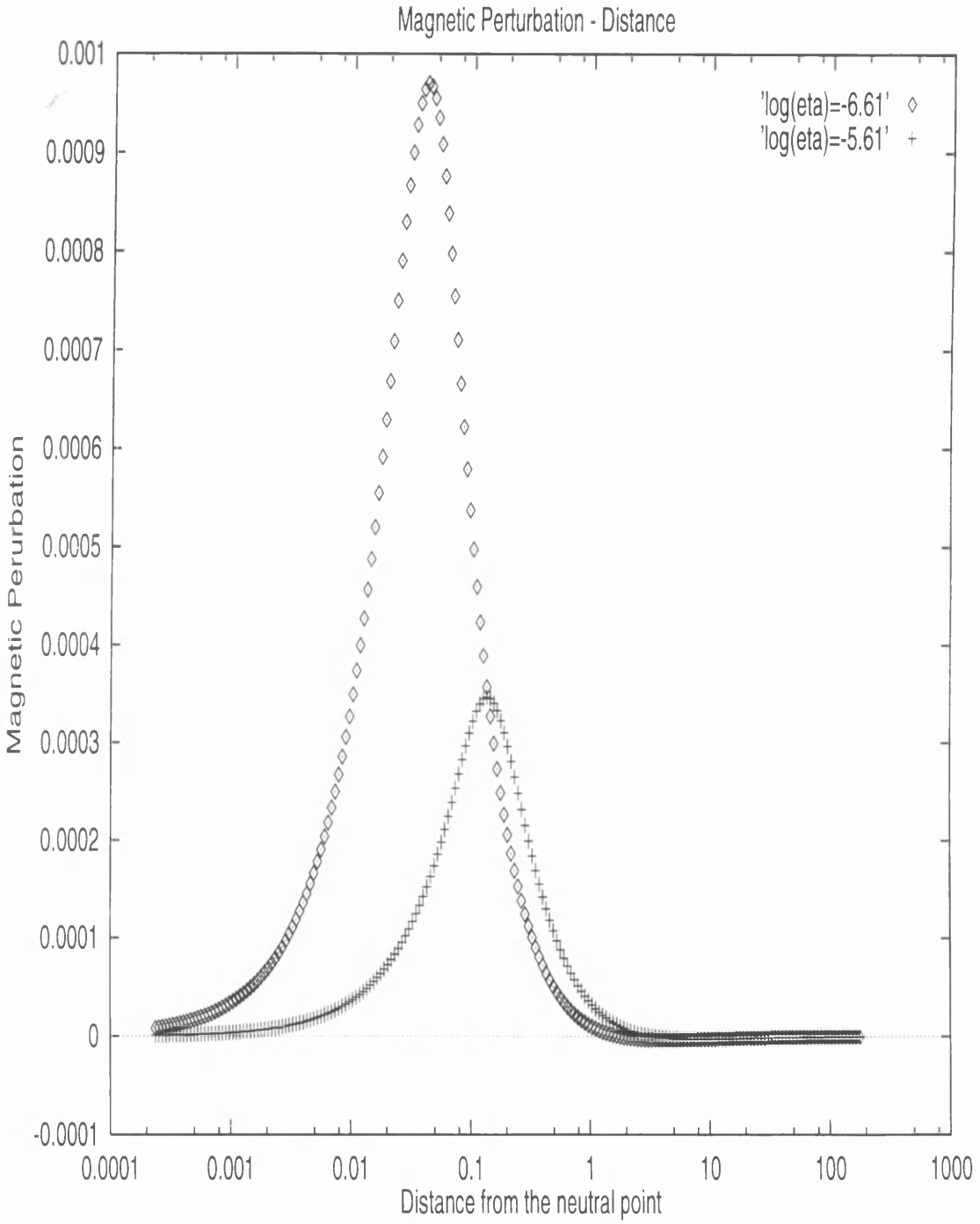

Figure 5.5: The spatial evolution of the magnetic field perturbation for $\eta = 3.1724 \times 10^{-7}$ and $\eta = 3.1724 \times 10^{-6}$ for eigenvalue n=0. The distance is given in our dimensionless units, the boundary is at r=178.

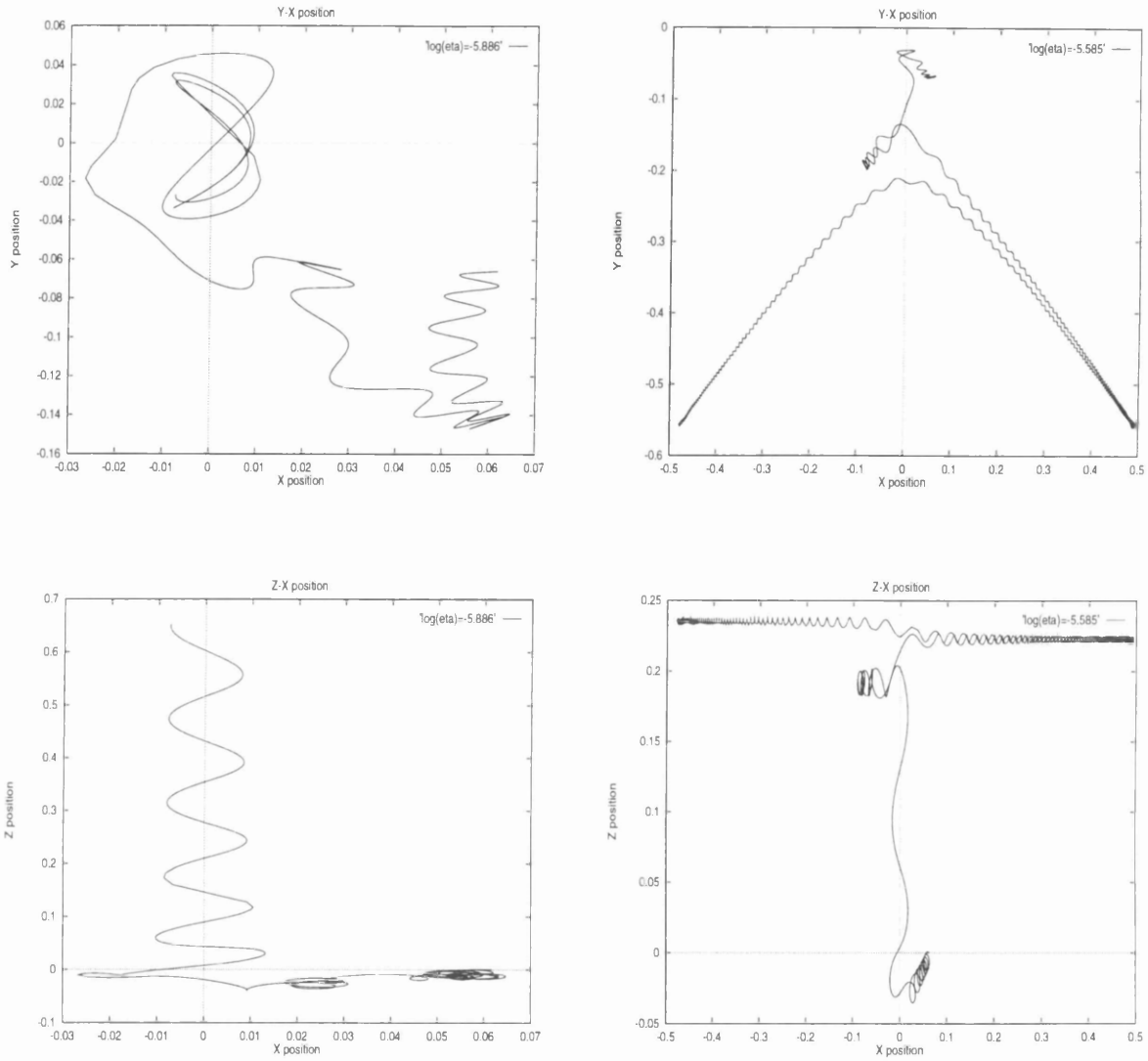

Figure 5.6: Orbit of a proton in the model electromagnetic field that results for $\eta = 1.3006 \times 10^{-6}$, $\eta = 2.6012 \times 10^{-6}$, and n=0. The projection on the X-Y plane and X-Z plane are shown here. All initial conditions are the same.

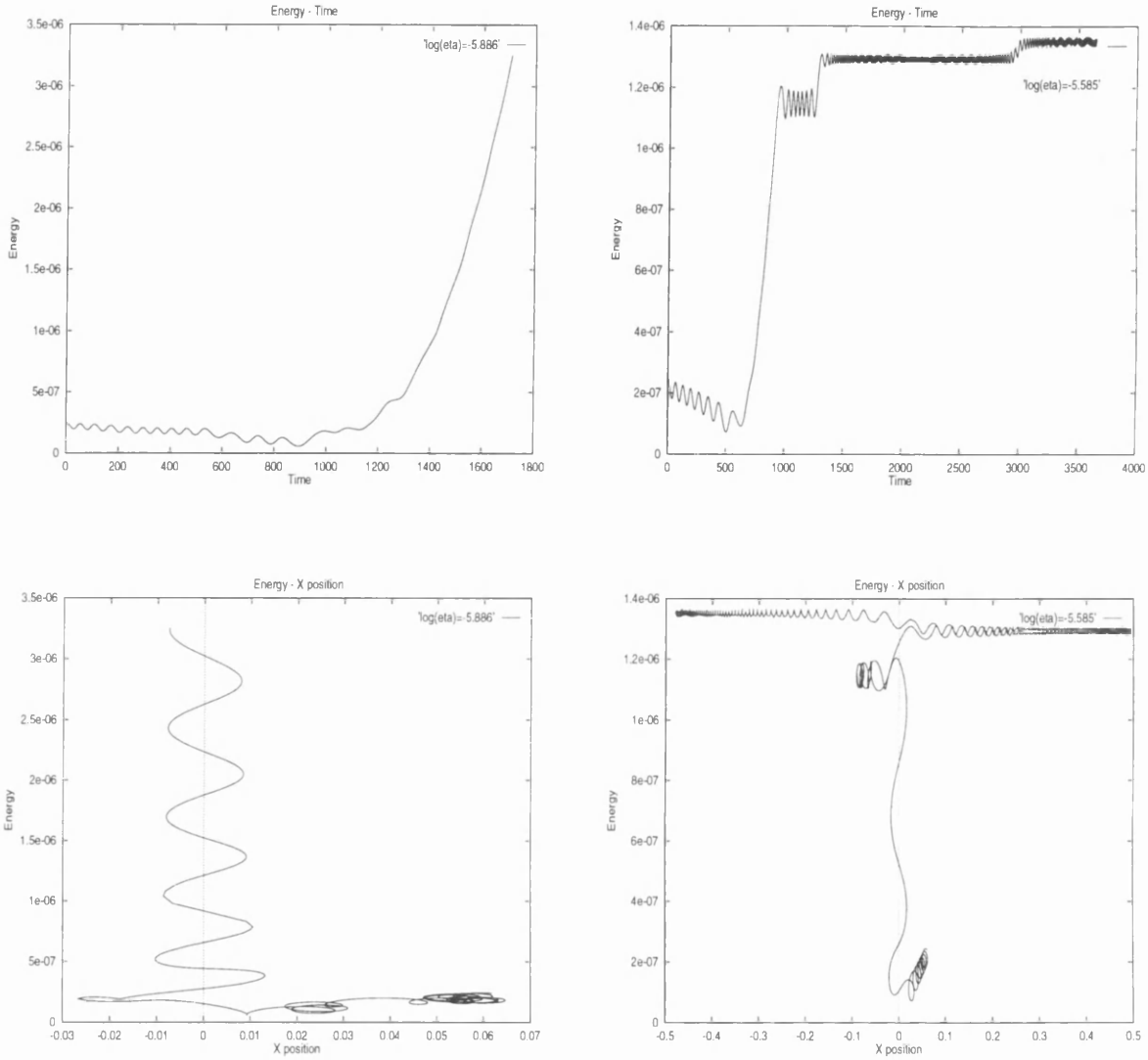

Figure 5.7: Orbit of a proton in the model electromagnetic field that results for $\eta = 1.3006 \times 10^{-6}$, $\eta = 2.6012 \times 10^{-6}$, and n=0 (the same as in fig. (5.6). The energy versus x position and energy versus time are shown here. All initial conditions are the same.

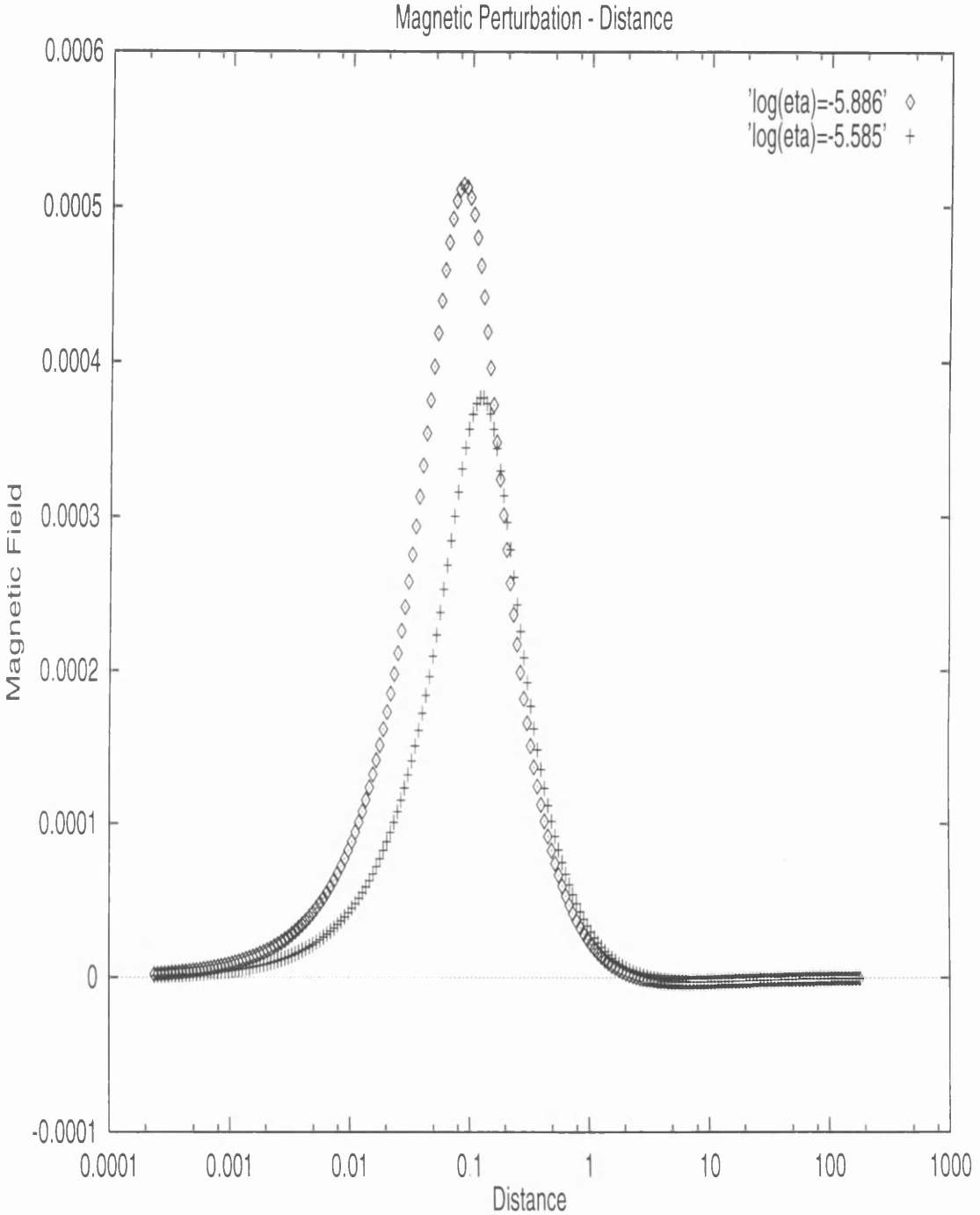

Figure 5.8: The spatial evolution of the magnetic field perturbation for $\eta = 1.3006 \times 10^{-6}$, $\eta = 2.6012 \times 10^{-6}$ for eigenvalue n=0. The distance is given in our dimensionless units, the boundary is at r=178.

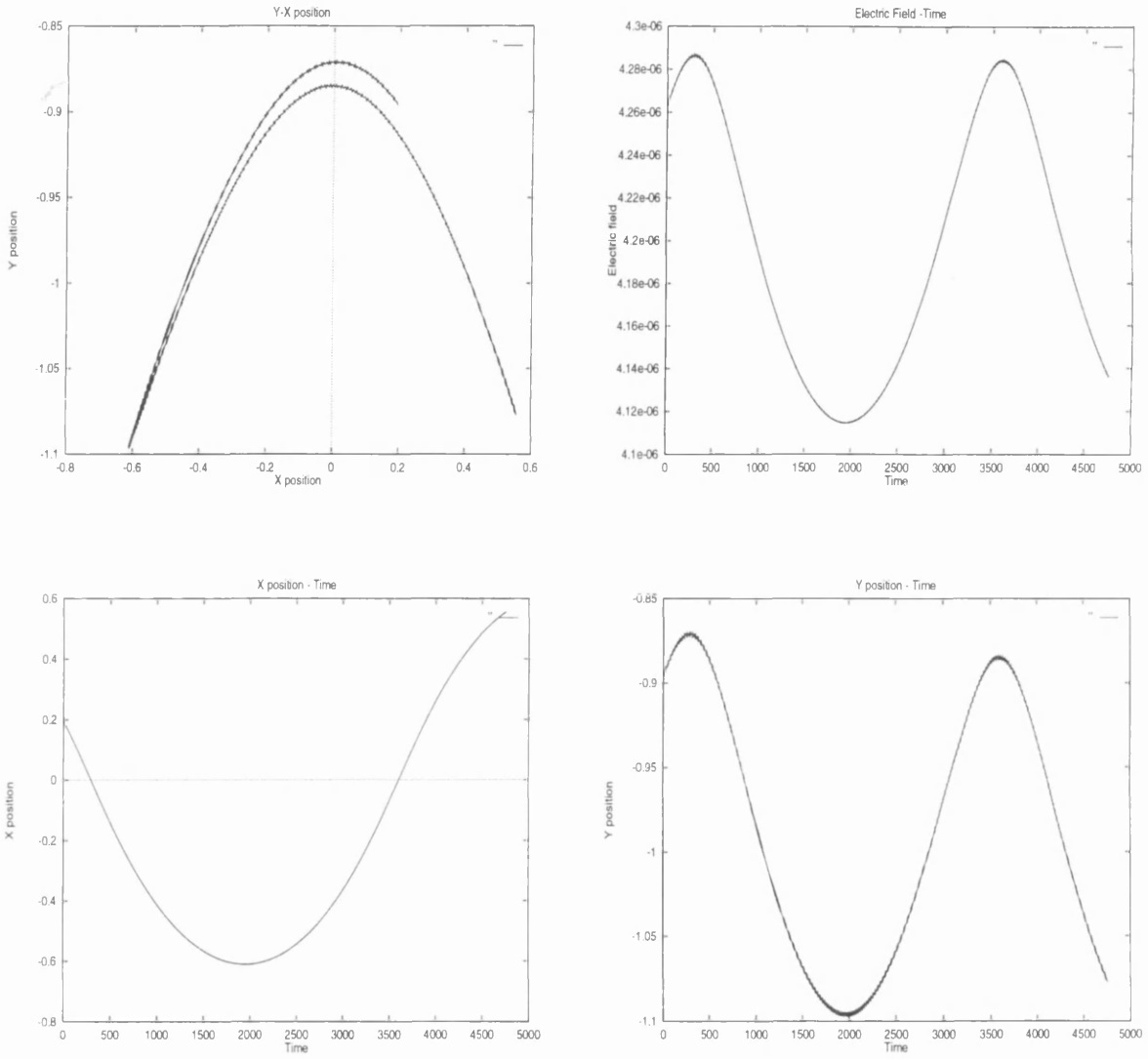

Figure 5.9: Orbit of a proton in the model electromagnetic field that results for $\eta = 3.1724 \times 10^{-6}$ and n=0. This orbit is adiabatic.

in this section. In fig. (5.10) we see the orbit of a proton in the electromagnetic field resulting from four different values of the resistivity when every other condition is kept the same (initial position and velocity, eigenmode, amplitude). The resistivities used are $\eta = 3.1724 \times 10^{-9}$, $\eta = 3.1724 \times 10^{-8}$, $\eta = 3.1724 \times 10^{-7}$, $\eta = 3.1724 \times 10^{-6}$ and the eigenmode n=0. For $\eta = 3.1724 \times 10^{-9}$ the encounter with the adiabatic region is very brief, it increases for $\eta = 3.1724 \times 10^{-8}$. For $\eta = 3.1724 \times 10^{-7}$ the particle gets trapped close to the neutral point and gets freely accelerated during the integration time. When the resistivity is $\eta = 3.1724 \times 10^{-6}$ the trapping effect doesn't persist, as happened when the amplitude was bigger. In fig. (5.11) the electric field is shown as viewed by the particle during its motion for all four resistivities. When the resistivity is $\eta = 3.1724 \times 10^{-7}$ the particle sees an almost constant electric field. In fig. (5.12) the energy of the particle is plotted versus x-position for all four resistivities. Close to the neutral point area is where the particle's energy changes.

5.2.2 Orbits for n=32

In fig. (5.13) we see the orbit of a proton in the electromagnetic field produced when the resistivity is $\eta = 3.1724 \times 10^{-7}$, and $\eta = 3.1724 \times 10^{-6}$ for the eigenvalue n=32. All other initial conditions are left the same (initial position, velosity and amplitude). The orbits are different. The particle does not increase its energy significantly. The orbits are not adiabatic since several crossings from the neutral point take place. The trapping of particles observed when n=0, does not happen now. For $\eta = 3.1724 \times 10^{-7}$ we can see the 'wobbling' of the orbit. For $\eta = 3.1724 \times 10^{-6}$ one cannot see the same 'wobbling' in the orbit. The position in respect to the neutral point where the perturbation is present (see fig. (4.7) moves further out as the resistivity increases. The magnitude of the magnetic perturbation decreases as the resistivity increases. These two effects make the presence of the magnetic perturbation when $\eta = 3.1724 \times 10^{-6}$ unimportant for the particle's orbit. So, the particle's orbit is such as if the magnetic perturbation is not present.

5.2.3 3-D magnetic field

In fig. (5.3) the particle moves in an area of almost constant electric field. It is trapped in the nonadiabatic region and continuously increases its energy during the integration time. It is almost a free acceleration A similar effect was observed by Speiser (1965) and was

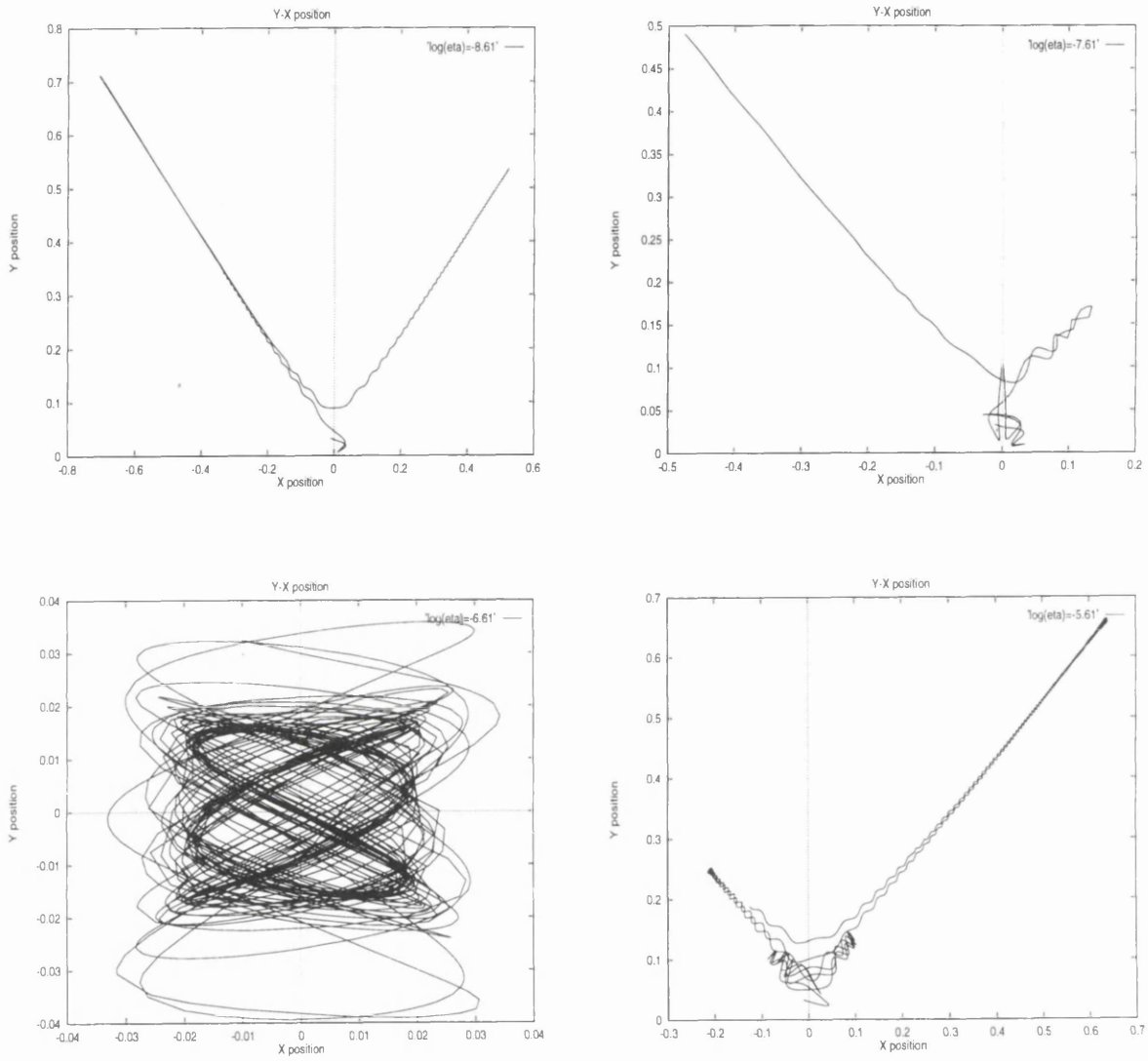

Figure 5.10: Orbit of a proton in the model electromagnetic field that results for $\eta = 3.1724 \times 10^{-9}$, $\eta = 3.1724 \times 10^{-8}$, $\eta = 3.1724 \times 10^{-7}$, $\eta = 3.1724 \times 10^{-6}$ and n=0.

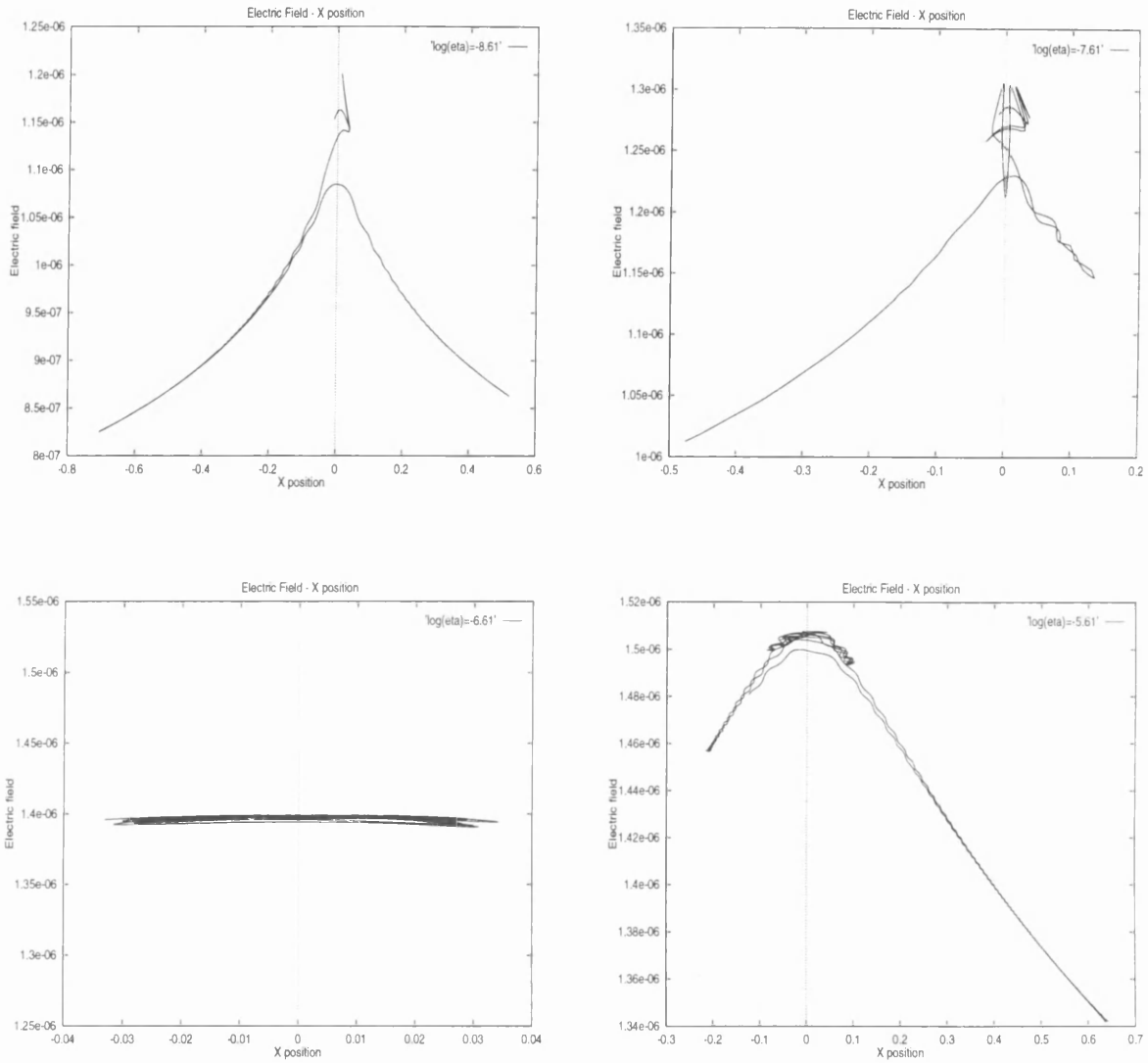

Figure 5.11: Orbit of a proton in the model electromagnetic field that results for $\eta = 3.1724 \times 10^{-9}$, $\eta = 3.1724 \times 10^{-8}$, $\eta = 3.1724 \times 10^{-7}$, $\eta = 3.1724 \times 10^{-6}$ and n=0. The electric field as seen by the particle is shown here.

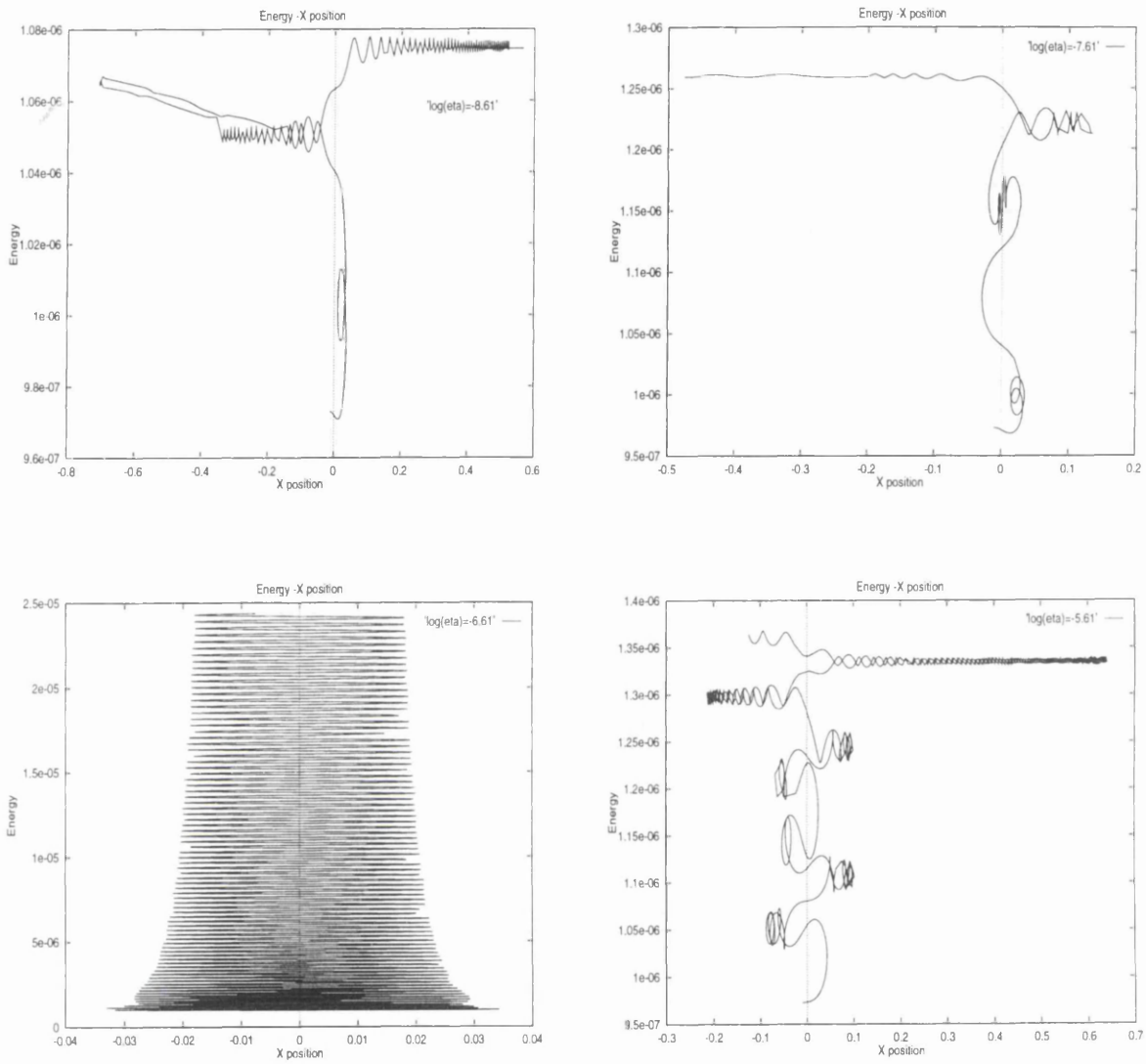

Figure 5.12: Orbit of a proton in the model electromagnetic field that results for $\eta = 3.1724 \times 10^{-9}$, $\eta = 3.1724 \times 10^{-8}$, $\eta = 3.1724 \times 10^{-7}$, $\eta = 3.1724 \times 10^{-6}$ and n=0. The energy versus x-position is shown here.

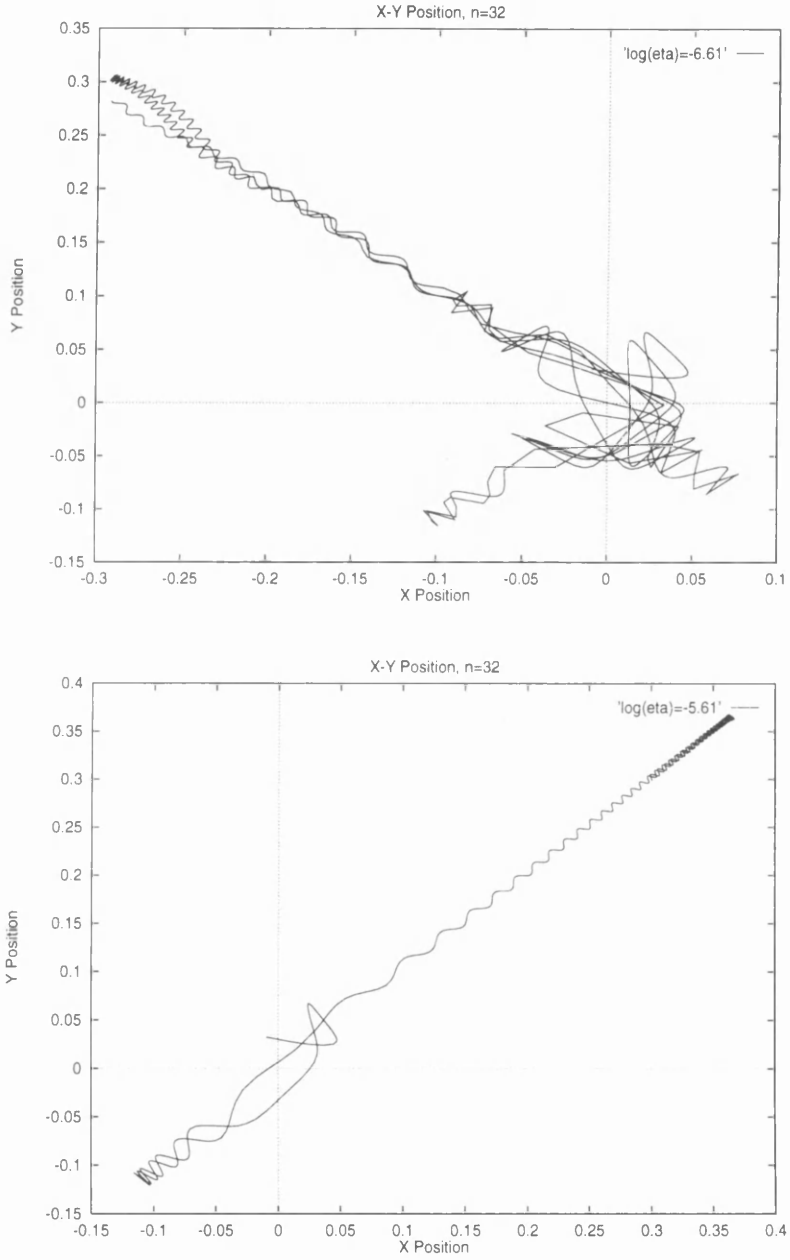

Figure 5.13: Orbit of a proton in the model electromagnetic field that results for $\eta = 3.1724 \times 10^{-7}$, and $\eta = 3.1724 \times 10^{-6}$ for the eigenvalue n=32. The X-Y projection of the trajectory is shown here.

thought to be a result of the (2-D) form of the magnetic field. When a small component of the magnetic field was added in the z-direction, the particles were expelled from the neutral point region. When we try the same initial conditions as in fig. (5.3), with a small component of the magnetic field in the z-direction little difference to the orbit was observed. The particle was not expelled from the neutral point area. The magnitude of the B_z component was chosen to be comparable to the size of the electric field. Even when much bigger values were tried very little difference was noticed. Of course to draw any conclusions here one needs to calculate a reasonable amount of orbits in the presence of the B_z component. However, such a treatment is an ad hoc expedient in the absence of a full 3-D treatment. We choose not to pursue this expedient at present, anticipating a fuller 3-D treatment in the future.

When a small B_z component is added, for the orbits given in fig. (5.9), the orbit does not change significantly. The energy that the particle gain changes slowly as the size of the B_z grows. It is clear that particle behaviour arises primarily from the spatial form of the eigenfunctions, rather than from our 2-D simplification.

5.3 Conclusions and Discussion

A general feature of the orbits is that particles remain relatively close to the neutral point during the integration time of 1 second. This is true for the low (n=0) and the high eigenvalues (n=9 and n=32) that we calculated orbits for (even those that do not gain much energy). The particles that are accelerated to high energies are those that are trapped close to neutral point area (see fig. 5.12). The particles are freely accelerated by the electric field. The radius of the orbit is decreased as the energy increases. We observe a compression of the acceleration region (see also Burkhart et al. (1991)).

During the integration time that we use the form of the magnetic and electric fields, for the fundamental eigenvalue n=0, don't change very significantly, since the timescale for decay and oscillation of the eigenmodes discussed here are much longer (see (4.7)). So the fields shown in figures (5.4), (5.5), and (5.8) could be considered almost constant in time. When the resistivity has a value from $\eta = 3.1724 \times 10^{-7}$ to about $\eta = 1.3006 \times 10^{-6}$, particles are trapped close to the neutral point where they get accelerated to more than a few hundred times their initial energy. In chapter 4 we discussed the trapping of particles

close to the neutral point due to geometric effects (magnetic mirroring) which led to a 'Fermi' type acceleration. In this chapter we saw the trapping of particles due to the interaction with waves.

More thorough discussion about these properties we give in the next chapter. For the eigenvalues n=32 the particle energy do not increase their energy a lot during the integration time. Still some are accelerated but not at the rates found for n=0. This is due to the spatial form of the electric and magnetic field perturbation. The fields magnitude is a rapidly changing function of position. Also, particles are not trapped close to the neutral point anymore.

Implications for the particle energy distributions and the consistency of microscopic and macroscopic approaches will be drawn in the next chapter.

Chapter 6

Matching of the MHD and Test Particle Calculations

6.1 Introduction

In chapter 4 we introduced the MHD description of a disturbance in a medium with a magnetic neutral point. In chapter 5 we described the characteristics of particle orbits in the presence of such a disturbance. In both calculations the scalar resistivity was an assumed parameter of the problem.

With our test particle calculations thus in an advanced state, we explore here the possibility of obtaining rough consistency of the test particle and MHD descriptions. We try to do this by adjusting the resistivity until the particles gain energy at the same rate that the wave loses it. Of course this cannot give a complete description of the wave, but it might prove useful for estimation of timescales, particles energy, etc.

In practice such matching proves impossible, for reasons that throw light on the limitations of a MHD description with scalar resistivity. Following the discussion in chapter 5 we restrict attention to only one eigenmode at a time.

6.2 Energy in the Electromagnetic Wave

We normalise the wave energy to the total energy of the background field which is

$$W = \frac{1}{8\pi} \int \underline{\mathrm{B}} \cdot \underline{\mathrm{B}} dV. \tag{6.1}$$

Per unit length in the z direction this is

$$W_{equi} = \frac{B_o^2}{8\pi}\int_0^{2\pi} d\phi \int_0^D r dr = \frac{B_o^2 D^2}{8} \tag{6.2}$$

Taking $B_o = 100$ gauss and size of the region $D = 10^9$ cm this is 1.25×10^{21} ergs/cm. The energy in the wave is the sum of the magnetic and the mechanical energy

$$W_{wave} = \frac{1}{2}[\int \frac{B^2}{8\pi} dV + \int \frac{\rho u^2}{2} dV] \tag{6.3}$$

where ρ is the plasma density, and u is the wave velocity. We normalise here the magnetic field perturbation to B_o and the velocity to the Alfvén velocity, using the normalization of Craig and McClymont (1991). So,

$$B = B_o \nabla \Psi \tag{6.4}$$

and

$$\begin{aligned} \frac{\rho u^2}{2} &= \frac{\rho}{2} u_A^2 \tilde{u}^2 \\ &= \frac{B_o^2}{8\pi} \tilde{u}^2. \end{aligned} \tag{6.5}$$

Inserting equations (6.4) and (6.5) into (6.3) we get the following expression for the energy of the wave per unit length

$$W = \frac{B_o^2}{8\pi}\frac{1}{2}\int \left[(\nabla\Psi)^2 + \tilde{u}^2\right] dV, \tag{6.6}$$

where, $dV = r dr d\phi$ (Craig and Watson, 1992). We have already assumed that the hypergeometric function is azimuthally symmetric and that there is no dependence on z. So, one can calculate the energy per unit length in z. The gradient of the magnetic field is given by

$$\nabla\Psi = e^{\lambda t}\frac{df(r)}{dr}. \tag{6.7}$$

Remembering the change of variables from eq. (4.46) and using the fact that $\mathcal{A}$=1 when the normalization of Craig and McClymont is used, we get

$$\nabla\Psi = e^{\lambda t}\frac{-2r}{\eta\lambda}{}_2F_1'(\alpha,\beta,c;z) \tag{6.8}$$

which is (Abramovitz and Stegun, 1964)

$$\nabla\Psi = e^{\lambda t}\frac{-2r}{\eta\lambda}\frac{\alpha\beta}{c}{}_2F_1(\alpha+1,\beta+1,c+1;z). \tag{6.9}$$

The velocity magnitude is given from the induction equation (Craig and Watson, 1992) by

$$\tilde{u}(r,t) = \frac{1}{r}(\eta\nabla^2\Psi - \frac{\partial\Psi}{\partial t}) \tag{6.10}$$

and by using the right hand side of 4.45 and

$$\dot{\Psi} = \lambda e^{\lambda t} f(r), \tag{6.11}$$

we get

$$\tilde{u} = -e^{\lambda t}\frac{\lambda r}{r^2+\eta\lambda}f(r). \tag{6.12}$$

So,

$$(\nabla\Psi)^2 = e^{-2\kappa t}[\frac{(\kappa^2+\omega^2)}{4\eta^2}r^2(f'^2_{Re}+f'^2_{Im})] \tag{6.13}$$

and

$$\tilde{u}^2 = e^{-2\kappa t}[\frac{(\kappa^2+\omega^2)r^2(f^2_{Re}+f^2_{Im})}{((r^2-\eta\kappa)^2+\omega^2\eta^2)}]. \tag{6.14}$$

Substituting equations (6.13) and (6.14) into eq. (6.6), normalizing r in units of D and integrating over ϕ, the integral for the energy becomes

$$W_{wave} = e^{-2\kappa t}\frac{B_o^2D^2}{4}\frac{1}{2}\int_0^1\left[\frac{(\kappa^2+\omega^2)}{4\eta^2}r^3(f'^2_{Re}+f'^2_{Im}) + \frac{(\kappa^2+\omega^2)r^3(f^2_{Re}+f^2_{Im})}{((r^2-\eta\kappa)^2+\omega^2\eta^2)}\right]dr \tag{6.15}$$

which gives the energy of the wave per unit length (per cm here) at a given time. The energy is given as a function of the resistivity and for the order of the eigenvalue. Of course W_{wave} should be multiplied by the amplitude of the wave. We are free to fix that from energy considerations.

In fig. (6.1) we plot the value of the following integral

$$W_{wave} = \pi\int_0^1\left[\frac{(\kappa^2+\omega^2)}{4\eta^2}r^3(f'^2_{Re}+f'^2_{Im}) + \frac{(\kappa^2+\omega^2)r^3(f^2_{Re}+f^2_{Im})}{((r^2-\eta\kappa)^2+\omega^2\eta^2)}\right]dr \tag{6.16}$$

for different values of the resistivity and for different eigenvalues. As, the eigenvalue increases so does the value of this integral. Also the integral increases with increasing resistivity. So, in order to have the same energy in the wave for different resistivities and eigenvalues we have to adjust the amplitude of the wave. This is important primarily to ensure that we stay in the linear regime.

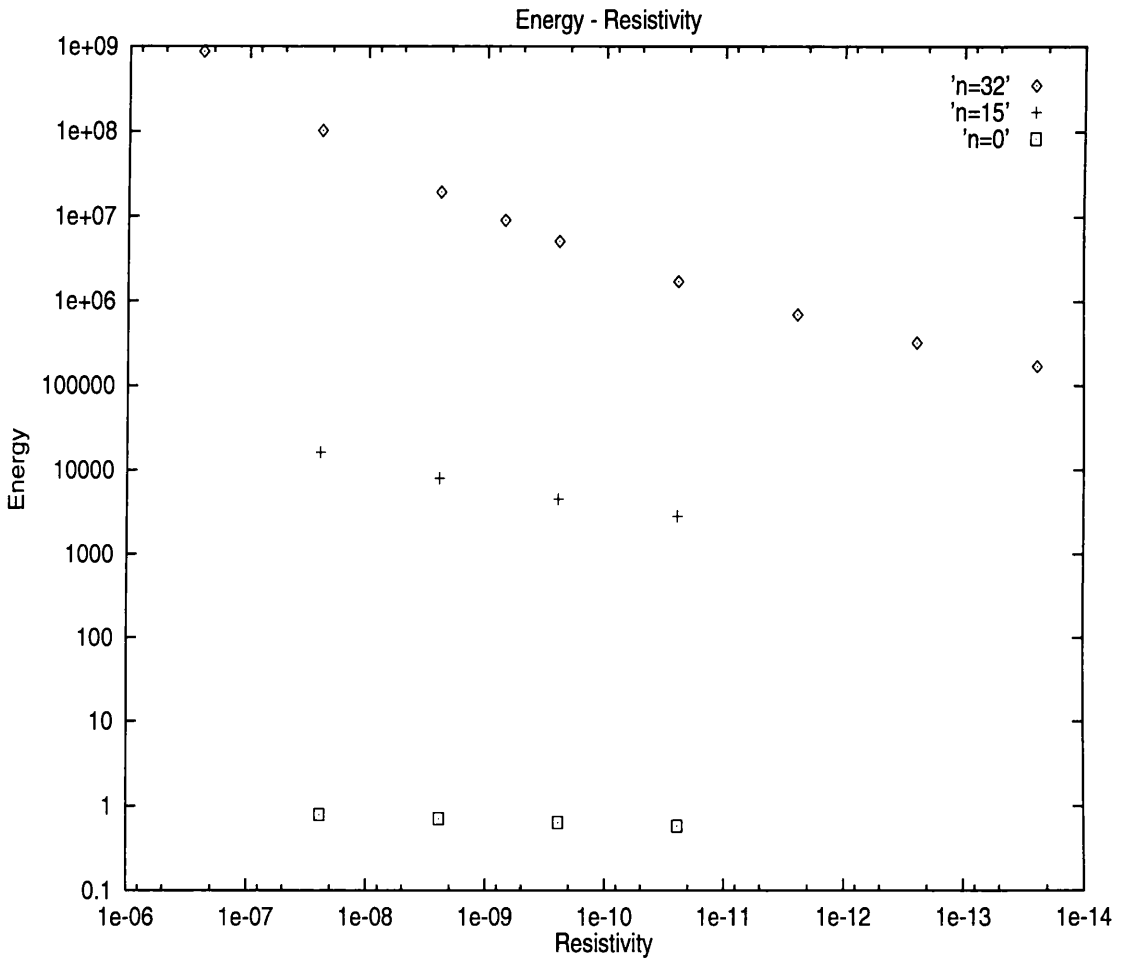

Figure 6.1: Energy of the perturbation versus the resistivity for n=0, n=15, n=32.

6.2.1 Energy in the Wave

We calculate the energy distributions that result when the perturbations on the electric and magnetic field are included. We integrate the equations of motion of the particles with the new electromagnetic fields. First we have to calculate the amplitude of the disturbance. Recall from the previous section that we choose to fix the total energy of the wave as η is varied. To do that we decide at the onset what fraction of the equilibrium magnetic field energy the wave should have. So, W_{wave} as given by (6.15) for t=0 is set equal to the desired energy,

$$W_{wave} = \frac{B_o^2 D^2}{8} \times \theta \tag{6.17}$$

where θ is the fraction of the energy of the background field. So, we have

$$(\text{amplitude})^2 \frac{1}{2} \int_0^1 \left[\frac{(\kappa^2+\omega^2)}{4\eta^2} r^3 (f'^2_{Re} + f'^2_{Im}) + \frac{(\kappa^2+\omega^2) r^3 (f^2_{Re} + f^2_{Im})}{((r^2-\eta\kappa)^2 + \omega^2\eta^2)} \right] dr = .5 \times \theta. \tag{6.18}$$

The left hand side of eq. (6.18) (without the amplitude) we calculate by numerical integration as above. There is equipartition in the energy at t=0. We use one eigenmode at a time.

From now we call on the energy in the wave E_{wave}. So, if the initial energy in the wave is E_{wave}, after time t the wave has lost energy due to damping $(1-\exp(-2\kappa t))E_{wave}$ which must have been absorbed by the particles.

In table (6.1) we see the values of amplitudes for different values of the resistivity. In the first column we have the logarithm of the resistivity. In the second column the amplitude of the perturbation when the energy in the wave is 10% of the equlibrium magnetic field energy. In column 3 we have the amplitude of the perturbation when the energy in the wave is 1% of the equlibrium magnetic field energy. To be in the linear regime the amount of energy that the particles gain as a function of the wave energy shouldn't change when the amplitude changes.

6.2.2 Energy in the Particles

In the calculations presented in this chapter, we use protons only. The reason is that the calculation for electrons is very time consuming and we need to develop faster integration methods for calculating electron orbits for a time comparable to the proton integration

log(η)	amplitude (10%)	amplitude (1%)
-10.613	0.736	0.233
-8.613	0.67	0.212
-7.613	0.63	0.199
-6.613	0.59	0.187
-5.613	0.55	0.174
-4.613	0.5	0.158
-3.613	0.448	0.142

Table 6.1: Amplitudes of the wave for different resistivities for n=0 and for two initial wave energies.

time. Also our earlier results suggest that electrons will not be energetically dominant (see Galeev et al. 1978).

We calculate the energy that the particles gain in the following way. We assume as we already said that the density n_o of the plasma is uniform. We start the particles in a certain area S around the neutral point. The energy gain per test particle is

$$\langle \mathcal{E} \rangle = \frac{1}{N} \sum_{i=0}^{N} [E_i(\Delta t) - E_i(0)] \tag{6.19}$$

where N is the number of particles in our calculation, Δt is the integration time, and E is the energy of the particles. Because the particles are initially uniformly distributed in the area S, the energy gain of *all* the particles in this area is $nS\langle \mathcal{E} \rangle$. We attempt to find a value of the resistivity η such that the quantity $nS\langle \mathcal{E} \rangle$ equals the energy lost by the wave. We pick the area S so that most of the energy gaining particles lie within it.

6.2.3 Note on the numerical method

For these calculations further tests on the numerical method were performed. In the equations of motion we included the perturbation on the magnetic field but not the electric field. Thus particle energy should be constant. In tables (6.2) and (6.3) we see some statistical analysis of the results. One can see that the moments of the initial distributions don't change during the integration time of 5360 timesteps. The initial distributions are randomly drawn from a maxwellian of temperature 5×10^6 K.

In fig. (6.2) we show the initial and final distributions for $\eta = 3.1724 \times 10^{-11}$, n=0 and $E_o = 0.736$ (i, ii), for $\eta = 3.1724 \times 10^{-8}$, n=0 and $E_o = 0.63$ (iii, iv) and for $\eta = 3.1724 \times 10^{-6}$, n=0 and $E_o = 0.55$ (v, vi). The energy in the magnetic field perturbation

is assumed to be 10% of the equilibrium magnetic energy in all cases. Similar results were found for different values of the resistivity that are not presented here.

log(η)	average	s.dev.	variance
-10.613	-6.32217	0.4223	0.1783
-7.613	-6.31688	0.3998	0.1599
-5.613	-6.31897	0.4190	0.1756

Table 6.2: Initial distribution statistics

log(η)	average	s.dev.	variance
-10.613	-6.32187	0.4223	0.1783
-7.613	-6.31670	0.3999	0.1599
-5.613	-6.31876	0.4190	0.1756

Table 6.3: Final distribution statistics

6.3 Energy Distributions

6.3.1 Fundamental Eigenmode, n=0

We start by calculating the particle acceleration consequences of the the fundamental eigenmode, n=0. We fix the ambient plasma density to 10^{10} particles per cm^3. This is important because the constant $\mathcal{A}$ depends on the number density and this changes the value of the eigenvalues in our units. Smaller density with constant magnetic field (B_o = 100 gauss at the boundary) means increased Alfvén velocity. The decay and oscillation times of the eigenmodes decrease (see also section 4.7), and the magnitude of the electric and magnetic field perturbation increase.

The area around the neutral point where particles are released is defined by

$$-0.4 \leq x0 \leq 0.4$$
$$-0.4 \leq y0 \leq 0.4.$$

This area is $S = 2 \times 10^{13} cm^2$. All particles are released on the $z = 0$ plane. Different initial release areas have been tried too, for statistical reasons. The particles are released with initial velocities randomly drawn out of a Gaussian which approximates a Maxwellian of temperature 5×10^6 K.

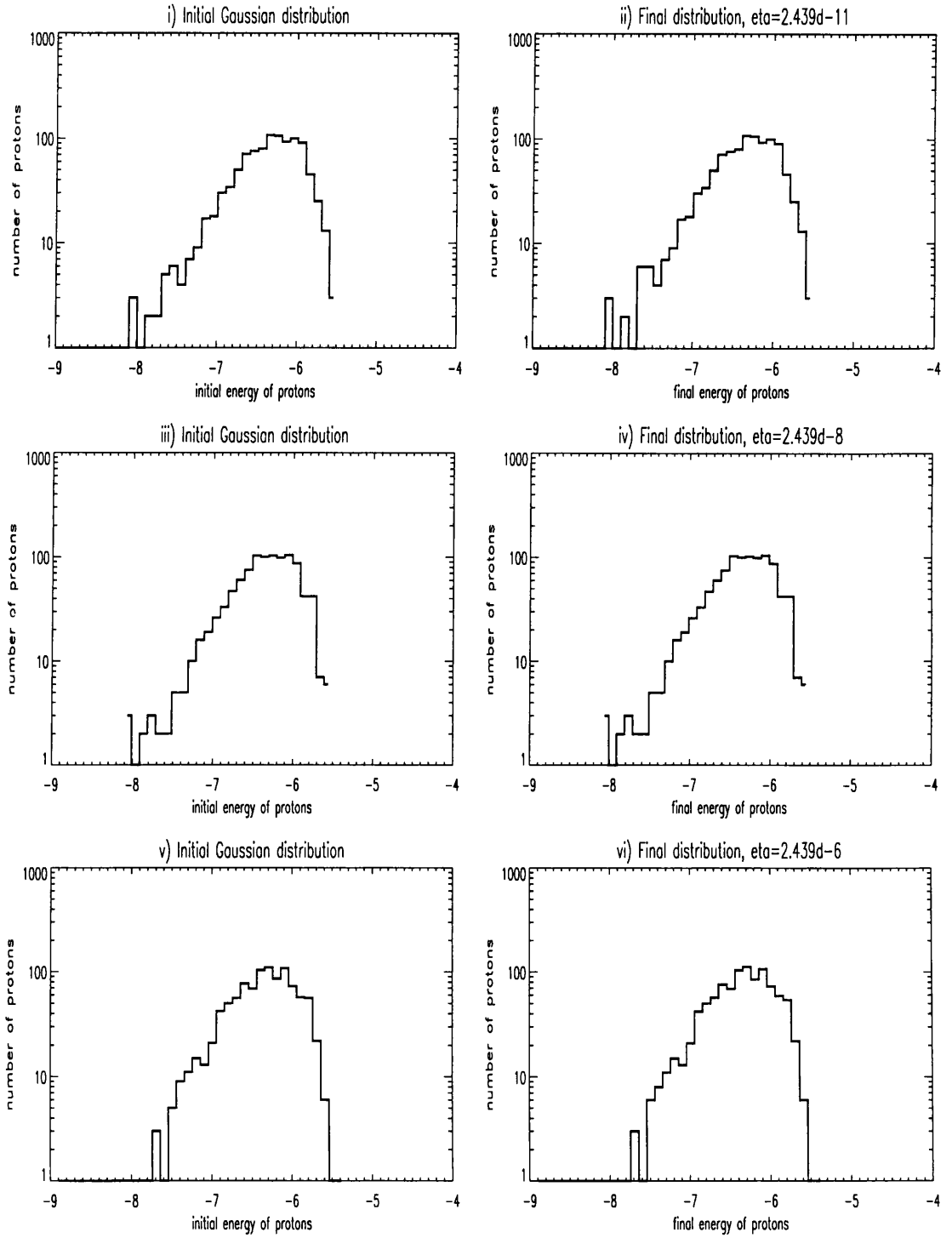

Figure 6.2: Initial and final distributions of protons. The final distributions are acquired after 5360 integration timesteps. In i) and ii) we have the distributions for $\eta = 3.1724 \times 10^{-11}$, n=0 and $E_o = 0.736$. In iii) and iv) we have the distributions for $\eta = 3.1724 \times 10^{-8}$, n=0 and $E_o = 0.63$. In v) and vi) we have the distributions for $\eta = 3.1724 \times 10^{-6}$, n=0 and $E_o = 0.55$.

The time of the calculation was 5360 timesteps (which as we have already mentioned corresponds to a real time of 1 second). The amplitude of the wave is calculated by assuming that the energy in the perturbation is 10% of that of the equilibrium magnetic field, which is $E_{wave} = 1.25 \times 10^{20}$ erg/cm.

$\log(\eta)$	energy in the wave	energy in the particles	ratio
-10.613	3.9×10^{17}	1.32×10^{14}	3.4×10^{-4}
-8.613	5.9×10^{17}	2.25×10^{14}	3.8×10^{-4}
-7.613	7.5×10^{17}	6.52×10^{14}	8.7×10^{-4}
-6.613	9.8×10^{17}	2.2×10^{15}	2.25×10^{-3}
-5.613	1.35×10^{18}	5.5×10^{13}	4.07×10^{-5}
-4.613	1.98×10^{18}	4.3×10^{13}	2.17×10^{-5}
-3.613	3.125×10^{18}	6.73×10^{13}	2.15×10^{-5}

Table 6.4: Energy in the wave and the particles for different resistivities, for n=0.

In table 6.4 we present the results for different values of the resistivity. In the first column we see the logarithm of the resistivity (which is given in our units). In the second column we see the energy that the wave loses due to damping in 1 sec (in units of erg/cm). In the third column we see the energy in the particles after 1 sec (in units of erg/cm). In the fourth column we see the ratio of the energy in the particles to the energy that the wave loses.

Certain features are apparent here. First the energy that the wave loses during 1 second increases as the resistivity increases. This is obvious from table 4.4 where the decay and oscillation times of the eigenmode n=0 are given for different values of the resistivity. The integration time of 1 second is obviously much smaller than the decay and oscillation times of the eigenmode n=0, for number density $n = 10^{10} cm^{-3}$. So, we expect that the shape and the amplitude of the wave do not change very significantly during the time of our calculation.

Another feature is that the ratio of the energy in the particles to the energy that the wave loses increases as the resistivity increases but only up to $\eta = 3.1724 \times 10^{-7}$. After that value of η the amount of energy that the particles gain decreases suddenly when $\eta = 3.1724 \times 10^{-6}$ and remains almost constant after that. The energy that particles gain cannot account for the energy that the wave loses, for any value of η.

In fig. (6.3) we plotted the final distributions of 1000 protons (number of particles in each distribution). From this graph we see that the shape of the proton distribution changes

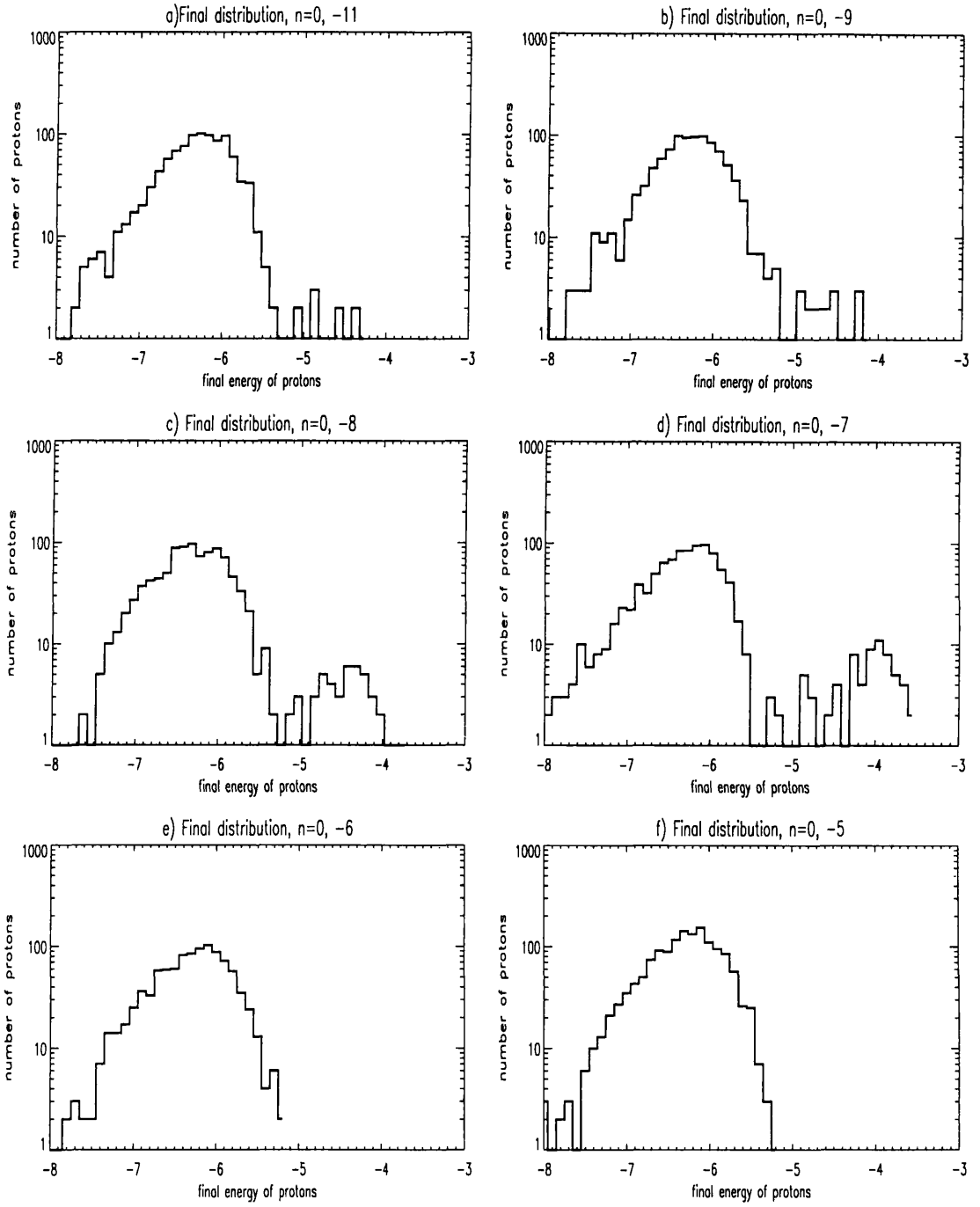

Figure 6.3: Final distributions of protons. The final distributions are acquired after 5360 integration timesteps, for the following values of the resistivity: a) $\eta = 3.1724 \times 10^{-11}$, b) $\eta = 3.1724 \times 10^{-9}$, c) $\eta = 3.1724 \times 10^{-8}$, d) $\eta = 3.1724 \times 10^{-7}$, e) $\eta = 3.1724 \times 10^{-6}$, and f) $\eta = 3.1724 \times 10^{-5}$. The fundamental eigenmode, n=0 is used in the calculation. The energy in the wave was 10% of the equilibrium magnetic field energy.

as the resistivity increases but again only up to resistivity $\eta = 3.1724 \times 10^{-7}$. After that little difference from the initial gaussian can be seen.

In fig. (6.4) we have plotted the mean energy of the distributions shown in fig. (6.3) versus the logarithm of the resistivity. The errorbars are the variance of each distribution on the mean energy. In table 6.5 we can see the numbers for mean energy, the variance, the skewness and kurtosis of the distributions in fig. (6.3). As the resistivity increases from $\eta = 3.1724 \times 10^{-11}$ to $\eta = 3.1724 \times 10^{-7}$ so do the mean energy and the variance of the distributions. A tail of high energy particles is developed. When the resistivity takes the value $\eta = 3.1724 \times 10^{-6}$ or above then no tail of high energy particles is developed. The mean energy of the distribution decreases and so does the variance.

log(η)	mean energy	variance	skewness	kurtosis
-10.613	-6.2648	0.2264	2.0996	-3.5615
-8.613	-6.2472	0.2504	1.9966	-2.8001
-7.613	-6.2211	0.3304	1.7379	-1.2560
-6.613	-6.1716	0.5307	1.3713	-1.3978
-5.613	-6.2580	0.2017	2.2245	-4.3336
-4.613	-6.2664	0.1978	2.2459	-4.4717

Table 6.5: Mean of the logarithm of energy, Variance, skewness and kurtosis of the final distributions, for n=0 and for the different values of the resistivity for the distributions in fig. (6.3).

In table (6.6) we see the percentage of the final distribution that gets accelerated for different values of the resistivity. I calculate the fraction of particles for which

$$\frac{E_{final} - E_{initial}}{E_{initial}} \geq constant \tag{6.20}$$

where *constant* takes the values 0.1,1, 10 and 100. In column one we see the fraction of the final distribution that increases its initial energy by 0.1 (10%). In column two we see the fraction of the final distribution that doubles its initial energy. In column three we see the fraction of the final distribution that increases its initial energy by 10 times. In column four the fraction of the final distribution that increases its initial energy by 100 times. In column five we see the highest energy that protons acquire during the calculation.

Several features can be seen in table (6.6). First, as the resistivity increases from $\log(\eta) = -10.613$ to $\log(\eta) = -4.613$ (for higher values, too) the fraction of the distribution that gets thermalised increases. For $\log(\eta) = -6.613$ we get the higher energy particles. For this value of the resistivity the highest fraction of the distribution increases energy by

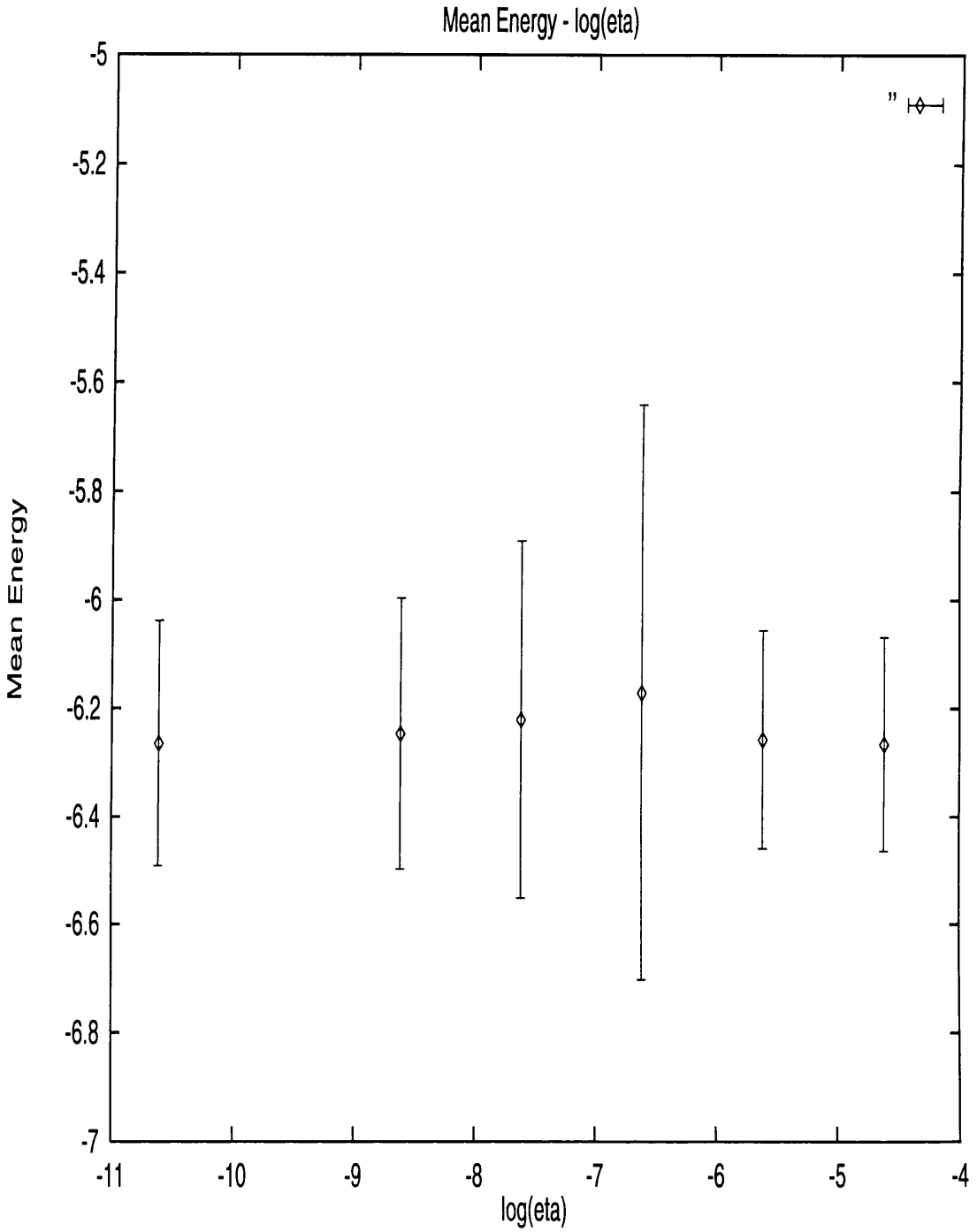

Figure 6.4: Mean of the logarithm of energy of the final distributions of protons versus the logarithm of the resistivity. The final distributions are acquired after 5360 integration timesteps, for the following values of the resistivity: a) $\eta = 3.1724 \times 10^{-11}$, b) $\eta = 3.1724 \times 10^{-9}$, c) $\eta = 3.1724 \times 10^{-8}$, d) $\eta = 3.1724 \times 10^{-7}$, e) $\eta = 3.1724 \times 10^{-6}$, and f) $\eta = 3.1724 \times 10^{-5}$. The fundamental eigenmode, n=0 is used in the calculation. The energy in the wave was 10% of the equilibrium magnetic field energy. The errorbars are the variance on the mean energy. The enrgy is given in units of the protons rest mass.

more than 100 times.

log(η)	> 10%	> 1	> 10	> 100	MeV
-10.613	0.322	0.061	0.02	0.002	0.06
-8.613	0.372	0.073	0.026	0.003	0.08
-7.613	0.373	0.088	0.043	0.014	0.19
-6.613	0.37	0.108	0.07	0.041	0.27
-5.613	0.436	0.11	0.005	0	-
-4.613	0.50	0.073	0.001	0	-

Table 6.6: Fraction of final distribution that is accelerated by 0.1,1, 10 and 100 times. The distributions are shown in fig. (6.3).

We investigate now how the energy distributions change for the values of the resistivity between the values $\eta = 3.1724 \times 10^{-7}$ and $\eta = 3.1724 \times 10^{-6}$. The values of the resistivities that we calculate distributions for are: a) $\eta = 9.1042 \times 10^{-7}$, b) $\eta = 1.17054 \times 10^{-6}$, c) $\eta = 1.3006 \times 10^{-6}$, d) $\eta = 1.43066 \times 10^{-6}$, e) $\eta = 1.56072 \times 10^{-6}$, and f) $\eta = 2.6012 \times 10^{-6}$. In fig. (6.5) we see the final distributions for these values of the resistivity.
Similar features as before are observed. The energy that the particles gain increases with resistivity between $\eta = 9.1042 \times 10^{-7}$ and $\eta = 1.43066 \times 10^{-6}$ and then decreases again. So, particles gain the most energy when the resistivity takes the value $\eta = 1.43066 \times 10^{-6}$. The highest ratio of the energy that the particles gain to the energy that the wave loses is 4.6×10^{-3}. In table 6.7 we show the values for energy lost by the wave, energy gained by the particles and their ratio for the distributions in fig. (6.5). Again the energy gain of the particles is much smaller than the energy that the wave loses during the 1 second of our calculation.

log(η)	energy in the wave	energy in the particles	ratio
-6.041	1.13×10^{18}	3.6×10^{15}	3.2×10^{-3}
-5.932	1.16×10^{18}	3.9×10^{15}	3.4×10^{-3}
-5.886	1.18×10^{18}	4.51×10^{15}	3.8×10^{-3}
-5.844	1.2×10^{18}	5.5×10^{15}	4.6×10^{-3}
-5.807	1.22×10^{18}	4.81×10^{15}	4.0×10^{-3}
-5.585	1.31×10^{18}	6.012×10^{13}	4.6×10^{-5}

Table 6.7: Energy in the wave and the particles for different resistivities, for n=0. The distributions are shown in fig. (6.5).

In fig. (6.6) we plotted the mean of the logarithm of the energy of the distributions in fig. (6.5) versus the logarithm of the resistivity. The errorbars are the variance on the

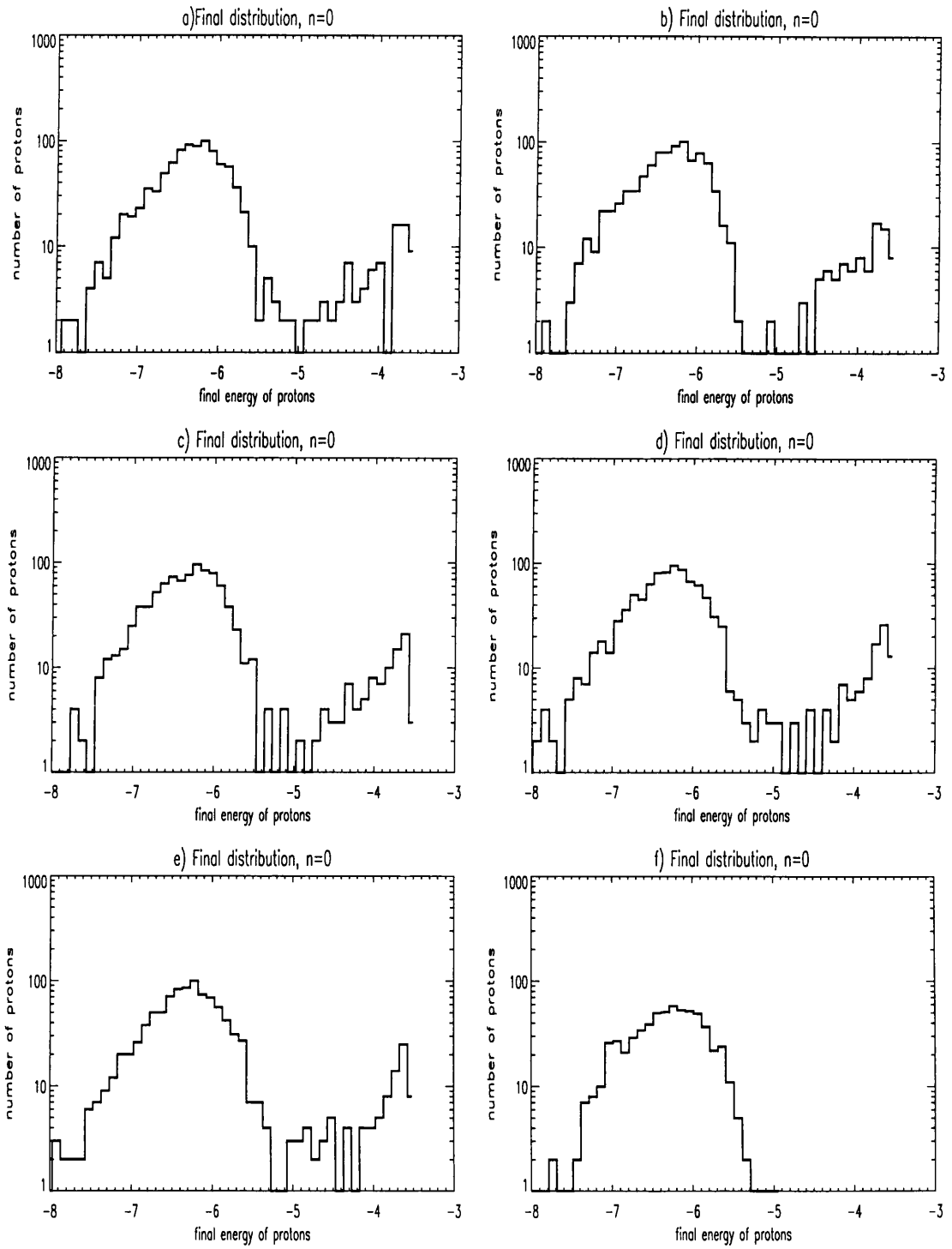

Figure 6.5: Final distributions of protons. The final distributions are acquired after 5360 integration timesteps, for the following values of the resistivity: a) $\eta = 9.1042 \times 10^{-7}$, b) $\eta = 1.17054 \times 10^{-6}$, c) $\eta = 1.3006 \times 10^{-6}$, d) $\eta = 1.43066 \times 10^{-6}$, e) $\eta = 1.56072 \times 10^{-6}$, and f) $\eta = 2.6012 \times 10^{-6}$. The fundamental eigenmode, n=0 is used in the calculation. The energy in the wave was 10% of the equilibrium magnetic field energy.

mean energy of each distribution. As before we have an increase in the mean energy and the variance when the resistivity increases from $\eta = 9.1042 \times 10^{-7}$ to $\eta = 1.43066 \times 10^{-6}$. After that the mean energy and the variance decreases again.

$\log(\eta)$	mean energy	variance	skewness	kurtosis
-6.0408	-6.1270	0.6183	1.2704	-1.1315
-5.9316	-6.1080	0.6545	1.2348	-1.1845
-5.8859	-6.0937	0.6920	1.2009	-1.1600
-5.8445	-6.0588	0.7568	1.1483	-1.3701
-5.8067	-6.0888	0.6882	1.2042	-1.2136
-5.5848	-6.2746	0.2143	2.1565	-4.0101

Table 6.8: Mean Energy, Variance, skewness and kurtosis of the final distributions, for n=0 and for the different values of the resistivity for the distributions in fig. (6.5).

$\log(\eta)$	> 10%	> 1	> 10	> 100	MeV
-6.0408	0.360	0.119	0.086	0.055	0.3
-5.9316	0.375	0.116	0.095	0.062	0.29
-5.8859	0.382	0.14	0.10	0.074	0.3
-5.8445	0.412	0.146	0.107	0.08	0.3
-5.8067	0.403	0.137	0.091	0.069	0.3
-5.5848	0.247	0.074	0.003	0.001	0.01

Table 6.9: Fraction of final distribution that is accelerated by more than 0.1, 1, 10 and 100 times. The distributions are shown in fig. (6.5).

In fig. (6.7) we plotted the energy lost by the wave after 5360 timesteps as a function of the resistivity. Also in the same graph we have plotted the energy gain of the particles for the same time as a function of the resistivity. Both energies are normalised to the initial wave energy.

The resistivity was treated as a parameter in our calculations. We were increasing the value of the resistivity trying to match the wave energy loss to the particles energy gain. As the resistivity was increasing, so was the size of the diffusion region. This means that the adiabaticity radius is defined by assuming the presence of higher energy particles.

One would expect that as the resistivity increases so should the energy that particles gain until a value of the resistivity is found where the energy lost by the wave matches the energy gained by the particles. For fig. (6.7) this is obviously not the case. In chapter 5 we saw that the details of the particle orbits are very important. Up to $\eta = 1.43066 \times 10^{-6}$,

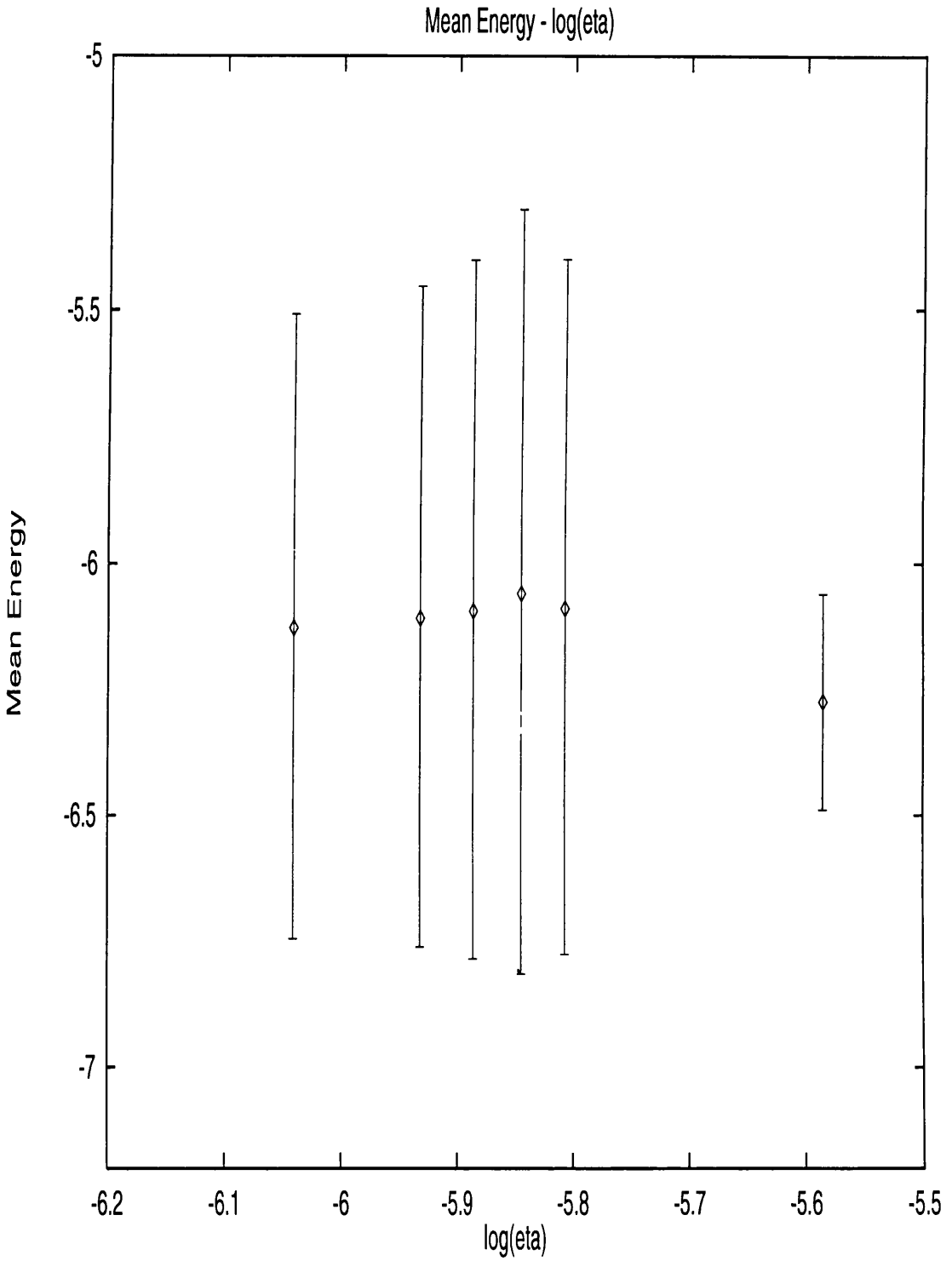

Figure 6.6: Mean Energy of the final distributions of protons versus the logarithm of the resistivity. The final distributions are acquired after 5360 integration timesteps, for the following values of the resistivity: a) $\eta = 9.1042 \times 10^{-7}$, b) $\eta = 1.17054 \times 10^{-6}$, c) $\eta = 1.3006 \times 10^{-6}$, d) $\eta = 1.43066 \times 10^{-6}$, e) $\eta = 1.56072 \times 10^{-6}$, and f) $\eta = 2.6012 \times 10^{-6}$. The fundamental eigenmode, n=0 is used in the calculation. The energy in the wave was 10% of the equilibrium magnetic field energy. The errorbars are the variance on the mean energy.

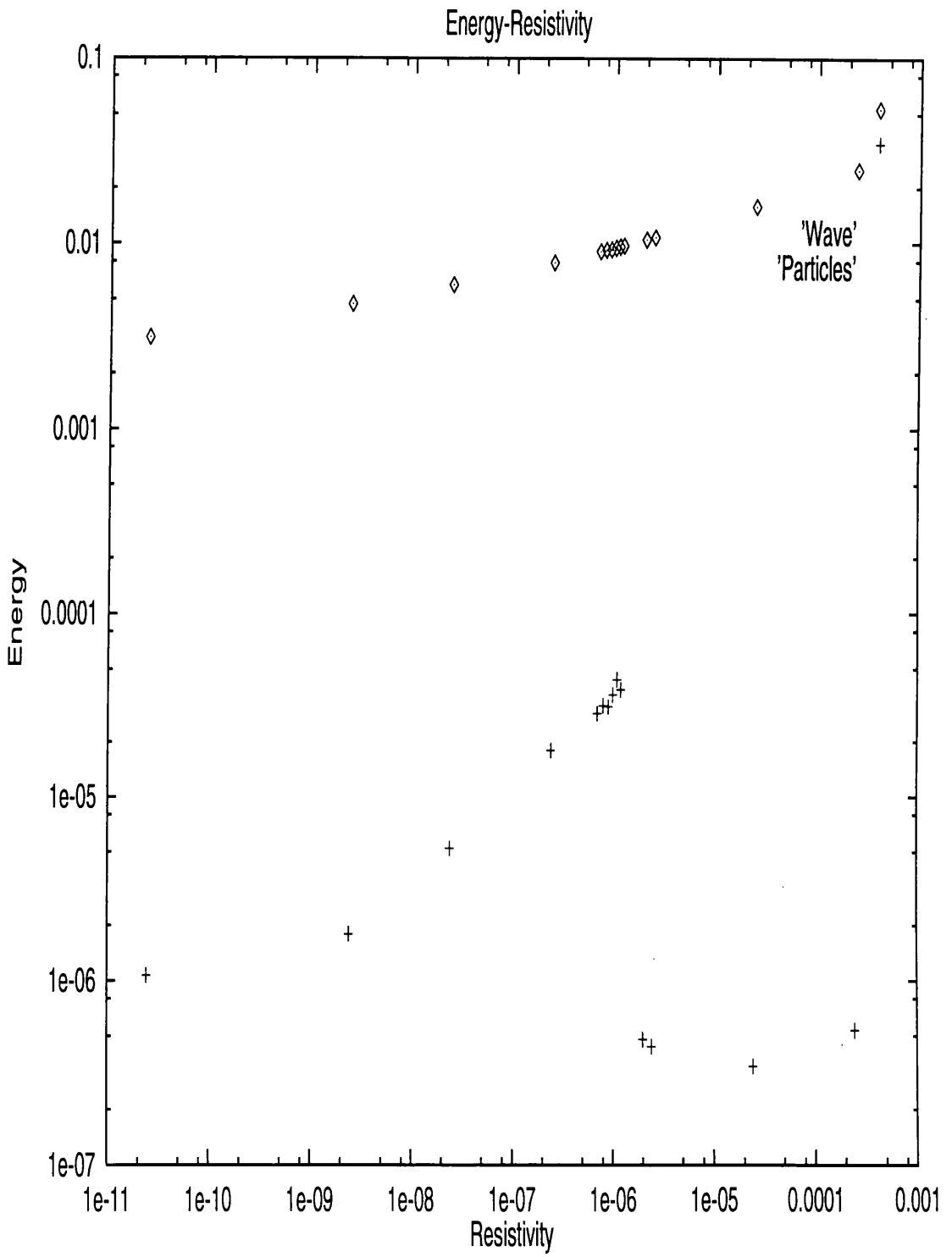

Figure 6.7: Energy lose of the wave, and energy gain of the particles versus resistivity. All the calculation are for the fundamental eigenmode in each value of the resistivity. Both energies are normalised to the initial wave energy. The energy in the wave was 10% of the equilibrium magnetic field energy.

some particles are trapped close to the neutral point region and they are performing a field-free acceleration by the electric field (see section 5.2). For higher resistivities, the diffusion region increases so much that the perturbation is totally insignificant compared to the background magnetic field. For higher resistivities more particles are heated (increases their energy by 10%) but very few are accelerated to high energies.

6.3.2 Effect of the Ambient Density

A different value of the ambient density gives a completely new set of eigenvalues for the same value of the resistivity. So, even though the spatial form of the eigenmodes does not change, the magnitude of the electric and magnetic field perturbations change. Also, the decay and oscillation times change. In fact, the decay and oscillation times decrease with decreasing density. Recall the definition of constant $\mathcal{A}$ in section 4.2

$$\mathcal{A} = \frac{{u_A}^2}{c^2}\frac{{d_p}^2}{D^2}. \tag{6.21}$$

Here u_A is the Alfvén velocity at the boundary of the system. When the ambient density decreases the Alfvén velocity increases. In fig. (6.8) we see final distributions for the same spatial form of the electric and magnetic field perturbations (those shown in figures (5.4) and (5.5)) but for different values of the ambient density. The values of the ambient density and the corresponding resistivities are: (a) 10^6 cm^{-3} ($\eta = 3.1724 \times 10^{-5}$), (b) 10^8 cm^{-3} ($\eta = 3.1724 \times 10^{-6}$), (c) 10^9 cm^{-3} ($\eta = 1.0032 \times 10^{-6}$), and (d) 10^{10} cm^{-3} ($\eta = 3.1724 \times 10^{-7}$). Decreasing the density produces a greater proportion of high energy particles, but fails to remedy the discrepancy between wave and particles.

6.3.3 Increasing the integration time

Since the energy that the wave loses does not match the energy that the protons gain during the time of 1 sec that we use in our calculation, we have tried longer integration times. Maybe the matching of the energies could be done after averaging over longer times.

In fig. (6.9) we the final distribution of protons for different integration times. The resistivity is $\eta = 1.0032 \times 10^{-6}$ and the ambient density is 10^9 cm^{-3}. The spatial form of the electric and magnetic fields is the same as for $\eta = 3.1724 \times 10^{-7}$ when the ambient density is 10^{10} cm^{-3}. The decay time of the wave is $\sim$ 81 sec and the oscillation time is

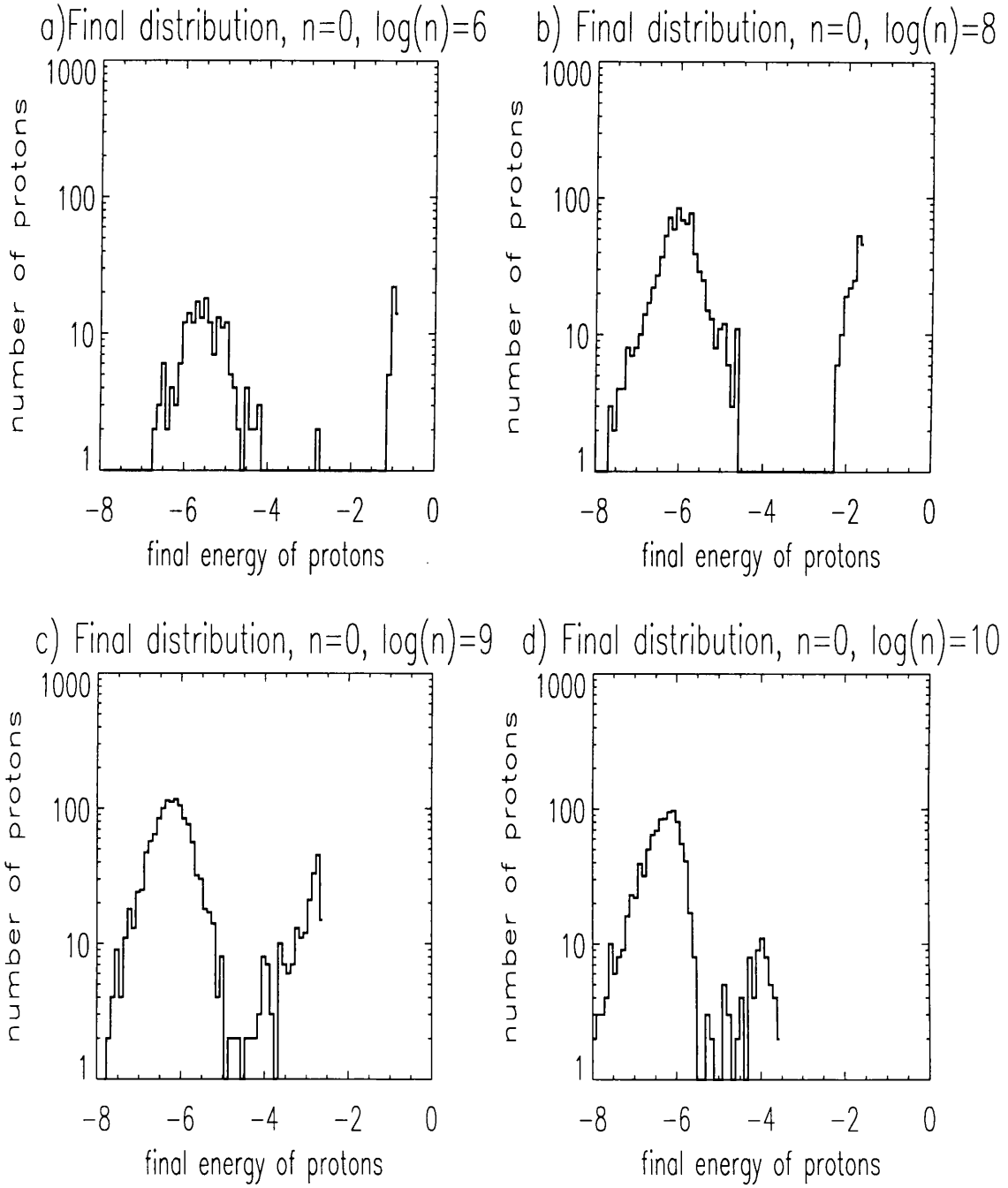

Figure 6.8: Final distributions of protons. The final distributions are acquired for different densities and different resistivities but for the same spatial form of the electric and magnetic fields. The fundamental eigenmode, n=0 is used in the calculation. The energy in the wave was 10% of the equilibrium magnetic field energy. The ambient density is (a) 10^6 cm^{-3} ($\eta = 3.1724 \times 10^{-5}$), (b) 10^8 cm^{-3} ($\eta = 3.1724 \times 10^{-6}$), (c) 10^9 cm^{-3} ($\eta = 1.0032 \times 10^{-6}$), and (d) 10^{10} cm^{-3} ($\eta = 3.1724 \times 10^{-7}$).

$\sim$ 49 sec. The distribution was plotted after a) 0.25 sec, b) 0.5 sec, c) 1 sec, d) 2 sec, e) 5 sec, and f) 8 sec. Longer integration times are too time consuming computationally, and were not attemped. When the particles are followed for longer times, we see that some of them gain very high energies. The highest energy that they gain for the t=8 sec is $\sim$ 110 MeV. As we see 8 sec is a significant fraction of the oscillation period. The particles keep on increasing their energy during this time. Still the total energy of the distribution does not match the energy lost by the wave.

In fig. (6.10) we have plotted the energy lost by the wave for times a) - f) and the energy gain by the particles for the same times. Both energies were normalised to the initial energy in the perturbation. As the integration time increases the particles gain energy faster than the wave loses energy.

However, even after the averaging over longer integration times the energy that the wave loses does not match the energy that particles gain.

6.3.4 Higher Eigenmodes

When the resistivity is $\eta = 3.1724 \times 10^{-11}$ and the eigenvalue is n=32, then the magnitude of the perturbation has to be $E_o = 4.3 \times 10^{-4}$ so that the wave energy is 10% of the equilibrium magnetic field energy. After 5360 timesteps, the wave loses, 2.88×10^{19} erg/cm and the particles gain 2.71×10^{13} erg/cm. The ratio of the two is 9.4×10^{-7}. If we compare this with the result for the same value of the resistivity but for n=0 (see table 6.4) we see that for the higher eigenvalue the particles gain less energy during the same time. The wave loses more energy during the time of our calculation (decay and oscillation times for n=32 and number density 10^{10} cm^{-3} are given in table 4.5). So, the fraction of the wave energy that particles absorb is much smaller than when the eigenmode is n=0. The main reason that particles don't gain as much energy is that they are not trapped close to the neutral point anymore.

We had similar results for the same eigenmode but for lower ambient density. The following two examples are for ambient density of 10^9 cm^{-3}. When the resistivity is $\eta = 1.0032 \times 10^{-6}$ and the eigenvalue is n=9, then the magnitude of the perturbation has to be $E_o = 1.56 \times 10^{-2}$ so that the wave energy is 10% of the equilibrium magnetic field energy. After 5360 timesteps, the wave loses, 5.68×10^{19} erg/cm and the particles gain 1.67×10^{14} erg/cm. The ratio of the two is 2.94×10^{-6}.

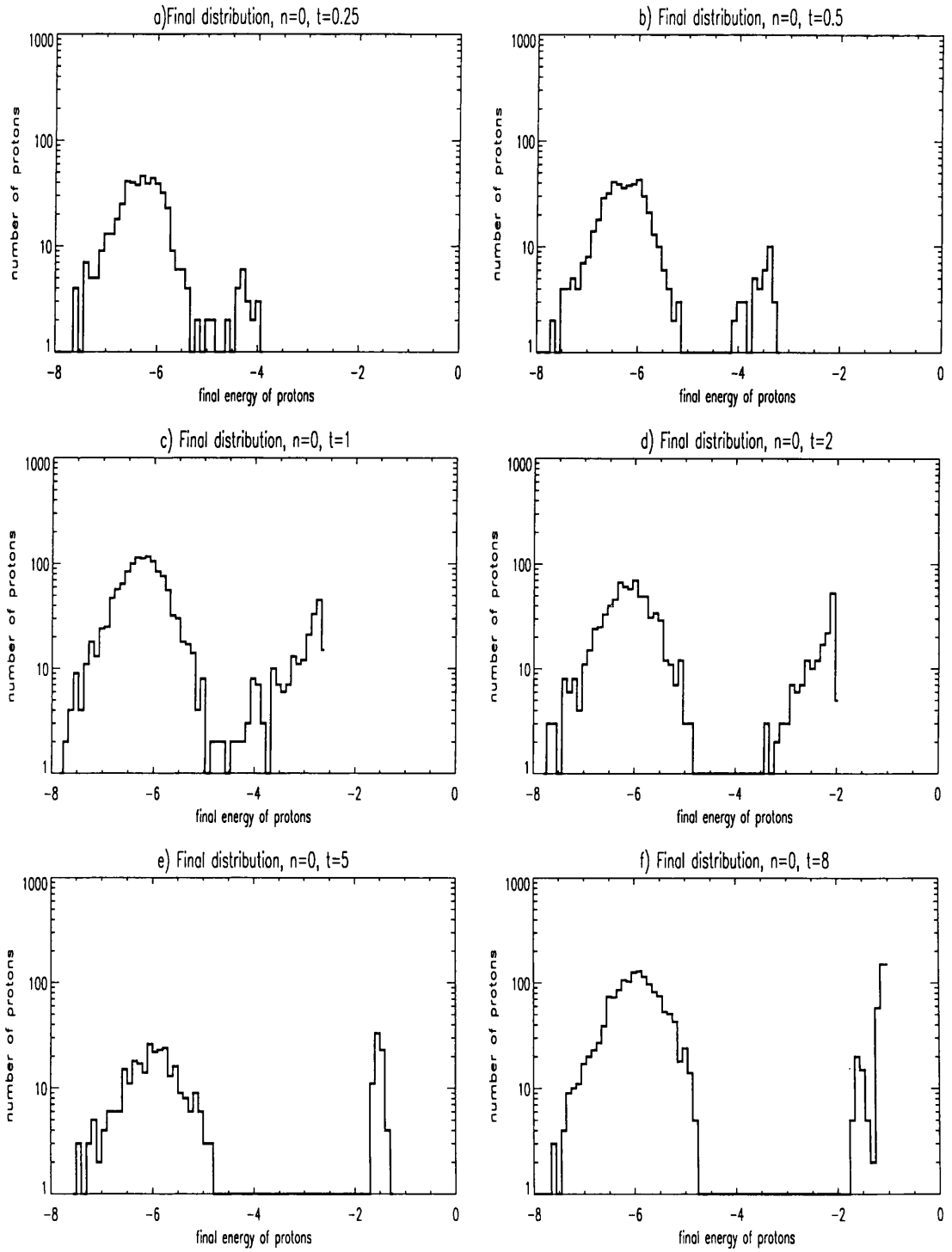

Figure 6.9: Final distributions of protons. The final distributions are acquired for $\eta = 1.0032 \times 10^{-6}$ after a) 1340 timesteps, b) 2680 timesteps, c) 5360 timesteps, d) 11720 timesteps, e) 26800 timesteps, and f) 42880 timesteps. The fundamental eigenmode, n=0 is used in the calculation. The energy in the wave was 10% of the equilibrium magnetic field energy. The ambient density is 10^9 cm^{-3}.

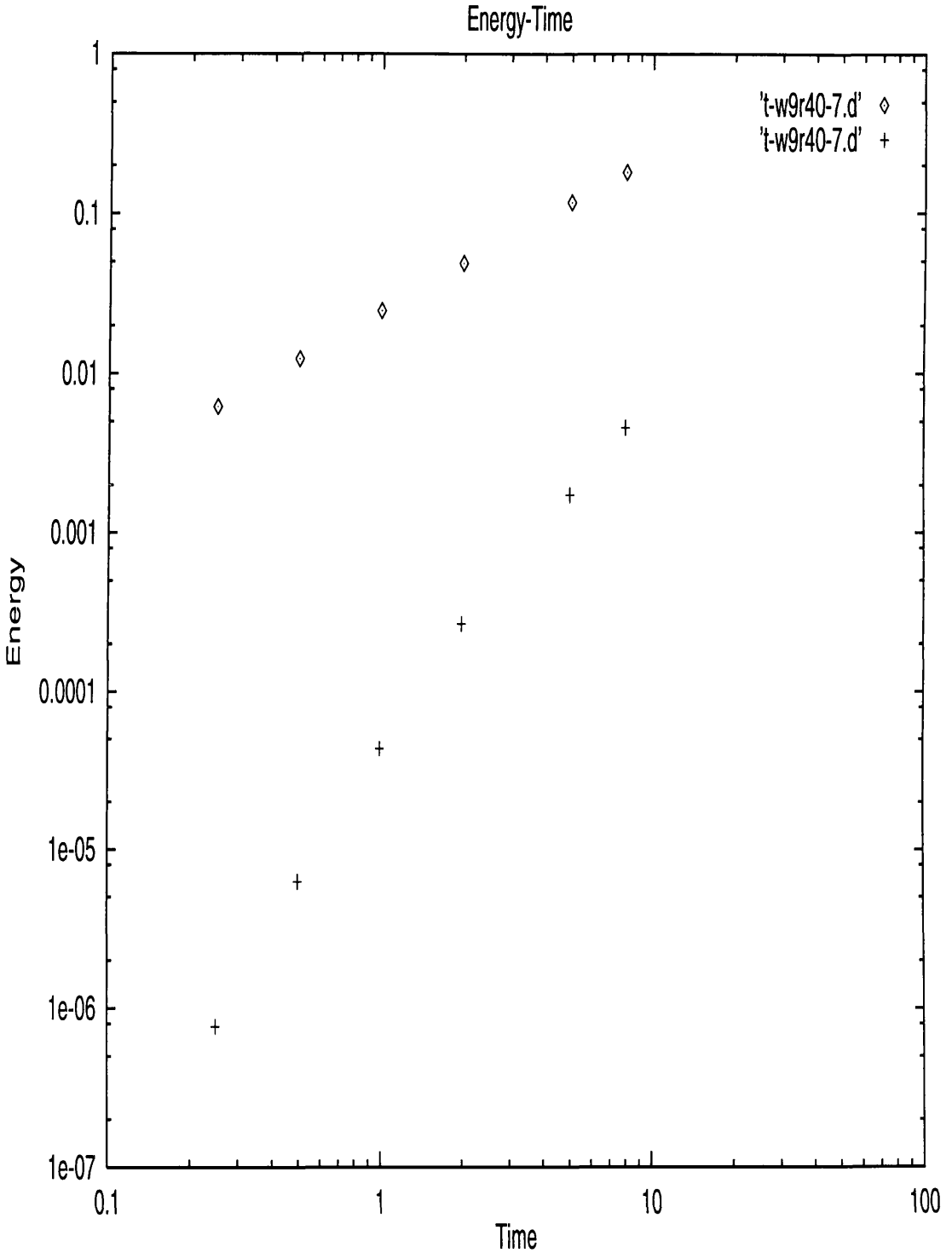

Figure 6.10: Enegry loss of the wave versus time and Energy gain of particles versus time for the distributions of protons in fig. (6.9).

For n=32 and the same value of the resistivity, the magnitude of the perturbation is $E_o = 2 \times 10^{-5}$. After 5360 timesteps, the wave loses, 1.14×10^{20} erg/cm and the particles gain 2.45×10^{12} erg/cm. The ratio of the two is 2.15×10^{-8}.

So, as the eigenvalue increases the energy that the wave loses in a specific amount of time increases, but the energy that particles gain in the same time decreases. No higher eigenmodes than n=32 where tried. In fig. (6.11) we see the initial and final distributions of protons for $\eta = 1.0032 \times 10^{-6}$ after 5360 timesteps. The eigenmodes n=9 and n=32 were used in the calculation. The ambient density is 10^9 cm^{-3}. Very little change from the initial distribution can be seen in both cases (even less when n=32).

6.4 Check of Linearity

To be in the linear regime, the amplitude of the disturbance shouldn't change the results. To test that we calculated the amplitudes assuming that the wave has 1% of the equilibrium magnetic field energy. The amplitudes for several values of the resistivity and for number density 10^{10} cm^{-3} are given in table 6.1. Using these amplitudes we calculated particle distributions for different values of the resistivity and we compared the results with those in section 6.3.

6.4.1 n=0

The energy that the wave has at t=0 is $E_{wave} = 1.25 \times 10^{19}$ erg/cm.

log(η)	energy in the wave	energy in the particles	ratio
-6.613	9.8×10^{16}	1.3×10^{14}	1.33×10^{-3}
-5.613	1.35×10^{17}	1.08×10^{13}	8×10^{-5}

Table 6.10: Energy in the wave and the particles for different resistivities, for n=0. $E_{wave} = 1.25 \times 10^{19}$ erg/cm.

Again by increasing the resistivity by one order of magnitude from $\eta = 3.1724 \times 10^{-7}$ to $\eta = 3.1724 \times 10^{-6}$, the total energy that particles gain decreases significantly. When the resistivity is $\eta = 3.1724 \times 10^{-6}$ more particles are heated (increase their energy by 10%) but no high energy particles are produced. In table 6.10 we see the energy lost by the wave, the energy gained by the particles and their ration for these two values of the resistivity. Although the ratio are not exactly the same as those in table 6.4, they are so

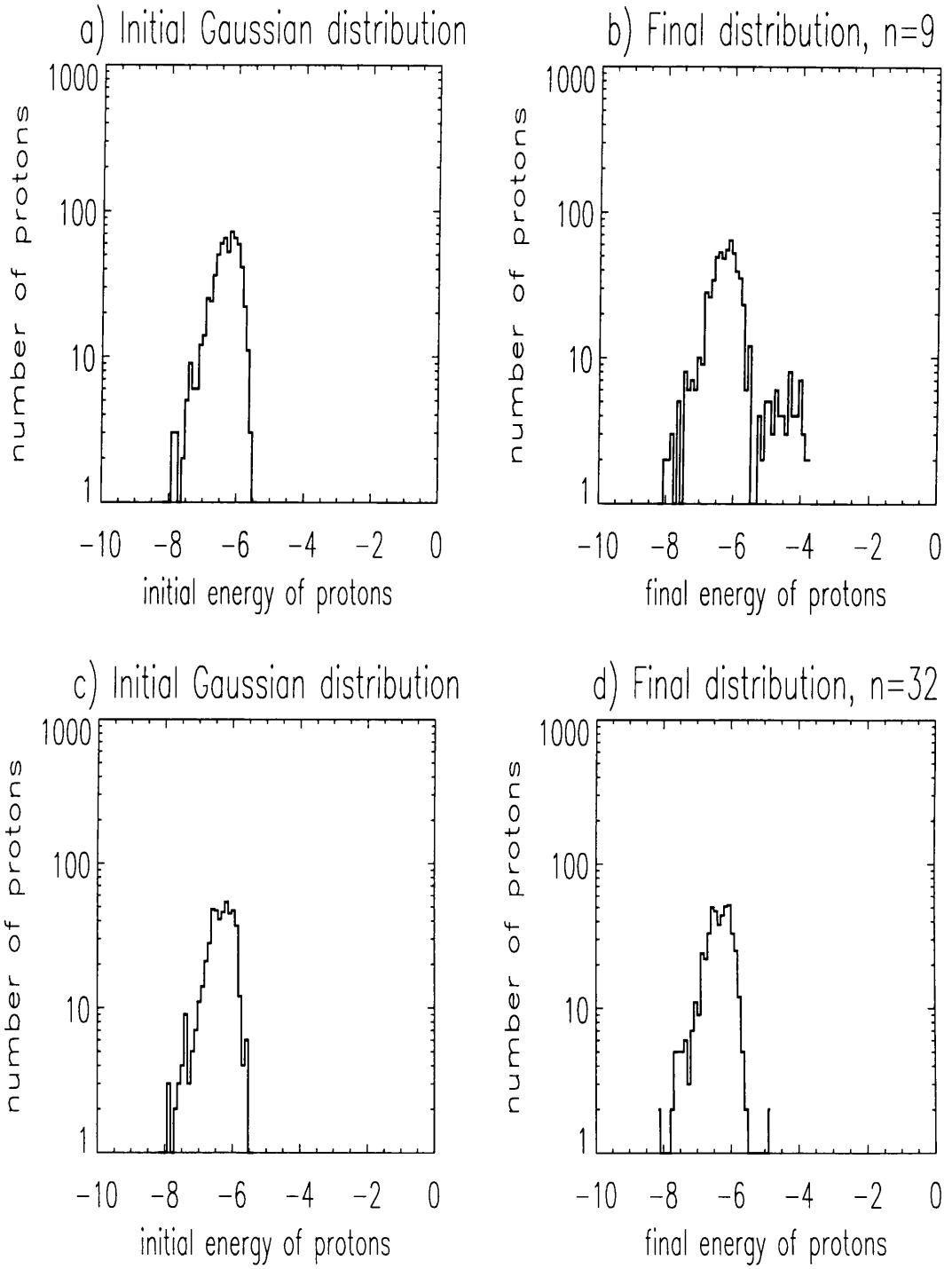

Figure 6.11: Final distributions of protons. The final distributions are acquired for $\eta = 1.0032 \times 10^{-6}$ after 5360 timesteps. Two eigenmodes were used in the calculation, n=9 and n=32. The energy in the wave was 10% of the equilibrium magnetic field energy. The ambient density is 10^9 cm^{-3}. In this graph the initial distributions of the particles are shown too.

in order of magnitude.

Thus it appears that we are generally in the linear regime in that our results are fairly independent of the wave amplitude

6.4.2 Ambient density of 10^9 cm^{-3}

We checked linearity for lower densities too. In table 6.11 we see the results for $\eta = 1.0032 \times 10^{-6}$ and $\eta = 1.0032 \times 10^{-5}$ for the fundamental eigenmode. The spatial form of the wave is the same as for $\eta = 3.1724 \times 10^{-7}$ to $\eta = 3.1724 \times 10^{-6}$, when the ambient density is 10^{10} cm^{-3}.

The decrease in the particles energy gain is observed once more when we go from $\eta = 1.0032 \times 10^{-6}$ to $\eta = 1.0032 \times 10^{-5}$.

log(η)	energy in the wave	energy in the particles	ratio
-5.999	3.075×10^{16}	2.2×10^{14}	7.2×10^{-4}
-4.999	2.11×10^{17}	3.52×10^{12}	1.7×10^{-5}

Table 6.11: Energy in the wave and the particles for different resistivities, for n=0. The values of the resistivity are $\eta = 1.0032 \times 10^{-6}$ and $\eta = 1.0032 \times 10^{-5}$. $E_{wave} = 1.25 \times 10^{19}$ erg/cm and $n = 10^9$ cm^{-3}.

6.5 Conclusions

The calculations presented in this chapter force us to re-examine the nature of 'resistivity'. Particles trapped for long periods near the neutral point are freely accelerated and clearly extract energy from the wave. However, they do not contribute to the resistivity (cf section 4.3). Perhaps a more correct description of the form of the resistivity might proceed retaining the $\partial \underline{j}/\partial t$ term in Ohm's law (2.9).

Irrespective of difficulties in defining the 'correct' value of the 'resistivity', we have demonstrated that the passage of such a reconnective disturbance may accelerate protons to γ ray producing energies (see section 1.3.5), or at least to energies where they could play a role in energy transport (see Brown et al. 1990).

The fraction of high energy protons depends on the ambient density. The highest energy particles are produced when the ambient density has the smaller value.

Chapter 7

Conclusions and Future Work

The work presented in this thesis is an attempt to understand the micro-physics of particle acceleration in the central area of the reconnection (where kinetic phenomena are important) and tie it to the behaviour of the larger active region area using a magnetic configuration that contains an X-type neutral point.

First we calculated particle orbits in a magnetic field containing an X-type neutral point with a time varying electric field imposed. The acceleration mechanism does not act only on the tail of the Maxwellian distribution but on a large fraction of it. The effectiveness of acceleration of protons and electrons varies according to the frequency of oscillation invoked. When electrons are accelerated, they are accelerated more rapidly than protons.

We calculated numerically the eigenmodes resulting from the Craig and McClymont (1991) analysis of an MHD disturbance in an X-type neutral point. Also, we calculated the electric field and the magnetic field perturbation resulting and showed their spatial and temporal structure. We used these fields to calculate particle orbits and particle distributions. Our aim was to match the MHD calculation with the test particle calcualtion. This has not proved possible for the form of scalar resistivity that we used in our calculations. However high energy protons are produced from such a linear reconnective disturbance. The fraction of high energy particles increases as the ambient density decreases.

As a next step we would like to investigate the behaviour of a linear reconnective disturbance when a time dependent form of the resistivity is assumed. We will be interested on the effect on particle acceleration of such a disturbance.

7.1 Development of Self-Consistent Reconnection Models

Particles get trapped in the magnetic field configuration that contains an X-type neutral point and some of them (the most unmagnetised initially) after crossing the neutral point several times gain a significant amount of energy. The ones that don't attain high energies seem to get heated. The X-type neutral point geometry discussed above is very enlightening but simple in comparison with the complexity of the solar corona. In order to simulate a realistic magnetic field configuration (3-D) several steps are required. First, a more realistic magnetic field configuration is one where a small 'normal' component of the magnetic field is present at the neutral point. A second step thus would be to use the geometry discussed in Van Tend and Kuperus (1978) and more exactly in Forbes and Isenberg (1992). The Forbes and Isenberg (1992) magnetic field is a model for the field in the corona with a current sheet present. It is mathematically tractable yet significantly more realistic than a simple magnetic field containing an X-type neutral point. I will study the case where the current sheet breaks up into many neutral points (for instance as a consequence of the tearing mode instability) and consider both particle orbits near the sheet and the fates of particles in the wider coronal environment (MacKinnon and Petkaki 1995). Particles accelerated in one X-type neutral point could proceed to a second stage of acceleration or into multiple stages of acceleration (Kliem 1994).

Further development of the integration schemes for particle trajectories is needed. An attempt will be made to use symplectic integration schemes in order to achieve higher accuracy and reduce the computation time (Yoshida 1993). This is very important for calculating the details of electron orbits for a time comparable to the time that proton orbits are calculated.

7.2 Development of Current Sheets

From observations we know that the footpoints of the bipolar magnetic field in the solar corona are anchored in the photosphere and the convection zone, and are moved around and mixed randomly by the motions in the convective zone. It is possible that several 'tangential discontinuities', that is current sheets or X-type neutral points, are produced due to this motion. When the development of the calculation that I describe in the previous paragraph is clear and well understood I will attempt to see how a magnetic configuration

that contains several X-type geometries is evolving when magnetic reconnection occurs in more that one neutral points. If energy is released in some neutral points then this can trigger similar processes in others near by. A point could be reached where such a configuration becomes unstable and catastrophic energy release occurs on a large scale.

7.3 Solar Noise Storms

Signatures of particle acceleration are found in noise storms in the corona. At that time the corona is not flaring and the mechanism that could cause this particle acceleration is not clear. The possibility of small scale magnetic reconnection as a mechanism for producing high energy particles that cause noise storms becomes very apparent. New emerging magnetic flux could cause the small scale reconnection. A small scale enhancement in hard X-rays should be observed at about the same time as noise storms but has not been detected yet. The possibility exists that the hard X-rays are observed first and after a small delay the energetic electrons propagate into the corona exciting plasma waves. This part of the work would be a continuation of what I have been doing with Dr N. Vilmer and will be done in collaboration with her. I will look at observations of Hard X-rays (BATSE data), Soft X-rays (GOES data) and radio observations in the decimetric and metric band with the Nancay RadioHeliograph in order to confirm this hypothesis or to find a possible relationship.

7.4 Analytic calculations of Particle Orbits

Using Mathieu functions one can approximate the trajectories of particles close to the neutral point in the presence of a timevarying electric field. Such approximate trajectories might form the basis of a more self-consistent calculation.

7.5 Chaotic Conductivity

A numerical integration method should respect the conservation of energy and of the volume of phase space in an integrable Hamiltonian system. A symplectic integrator may be constructed that does conserve the above mentioned quantities (Yochida 1993). But for non-integrable systems one cannot expect to conserve energy in each step (Ge and

Marsden, 1988). Despite this fact there is an advantage for symplectic schemes when a method of constant time step is used. The Bulirsch-Stoer is a variable step method so is not appropriate for using in symplectic integrators. If one uses the adiabatic description of the motion away from the neutral point area then a method with constant step could be used inside the region where chaotic properties are observed.

We would like to calculate the chaotic characteristics of particles orbits in time-varying electromagnetic fields rigorously. Important tools in the study of chaos are: particle trajectories, Lyapunov characteristic exponent, the Painleve property (which implies integrability if it stands) and the Poincare surface of section plots. Calculation of chaotic conductivity would be the objective of calculating the chaotic characteristics (Martin 1986). If chaotic motion can indeed produce the collisionless resistivity necessary for reconnection then it is a mechanism of central importance in the modelling of solar flares. Collective effects such as wave-particle interactions could also be important in determining the chaotic conductivity.

7.6 Reconnection in nonzero B_z

Prelimilary investigations have shown that when a significant component of the magnetic field is present along the X-line then the particles do not cross from the neutral line more than once in the presence of an ad hoc time varying electric field. The multiple passage of a particle through the neutral point is not observed any more. Instead the particle gets injected from the nonadiabatic area and leaves the system very quickly. This happens faster as the perpendicular component of the magnetic field increases. Thorough investigation of the consequences on particle acceleration from an ad hoc time varying electric field will be attempted in future work.

In the presence of wave as discussed in Chapters 4 and 5 preliminary results have shown that particle orbits are not influenced significantly. Understanding of the particle orbits details in the presence of finite B_z component requires a fuller 3-d treatment.

Bibliography

[1] Abramovitz M., and Stegun I.A. :1964, *Handbook of Mathematical functions*, Applied Mathematics series, vol. 55 (Washington: national Bureau of standards; reprinted 1968 by Dover Publications, New York)

[2] Ambrosiano J., Matthaeus W.H. Goldstein M.L. and Plante D. :1988, *J. Geophys. Res.*, **93**, A12, 14383

[3] Antonucci, E. et al. :1982, *Solar Phys.*, **78**, 107

[4] Athay G. R. :1986 in *Physics of the Sun Vol. II*, edited by P.A. Sturrock, T.E. Holzer, D.M. Mihalas, and R.K. Ulrich, Reidel

[5] Axford W.I. :1984, in *Magnetic reconnection in space and laboratory plasmas*, **Geophysical Monograph 30**, AGU Publishers, Washington, D.C., U.S.A.G.R.

[6] Bai T. and Dennis B.R. :1985, *Astrophys. J.*, **292**, 699

[7] Bai T. and Sturrock P.A. :1989, *Ann. Rev. Astron. Astrophys.*, **27**, 421-67

[8] Biskamp D. :1986, *Phys. Fluids*, bf 29, 1520

[9] Brown J.C. :1971, *Solar Phys.*, **18**, 489

[10] Brown J.C. :1975, in *Solar Gamma-, X-, and EUV Radiation*, 245 edited by S.R. Kane

[11] Brown J.C., Smith D. F. :1980 *Reports on Progress in Physics*, **43**, 125

[12] Brown, J.C., Cassinelli, J.P. and Collins, G.W. II : 1991, *Astrophys. J.* **378**, 307

[13] Brown J.C., Karlicky M., MacKinnon A.L., and van den Oord G.H.J. :1990, *Astrophys. J. Suppl. Ser.*, **73**, 343

[14] Brown J.C., Loran J.M., and MacKinnon A.L. :1984, *Astr. Astroph.*, **147**, L10

[15] Brown J.C., Smith D. F., Spicer D. S. :1981 NASA *The Sun as a Star*, 181

[16] *Brown J.C., Mundell C.G., Petkaki P., Jenkins G., 1994 in press *Astron. Astrophys*

[17] Bruggmann G., Vilmer N., Klein K.-L., and Kane S.R. :1994 *Solar Phys.*, **149**, 171

[18] Bruhwiler D.L. and Zweibel E.G. :1992, *J.Geophys.R.*, **97**, A7, 10825

[19] Bulanov S. V. :1980 *Sov. Astron. Lett.*, **6**, 206

[20] Bulanov S. V. and Sasarov P.V. :1976 *Sov. Astron.*, **19**, 464

[21] Burkhart G.R. Drake J.F. and Chen J. :1990 *J. Geophys. Res.*, **95**, NO. A11, 18833

[22] Burkhart G.R. Drake J.F. and Chen J. :1990 *J. Geophys. Res.*, **96**, 11539

[23] Cane H.V., McGuire R.E., von Rosenvinge T.T. :1986, *Astrophys. J.*, **301**, 448

[24] Chen F.F. :1984 in *Introduction to Plasma Physics and Controlled Fusion* Plenum Press

[25] Chen J. :1992, *J.Geophys.R.*, **97**, A10, 15011

[26] Chen J. and Palmadeso :1986, *J.Geophys.R.*, **91**, 1499

[27] Cheng C.-C. and Acton L. :1994 on *X-Ray Solar Physics from Yohkoh*, 83

[28] Chubb T.A. Kreplin R.W., Friedman H. :1966, *J. Geophys. Res.*, **71**, 3611

[29] Chupp, E.L., Forrest, D.J., Ryan, J.M., Heslin, J., Reppin, C., Pinkau, K., Kanbach, G. Riger, E. Share, G.H. : 1982 *Astrophys. J.*, **263**, L95

[30] Cliver E.W., Dennis B.R., Kiplinger A.L., Kane S.R., Neidig D.F., Sheeley N.R., Jr, and Koomen M.J. :1986 *Astrophys. J.*, **305**, 920

[31] Cowley, S.W.H. :1985 in *Solar System Magnetic fields*,edited by E.R. Priest (D.Reidel Publishing Company)

[32] Craig I.J.D. :1994, *Astron. Astroph*, **283**, 331

[33] Craig I.J.D., McClymont A.N. :1991 *Ap.J.*, **371**, L41-L44

[34] Craig I.J.D., McClymont A.N. :1993 *Ap.J.*, **405**, 207-215

[35] Craig I.J.D. and Watson P.G. :1992, *Astrophys. J.*, **393**, 385

[36] Decker R.B. :1988, *Space Sci. Rev.*, **48**, 195

[37] Dennis B.R. :1985, *Solar Phys. 100*, **100**, 465

[38] Dennis B.R. :1988, *Solar Phys. 118*, 49

[39] Dennis B.R. and Schwartz R.A. :1989, *Solar Phys.*, **121**, 75

[40] Doxas I. Horton W., Sandusky K. Tajima T., and Steinolfson R. :1990, *J. Geophys. Res.*, **95**, 12033

[41] Dreicer H. :1959, *Phys. Rev.***115**, 238

[42] Dulk G.A. :1985, *Ann. Rev. Astron. Astrophys.*, **23**, 169

[43] Dungey, J.W. :1953 *Phil. Mag., Ser. 7*, **44**, 725-738

[44] Dungey J.W. 1961, *Phys.Rev.Lett*, **6**, 47

[45] Eckhardt B 1988 *Physica D*, **33**, 89

[46] Feldman U. :1994, on *X-Ray Solar Physics from Yohkoh*, 139

[47] Fisher, G.H., Canfield R.C. and McClymont, A.N. 1984, *Astrophys. J. Lett.*, **281**, L79

[48] Forbes T.G., Isenberg P.A., :1991, *Ap.J.*, **373**, 294

[49] Forbes T.G. and Priest E.R. :1987, *Rev. Geophys.*, **25**, No. 8, 1583

[50] Forman M.A., Ramaty R. and Zweibel E. G. :1986 in *Physics of the Sun Vol. II*, edited by P.A. Sturrock, T.E. Holzer, D.M. Mihalas, and R.K. Ulrich, Reidel

[51] Forrest, D.J. : 1983, in *Positron and Electron Pairs in Astrophysics*, edited by M.L. Burns, A.K. Harding, and R. Ramaty, AIP, New York, p. 3

[52] Foukal P., Hoyt C., and Gilliam L. :1986, *Astroph. J.*, **303**, 861

[53] Foukal P., Little R., and Gilliam L. :1988, *Solar Phys.*, **114**, 65

[54] Foukal P. :1990, *Solar Astrophysics*, Wiley Interscience

[55] Friedman M. :1969, *Phys. Rev.*, **182**, 1408

[56] Furth, H.P., Killeen, J. and Rosenbluth, M.N. :1963, *Phys. Fluids*, **6**, 459

[57] Gabriel A.H. :1992 *The Sun: A Laboratory For Astrophysics*, 277-296 edited by J.T. Schmelz and J.C. Brown, Kluwer Academic Publishers

[58] Galeev A. A., Corotini F. V., and Ashour-Abdalla M. :1978, *Geophys. REv. Lett.*, **5**, 707

[59] Ge, Z. and Marsden, J.E. :1988 *Phys. Lett. A*, **133**, 134-139

[60] Harris E.G., 1962 *Nuovo Cimento*, **23**, 115

[61] Hagyard, M.J., Smith J.B. Jr., Teuber D.,and West E.A. :1984, *Solar Phys.*, bf 91, 115

[62] Heyvaerts J., Priest E.R. and Rust D.M. :1977, *Astroph. J.*, **216**, 123

[63] Heyvaerts J. :1981 *Solar Flare Magnetohydrodynamics*, edited by Priest E.R.

[64] Heyvaerts J. :1985, in *Unstable Current Systems and Plasma Instabilities in Astrophysics*, ed. M.R. Kundu and G.D. Holman (Boston, Reidel), p. 95

[65] Hoyng P., Brown J.C., and van Beek H. F. :1976, *Solar Phys.*, **48**, 197

[66] Howard R. and Svestka Z :1977, *Solar Phys.*, **54**, 65

[67] Hudson H. S. :1994, *Proceedings of Kofu Symposium*, 143, NRO Report N. 360

[68] Jackson J.D. :1965, *Classical Electrodynamics*, John Wiley and Sons, Inc.

[69] Jardine M. 1991, in *Advances In Solar System Magnetohydrodynamics*, p 203

[70] Kane S.R. and Anderson K.A. :1970, *Astroph. J.*, **162**, 1003

[71] Kane S.R., Chupp, E.L., Forrest, D.J., Share G.H., and Rieger E. :1986 *Astrophys. J.*, **300**, L95

[72] Kiplinger A.L., Dennis B.R., Frost K.J. and Orwig L.E. :1983, *Astrophys. J.*, **265**, L99

[73] Kliem B. :1994, *ApJ Suppl. Ser.*, **90**, 719

[74] Klein K.-L., Trottet G., and Magun A. :1986, *Solar Phys.*, **104**, 243

[75] Koch H.W. and Motz J.W. :1959 *Rev. Mod. Phys.*, **31**, 920

[76] Kopp R.A. and Poletto G. :1986, in Coronal and Prominence Plasmas, edited by A. Poland (NASA CP 2442), p. 469

[77] Kosugi T. :1994 *Proceedings of Kofu Symposium*, 11, NRO Report N. 360

[78] Krall N.A. and Trivelpiece A.W., :1973, *Principles of Plasma Physics*, McGraw-Hill

[79] Kuijpers, J. :1993 in *The Sun: A Laboratory for Astrophysics* NATO ASI Series, edited by J.T.Schmelz and J.C. Brown, Kluwer Academic Publishers

[80] Kuijpers J. :1989, *Solar Phys.*, **121**, 163-185

[81] Lau and Finn :1990, *Astr. Astroph.*, **350**, 672

[82] Lau and Finn :1991, *Astr. Astroph.*, **366**, 577

[83] Lee L.C. and Fu Z.F. :1986, *J.Geophys.R.*, **91**, 4551

[84] Lin R.R. :1987 *Rev Geophys.*, **25**, 676

[85] Litvinenko Yu. E. and Somov B. V. :1995, *Solar Phys.*, **158**, 317

[86] Low B.C. :1982, *Solar Phys.*, **77**, 43

[87] MacKinnon 1983 *PhD Thesis*, (University of Glasgow)

[88] MacKinnon A.L. :1986 in *Flares: Solar and Stellar* Edited by P.M. Gondhalekar, RAL-86-085

[89] MacKinnon A. L. :1989 *Astr. Astroph.*, **226**, 284

[90] MacKinnon A. L. and Petkaki P. :1995 *On Coronally confined Hard X-Ray Sources*, in preparation

[91] McLean D.J. and Labrum N.R. :1985, *Solar Radiophysics* Cambridge University Press

[92] Martens, P.C.H. :1988, *Ap.J.*, **330**, L131-L133

[93] Martin R.F., :1986 *J.Geophys.R.*, **91**, 11985

[94] Masuda S. :1994, PhD Thesis (University of Tokyo)

[95] Matthaeus, W.H., Ambrosiano, J.J. and Goldstein, M.L. :1984, *Phys. Rev. Lett.*, **53**, No 15, 1449

[96] Melrose D.B. :1974, *Solar Phys.*, **37**, 353

[97] Melrose D.B. :1980, *Solar Phys.*, **67**, 357

[98] Miller J.A. and Vinas A.F. :1993, *Ap.J.*, **412**, 386

[99] Moore R., Hurford G.J., Jones H.P., and Kane S.R. :1984 *Astrophys. J.*, **276**, 379

[100] Moore R. 1988 *Astrophys. J.*, **324**, 1132

[101] Moore R. and Rabin D :1985 *Ann. Rev. Astron. Astrophys.*, **23**, 239

[102] Nakajima H. :1983, *Solar Phys.*, **86**, 427

[103] Northrop, T.G. :1963 in it The Adiabatic motion of charged Particles, Interscience Publishers

[104] Pallavicini R. :1986 in *Flares: Solar and Stellar* RAL Workshop edited by P.M. Gondhalekar

[105] Pallavicini R. in :1992 *The Sun: A Laboratory For Astrophysics*, 277-296 edited by J.T. Schmelz and J.C. Brown, Kluwer Academic Publishers

[106] Pallavicini R., Serio S., and Vaiana G.S. :1977, *Astrophys. J.*, **216**, 108

[107] Papadopoulos K. :1978, *Rev. Geophys. Space Phys.*, **15**, 113-127

[108] Parker, E.N. :1963, *Astrophys. J. Suppl. Ser.*, **77**, 177

[109] Patterson A. and Zirin H. :1981, *Ap. J. Letters*, **234**, L99

[110] Peterson L.E. and Winckler J.R. : 1959, *J. Geophys. Res.*, **64**, 697

[111] Petschek, H. :1964 in *AAS/NASA Symposium on the Physics of Solar Flares*, edited by W.N. Hess (NASA, Washington, D.C.)

[112] *P.Petkaki, A.L. MacKinnon, 1994, CESRA Meeting on *'Fragmented Energy Release in Sun and Stars', Utrecht 1993, Space Science Reviews*, **68**, 117.

[113] *P.Petkaki, A.L. MacKinnon, 1995 in preparation

[114] Phillips K.J.H. :1986 in *Flares: Solar and Stellar* RAL Workshop edited by P.M. Gondhalekar

[115] Press W.H., Teukolsky S.A., Vettering W.T., Flannery B.P. :1992 *Numerical Recipes in FORTRAN*, Cambridge University Press

[116] Priest E.R. :1981 *Solar Flare Magnetohydrodynamics*, chapter 3 edited by Priest E.R.

[117] Priest E.R. :1982 *Solar Magnetohydrodynamics*, D.Reidel Publishing Company

[118] Priest E.R. and Forbes T.G. :1986, *J.Geophys.R.*, **91**, 5579

[119] Ramaty R. :1986 in *Physics of the Sun Vol. II*, edited by P.A. Sturrock, T.E. Holzer, D.M. Mihalas, and R.K. Ulrich, Reidel

[120] Ramaty R. and Murphy R.J. :1987 *Space Sci. Rev.*, **45**, 213

[121] Reames D.V. :1990 *Ap. J. Supp. Ser.*, **73**, 235

[122] Rieger E., : 1989, *Sol. Phys.*, **121**, 323

[123] Rieger E., Share G.H., Forrest D.J. Kanback G., Reppin C. and Chupp E.L. :1985, *Nature*, **312**, 623

[124] Roach G.F. :1982 in *Green's Functions*, Cambridge University Press

[125] Robinson R.D. :1980, *Astrophys. J.*, **239**,961

[126] Rusbridge M.G. :1971, *Plasma Physics*, **13**, 977

[127] Schindler K., Hesse M. and Birn J. :1988, *J.Geophys. Res*, bf 93, A3, 5547

[128] Sonnerup B.U. Ö :1970, *J. Plasma Phys.*, **4**, 161

[129] Sonnerup B.U. Ö. :1971 *J. Geophys. Res.*, **76**, 8211

[130] Speiser, T.W. :1965, *J. Geophys. Res.*, **70**, 4219

[131] Speiser, T.W. :1970, *Planet. Space Sci.*, **18**, 613

[132] Spicer, D. S. :1976, *NRL Report*, Washington, D.C.

[133] Spicer, D. S. :1977, *Solar Phys.*, **53**, 305

[134] Spicer, D. S. :1982, *Adv. Space Res.*, **2**, no11, 135

[135] Spitzer L. JR. : 1962 in *Physics of fully ionised gases*, Interscience Publishers

[136] Stenflo J. O. :1994: in *Solar Magnetic Fields: Polarised Radiation Diagnostics*, Kluwer Academic Publishers

[137] Stoer, J., Bulirsch, R., :1980 in *Introduction to numerical analysis*, (Springer-Verlag)

[138] Svestka Z. : 1976 *Solar Flares*, D.Reidel Publishing Company

[139] Svestka Z. and Hick P. :1986, *Solar Phys.*, **104**, 187

[140] Sweet P.A. :1958 in *Electromagnetic Phenomena in Cosmical Physics*, edited by B. Lehnert, CUP, London.

[141] Syrovatskii S.I. :1966, *Sov. Astr.*, **10**, 270

[142] Syrovatskii S.I. :1966, *Sov. Phys. JETP*, **33**, 933

[143] Syrovatskii S.I. :1981, *Ann. Rev. Astron. Astrophys.*, **19**, 163-229

[144] Tucker W.H. : 1975 in *Radiation processes in astrophysics*, The MIT Press

[145] Tanaka K. :1978, *Solar Phys.*, **58**, 149

[146] Tanaka K. : 1983 *Activity in Red-Dwarf Stars*, Proc. IAU Colloquium 71, edited by Byrne P.B. and Rodono M., Reidel, Dordrecht

[147] Uchida Y. and Sakurai T. :1983, in *Activity in Red Dwarf Stars, IAU Colloq. 71*, edited by M. Rodono, and P. Byrne, Reidel

[148] Van Tend W., Kuperus M. :1978, *Sol. Phys.*, **59**, 115

[149] Vasyliunas V.M. :1975, *Rev. Geophys.*, **13**, 303

[150] Vernazza J. E., Avrett E.H. and Loeser R. :1981, *Ap. J. Supp. Ser.*, **45**, 635

[151] Vlahos L. :1989, *Sol. Phys.*, **121**, 431

[152] Wang H.T. and Ramaty R. : 1974, *Solar Phys.*, **36**, 129

[153] White S.M. :1994, in *High Energy Solar Phenomena - A New Era of Spacecraft Measurements*, edited by J.M. Ryan and W.T. Vestrand, AIP 294

[154] Yaji K., Kosugi T., Sakao T., Masuda S., Inda-Koide M., and Hanaoka Y. :1994 *Proceedings of Kofu Symposium*, 143, NRO Report N. 360

[155] Yoshida, H. :1993 *Celest. Mech.*, **56**, 27-43

[156] Zirker J.B. 1993, *Solar Phys.*, **148**, 43

[157] Zirin H. :1988 *Astrophysics of the Sun* Cambridge University Press